frontiers | Research Topics

Insights in cancer imaging and image-directed interventions: 2021

Edited by
Zaver Bhujwalla and Giuseppe Esposito

Published in
Frontiers in Oncology

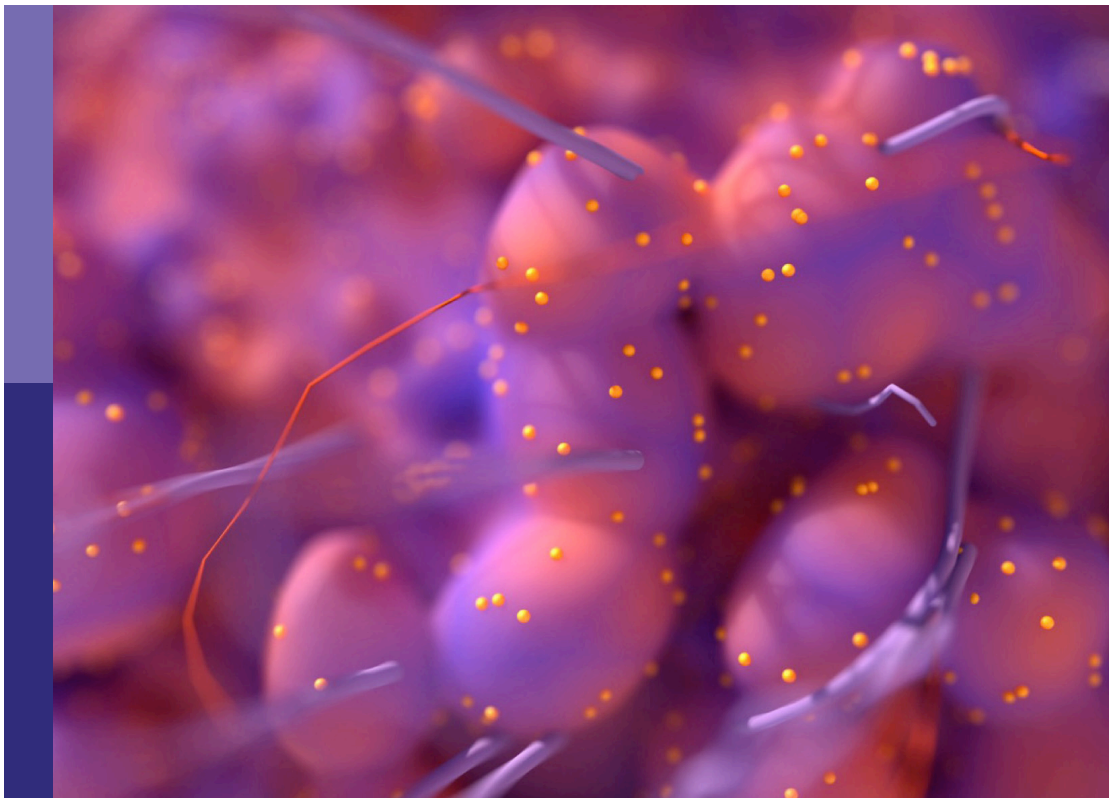

ISSN 1664-8714
ISBN 978-2-83251-573-0
DOI 10.3389/978-2-83251-573-0

About Frontiers

Frontiers is more than just an open access publisher of scholarly articles: it is a pioneering approach to the world of academia, radically improving the way scholarly research is managed. The grand vision of Frontiers is a world where all people have an equal opportunity to seek, share and generate knowledge. Frontiers provides immediate and permanent online open access to all its publications, but this alone is not enough to realize our grand goals.

Frontiers journal series

The Frontiers journal series is a multi-tier and interdisciplinary set of open-access, online journals, promising a paradigm shift from the current review, selection and dissemination processes in academic publishing. All Frontiers journals are driven by researchers for researchers; therefore, they constitute a service to the scholarly community. At the same time, the *Frontiers journal series* operates on a revolutionary invention, the tiered publishing system, initially addressing specific communities of scholars, and gradually climbing up to broader public understanding, thus serving the interests of the lay society, too.

Dedication to quality

Each Frontiers article is a landmark of the highest quality, thanks to genuinely collaborative interactions between authors and review editors, who include some of the world's best academicians. Research must be certified by peers before entering a stream of knowledge that may eventually reach the public - and shape society; therefore, Frontiers only applies the most rigorous and unbiased reviews. Frontiers revolutionizes research publishing by freely delivering the most outstanding research, evaluated with no bias from both the academic and social point of view. By applying the most advanced information technologies, Frontiers is catapulting scholarly publishing into a new generation.

What are Frontiers Research Topics?

Frontiers Research Topics are very popular trademarks of the *Frontiers journals series*: they are collections of at least ten articles, all centered on a particular subject. With their unique mix of varied contributions from Original Research to Review Articles, Frontiers Research Topics unify the most influential researchers, the latest key findings and historical advances in a hot research area.

Find out more on how to host your own Frontiers Research Topic or contribute to one as an author by contacting the Frontiers editorial office: frontiersin.org/about/contact

Insights in cancer imaging and image-directed interventions: 2021

Topic editors

Zaver Bhujwalla — Johns Hopkins University, United States

Giuseppe Esposito — MedStar Georgetown University Hospital, United States

Citation

Bhujwalla, Z., Esposito, G., eds. (2023). *Insights in cancer imaging and image-directed interventions: 2021*. Lausanne: Frontiers Media SA.

doi: 10.3389/978-2-83251-573-0

Table of contents

frontiers in Oncology

ORIGINAL RESEARCH
published: 31 May 2021
doi: 10.3389/fonc.2021.673775

Automatic Image Selection Model Based on Machine Learning for Endobronchial Ultrasound Strain Elastography Videos

Xinxin Zhi[1,2,3†], *Jin Li*[4†], *Junxiang Chen*[1,2,3], *Lei Wang*[5], *Fangfang Xie*[1,2,3], *Wenrui Dai*[4*], *Jiayuan Sun*[1,2,3*] *and Hongkai Xiong*[4]

[1] Department of Respiratory Endoscopy, Shanghai Chest Hospital, Shanghai Jiao Tong University, Shanghai, China, [2] Department of Respiratory and Critical Care Medicine, Shanghai Chest Hospital, Shanghai Jiao Tong University, Shanghai, China, [3] Shanghai Engineering Research Center of Respiratory Endoscopy, Shanghai, China, [4] School of Electronic Information & Electrical Engineering, Shanghai Jiao Tong University, Shanghai, China, [5] Department of Ultrasound, Shanghai Chest Hospital, Shanghai Jiao Tong University, Shanghai, China

OPEN ACCESS

Edited by:
Po-Hsiang Tsui,
Chang Gung University, Taiwan

Reviewed by:
Roel Verhoeven,
Radboud University Nijmegen Medical Centre, Netherlands
Man Chen,
Shanghai Jiao Tong University, China

***Correspondence:**
Jiayuan Sun
xkyyjysun@163.com
Wenrui Dai
daiwenrui@sjtu.edu.cn

[†]These authors have contributed equally to this work

Specialty section:
This article was submitted to Cancer Imaging and Image-directed Interventions, a section of the journal Frontiers in Oncology

Received: 28 February 2021
Accepted: 10 May 2021
Published: 31 May 2021

Citation:
Zhi X, Li J, Chen J, Wang L, Xie F, Dai W, Sun J and Xiong H (2021) Automatic Image Selection Model Based on Machine Learning for Endobronchial Ultrasound Strain Elastography Videos. Front. Oncol. 11:673775. doi: 10.3389/fonc.2021.673775

Background: Endoscopic ultrasound (EBUS) strain elastography can diagnose intrathoracic benign and malignant lymph nodes (LNs) by reflecting the relative stiffness of tissues. Due to strong subjectivity, it is difficult to give full play to the diagnostic efficiency of strain elastography. This study aims to use machine learning to automatically select high-quality and stable representative images from EBUS strain elastography videos.

Methods: LNs with qualified strain elastography videos from June 2019 to November 2019 were enrolled in the training and validation sets randomly at a quantity ratio of 3:1 to train an automatic image selection model using machine learning algorithm. The strain elastography videos in December 2019 were used as the test set, from which three representative images were selected for each LN by the model. Meanwhile, three experts and three trainees selected one representative image severally for each LN on the test set. Qualitative grading score and four quantitative methods were used to evaluate images above to assess the performance of the automatic image selection model.

Results: A total of 415 LNs were included in the training and validation sets and 91 LNs in the test set. Result of the qualitative grading score showed that there was no statistical difference between the three images selected by the machine learning model. Coefficient of variation (CV) values of the four quantitative methods in the machine learning group were all lower than the corresponding CV values in the expert and trainee groups, which demonstrated great stability of the machine learning model. Diagnostic performance analysis on the four quantitative methods showed that the diagnostic accuracies were range from 70.33% to 73.63% in the trainee group, 78.02% to 83.52% in the machine learning group, and 80.22% to 82.42% in the expert group. Moreover, there were no statistical differences in corresponding mean values of the four quantitative methods between the machine learning and expert groups ($p > 0.05$).

Conclusion: The automatic image selection model established in this study can help select stable and high-quality representative images from EBUS strain elastography videos, which has great potential in the diagnosis of intrathoracic LNs.

Keywords: endobronchial ultrasound, strain elastography, machine learning, lymph nodes, image selection

INTRODUCTION

The differential diagnosis of malignant and benign intrathoracic lymph nodes (LNs) is an important medical problem related to the diagnosis and prognosis of intrathoracic diseases. Compared with surgical examination, needle techniques are recommended as the first choice to obtain tissues (1, 2). Endobronchial ultrasound guided transbronchial needle aspiration (EBUS-TBNA) is an important minimally invasive tool to evaluate the benign and malignant intrathoracic LNs.

Previous literature mentioned that ultrasonographic features were suggested to be used for predicting benign and malignant diagnosis of patients undergoing EBUS-TBNA (3). EBUS imaging includes three modes of grayscale, blood flow Doppler and strain elastography. Studies indicated that strain elastography had the best diagnostic value among the three modes (4, 5). Elastography has been widely used in breast lesions, thyroid, pancreas, prostate, liver and endoscopic ultrasound (6–11). Through exerting repeated and slight pressure on the examined lesions, elastography can quantify the elasticity of tissues by measuring the deformation and present it in the form of various colors (12–14). The colors from yellow/red, green to blue represent tissues from lower to higher relative stiffness, respectively (13). Malignant infiltration of tumor cells can alter cell morphology and overall histology of tissues resulting in a stiffer property. Elastography can indirectly predict malignant lesions by reflecting its relative stiffness (15). EBUS strain elastography plays an important role in differentiating intrathoracic benign and malignant LNs (16). The bronchoscopist can select the target LN and possible metastatic sites within the LN for biopsy according to strain elastography during EBUS-TBNA (17, 18).

With respect to qualitative analysis of strain elastography image, the five-score grading method had specific classification and when score 1–3 was defined as benign and score 4–5 as malignant, the diagnostic accuracy in predicting malignant LNs can reach 83.32% (4). Quantitative methods include stiff area ratio (SAR), elasticity ratio of blue/green (B/G), mean hue value and mean gray value can comprehensively evaluate the quality of elastography images (4, 5, 18–23). Qualitative methods are more convenient for clinical application, but strong subjectivity exists inevitably. Therefore, doctors with various experience may have different judgement on the same strain elastography video. Although the quantitative method are relatively objective, the images used for quantitative analysis are still selected subjectively. Moreover, ultrasound imaging is the specialty of ultrasound doctors, and endoscopists may not make full use of strain elastography due to the limited experience.

In recent years, with the development of machine learning algorithm, machine learning has shown an important role in the field of medical imaging with favorable performance, such as skin cancer, retinal fundus photographs, gastrointestinal endoscopy, chest CT and other aspects (24–27). By extracting multiple quantitative image features which may be difficult for doctors to observe, machine learning can give a likelihood of each case and classify images accurately. Research demonstrated that machine learning combined with colorectal endoscopy for colorectal lesions diagnosis was comparable to that of experts (28). In the field of bronchoscopy, a computer-assisted diagnosis (CAD) system has been used to classify normal mucosa, chronic bronchitis and lung tumors under the white-light bronchoscopy, which achieved a classification rate of 80% (29). In addition, a machine learning texture model can get an accuracy of 86% in classifying cancer subtypes using bronchoscopic findings (30). However, there are few applications of machine learning on EBUS strain elastography. Therefore, the purpose of this study was to establish a machine learning model which can realize automatic selection of representative images from strain elastography videos.

MATERIALS AND METHODS

Patients and LNs

Patients who met the following criteria and underwent EBUS-TBNA examination in Shanghai Chest Hospital from June to December 2019 were enrolled in this study (1): At least one enlarged intrathoracic LNs (short axis >1 cm) based on computed tomography (CT), or at least one positive ^{18}F-FDG uptake detected (standardized uptake value >2.5) by positron emission tomography (2); Pathological confirmation was clinically required and EBUS-TBNA examination was feasible (3); Patients who did not have contraindications to EBUS-TBNA and signed informed consent. LNs with qualified strain elastography videos were analyzed in the study. LNs in December were used as the test set to assess the automatic representative images selection model and the remained were used as the training set and validation set. This study was approved by the local Ethics Committee of Shanghai Chest Hospital (No. KS1947) and registered at ClinicalTrials.gov PRS (NCT04328792).

EBUS Strain Elastography Procedure

LNs were examined by the ultrasound bronchoscopy (BF-UC260FW, Olympus, Tokyo, Japan) and EBUS strain elastography videos were recorded by the ultrasound processor

(EU-ME2, Olympus, Tokyo, Japan). The operator detected the location of the target LN and measured the EBUS size at the maximal cross-section of grayscale mode. After observing the grayscale and blood flow Doppler modes, the operator switches to the strain elastography mode and elastography imaging was formed through the patient's respiration, cardiac impulse and blood vessel pulse generally. In the case of unsatisfactory imaging, the operator shall exert appropriate pressure to the target LN by pressing the up-down angle lever of bronchoscope at a frequency of three to five times per second to obtain better imaging. The maximal cross-section of the LN was recorded and two 20-second videos were saved (4). Subsequently, EBUS-TBNA was performed to obtain the cytological specimens for pathological examination. All operators retained strain elastography videos and sampled LNs according to the above standard steps. The final diagnosis of LNs was determined on EBUS-TBNA, thoracoscopy, mediastinoscopy, transthoracic thoracotomy or other pathological examinations, microbiological examination or clinical follow-up for more than one year.

Development of Automatic Representative Images Selection Model for Strain Elastography Videos

The training set and validation set were randomly divided at a quantity ratio of 3:1 to train the model with optimal hyper-parameters. The same proportion of benign and malignant LNs was maintained in the two datasets. We developed models with various values of hyper-parameters on the training set and assessed these models on the validation set to determine the hyper-parameter according to the performance. Once the hyper-parameter was determined, we used both the training set and validation set to train the model for prediction and evaluation on the test set. In this paper, the hyper-parameters included the number of representation patterns and whether adopting the update-and-predict strategy or not. The candidate numbers of representation patterns included 32, 64, and 128. Blind to the final diagnosis of LNs, two experts with experience of EBUS images observation >500 LNs assessed the image quality of the validation sets together as following: score 1 (scattered soft, mixed green-yellow-red), score 2 (homogeneous soft, predominantly green), score 3 (intermediate, mixed blue-green-yellow-red), score 4 (scattered hard, mixed blue-green), score 5 (homogeneous hard, predominantly blue). Scores 1–3 are classified as benign and 4–5 as malignant (4). Four quantitative methods were also used to verify the diagnostic performance of the validation sets. Assessments on the validation set showed that we could yield the highest accuracy when adopting run-twice strategy and using 64 representative patterns (**Supplementary Tables 1** and **2**). When we trained the model with determined hyper-parameters, we used it to make prediction on the test set. Note that the test set is not used in the phase of training.

Figure 1 illustrated the process of representative strain elastography images selection with the proposed machine learning algorithm. Initially, the elastography video was converted into a sequence of frames with quality evaluated. According to the proportion of colored pixels and relative intensity of a frame (**Supplementary Material** and **Supplementary Figure 1**), the original frames were divided into qualified and unqualified, and only qualified frames were kept for succeeding procedures. Additionally, to avoid overwhelming qualified frames and reduce complexity, the adjacent two frames of selected qualified frame were dropped. Then, feature engineering was performed on the remaining frames. We constructed the features of each frame with the 512 bin color histogram to describe the color distribution of elastography images (31). Further, the principal component analysis (PCA) algorithm was applied to reduce the feature dimension, and a 40-dimension feature space was obtained. The number of dimensions depended on the training set, and 40-dimension was capable to keep 99% component in this study. Clustering plays an important role in video analysis (32–35). Considering the selective principle of experts that the most repeatable pattern across the video is selected as representative frames, we employed the k-means clustering algorithm in this study. In the phase of training, the k-means clustering was performed on the training set to obtain representative patterns (cluster centers). In the phase of prediction, the frame features from the test video were allocated to patterns extracted from the training set. Given a test video, the pattern owning most frames was regarded as the representative pattern and three frames closest to the representative pattern were selected as the representative images.

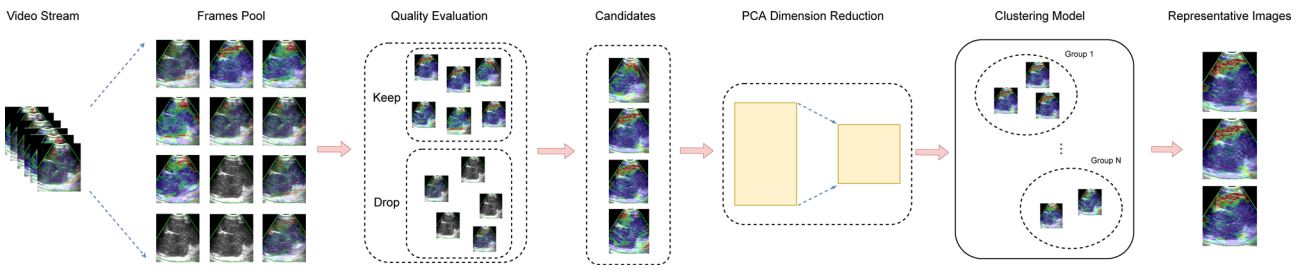

FIGURE 1 | The process of automatic selection of representative images. Frames were extracted from the video stream to construct a frame pool initially. Then, inferior frames are dropped during the quality evaluation procedure, and the eligible frames are kept as candidates for representative images. Next, the PCA was employed for dimension reduction. Ultimately, the clustering model select representative images from candidates. PCA, principal component analysis.

In real-world applications, however, it is hard to collect a training set that has sufficient examples to cover all possible situations and guarantee the generalization ability of the trained model. Consequently, a limited training set usually leads to a performance gap, when applied to the real data. To narrow this gap, in the phase of prediction, we proposed an update-and-predict strategy that ran the trained model twice on the test set. The first run produced the initial predictions of test videos which were used for updating the cluster centers in the model. Subsequently, the updated model was used to obtain the final predictions on the test set. Note that the K-means clustering is an unsupervised learning algorithm that does not require manual annotation or ground truth. Therefore, we leveraged K-means clustering in this paper to update our model using only the predictions of test videos rather than accessing their labels. The label information was not leaked in the phase of prediction. As a result, we can narrow the gap between the training set and test set and do not cause the leakage of label (supervision) information by using the update-and-predict strategy.

Evaluation of Representative Images

For the three images selected by the automatic image selection model on the test set, the same two experts evaluated grading score together. Expert group and trainee group (experience of CP-EBUS image observation less than 30 LNs) were employed to select representative images which were used for comparison with that of machine learning. The three experts reviewed two elastography videos of each LN and selected one representative image for qualitative evaluation, respectively. Qualified images shall cover the maximal cross-section of the target LN and have good repeatability (4). Three trainees selected representative frames and evaluated qualitative score of corresponding pictures in the same way. The quantitative measurement of the three groups of images was operated by the elastography quantitative system (Registration number: 2015SR191866) developed by Matlab and the region of interest was outlined by an expert (**Figure 2**). Results of four quantitative methods including SAR, B/G, mean hue value and mean gray value were output by the program. The first method SAR was the ratio of blue pixels to pixels of the whole LN (5, 18–20). RGB is a color space model which represents the red, green and blue channel colors, and B/G was calculated in this study (21). Hue histogram analysis was performed for selected images and the third method mean hue value corresponds to the global elasticity of the LN (22). The fourth method mean gray value has been studied in the diagnosis of breast cancer and intrathoracic LNs (4, 23). All above procedures carried by experts and trainees were in the situation of blind to the clinical information and pathological results of target LNs.

Statistical Analysis

For qualitative score, the Friedman test was used for the differences among the three images selected by the automatic image selection model and experts, and the Wilcoxon signed-rank test was used for the pair comparison. For quantitative variables, receiver operating characteristic (ROC) curve was used to obtain the area under the curve (AUC) and the cut-off value with the best diagnostic performance. The paired t-test was used for quantitative mean values comparison between images of the machine learning model and experts. The stability of the quantitative results within the three groups was evaluated using the coefficient of variation (CV), and the comparison of

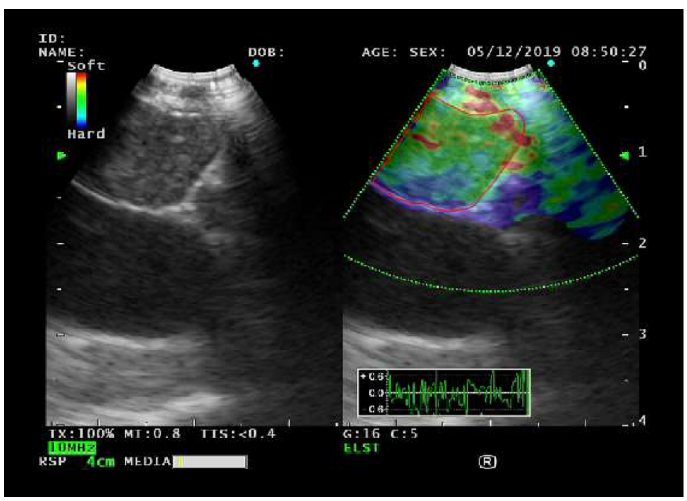

SAR: 0.14587

R channel: 72.2532

G channel: 121.6371

B channel: 85.5878

B/G: 0.70363

B/R: 1.1846

G/R: 1.6835

Mean hue value: 103.8785

Mean gray value: 182.2377

FIGURE 2 | Delineation of ROI on strain elastography images and output of quantitative parameters. Representative images of the machine learning group, expert group and trainee group were all input into a computer program developed by Matlab™. The schematic diagram showed an elastography image of a LN with nonspecific lymphadenitis in 4R station, and ROI was outlined on the elastography image. Results of the four quantitative methods including SAR, RGB, mean hue value and mean gray value were then output by the program. ROI, region of interest; LN, lymph node; SAR, stiff area ratio; B/G, elasticity ratio of blue/green; B/R, elasticity ratio of blue/red; G/R, elasticity ratio of green/red.

the CV among the three groups was further analyzed by the paired t-test. The p value <0.05 was considered statistically significant for above statistical analyses. Sensitivity, specificity, positive predictive value (PPV), negative predictive value (NPV), and accuracy for differentiating benign and malignant LNs were calculated by the corresponding formulas. All statistical analyses were performed by SPSS version 25.0 (IBM Corp., Armonk, NY, USA).

RESULTS

Patients and LNs

A total of 415 LNs from 351 patients (247 men, 104 women; age: 60.45 ± 11.31 years) were analyzed in the training and validation sets, and 91 LNs from 73 patients (52 men, 21 women; age:58.82 ± 10.95 years) were used as the test set (**Table 1**). 311 LNs were included in the training set and 104 LNs in the validation set. Malignant LNs accounted for 61.69% in the training and validation sets and 58.24% in the test set. **Figure 3** displayed the representative images selected by machine learning, expert and trainee groups.

Stability and Diagnostic Performance Analysis by the Qualitative Grading Score

To evaluate the stability of machine learning selected images, we analyzed the differences between the three pictures of machine learning, expert and trainee groups, respectively. Results demonstrated that there was a statistical difference in the expert group, while the images of machine learning and trainee groups were relatively stable (**Table 2**). Besides, diagnostic performance in **Table 3** showed that the diagnostic accuracies of machine learning group were 82.42, 79.12 and 75.82% respectively, slightly lower than experts (p = 0.121), but significantly higher than trainee group (p <0.001).

Stability Analysis by Quantitative Methods

In order to assess machine learning selected images more objectively, paired t-test was conducted on quantitative results of machine learning and expert groups. No statistical difference between the two groups was found which demonstrated that images selected by machine learning can reach the expert level (**Table 4**). In terms of the stability analysis of the images within and between the three groups, **Table 5** showed that CV values of machine learning group were lower than expert and trainee groups for each indicator, and among which the trainee group had the highest CV values. Besides, for SAR and B/G, there were statistical differences between machine learning and the other two groups, indicating that machine learning selected images in the test set were more stable than those selected by expert and trainee groups (**Table 5**).

Diagnostic Performance Analysis by Quantitative Methods

The ROC curves were performed on quantitative results of the three groups and cut-off values with the best diagnostic performances were drawn (**Figure 4**). **Table 6** reflected that the accuracies of four quantitative methods including SAR, B/G, mean hue value and mean gray value in the machine learning group were 83.52%, 78.01%, 80.22% and 80.22% respectively. Correspondingly the expert groups were 80.22%, 81.32%, 82.42% and 82.42% respectively. By contrast, the best indicator in the trainee group was B/G, with the highest accuracy of only 73.63%.

TABLE 1 | Characteristic of LNs in the training, validation and test sets.

Characteristic of LNs	Training and validation sets No. (%)	Test set No. (%)
EBUS size		
Long axis, mean ± SD, mm	21.55 ± 6.71	22.48 ± 7.18
Short axis, mean ± SD, mm	17.90 ± 9.56	17.23 ± 6.45
CT size※		
Long axis, mean ± SD, mm	25.50 ± 9.48	24.35 ± 8.49
Short axis, mean ± SD, mm	16.70 ± 6.73	16.45 ± 7.02
Station		
2L	1 (0.24)	0 (0.00)
2R	8 (1.93)	1 (1.10)
3P	2 (0.48)	0 (0.00)
4L	19 (4.58)	7 (7.69)
4R	135 (32.53)	30 (32.97)
7	160 (38.55)	26 (28.57)
10L	2 (0.48)	1 (1.10)
10R	3 (0.72)	1 (1.10)
11L	32 (7.71)	10 (10.99)
11Rs	32 (7.71)	5 (5.49)
11Ri	19 (4.58)	10 (10.99)
12L	1 (0.24)	0 (0.00)
12R	1 (0.24)	0 (0.00)
Diagnosis		
Malignant	256 (61.69)	53 (58.24)
Adenocarcinoma	110 (26.51)	25 (27.47)
Squamous carcinoma	39 (9.40)	5 (5.49)
NSCLC-NOS	13 (3.13)	4 (4.40)
Small cell lung cancer	60 (14.46)	15 (16.48)
Large cell neuroendocrine carcinoma	1 (0.24)	0 (0.00)
NET-NOS	11 (2.65)	2 (2.20)
Unknown type of lung cancer	13 (3.13)	1 (1.10)
Carcinosarcoma	1 (0.24)	0 (0.00)
Lymphoma	3 (0.72)	0 (0.00)
Metastatic tumors (non-lung primary malignancy)	5 (1.20)	1 (1.10)
Benign	159 (38.31)	38 (41.76)
Nonspecific lymphadenitis	97 (23.37)	16 (17.58)
Sarcoidosis	53 (12.77)	15 (16.48)
Tuberculosis	9 (2.17)	7 (7.69)

※*The size of LNs on CT images was measured on 393 LNs in the training and validation sets and 88 LNs in the test set. A total of 25 LNs were missing on CT in both groups.*
LNs, lymph nodes; NSCLC-NOS, non-small cell lung cancer not otherwise specified; NET-NOS, neuroendocrine tumor not otherwise specified.

DISCUSSION

Lung cancer is the leading cause of cancer associated morbidity and mortality around the world (36). Pulmonary diseases can be

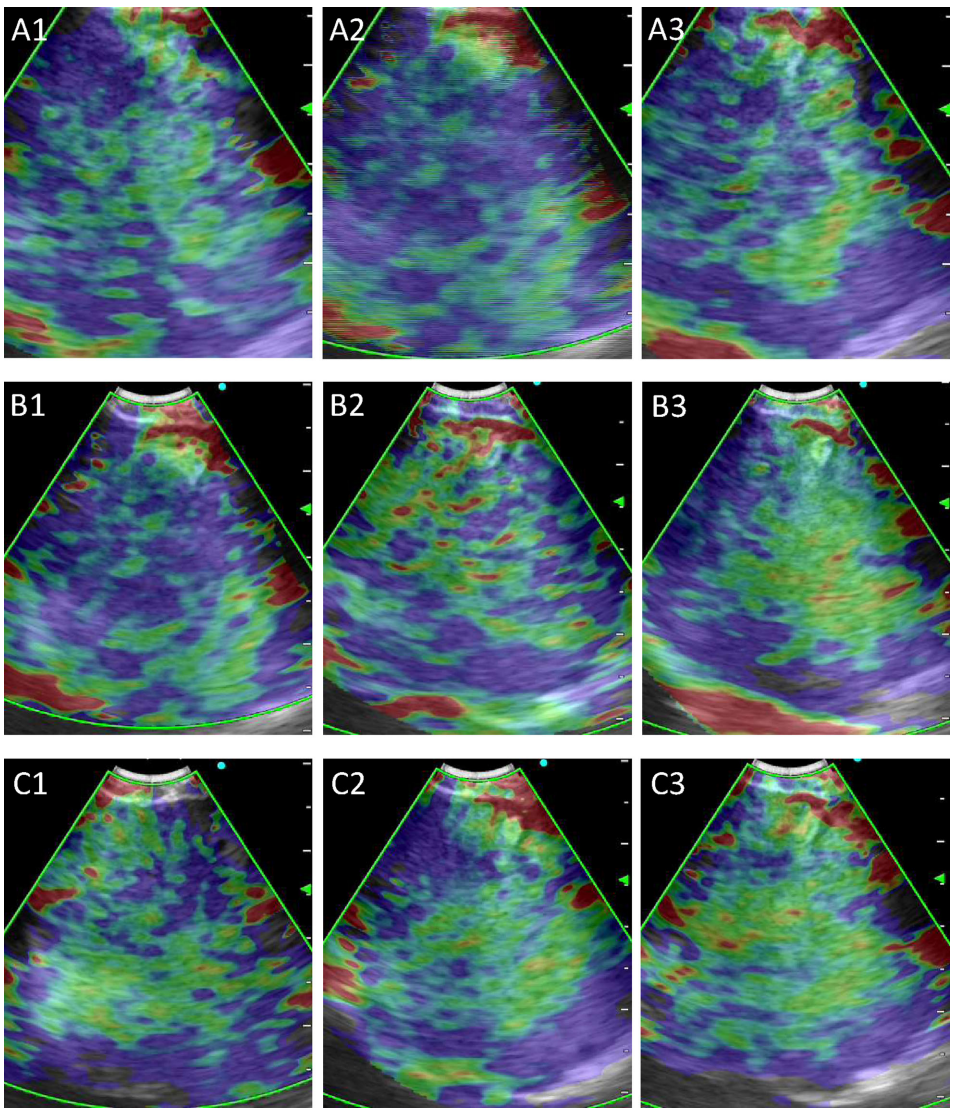

FIGURE 3 | Representative images selected by machine learning, expert and trainee groups. **(A)** 1–3 are representative images selected by the machine learning model; **(B)** 1–3 are representative images selected by the three experts; **(C)** 1–3 are representative images selected by the three trainees.

TABLE 2 | Differences between images within each group by qualitative grading score.

	p value		
	Machine learning group	**Expert group**	**Trainee group**
Image 123	0.210	0.036	0.205
Image 12	0.134	0.058	0.862
Image 13	0.088	0.029	0.105
Image 23	0.637	0.366	0.059

diagnosed by draining LNs, therefore the diagnosis of intrathoracic LNs is related to subsequent treatment strategies. EBUS strain elastography imaging is a useful noninvasive tool in differentiating benign from malignant LNs. The machine learning algorithm was used to automatically select representative images from the EBUS strain elastography videos in this study and the image quality was equivalent to the expert level.

Traditional qualitative methods are convenient for clinical application, but subjectivity and the difference in experience between different doctors can affect the accurate diagnosis. Images used for quantitative analysis are still manually selected which cannot avoid subjectivity. The CV values in **Table 5** reflect the instability of manual selection, and the images selected by doctors with different experience had various quality. For qualitative results, there was a statistical difference between the images selected by experts ($p = 0.036$) but not by trainees ($p =$

TABLE 3 | Diagnostic efficiency of the three groups by qualitative grading score.

Group	Sen	Spe	PPV	NPV	Acc	FPR	FNR
Machine learning 1	84.91%	78.95%	84.91%	78.95%	82.42%	21.05%	15.09%
Machine learning 2	83.02%	73.68%	81.48%	75.68%	79.12%	26.32%	16.98%
Machine learning 3	79.25%	71.05%	79.25%	71.05%	75.82%	28.95%	20.75%
Expert 1	92.45%	73.68%	83.05%	87.50%	84.62%	26.32%	7.55%
Expert 2	90.57%	73.68%	82.76%	84.85%	83.52%	26.32%	9.43%
Expert 3	88.68%	78.95%	85.45%	83.33%	84.62%	21.05%	11.32%
Trainee 1	62.26%	60.53%	68.75%	53.49%	61.54%	39.47%	37.74%
Trainee 2	64.15%	71.05%	75.56%	58.70%	67.03%	28.95%	35.85%
Trainee 3	69.81%	60.53%	71.15%	58.97%	65.93%	39.47%	30.19%

Sen, sensitivity; Spe, specificity; PPV, positive predictive value; NPV, negative predictive value; Acc, accuracy; FPR, false positive rate; FNR, false negative rate.

TABLE 4 | Comparison of quantitative mean values between machine learning and expert groups.

Variable	p value
SAR	0.801
B/G	0.693
Mean hue value	0.862
Mean gray value	0.514

SAR, stiff area ratio; B/G, elasticity ratio of blue/green.

0.205) (**Table 2**). However, a bigger difference presented in diagnostic accuracies among trainees than experts. This was because the diagnosis performance was calculated based on the dichotomy, that is, 1–3 were classified as benign and 4–5 as malignant, yet the differences of qualitative score were counted according to the five categories. Besides, regarding the diagnostic performance among the three groups, the qualitative diagnostic performance of expert group was the highest in the whole study. However, the quantitative results were similar to that of machine learning group, possibly due to the subjectivity of qualitative assessment among different experts. Compared with the qualitative results, the quantitative methods can evaluate the image quality selected by machine learning more objectively. Elastography can only reflect the relative hardness of target lesion, and fibrosis within sarcoidosis may result in stiffer tissue and necrosis within malignant LNs may lead to softer lesions (37, 38). Thus, the highest diagnostic accuracy of automatic image selection model by qualitative and quantitative methods can only reach 83.52%, which was not only due to inaccurate image selection but also the property of the lesion itself. In addition to the four quantitative methods used in this study, strain ratio and strain histogram are also quantitative methods and study found that strain histogram showed better predictive value than strain ratio with a diagnostic rate of 82% in malignant LNs prediction (39). It can be seen that different quantitative methods can lead to various diagnostic results, and there is no unified quantitative method at present. In this study, different results were produced by the four methods in the three groups, but the quality of the images had more effect than the quantitative method on the final results. Notably, the machine learning algorithm in this study was valid for representative images selection of EBUS strain elastography videos, but the implementation of this algorithm needed integration by the manufacturer to become clinically applicable.

This study still had some limitations. Since there was no restriction on the type of disease included, the machine learning model was only suitable for the diagnosis of intrathoracic LNs enlargement, and further studies were need to determine whether or not this technique is valid to the stage of lung cancer. Besides, although high-quality images were selected from elastography videos, no diagnosis was made by the model for these images, and EBUS modes of grayscale and blood flow Doppler were not applied. The automatic EBUS multimodal image selection and diagnosis may be more convenient for clinical application. Moreover, this was a single-center retrospective study with limited number of LNs and some diseases accounted for limited proportions. Prospective studies and more LNs to train, validate and test the model may acquire more stable models and more convincing results. Thus, it was worthwhile to carry out multi-center studies to improve the outcome of the model (40).

TABLE 5 | Differences in CV values of quantitative methods among the three groups.

Indicator	Machine learning (mean ± SD)	Experts (mean ± SD)	Trainees (mean ± SD)	Machine learning *vs.* Experts (p value)	Machine learning *vs.* Trainees (p value)	Experts *vs.* Trainees (p value)
SAR	0.127 ± 0.109	0.167 ± 0.124	0.200 ± 0.156	2.18E–03	3.22E–06	5.68E–02
B/G	0.079 ± 0.061	0.105 ± 0.067	0.127 ± 0.070	6.69E–03	2.72E–06	2.86E–02
Mean hue value	0.036 ± 0.029	0.042 ± 0.024	0.053 ± 0.036	1.44E–01	7.57E–05	9.50E–03
Mean gray value	0.013 ± 0.044	0.020 ± 0.062	0.022 ± 0.062	3.96E–01	2.56E–01	8.07E–01

CV, coefficient of variation; SD, standard deviation; SAR, stiff area ratio; B/G, elasticity ratio of blue/green.

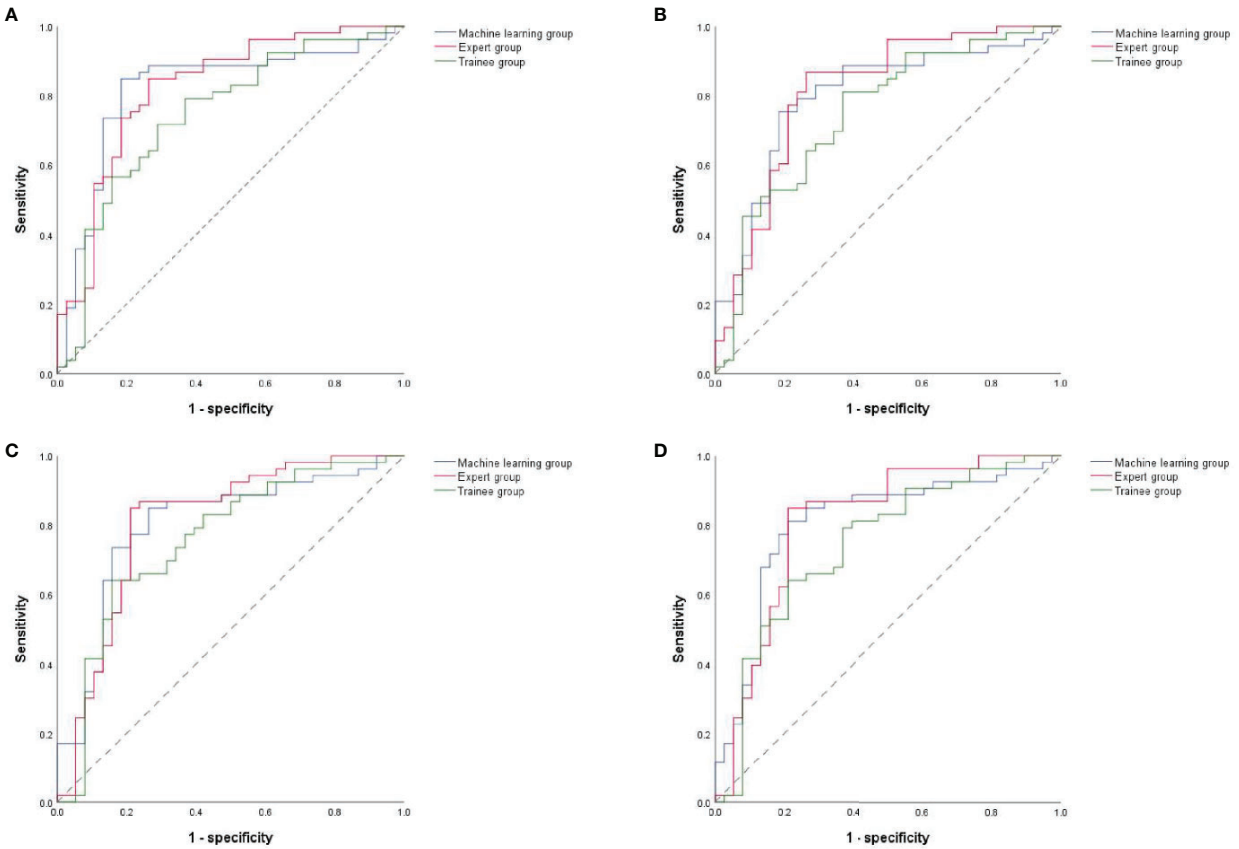

FIGURE 4 | ROC curves of four quantitative methods for machine learning, expert and trainee groups. **(A–D)** illustrate four quantitative indicators including SAR, B/G, mean hue value and mean gray value, respectively. ROC, receiver operating characteristic; SAR, stiff area ratio; B/G, elasticity ratio of blue/green.

TABLE 6 | Diagnostic efficiency of the three groups by quantitative methods.

Group	AUC	Cut-off	Sen	Spe	PPV	NPV	Acc
Machine learning							
SAR	0.819	0.402	84.91%	81.58%	86.54%	79.49%	83.52%
B/G	0.798	1.176	75.47%	81.58%	85.11%	70.45%	78.02%
Mean hue value	0.801	133.762	84.91%	73.68%	81.82%	77.78%	80.22%
Mean gray value	0.805	194.632	81.13%	78.95%	84.31%	75.00%	80.22%
Expert							
SAR	0.822	0.403	84.91%	73.68%	81.82%	77.78%	80.22%
B/G	0.812	1.116	86.79%	73.68%	82.14%	80.00%	81.32%
Mean hue value	0.808	134.870	84.91%	78.95%	84.91%	78.95%	82.42%
Mean gray value	0.809	194.329	84.91%	78.95%	84.91%	78.95%	82.42%
Trainee							
SAR	0.746	0.452	71.70%	71.05%	77.55%	64.29%	71.43%
B/G	0.750	1.043	81.13%	63.16%	75.44%	70.59%	73.63%
Mean hue value	0.758	139.811	64.15%	84.21%	85.00%	62.75%	72.53%
Mean gray value	0.744	195.976	64.15%	78.95%	80.95%	61.22%	70.33%

SAR, stiff area ratio; B/G, elasticity ratio of blue/green; AUC, area under curve; Sen, sensitivity; Spe, specificity; PPV, positive predictive value; NPV, negative predictive value; Acc, accuracy.

In conclusion, through the application of machine learning algorithm to EBUS strain elastography, we realized the automatic selection of high-quality and stable images from strain elastography videos. The automatic image selection model needs further prospective clinical validation and has potential value in guiding the diagnosis of intrathoracic LNs.

DATA AVAILABILITY STATEMENT

The original contributions presented in the study are included in the article/**Supplementary Material**. Further inquiries can be directed to the corresponding authors.

ETHICS STATEMENT

The studies involving human participants were reviewed and approved by Ethics Committee of Shanghai Chest Hospital. Written informed consent for participation was not required for this study in accordance with the national legislation and the institutional requirements. Written informed consent was not obtained from the individual(s) for the publication of any potentially identifiable images or data included in this article.

AUTHOR CONTRIBUTIONS

XZ collected videos, selected representative images, conducted qualitative and quantitative analysis of LNs, and performed statistical analysis. JL designed the machine learning model for automatic selection of representative images. JC and XZ evaluated images selected by machine learning. FX, LW, and JS selected representative images and scored them qualitatively as the expert group. JS and WD designed the study and reviewed the manuscript. JS and HX supported this study. All authors contributed to the article and approved the submitted version.

FUNDING

This work was supported by National Natural Science Foundation of China (grant numbers 81870078, 61720106001, 61971285, and 61932022), Shanghai Municipal Health and Medical Talents Training Program (grant number 2018BR09), Shanghai Municipal Education Commission-Gaofeng Clinical Medicine Grant Support (grant number 20181815), and the Program of Shanghai Academic Research Leader (grant 17XD1401900).

ACKNOWLEDGMENTS

The authors acknowledged the doctors in the Department of Respiratory and Critical Care Medicine of Shanghai Chest Hospital for the collection of strain elastography videos.

SUPPLEMENTARY MATERIAL

The Supplementary Material for this article can be found online at: https://www.frontiersin.org/articles/10.3389/fonc.2021.673775/full#supplementary-material

REFERENCES

1. Silvestri GA, Gonzalez AV, Jantz MA, Margolis ML, Gould MK, Tanoue LT, et al. Methods for Staging non-Small Cell Lung Cancer: Diagnosis and Management of Lung Cancer, 3rd Ed: American College of Chest Physicians Evidence-Based Clinical Practice Guidelines. *Chest* (2013) 143(5 Suppl):e211S–e50S. doi: doi: 10.1378/chest.12-2355
2. Um SW, Kim HK, Jung SH, Han J, Lee KJ, Park HY, et al. Endobronchial Ultrasound Versus Mediastinoscopy for Mediastinal Nodal Staging of non-Small-Cell Lung Cancer. *J Thorac Oncol* (2015) 10(2):331–7. doi: 10.1097/JTO.0000000000000388
3. Wahidi MM, Herth F, Yasufuku K, Shepherd RW, Yarmus L, Chawla M, et al. Technical Aspects of Endobronchial Ultrasound-Guided Transbronchial Needle Aspiration: Chest Guideline and Expert Panel Report. *Chest* (2016) 149(3):816–35. doi: 10.1378/chest.15-1216
4. Sun J, Zheng X, Mao X, Wang L, Xiong H, Herth FJF, et al. Endobronchial Ultrasound Elastography for Evaluation of Intrathoracic Lymph Nodes: A Pilot Study. *Respiration* (2017) 93(5):327–38. doi: 10.1159/000464253
5. Fujiwara T, Nakajima T, Inage T, Sata Y, Sakairi Y, Tamura H, et al. The Combination of Endobronchial Elastography and Sonographic Findings During Endobronchial Ultrasound-Guided Transbronchial Needle Aspiration for Predicting Nodal Metastasis. *Thorac Cancer* (2019) 10 (10):2000–5. doi: 10.1111/1759-7714.13186
6. Garra BS, Cespedes EI, Ophir J, Spratt SR, Zuurbier RA, Magnant CM, et al. Elastography of Breast Lesions: Initial Clinical Results. *Radiology* (1997) 202 (1):79–86. doi: 10.1148/radiology.202.1.8988195
7. Lyshchik A, Higashi T, Asato R, Tanaka S, Ito J, Mai JJ, et al. Thyroid Gland Tumor Diagnosis At US Elastography. *Radiology* (2005) 237(1):202–11. doi: 10.1148/radiol.2363041248
8. Nemakayala D, Patel P, Rahimi E, Fallon MB, Thosani N. Use of Quantitative Endoscopic Ultrasound Elastography for Diagnosis of Pancreatic Neuroendocrine Tumors. *Endoscopic ultrasound* (2016) 5(5):342–5. doi: 10.4103/2303-9027.191680
9. Cochlin DL, Ganatra RH, Griffiths DF. Elastography in the Detection of Prostatic Cancer. *Clin Radiol* (2002) 57(11):1014–20. doi: 10.1053/crad.2002.0989
10. Sandrin L, Fourquet B, Hasquenoph JM, Yon S, Fournier C, Mal F, et al. Transient Elastography: A New Noninvasive Method for Assessment of Hepatic Fibrosis. *Ultrasound Med Biol* (2003) 29(12):1705–13. doi: 10.1016/j.ultrasmedbio.2003.07.001
11. Okasha HH, Mansour M, Attia KA, Khattab HM, Sakr AY, Naguib M, et al. Role of High Resolution Ultrasound/Endosonography and Elastography in Predicting Lymph Node Malignancy. *Endoscopic ultrasound* (2014) 3(1):58–62. doi: 10.4103/2303-9027.121252
12. Ophir J, Céspedes I, Ponnekanti H, Yazdi Y, Li X. Elastography: A Quantitative Method for Imaging the Elasticity of Biological Tissues. *Ultrasonic Imaging* (1991) 13(2):111–34. doi: 10.1177/016173469101300201
13. Zaleska-Dorobisz U, Kaczorowski K, Pawluś A, Puchalska A, Inglot M. Ultrasound Elastography - Review of Techniques and its Clinical Applications. *Adv Clin Exp Med Off Organ Wroclaw Med Univ* (2014) 23 (4):645–55. doi: 10.17219/acem/26301
14. Dietrich CF, Jenssen C, Herth FJ. Endobronchial Ultrasound Elastography. *Endoscopic ultrasound* (2016) 5(4):233–8. doi: 10.4103/2303-9027.187866
15. Ozturk A, Grajo JR, Dhyani M, Anthony BW, Samir AE. Principles of Ultrasound Elastography. *Abdom Radiol (NY)* (2018) 43(4):773–85. doi: 10.1007/s00261-018-1475-6
16. Zhi X, Chen J, Xie F, Sun J, Herth FJF. Diagnostic Value of Endobronchial Ultrasound Image Features: A Specialized Review. *Endoscopic ultrasound* (2020) 10(1):3–18. doi: 10.4103/eus.eus_43_20
17. Nakajima T, Shingyouji M, Nishimura H, Iizasa T, Kaji S, Yasufuku K, et al. New Endobronchial Ultrasound Imaging for Differentiating Metastatic Site Within a Mediastinal Lymph Node. *J Thorac Oncol* (2009) 4(10):1289–90. doi: 10.1097/JTO.0b013e3181b05713

18. Nakajima T, Inage T, Sata Y, Morimoto J, Tagawa T, Suzuki H, et al. Elastography for Predicting and Localizing Nodal Metastases During Endobronchial Ultrasound. *Respiration* (2015) 90(6):499–506. doi: 10.1159/000441798
19. Abedini A, Razavi F, Farahani M, Hashemi M, Emami H, Mohammadi F, et al. The Utility of Elastography During EBUS-TBNA in a Population With a High Prevalence of Anthracosis. *Clin Respir J* (2020) 14(5):488–94. doi: 10.1111/crj.13159
20. Mao XW, Yang JY, Zheng XX, Wang L, Zhu L, Li Y, et al. [Comparison of Two Quantitative Methods of Endobronchial Ultrasound Real-Time Elastography for Evaluating Intrathoracic Lymph Nodes]. *Zhonghua Jie He He Hu Xi Za Zhi* (2017) 40(6):431–4. doi: 10.3760/cma.j.issn.1001-0939.2017.06.007
21. Săftoiu A, Vilmann P, Hassan H, Gorunescu F. Analysis of Endoscopic Ultrasound Elastography Used for Characterisation and Differentiation of Benign and Malignant Lymph Nodes. *Ultraschall Med* (2006) 27(6):535–42. doi: 10.1055/s-2006-927117
22. Săftoiu A, Vilmann P, Ciurea T, Popescu GL, Iordache A, Hassan H, et al. Dynamic Analysis of EUS Used for the Differentiation of Benign and Malignant Lymph Nodes. *Gastrointest Endosc* (2007) 66(2):291–300. doi: 10.1016/j.gie.2006.12.039
23. Landoni V, Francione V, Marzi S, Pasciuti K, Ferrante F, Saracca E, et al. Quantitative Analysis of Elastography Images in the Detection of Breast Cancer. *Eur J Radiol* (2012) 81(7):1527–31. doi: 10.1016/j.ejrad.2011.04.012
24. da Silva GLF, Valente TLA, Silva AC, de Paiva AC, Gattass M. Convolutional Neural Network-Based PSO for Lung Nodule False Positive Reduction on CT Images. *Comput Methods Programs BioMed* (2018) 162:109–18. doi: 10.1016/j.cmpb.2018.05.006
25. Esteva A, Kuprel B, Novoa RA, Ko J, Swetter SM, Blau HM, et al. Dermatologist-Level Classification of Skin Cancer With Deep Neural Networks. *Nature* (2017) 542(7639):115–8. doi: 10.1038/nature21056
26. Gulshan V, Peng L, Coram M, Stumpe MC, Wu D, Narayanaswamy A, et al. Development and Validation of a Deep Learning Algorithm for Detection of Diabetic Retinopathy in Retinal Fundus Photographs. *JAMA* (2016) 316 (22):2402–10. doi: 10.1001/jama.2016.17216
27. Min JK, Kwak MS, Cha JM. Overview of Deep Learning in Gastrointestinal Endoscopy. *Gut Liver* (2019) 13(4):388–93. doi: 10.5009/gnl18384
28. Misawa M, Kudo SE, Mori Y, Takeda K, Maeda Y, Kataoka S, et al. Accuracy of Computer-Aided Diagnosis Based on Narrow-Band Imaging Endocytoscopy for Diagnosing Colorectal Lesions: Comparison With Experts. *Int J Comput Assist Radiol Surg* (2017) 12(5):757–66. doi: 10.1007/s11548-017-1542-4
29. Benz M, Rojas-Solano JR, Kage A, Wittenberg T, Munzenmayer C, Becker HD. Computer-Assisted Diagnosis for White Light Bronchoscopy: First Results. *Chest* (2010) 138(4):433A. doi: 10.1378/chest.10959
30. Feng PH, Lin YT, Lo CM. A Machine Learning Texture Model for Classifying Lung Cancer Subtypes Using Preliminary Bronchoscopic Findings. *Med Phys* (2018) 45(12):5509–14. doi: 10.1002/mp.13241
31. Novak CShafer SJPICSCoCV and Recognition P. Anatomy of a Color Histogram. *Proc 1992 IEEE Comput Soc Conf Comput Vision Pattern Recognit* (1992) 599–605. doi: 10.1109/CVPR.1992.223129
32. Arandjelovi R, Gronát P, Torii A, Pajdla TSivic JJIToPA and Intelligence M. Netvlad: CNN Architecture for Weakly Supervised Place Recognition. *IEEE Trans Pattern Anal Mach Intell* (2018) 40:1437–51. doi: 10.1109/TPAMI.2017.2711011
33. Jégou H, Douze M, Schmid C, PJICSCoCV Pérez, Recognition P. Aggregating Local Descriptors Into a Compact Image Representation. *IEEE Comput Soc Conf Comput Vision Pattern Recognit* (2010) 3304–11. doi: 10.1109/CVPR.2010.5540039
34. Lin R, Xiao J, Fan JJA. Nextvlad: An Efficient Neural Network to Aggregate Frame-Level Features for Large-scale Video Classification. *ArXiv* (2018). doi: 10.1007/978-3-030-11018-5_19
35. Yeung M, Yeo B, Liu BJCVIU. Segmentation of Video by Clustering and Graph Analysis. *Comput Vis Image Underst* (1998) 71:94–109. doi: 10.1006/cviu.1997.0628
36. Bray F, Ferlay J, Soerjomataram I, Siegel RL, Torre LA, Jemal A. Global Cancer Statistics 2018: GLOBOCAN Estimates of Incidence and Mortality Worldwide for 36 Cancers in 185 Countries. *CA: Cancer J Clin* (2018) 68(6):394–424. doi: 10.3322/caac.21492
37. Livi V, Cancellieri A, Pirina P, Fois A, van der Heijden E, Trisolini R. Endobronchial Ultrasound Elastography Helps Identify Fibrotic Lymph Nodes in Sarcoidosis. *Am J Respir Crit Care Med* (2019) 199(3):e24–e5. doi: 10.1164/rccm.201710-2004IM
38. Lin CK, Yu KL, Chang LY, Fan HJ, Wen YF, Ho CC. Differentiating Malignant and Benign Lymph Nodes Using Endobronchial Ultrasound Elastography. *J Formos Med Assoc* (2019) 118(1 Pt 3):436–43. doi: 10.1016/j.jfma.2018.06.021
39. Verhoeven RLJ, de Korte CL, van der Heijden E. Optimal Endobronchial Ultrasound Strain Elastography Assessment Strategy: An Explorative Study. *Respiration* (2019) 97(4):337–47. doi: 10.1159/000494143
40. Verhoeven RLJ, Trisolini R, Leoncini F, Candoli P, Bezzi M, Messi A, et al. Predictive Value of Endobronchial Ultrasound Strain Elastography in Mediastinal Lymph Node Staging: The E-Predict Multicenter Study Results. *Respiration* (2020) 99:484–92. doi: 10.1159/000507592

Conflict of Interest: The authors declare that the research was conducted in the absence of any commercial or financial relationships that could be construed as a potential conflict of interest.

The reviewer MC declared a shared affiliation with the authors to the handling editor at time of review.

frontiers in Oncology

ORIGINAL RESEARCH
published: 24 June 2021
doi: 10.3389/fonc.2021.693146

Irradiation-Modulated Murine Brain Microenvironment Enhances GL261-Tumor Growth and Inhibits Anti-PD-L1 Immunotherapy

Joel R. Garbow[1,2], Tanner M. Johanns[3,2], Xia Ge[1], John A. Engelbach[1], Liya Yuan[4], Sonika Dahiya[5], Christina I. Tsien[6†], Feng Gao[7], Keith M. Rich[4] and Joseph J. H. Ackerman[1,2,3,8]*

[1] Department of Radiology, Washington University, Saint Louis, MO, United States, [2] Alvin J. Siteman Cancer Center, Washington University, Saint Louis, MO, United States, [3] Department of Internal Medicine, Washington University, Saint Louis, MO, United States, [4] Department of Neurosurgery, Washington University, Saint Louis, MO, United States, [5] Division of Neuropathology, Department of Pathology and Immunology, Washington University, Saint Louis, MO, United States, [6] Department of Radiation Oncology, Washington University, Saint Louis, MO, United States, [7] Department of Surgery, Washington University, Saint Louis, MO, United States, [8] Department of Chemistry, Washington University, Saint Louis, MO, United States

OPEN ACCESS

Edited by:
Ellen Ackerstaff, Memorial Sloan Kettering Cancer Center, United States

Reviewed by:
Rui Vasco Simoes, Champalimaud Foundation, Portugal
Natarajan Raghunand, Moffitt Cancer Center, United States
Kumar Pichumani, Houston Methodist Research Institute, United States

***Correspondence:**
Joel R. Garbow
garbow@wustl.edu

†Present address:
Christina I. Tsien, Department of Radiation Oncology, Johns Hopkins Medicine, Baltimore, MD, United States

Specialty section:
This article was submitted to Cancer Imaging and Image-directed Interventions, a section of the journal Frontiers in Oncology

Received: 09 April 2021
Accepted: 02 June 2021
Published: 24 June 2021

Citation:
Garbow JR, Johanns TM, Ge X, Engelbach JA, Yuan L, Dahiya S, Tsien CI, Gao F, Rich KM and Ackerman JJH (2021) Irradiation-Modulated Murine Brain Microenvironment Enhances GL261-Tumor Growth and Inhibits Anti-PD-L1 Immunotherapy. Front. Oncol. 11:693146. doi: 10.3389/fonc.2021.693146

Purpose: Clinical evidence suggests radiation induces changes in the brain microenvironment that affect subsequent response to treatment. This study investigates the effect of previous radiation, delivered six weeks prior to orthotopic tumor implantation, on subsequent tumor growth and therapeutic response to anti-PD-L1 therapy in an intracranial mouse model, termed the Radiation Induced Immunosuppressive Microenvironment (RI^{2}M) model.

Method and Materials: C57Bl/6 mice received focal (hemispheric) single-fraction, 30-Gy radiation using the Leksell GammaKnife® Perfexion™, a dose that does not produce frank/gross radiation necrosis. Non-irradiated GL261 glioblastoma tumor cells were implanted six weeks later into the irradiated hemisphere. Lesion volume was measured longitudinally by *in vivo* MRI. In a separate experiment, tumors were implanted into either previously irradiated (30 Gy) or non-irradiated mouse brain, mice were treated with anti-PD-L1 antibody, and Kaplan-Meier survival curves were constructed. Mouse brains were assessed by conventional hematoxylin and eosin (H&E) staining, IBA-1 staining, which detects activated microglia and macrophages, and fluorescence-activated cell sorting (FACS) analysis.

Results: Tumors in previously irradiated brain display aggressive, invasive growth, characterized by viable tumor and large regions of hemorrhage and necrosis. Mice challenged intracranially with GL261 six weeks after prior intracranial irradiation are unresponsive to anti-PD-L1 therapy. K-M curves demonstrate a statistically significant difference in survival for tumor-bearing mice treated with anti-PD-L1 antibody between RI^{2}M *vs.* non-irradiated mice. The most prominent immunologic change in the post-irradiated brain parenchyma is an increased frequency of activated microglia.

Conclusions: The RI^{2}M model focuses on the persisting (weeks-to-months) impact of radiation applied to normal, control-state brain on the growth characteristics and immunotherapy response of subsequently implanted tumor. GL261 tumors growing in the RI^{2}M grew markedly more aggressively, with tumor cells admixed with regions of hemorrhage and necrosis, and showed a dramatic loss of response to anti-PD-L1 therapy compared to tumors in non-irradiated brain. IHC and FACS analyses demonstrate increased frequency of activated microglia, which correlates with loss of sensitivity to checkpoint immunotherapy. Given that standard-of-care for primary brain tumor following resection includes concurrent radiation and chemotherapy, these striking observations strongly motivate detailed assessment of the *late effects* of the RI^{2}M on tumor growth and therapeutic efficacy.

Keywords: MRI, radiation, tumor, microenvironment, immunotherapy, checkpoint inhibitors, microglia

INTRODUCTION

Radiotherapy combined with immunotherapy is an active area of investigation in the treatment of brain tumors. Active areas of study include investigations of (i) radiation dose and fractionation required to induce immunologic cell death (1); (ii) concurrent *vs.* sequential therapies (2–4); and (iii) outcomes following whole brain radiation therapy *vs.* stereotactic radiosurgery.

Clinical evidence suggests radiation induces changes in the brain microenvironment that affect subsequent response to treatment. Studies of patients with metastatic brain tumors noted metastatic lesions that progress after initial irradiation are often less responsive to subsequent treatment. Previously irradiated melanoma and NSCLC brain metastases failed to respond to pembrolizumab, while non-irradiated lesions had similar response rate to those of extracranial disease (5). Similar observations were noted in a separate cohort of patients with melanoma brain metastases, in which the cohort with lesions that progressed following prior irradiation had a substantially lower response rate to immunotherapy compared to the cohort with irradiation-naïve lesions (6). In recurrent glioblastoma, PD-1 monotherapy and PD-1/CTLA-4 combination therapy alone failed to demonstrate clinical benefit or objective response rates (7–9). These patients were all treated previously with chemoradiotherapy per standard-of-care. Together, these clinical observations suggest that late effects of prior irradiation to the brain microenvironment may be associated with resistance to immune checkpoint inhibition (ICI) therapy.

We have developed a novel, Gamma Knife® (GK) enabled, focal (hemispheric) brain-irradiation mouse model (10), termed the Radiation-Induced Immunosuppressive Microenvironment (RI^{2}M) model, that provides a powerful platform for investigation into the late effects of irradiation on the brain parenchyma microenvironment. Earlier studies of GK-enabled focal-irradiation of mouse brain from this laboratory employed substantially greater radiation doses and were purposefully designed to reliably elicit late-time-to-onset radiation necrosis in an experimentally tractable time frame, with radiation necrosis consistently appearing approximately four to eight weeks post-irradiation (11–17). Importantly, the resultant radiation necrosis in the mouse brain recapitulated all of the key histologic hallmarks of the clinically observed pathology, giving strong confidence regarding the platform's clinical relevance.

In a recent study (10), we observed that non-irradiated DBT glioblastoma cells, implanted into the RI^{2}M of syngeneic mice six weeks post-irradiation – thus, absent acute radiation effects – showed remarkable changes in growth characteristics. Specifically, tumors displayed aggressive, invasive growth, characterized by viable tumor and large regions of hemorrhage and necrosis, resulting in decreased survival compared to tumors growing in non-irradiated brain. Importantly, for these studies, we employed irradiation doses that elicit no frank/gross evidence (MRI and H&E histology) of radiation necrosis, or other outward pathology (e.g., behavior), in the post-irradiation setting. Thus, these data suggest that orthotopic tumors originating from naïve (non-irradiated) glioblastoma cells growing in the previously (six weeks) irradiated brain show many of the histologic hallmarks of recurrent GBM in patients.

Utilizing this model, we are able to evaluate the effects of prior irradiation of the brain parenchyma on the efficacy of a known immune checkpoint sensitive orthotopic transplant glioblastoma model, GL261. We demonstrate that mice challenged intracranially with non-irradiated (naïve) GL261 cells after prior (six weeks) intracranial irradiation with a dose eliciting no frank/gross evidence of radiation necrosis or other pathology are unresponsive to anti-PD-1/PD-L1 directed therapy. The observations of enhanced tumor growth and resistance to checkpoint inhibitors for tumors growing in RI^{2}M are distinct from studies employing combined radiation and immunotherapy to treat existing tumors (18, 19). The most prominent immunologic change in the post-irradiated brain parenchyma is an increased frequency of activated microglia, suggesting they may play a role in the immunosuppressive effects observed. These striking findings have important implications regarding the clinical effects of prior, standard-of-care irradiation on the brain parenchyma and on the subsequent use of ICI therapy in patients with brain tumors. Specifically, a better understanding of the delayed effects of irradiation on the brain/tumor microenvironment will be crucial to identifying effective therapies

that can safely synergize with immune checkpoint inhibitors to enhance immune responsiveness and improve outcome for brain tumor patients.

MATERIALS AND METHODS

Animals

All experiments were performed in accordance with the guidelines of Washington University's Institutional Animal Care and Use Committee and were approved by that committee. Seven-to eight-week-old female C57Bl/6 mice (Envigo Laboratories, Indianapolis, IN), housed five per cage in a light- and temperature-controlled facility, were used in this study. These mice were observed daily to ensure that interventions were well tolerated. A subset of healthy-appearing mice was sacrificed for histology, and mice were also euthanized if they lost more than 20% body weight or suffered obvious behavioral deficits (e.g., ataxia).

Gamma Knife Irradiation

Mice were anesthetized and restrained on a custom-built platform mounted to the stereotactic frame that attaches to the treatment couch of the Leksell GK Perfexion™ (Elekta, Stockholm, Sweden), a device used for stereotactic radiosurgery of patients with malignant brain tumors. Mice were anesthetized with a mixture of ketamine (25 mg/kg) and xylazine (5 mg/kg), injected intraperitoneally (IP) five minutes before the start of irradiation. Single 30-Gy radiation fractions (50% isodose), generated using the GK's 4-mm collimator, were focused on the left cortex at a site ~ 3 mm posterior to bregma.

Tumor Implantation

Tumor cells were implanted in mice, as described previously (20). Briefly, mice were anesthetized with isoflurane and secured in a stereotactic head holder. Murine GL261 glioblastoma cells were implanted (~50,000 cells suspended in 10 μL per mouse) over three minutes in the striatum at a site 2-mm posterior and 3-mm to the left of bregma, 2-mm below the cortical surface.

Experimental Scheme

These experiments were designed to assess tumor growth and response to anti-PD-L1 immunotherapy in the setting of previously irradiated brain tissue. Cohorts of mice received a single fraction dose of 0 or 30 Gy (50% isodose), respectively, of GK radiation. At a radiation dose of 30 Gy, no frank radiation necrosis is observed, visualized by either anatomic MR imaging or standard H&E staining, up to 20 weeks post irradiation (19). Naïve (non-irradiated) GL261 tumor cells were implanted into the ipsilateral hemisphere six weeks post-brain-irradiation – thus obviating acute radiation effects – to evaluate the consequences for tumor growth and immuno-therapeutic response imposed by the RI^2M. Mice treated with anti-PD-L1 antibody received IP injections on days 3, 6, 9, 12, and 15 post tumor implantation; untreated mice received injections of PBS vehicle on these same days (21).

Magnetic Resonance Imaging

Imaging was performed with a 4.7-T small-animal MR scanner (Agilent/Varian, Santa Clara, CA) employing an actively decoupled coil pair: a 9-cm inner diameter volume coil (transmit) and a 1.5-cm outer diameter surface coil (receive). Before all imaging experiments, mice were anesthetized with isoflurane/O_2 [2% (vol/vol)] and maintained on isoflurane/O_2 [1% (vol/vol)] throughout the experiment. Mice were restrained in a laboratory-built, three-point, Teflon head holder and were placed on a water pad with circulating warm water to maintain body temperature at approximately 37 ± 1°C. Before being placed into the magnet, each mouse was injected intraperitoneally with 0.25 mL of MultiHance (gadobenate dimeglumine; Bracco Diagnostics Inc, Princeton, NJ) contrast agent, diluted 2:10 in sterile saline. This procedure highlights regions of impaired blood brain barrier integrity *via* vascular leakage of contrast agent into the parenchyma.

Mice were imaged on post-implantation (GL261 cells) days 10, 14, and 18, and then, every two-to-three weeks, until they were sacrificed, or died due to disease progression. Post-contrast T1-weighted images were acquired with the following parameters: time-to-repetition (TR) = 650 ms, time-to-echo (TE) = 11 ms, number of transient (NT) = 4, field of view = 15 x 15 mm^2, matrix size = 128 x 128, slice thickness = 0.5 mm, 21 slices to cover the whole brain. T2-weighted images were collected with time-to-repetition (TR) = 1200 ms and time-to-echo (TE) = 50 ms, with all other parameters the same as for the T1W images.

Histology

Mice were sacrificed and their brains were immediately removed from the skulls and immersed in formalin. After 24 hours, brains were transferred to a 20% alcohol solution. A 3-mm thick transaxial block, centered at the irradiation site (~3 mm behind the bregma), was obtained from each brain. The blocks were then processed through graded alcohols and embedded in paraffin. All paraffin-fixed blocks were sectioned from the center, at a thickness of five microns. Tissue sections were stained with hematoxylin and eosin (H&E) according to standard protocols.

To measure levels of activated microglia, 5-micron thick tissue sections were immunostained using a rabbit monoclonal anti-IBA-1 antibody (1:1000; Abcam, Cambridge, MA USA), followed by incubation with SuperPicture Polymer Detection Kit, HRP (Life Technologies, Frederick, MD, USA). Slides were viewed with a Hamamatsu NanoZoomer 2.0-HT whole slide imaging system (Hamamatsu Photonics, Bridgewater Township, NJ USA). All histologic and immunohistochemical analyses were performed by a board-certified neuropathologist (S.D.).

Isolation of Tumor-Infiltrating Lymphocytes and Flow Cytometry Analysis

Flow cytometry experiments were performed on a separate cohort of animals that was not included in the survival study. Mice were sacrificed at post-implantation day 14 and intracranial tumors were harvested. Tumor-infiltrating leukocytes (TIL) were isolated by generating a single cell suspension through mechanical dissociation of the tumor tissue. Myelin was removed using a 30% Percoll density gradient. Red blood cells

were removed using ACK lysis buffer. The resulting cell pellet was stained with fluorophore-conjugated antibodies to CD45, CD3, CD4, CD8, NK1.1, CD11b, Gr-1, and Zombie NIR (live/dead). All antibodies were obtained through BioLegend (San Diego, CA). Flow cytometry was performed on a BD LSRFortessa flow cytometer (BD Biosciences, San Jose, CA). Analysis was performed through FlowJo software (BD Biosciences). Statistical analysis was performed using the Student t-test in Prism (GraphPad Software, San Diego, CA).

Live $CD45^+$ TIL were subgated into lymphoid and myeloid subsets to determine relative frequency among total TIL. Lymphoid cell populations were defined as CD4 or CD8 T cells ($CD3^+$ $NK1.1^-$ CD11b), NK cells ($CD3^-$ $NK1.1^+$ $CD11b^-$), or NKT cells ($CD3^+$ $NK1.1^+$ $CD11b^-$). Myeloid cell populations were defined as $CD3^-$ $NK1.1^-$ $CD11b^+$, and further gated on granulocytic MDSC (Gr-MDSC; $CD11b^{lo}$ $Gr\text{-}1^{hi}$), monocytic MDSC (M-MDSC; $CD11b^{hi}$ $Gr\text{-}1^{lo}$), or tumor-associated macrophage/microglia ($CD11b^+$ $Gr\text{-}1^-$). Gating on resting microglia ($CD45^{lo}$), activated microglia ($CD45^{int}$), and tumor-associated macrophage ($CD45^{hi}$) was performed on the $CD11b^+$ $Gr\text{-}1^-$ subset.

Antibody Treatment

Monoclonal mouse anti-PD-L1 antibody (InVivoMAb, clone 10F.92G) was purchased from Bio X Cell (West Lebanon, NH) and diluted in Bio X Cell InVivoPure dilution buffer prior to use. 500 µg of antibody per mouse was injected IP on days 3, 6, 9, 12, and 15 post-tumor-implantation.

Data Analysis and Statistics

Tumor volumes were derived using ImageJ (https://imagej.nih.gov/ij/), with regions of interest (ROIs) for the tumor lesions being drawn manually on the post-contrast T1-weighted images. In calculating lesion volumes, hypointense regions within the tumor were also treated as part of the lesions. MR-derived lesion volumes were calculated as the sum of the number of lesion voxels multiplied by the voxel volume. Changes in lesion volume over time were described using a linear mixed model, to account for potential correlation among multiple measurements from the same mouse, followed by *ad hoc* comparisons for between-group differences at each time point. Square-root transformation of lesions volumes was performed to better satisfy the normality and homoscedasticity assumptions for the linear mixed model. Distributions of survival times were described using the Kaplan-Meier (K-M) product limit method, and between-group differences were compared using a weighted log-rank test (22). All tests were two-sided and significance was set at a p-value of 0.05. Statistical analyses were performed using SAS 9.4 (SAS Institutes; Cary, NC).

RESULTS

Tumor Implanted Into Previously Irradiated Brain Grows More Aggressively and Hemorrhagically

Figure 1A shows representative contrast-enhanced, T1-weighted images of GL261 tumors growing in RI^2M (top panels) and non-irradiated (bottom panels) mouse brain. Irradiated brains received 30 Gy (50% isodose) of GK radiation six weeks prior to tumor implantation. As demonstrated in **Figure 2**, which shows T2-weighted images and contrast-enhanced, T1-weighted images of mouse brain collected ten weeks post-GK-irradiation (30 Gy @ 50% isodose), no acute radiation effects or blood-barrier breakdown are observed at the time of tumor implantation (10, 14). Nonetheless, as is evident in the images in **Figure 1A**, tumors in previously irradiated brain grow more aggressively than corresponding tumors in non-irradiated mice as reflected in the increased size and invasiveness of the lesions. **Figure 1B** shows plots of mean lesion volume as a function of time post-tumor-implantation for cohorts of irradiated (n=9) and non-irradiated (n=10) mice. A trend in lesion volumes (irradiated *vs.* non-irradiated brain) is observed on post-implantation day 14, and the difference is statistically significant on day 18 (p=0.03).

Tumors Growing in Previously Irradiated Mouse Brain Do Not Respond to Anti-PD-L1 Immunotherapy

Figure 3 (left) displays representative contrast-enhanced, T1- and T2-weighted MR images of tumors growing in mouse brain, collected on post-implantation day 21, for subjects treated with anti-PD-L1 mouse monoclonal antibody on post-implantation days 3, 6, 9, 12, and 15. Early therapeutic intervention prior to establishment of visible tumors was chosen to minimize the impact of the differences in growth kinetics observed at later time points. By post-implantation day 21, the therapeutic responsiveness to anti-PD-L1 inhibition of tumor in non-irradiated brain, compared with irradiated brain, is clearly evident. **Figure 3** (right) shows Kaplan-Meier survival curves for cohorts of tumor-bearing, anti-PD-L1-treated mice. The survival of tumor-bearing mice whose brains were not irradiated (n=15; dashed line) is significantly greater than for mice whose brains were irradiated six weeks prior to tumor implantation (n=14; solid line). The ~50% survival of anti-PD-L1-treated, non-irradiated mice is consistent with previously published studies of ICI-treated mice (21, 23–25).

Activated Microglia Are More Prevalent in Irradiated Mouse Brain

Immunohistochemical staining utilized IBA-1 antibodies to identify activated microglia and macrophages. **Figure 4A** compares IBA-1 staining of non-irradiated and (focally) irradiated mouse brain, in the absence of tumor. Increased levels of activated microglia and macrophages are found in the irradiated hemisphere, which looks normal by standard H&E staining. Populations of activated microglia and macrophages on the non-irradiated side are comparable to those seen bi-hemispherically in non-irradiated mice.

Figure 4B displays IBA-1 staining of tumor-bearing mouse brain, with the top panel showing tumor growing in non-irradiated brain, and the bottom panel tumor growing in RI^2M. Non-irradiated

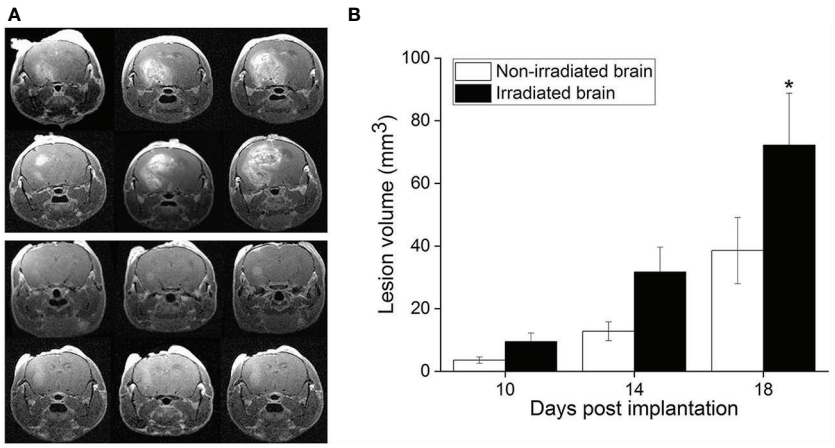

FIGURE 1 | **(A)** Representative, contrast-enhanced T1-weighted MR images of GL261 tumor-bearing C57Bl/6 mice, collected 18 days after tumor implantation. The top panel shows three contiguous image slices for two animals whose brains were focally irradiated with 30-Gy (50% isodose) Gamma Knife radiation six weeks prior to GL261 cell implantation in the RI^2M. The bottom panel shows similar images for non-irradiated mice. Tumors growing in the RI^2M are larger and more hyperintense (reflecting greater leakage of contrast agent) compared with tumors growing in non-irradiated brain. **(B)** Plots showing mean lesion volume (+/- SEM) for tumors growing in irradiated (n = 9; black) and non-irradiated (n = 10; white) brain at post-implantation days 10, 14, and 18. At post-implantation day 14, there is a trend toward larger lesion volumes in irradiated brain ($p = 0.07$). At post-implantation day 18, the difference in lesion volumes is statistically significant (*$p = 0.030$).

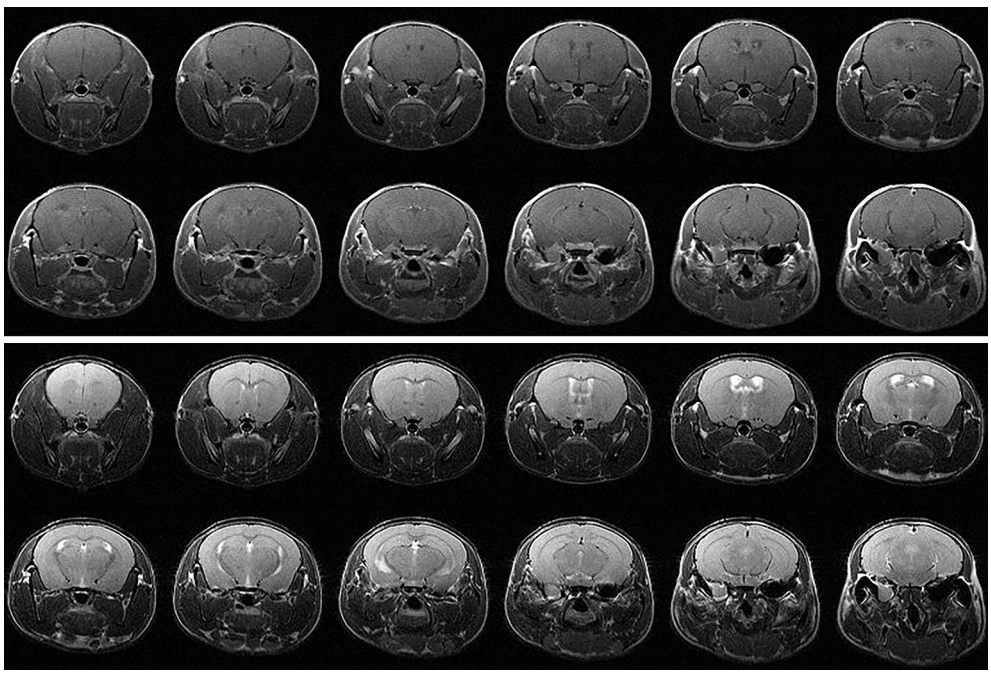

FIGURE 2 | (top) Contrast-enhanced T1-weighted and (bottom) T2-weighted MR images of a C57BL/6 mouse 10 weeks following hemispheric 30-Gy (50% isodose) GK-irradiation. Each panel shows twelve contiguous, 1-mm thick transaxial slices. Both the T1W and T2W images are indistinguishable from the corresponding images of non-irradiated mice and show no evidence of radiation-induced tissue damage.

mice generally had solid well-circumscribed tumor with activated microglia/macrophages within the tumor and at the periphery. Rarely, cuffing of macrophages/microglial cells at the interface of tumor with normal parenchyma was also observed. When present, it was thin or partial and never as complete/circumferential and dense as seen in the irradiated groups. Outside of the tumor, there were substantial numbers of activated microglia and macrophages on the ipsilateral side, with little IBA-1

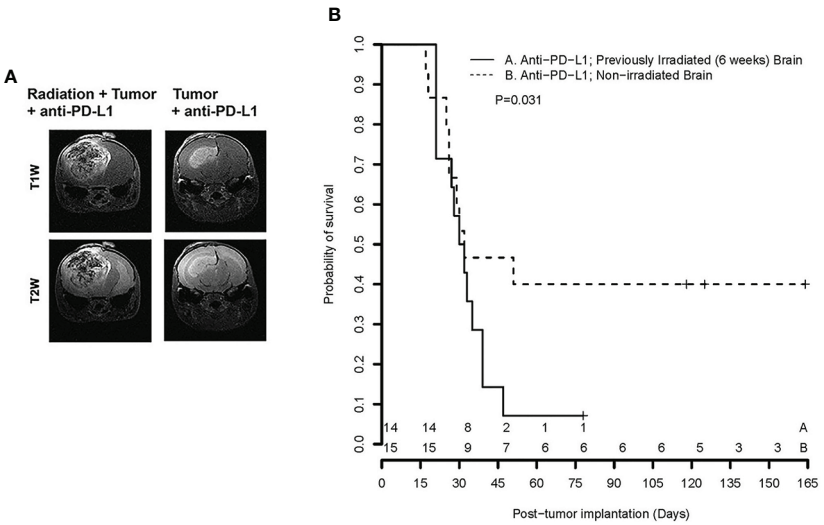

FIGURE 3 | **(A)** Representative contrast-enhanced, T1- and T2-weighted MR images of the brains of C57Bl/6 mice, previously irradiated focally, or not, implanted with GL261 cells in the irradiated hemisphere and treated with anti-PD-L1 therapy; **(B)** Kaplan-Meier curves show that survival of tumor-bearing mice whose brains were not irradiated (n = 15; dashed line) is significantly greater than for mice whose brains were irradiated six weeks prior to tumor implantation (n = 14; solid line), p = 0.031 [extended log-rank test (22)]. + signs indicate mice that were sacrificed for histology; numerals near the bottom of the plot reflect the number of surviving mice in groups A (Anti-PD-L1; RI^2M) and B (Anti-PD-L1; non-irradiated brain).

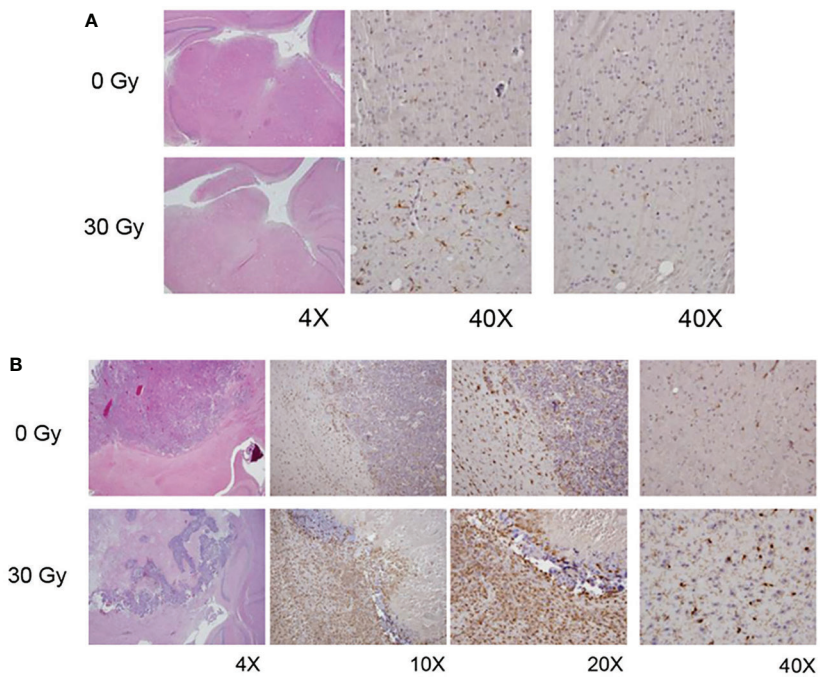

FIGURE 4 | **(A)** H&E (left column) and IBA1 images (middle, right columns) from non-irradiated (0 Gy; top panel) and focally irradiated (30 Gy; bottom panel) mice in the absence of tumor. Increased IBA1 staining, indicative of increased levels of activated microglia and macrophages, is observed in the irradiated hemisphere, which looks normal by standard H&E staining. **(B)** H&E (left column) and IBA1 (all other columns) images from non-irradiated (0 Gy; top panel) and irradiated (30 Gy; bottom panel) tumor-bearing mice. Non-irradiated mice generally have well-circumscribed tumor with microglial activation both within the tumor and at its periphery. Tumors implanted into RI^2M are characterized by large areas of hemorrhage and necrosis with lesser viable tumor. However, there was marked activation of microglia within the tumor and surrounding it.

staining on the contralateral side. Tumors implanted into the RI^{2}M were characterized by large areas of hemorrhage and necrosis with lesser viable tumor. However, a thick cuff of macrophages/microglial cells formed around the tumor and at its interface with the normal brain parenchyma. Interestingly, for larger tumors/lesions, the contralateral side also had increased numbers of activated microglia and macrophages compared to tumor in non-irradiated brain. Microglia/macrophages within the tumor itself were comparable in the two groups (data not shown).

Having observed a thick circumferential cuffing of activated macrophages/microglia surrounding tumor implanted in previously irradiated brain, we hypothesized that one mechanism of acquired resistance to anti-PD-L1 inhibition therapy in previously irradiated mice is exclusion of effector T cells from homing into the tumor microenvironment. Using fluorescence-activated cell sorting (FACS), changes in immune cell populations in orthotopic mouse tumors grown in RI^{2}M *vs.* non-irradiated brain were compared. There were no differences in absolute number or relative frequency of T cell subsets or NK/NKT cells (**Figure 5A**). However, there were significant differences in the relative frequency of myeloid subpopulations in tumor-bearing mice. **Figure 5B** is a representative flow plot demonstrating the gating strategy used to identify resting microglia (CD45^{lo}), activated microglia (CD45^{int}), and macrophages/monocytes (CD45^{hi}) within the CD11b$^+$ Gr-1$^-$ subpopulation. **Figure 5C** quantifies the relative frequency of CD11b$^+$ Gr-1$^-$ TIL that are CD45^{hi}, CD45^{int}, or CD45^{lo}. Overall, the difference in total number of microglia (resting + activated) between irradiated and non-irradiated groups is not statistically significant (data not shown), suggesting that irradiation does not induce proliferation of microglia. However, there is a significant difference in the relative frequency of activated *vs.* resting microglia in the irradiated tumor-bearing mice. Thus, these results suggest that the impact of irradiation on the brain parenchyma is primarily in changing the activation state of microglia.

DISCUSSION

Radiation is a key component of early therapeutic strategies for many malignant brain tumors and improves overall survival in newly diagnosed glioblastoma. The late effects of irradiation on the tumor microenvironment have an important impact on response to subsequent systemic therapies for treatment of recurrent malignant tumors. A better understanding of the immune and vascular components of the brain microenvironment is needed for improving clinical treatment strategies in patients with recurrent tumors.

We have developed a novel GK-enabled focal brain-irradiation mouse model (10) that provides a powerful platform for investigation of the late (six weeks) post-irradiation induced immunologic modulation of the brain tissue microenvironment. We emphasize that ours is not a model of radiotherapy aimed at treating existing brain tumors, but instead was developed for studying the growth and response to immunotherapy of tumors growing in previously irradiated brain. Consistent with our recently published study of naïve (non-irradiated) DBT tumors growing in the RI^{2}M of Balb/C mice (10), naïve GL261 cells orthotopically implanted in the RI^{2}M of C57Bl/6 mice show similarly remarkable changes in growth characteristics (**Figure 1**). Specifically, such tumors display aggressive, invasive growth, characterized by viable tumor and large regions of hemorrhage and necrosis, compared to tumors growing in non-irradiated brain. In short, tumors originating from naïve (non-irradiated) tumor cells orthotopically implanted in previously irradiated brain show many of the histologic hallmarks of recurrent glioblastoma in patients, features that are not observed in tumor cells growing in non-irradiated brain parenchyma. The model has direct clinical relevance because recurrent GBM is almost always growing in previously irradiated brain. Prior irradiation dramatically affects the growth and histologic features of tumors in the orthotopic mouse model.

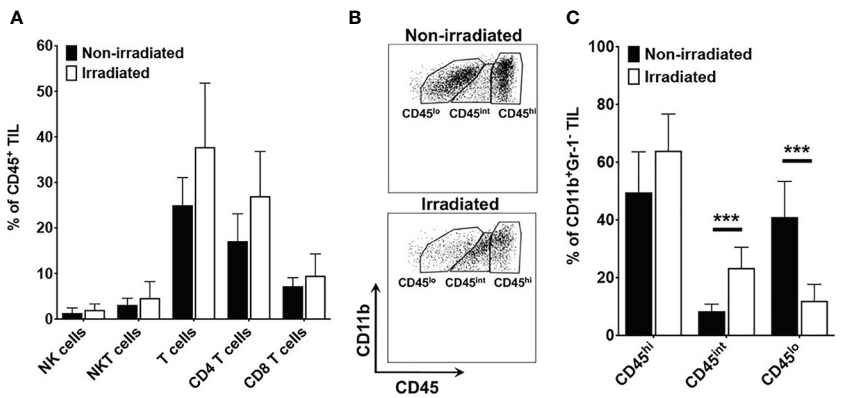

FIGURE 5 | **(A)** quantifies the relative frequency of CD45$^+$ tumor-infiltrating leukocytes (TIL) that are NK cells (CD3$^-$NK1.1$^+$), NKT (CD3$^+$NK1.1$^+$), total T cells (CD3$^+$), CD8 T cells (CD3$^+$CD8$^+$), and CD4 T cells (CD3$^+$CD4$^+$). **(B)** is a representative flow plot demonstrating the gating strategy to identify resting microglia (CD45^{lo}), activated microglia (CD45^{int}), and macrophages/monocytes (CD45^{hi}). Cells are gated on lineage negative (i.e., Non-T cells, Non-NK cells), CD11b-positive, Gr-1-negative TIL). **(C)** quantifies the percentage of CD11b$^+$ Gr-1$^-$ TIL that are CD45^{hi}, CD45^{int}, or CD45^{lo}. Data are representative of two independent experiments with 4-5 mice in each experiment. Black bars represent non-irradiated mice; white bars previously irradiated mice. Differences in CD45^{int} and CD45^{lo} are statistically significant (***$p < 0.0005$).

Previous radiation altered the brain microenvironment, resulting in dramatic loss of sensitivity to anti-PD-L1 treatment in our mouse model. We remind the reader that our studies were designed to explore the effects of previous brain irradiation on the efficacy of immunotherapy, as distinct from therapy studies on existing tumors employing concomitant radiation and checkpoint inhibition (18, 19). The survival data reported in **Figure 2** are consistent with radiation generating an increased immunosuppressive tumor microenvironment that promotes therapeutic resistance and loss of sensitivity to PD-L1 therapy in aggressive recurrent mouse gliomas. This finding has significant implications for the rational design of immunotherapy trials in brain tumors. Specifically, a better understanding of the late effects of radiation on the brain/tumor microenvironment will be crucial to identifying effective therapies that can safely synergize with immune checkpoint inhibitors to enhance immune response and improve outcome for brain tumor patients.

Given the differences in tumor growth kinetics between tumor cells implanted in irradiated and non-irradiated brains, we initiated PD-L1 inhibition therapy early (day 3) post-implantation to avoid confounding variables associated with differences in tumor size. Thus, to see differences in survival following PD-L1 inhibition therapy was somewhat surprising. We reasoned that the impact of prior irradiation on the microenvironment and its impact on responsiveness to PD-(L)1 inhibition therapy was present at the time of implantation of tumor cells, rather than after the tumor was established. Therefore, we initially evaluated the primary immune cell subset present within the brain parenchyma at steady state, the microglia. As demonstrated by IBA-1 staining in **Figure 4**, microglia/macrophages do not proliferate in response to irradiation but rather acquire an activated phenotype (i.e., IBA-1 positive) in post-irradiated brain parenchyma, even in the absence of tumor. The observation of increased activated microglia following radiation is aligned with the chronic activation of microglia reported following irradiation in adult rats (26) and in C57BL/6 mice (27). In previously irradiated, tumor-bearing mice, there was significant activation of microglia and macrophages in and around the tumor, forming a thick ring of macrophages/microglial cells around the tumor and at its interface with the normal brain parenchyma. These IHC observations were further corroborated with flow cytometry experiments. Results reported in **Figure 5** demonstrate that there is a statistically significant increase in the relative frequency of activated microglia and a decrease in resting microglia among TIL isolated from irradiated compared to non-irradiated tumor microenvironment. The FACS results are consistent with and provide complementary support to the conclusions drawn from IBA-1 IHC. The changes in the orthotopic tumors growing in previously irradiated brain are consistent with an increased immunosuppressive environment and subsequent loss of response to immune checkpoint blockade.

The tumor-permissive and immunosuppressive characteristics of tumor-associated macrophages (TAM) have driven interest in development of novel therapeutic strategies to target these cells. Colony stimulating factor (CSF-1) is an important cytokine involved in survival, proliferation, and differentiation of tissue macrophages and their precursors. As a consequence, there has been considerable interest in CSF1 and its receptor (CSF1R), and various approaches targeting either the ligand or the receptor are currently in clinical development. In addition to CSF-1/CSF-1R pathway inhibition, other myeloid-directed targets are also being developed. Kaneda and colleagues demonstrated that administration of a PI3K-gamma inhibitor resulted in improved responsiveness of the tumor (28). In addition to the CSF-1 pathway and PI3K-gamma, CD40 agonists (29) have also been shown to remodel the myeloid compartment and are being explored as microenvironment modulators to combine with ICI. Likewise, CD47 agonists are thought to have a similar effect on remodeling the myeloid compartment (30). Thus, identifying novel agents that target the microenvironment, namely the myeloid compartment, to sensitize tumors to PD-L1 inhibition therapy is an active area of investigation and may be particularly needed in the post-irradiation setting.

To summarize, in our GK-enabled hemispheric brain irradiation mouse model, the persistent (six weeks post-irradiation) effects of the irradiation on the brain microenvironment are shown to induce substantial changes in tumor growth characteristics and response to immunotherapy. Specifically, naïve (non-irradiated) GL261 tumors growing in the RI^2M grew markedly more aggressively, with tumor cells admixed with regions of hemorrhage and necrosis, and showed a dramatic loss of response to anti-PD-L1 therapy compared to tumors in non-irradiated brain. IHC and FACS analyses demonstrated increased relative frequency of different myeloid cell infiltration and increased activated microglia, which correlated with the loss of sensitivity to checkpoint immunotherapy. We are currently performing experiments using high-dimensional single-cell techniques to define changes in myeloid cell populations. Metabolism studies can also contribute important insights towards understanding the enhanced tumor growth and lack of responsiveness to checkpoint inhibitors observed in our model. Ongoing studies in our lab are directed at developing Deuterium Metabolic Imaging (DMI) (31, 32) for characterization of the RI^2M. While there are well-recognized imperfections in murine models *vs.* the human condition, the changes in tumor growth and loss of sensitivity to checkpoint inhibitors are not subtle and provide a framework that motivates further analysis of the late effects of the irradiated brain/tumor microenvironment on tumor growth and therapeutic efficacy.

DATA AVAILABILITY STATEMENT

The raw data supporting the conclusions of this article will be made available by the authors, without undue reservation.

ETHICS STATEMENT

The animal study was reviewed and approved by Washington University Institutional Animal Care and Use Committee.

AUTHOR CONTRIBUTIONS

Conceptualization/Study Design: JG, KR, and JA. Data acquisition, analysis, and curation: XG, JE, TJ, LY, and SD. Statistical analysis: TJ and FG. Writing – original draft: JG and JA. Writing – review and editing: JG, TJ, CT, KR, and JA. All authors contributed to the article and approved the submitted version.

FUNDING

This research was funded by the Alvin J. Siteman Cancer Center Investment Program (supported by the Foundation of Barnes-Jewish Hospital, Cancer Frontier Fund; National Cancer Institute, Cancer Center Support Grant, P30 CA091842; and Barnard Trust), NIH/NIBIB R01 EB029752, and Elekta Instrument AB (Stockholm, Sweden).

ACKNOWLEDGMENTS

The studies presented in this work were carried out, in part, using the Small Animal MR Facility of the Mallinckrodt Institute of Radiology, with support from the Small-Animal Cancer Imaging Shared Resource of the Siteman Cancer Center.

REFERENCES

1. Vanpouille-Box C, Alard A, Aryankalayil MJ, Sarfraz Y, Diamond JM, Schneider RJ, et al. DNA Exonuclease Trex1 Regulates Radiotherapy-Induced Tumour Immunogenicity. *Nat Commun* (2017) 8:15618. doi: 10.1038/ncomms15618
2. ElJalby M, Pannullo SC, Schwartz TH, Parashar B, Wernicke AG. Optimal Timing and Sequence of Immunotherapy When Combined With Stereotactic Radiosurgery in the Treatment of Brain Metastases. *World Neurosurg* (2019) 127:397–404. doi: 10.1016/j.wneu.2019.04.093
3. Lu VM, Kerezoudis P, Brown DA, Burns TC, Quinones-Hinojosa A, Chaichana KL. Hypofractionated Versus Standard Radiation Therapy in Combination With Temozolomide for Glioblastoma in the Elderly: A Meta-Analysis. *J Neurooncol* (2019) 143(2):177–85. doi: 10.1007/s11060-019-03155-6
4. Qian JM, Yu JB, Kluger HM, Chiang VL. Timing and Type of Immune Checkpoint Therapy Affect the Early Radiographic Response of Melanoma Brain Metastases to Stereotactic Radiosurgery. *Cancer* (2016) 122(19):3051–8. doi: 10.1002/cncr.30138
5. Goldberg SB, Gettinger SN, Mahajan A, Chiang AC, Herbst RS, Sznol M, et al. Pembrolizumab for Patients With Melanoma or Non-Small-Cell Lung Cancer and Untreated Brain Metastases: Early Analysis of a Non-Randomised, Open-Label, Phase 2 Trial. *Lancet Oncol* (2016) 17(7):976–83. doi: 10.1016/S1470-2045(16)30053-5
6. Long GV, Atkinson V, Lo S, Sandhu S, Guminski AD, Brown MP, et al. Combination Nivolumab and Ipilimumab or Nivolumab Alone in Melanoma Brain Metastases: A Multicentre Randomised Phase 2 Study. *Lancet Oncol* (2018) 19(5):672–81. doi: 10.1016/S1470-2045(18)30139-6
7. Omuro A, Vlahovic G, Lim M, Sahebjam S, Baehring J, Cloughesy T, et al. Nivolumab With or Without Ipilimumab in Patients With Recurrent Glioblastoma: Results From Exploratory Phase I Cohorts of CheckMate 143. *Neuro Oncol* (2018) 20(5):674–86. doi: 10.1093/neuonc/nox208
8. Reardon DA, Brandes AA, Omuro A, Mulholland P, Lim M, Wick A, et al. Effect of Nivolumab vs Bevacizumab in Patients With Recurrent Glioblastoma: The CheckMate 143 Phase 3 Randomized Clinical Trial. *JAMA Oncol* (2020) 6(7):1003–10. doi: 10.1001/jamaoncol.2020.1024
9. Weenink B, French PJ, Sillevis Smitt PAE, Debets R, Geurts M. Immunotherapy in Glioblastoma: Current Shortcomings and Future Perspectives. *Cancers (Basel)* (2020) 12(3):751. doi: 10.3390/cancers12030751
10. Duan C, Yang R, Yuan L, Engelbach JA, Tsien CI, Rich KM, et al. Late Effects of Radiation Prime the Brain Microenvironment for Accelerated Tumor Growth. *Int J Radiat Oncol Biol Phys* (2019) 103(1):190–4. doi: 10.1016/j.ijrobp.2018.08.033
11. Duan C, Perez-Torres CJ, Yuan L, Engelbach JA, Beeman SC, Tsien CI, et al. Can Anti-Vascular Endothelial Growth Factor Antibody Reverse Radiation Necrosis? *A Preclin Invest J Neurooncol* (2017) 133(1):9–16. doi: 10.1007/s11060-017-2410-3
12. Jiang X, Engelbach JA, Yuan L, Cates J, Gao F, Drzymala RE, et al. Anti-VEGF Antibodies Mitigate the Development of Radiation Necrosis in Mouse Brain. *Clin Cancer Res* (2014) 20(10):2695–702. doi: 10.1158/1078-0432.CCR-13-1941
13. Jiang X, Perez-Torres CJ, Thotala D, Engelbach JA, Yuan L, Cates J, et al. A GSK-3beta Inhibitor Protects Against Radiation Necrosis in Mouse Brain. *Int J Radiat Oncol Biol Phys* (2014) 89(4):714–21. doi: 10.1016/j.ijrobp.2014.04.018
14. Jiang X, Yuan L, Engelbach JA, Cates J, Perez-Torres CJ, Gao F, et al. A Gamma-Knife-Enabled Mouse Model of Cerebral Single-Hemisphere Delayed Radiation Necrosis. *PloS One* (2015) 10(10):e0139596. doi: 10.1371/journal.pone.0139596
15. Perez-Torres CJ, Engelbach JA, Cates J, Thotala D, Yuan L, Schmidt RE, et al. Toward Distinguishing Recurrent Tumor From Radiation Necrosis: DWI and MTC in a Gamma Knife–Irradiated Mouse Glioma Model. *Int J Radiat Oncol Biol Phys* (2014) 90(2):446–53. doi: 10.1016/j.ijrobp.2014.06.015
16. Perez-Torres CJ, Yuan L, Schmidt RE, Rich KM, Ackerman JJ, Garbow JR. Perilesional Edema in Radiation Necrosis Reflects Axonal Degeneration. *Radiat Oncol* (2015) 10:33. doi: 10.1186/s13014-015-0335-6
17. Perez-Torres CJ, Yuan L, Schmidt RE, Rich KM, Drzymala RE, Hallahan DE, et al. Specificity of Vascular Endothelial Growth Factor Treatment for Radiation Necrosis. *Radiother Oncol* (2015) 117(2):382–5. doi: 10.1016/j.radonc.2015.09.004
18. Clausi MG, Stessin AM, Zhao Z, Tsirka SE, Ryu S. Neuroinflammatory Changes of the Normal Brain Tissue in Cured Mice Following Combined Radiation and Anti-PD-1 Blockade Therapy for Glioma. *Sci Rep* (2021) 11 (1):5057. doi: 10.1038/s41598-021-84600-3
19. Zeng J, See AP, Phallen J, Jackson CM, Belcaid Z, Ruzevick J, et al. Anti-PD-1 Blockade and Stereotactic Radiation Produce Long-Term Survival in Mice With Intracranial Gliomas. *Int J Radiat Oncol Biol Phys* (2013) 86(2):343–9. doi: 10.1016/j.ijrobp.2012.12.025
20. Jost SC, Wanebo JE, Song SK, Chicoine MR, Rich KM, Woolsey TA, et al. In Vivo Imaging in a Murine Model of Glioblastoma. *Neurosurgery* (2007) 60 (2):360–70. doi: 10.1227/01.NEU.0000249264.80579.37
21. Reardon DA, Gokhale PC, Klein SR, Ligon KL, Rodig SJ, Ramkissoon SH, et al. Glioblastoma Eradication Following Immune Checkpoint Blockade in an Orthotopic, Immunocompetent Model. *Cancer Immunol Res* (2016) 4(2):124–35. doi: 10.1158/2326-6066.CIR-15-0151
22. Fleming TR, Harrington DP, O'Sullivan M. Supremum Versions of the Log-Rank and Generalized Wilcoxon Statistics. *J Am Stat Assoc* (1987) 82 (397):312–20. doi: 10.1080/01621459.1987.10478435
23. Belcaid Z, Phallen JA, Zeng J, See AP, Mathios D, Gottschalk C, et al. Focal Radiation Therapy Combined With 4-1BB Activation and CTLA-4 Blockade Yields Long-Term Survival and a Protective Antigen-Specific Memory Response in a Murine Glioma Model. *PloS One* (2014) 9(7):e101764. doi: 10.1371/journal.pone.0101764
24. Liu CJ, Schaettler M, Blaha DT, Bowman-Kirigin JA, Kobayashi DK, Livingstone AJ, et al. Treatment of an Aggressive Orthotopic Murine Glioblastoma Model With Combination Checkpoint Blockade and a Multivalent Neoantigen Vaccine. *Neuro Oncol* (2020) 22(9):1276–88. doi: 10.1093/neuonc/noaa050
25. Wainwright DA, Lesniak MS. Menage a Trois: Sustained Therapeutic Anti-Tumor Immunity Requires Multiple Partners in Malignant Glioma. *Oncoimmunology* (2014) 3:e28927. doi: 10.4161/onci.28927
26. Monje ML, Mizumatsu S, Fike JR, Palmer TD. Irradiation Induces Neural Precursor-Cell Dysfunction. *Nat Med* (2002) 8(9):955–62. doi: 10.1038/nm749
27. Li MD, Burns TC, Kumar S, Morgan AA, Sloan SA, Palmer TD. Aging-Like Changes in the Transcriptome of Irradiated Microglia. *Glia* (2015) 63(5):754–67. doi: 10.1002/glia.22782

28. Kaneda MM, Messer KS, Ralainirina N, Li H, Leem CJ, Gorjestani S, et al. PI3Kgamma Is a Molecular Switch That Controls Immune Suppression. *Nature* (2016) 539(7629):437–42. doi: 10.1038/nature19834
29. Gubin MM, Esaulova E, Ward JP, Malkova ON, Runci D, Wong P, et al. High-Dimensional Analysis Delineates Myeloid and Lymphoid Compartment Remodeling During Successful Immune-Checkpoint Cancer Therapy. *Cell* (2018) 175(5):1443. doi: 10.1016/j.cell.2018.11.003
30. Wu L, Yu GT, Deng WW, Mao L, Yang LL, Ma SR, et al. Anti-CD47 Treatment Enhances Anti-Tumor T-cell Immunity and Improves Immunosuppressive Environment in Head and Neck Squamous Cell Carcinoma. *Oncoimmunology* (2018) 7(4):e1397248. doi: 10.1080/2162402X.2017.1397248
31. De Feyter HM, Behar KL, Corbin ZA, Fulbright RK, Brown PB, McIntyre S, et al. Deuterium Metabolic Imaging (DMI) for MRI-Based 3D Mapping of Metabolism In Vivo. *Sci Adv* (2018) 4(8):eaat7314. doi: 10.1126/sciadv.aat7314
32. Kreis F, Wright AJ, Hesse F, Fala M, Hu DE, Brindle KM. Measuring Tumor Glycolytic Flux in Vivo by Using Fast Deuterium Mri. *Radiology* (2020) 294 (2):289–96. doi: 10.1148/radiol.2019191242

Conflict of Interest: The authors declare that the research was conducted in the absence of any commercial or financial relationships that could be construed as a potential conflict of interest.

frontiers in Oncology

REVIEW
published: 17 August 2021
doi: 10.3389/fonc.2021.714660

Ultrasound Elastography for the Evaluation of Lymph Nodes

Bin Wang[1†], Qi Guo[2†], Jia-Yu Wang[3], Yang Yu[3], Ai-Jiao Yi[1], Xin-Wu Cui[3*] and Christoph F. Dietrich[4]*

[1] Department of Ultrasound, The First People's Hospital of Yueyang, Yueyang, China, [2] Department of Medical Ultrasound, The Fifth Affiliated Hospital of Zhengzhou University, Zhengzhou, China, [3] Department of Medical Ultrasound, Tongji Hospital, Tongji Medical College, Huazhong University of Science and Technology, Wuhan, China, [4] Department of Internal Medicine, Hirslanden Clinic, Bern, Switzerland

The differential diagnosis of lymphadenopathy is important for predicting prognosis, staging, and monitoring the treatment, especially for cancer patients. Conventional computed tomography and magnetic resonance imaging characterize lymph node (LN) with disappointing sensitivity and specificity. Conventional ultrasound with the advantage of high resolution has been widely used for the LN evaluation. Ultrasound elastography (UE) using color map or shear wave velocity can non-invasively demonstrate the stiffness and homogeneity of both the cortex and medulla of LNs and can detect early circumscribed malignant infiltration. There is a need of a review to comprehensively discuss the current knowledge of the applications of various UE techniques in the evaluation of LNs. In this review, we discussed the principles of strain elastography and shear wave-based elastography, and their advantages and limitations in the evaluation of LNs. In addition, we comprehensively introduced the applications of various UE techniques in the differential diagnosis of reactive LNs, lymphoma, metastatic LNs, and other lymphadenopathy. Moreover, the applications of endoscopic UE and endobronchial UE are also discussed, including their use for improving the positive rate of diagnosis of fine-needle aspiration biopsy.

Keywords: lymph nodes, screening, ultrasonography, elastography, shear wave

OPEN ACCESS

Edited by:
Haibin Shi,
Soochow University, China

Reviewed by:
Li-Jen Liao,
Far Eastern Memorial Hospital, Taiwan
Ping Zhou,
Central South University, China

***Correspondence:**
Xin-Wu Cui
cuixinwu@live.cn
Ai-Jiao Yi
938186822@163.com

[†]These authors have contributed equally to this work

Specialty section:
This article was submitted to Cancer Imaging and Image-directed Interventions, a section of the journal Frontiers in Oncology

Received: *25 May 2021*
Accepted: *26 July 2021*
Published: *17 August 2021*

Citation:
Wang B, Guo Q, Wang J-Y, Yu Y, Yi A-J, Cui X-W and Dietrich CF (2021) Ultrasound Elastography for the Evaluation of Lymph Nodes. Front. Oncol. 11:714660. doi: 10.3389/fonc.2021.714660

INTRODUCTION

Various benign and malignant disorders can result in lymphadenopathy; the differential diagnosis of lymph node (LN) is important for predicting prognosis, staging, and monitoring the treatment. Conventional computed tomography (CT) and magnetic resonance imaging (MRI) characterize LN relying on size and topographic distribution, but with disappointing sensitivity and specificity, since it is not rare that malignant LN infiltration occurs in normal-sized LN.

Conventional ultrasound (US) with the advantage of high resolution has been widely used for imaging superficial organs, particularly for the LN evaluation. Compared with conventional CT and MRI, B-mode US can provide more detailed information on shape, contour, inner texture, maximum short axis diameter, long to short axis ratio, absence of hilus, and presence of necrosis. Color Doppler US and spectral Doppler US can image the hemodynamic characters of LN and add values for the differentiation of malignant from benign LNs. Benign LNs often show hilar predominant vessel

architecture and have lower resistive index (RI), while malignant LNs usually show peripheral or mixed vascularity and disappearance of hilar vascularization and have higher RI. However, Doppler techniques have limitations in small LN since the vascularity is often undetectable (**Figures 1**–**3**).

US elastography (UE) is a new technique that uses color map or shear wave velocity (SWV) to non-invasively demonstrate stiffness and homogeneity. It has rapidly become one of the most popular US-based techniques. Clinically, it can be used in the early detection and differential diagnosis of focal diseases; in improving the accuracy for diagnosing diffuse diseases, such as fibrosis and atherosclerosis; and in the assessment of response to treatments, such as thermal ablation and chemotherapy (1).

UE is able to demonstrate the stiffness of both the cortex and medulla of LNs and to detect early circumscribed malignant infiltration. Studies have been published on the evaluation of LNs by strain elastography (SE) or shear wave elastography (SWE). This review aims to comprehensively discuss the current knowledge of the applications of various UE techniques in the evaluation of LNs.

PRINCIPLES AND TECHNIQUES OF ULTRASOUND ELASTOGRAPHY

UE is a technique in which the stiffness of the tissue can be imaged as color map or SWV. The principle of UE is based upon tissue reactions, such as changes in displacement, strain, or speed, by applying an external or internal static (quasi-static) or dynamic excitation. Differences in tissue reactions are calculated, identified, and reflected by computers.

Depending on the type of excitation applied, UE is classified into two categories, i.e., 1) SE, which is composed of static or quasi-static strain imaging and acoustic radiation force impulse (ARFI) imaging; and 2), SWE which is composed of SWV measurement and SWV imaging (**Figure 4**).

Strain Elastography

Technique

SE includes static/quasi-static imaging and ARFI imaging. It is based upon the fact that hard tissue is more difficultly compressed than soft tissue. SE is a technique that measures

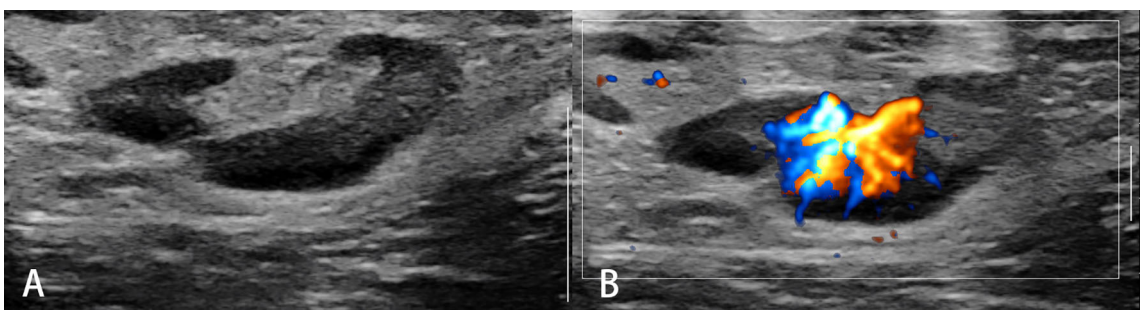

FIGURE 1 | Reactive lymph nodes. Typically, the architecture **(A)** and predominant vessel architecture **(B)** are preserved.

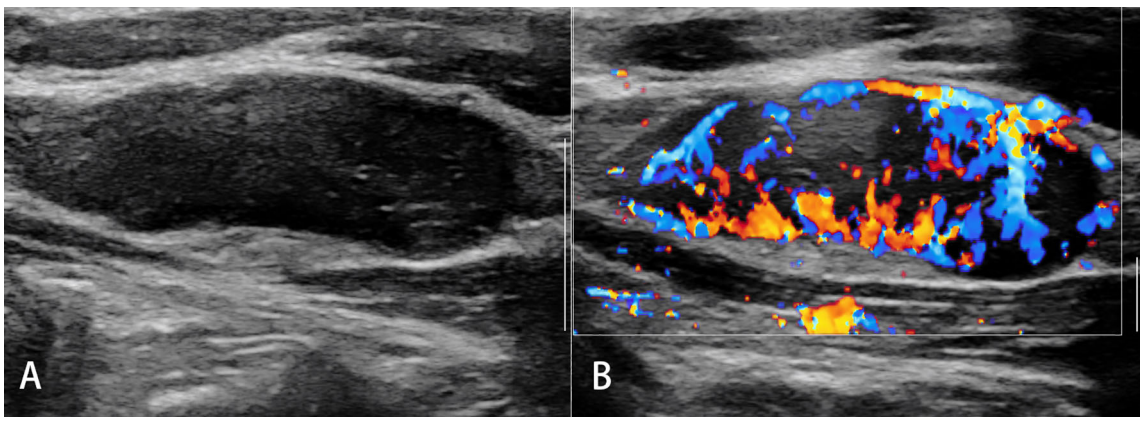

FIGURE 2 | Malignant lymph nodes (carcinoma infiltration). The eccentric hypoechoic cortical thickening **(A)** and vessel destruction **(B)** in the lymph node are observed.

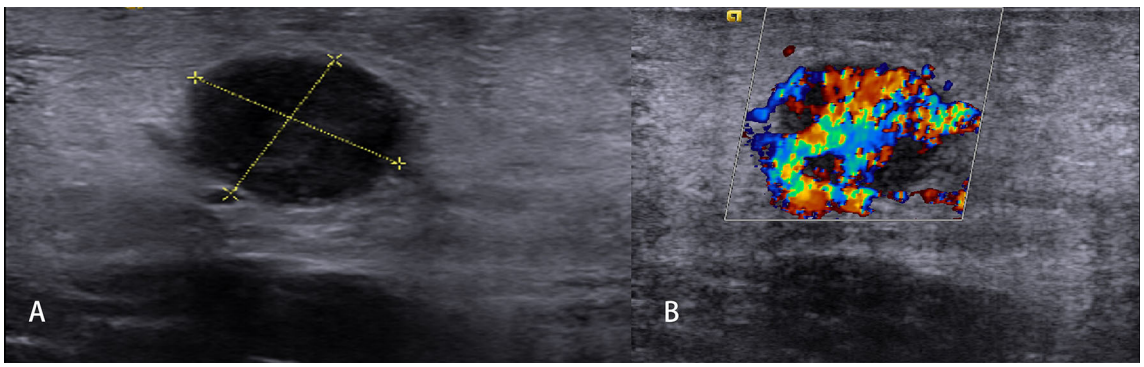

FIGURE 3 | Non-Hodgkin's lymphoma. The destroyed architecture, approximate sphere, and pseudocystic appearance **(A)** and rich vascularity **(B)** are observed.

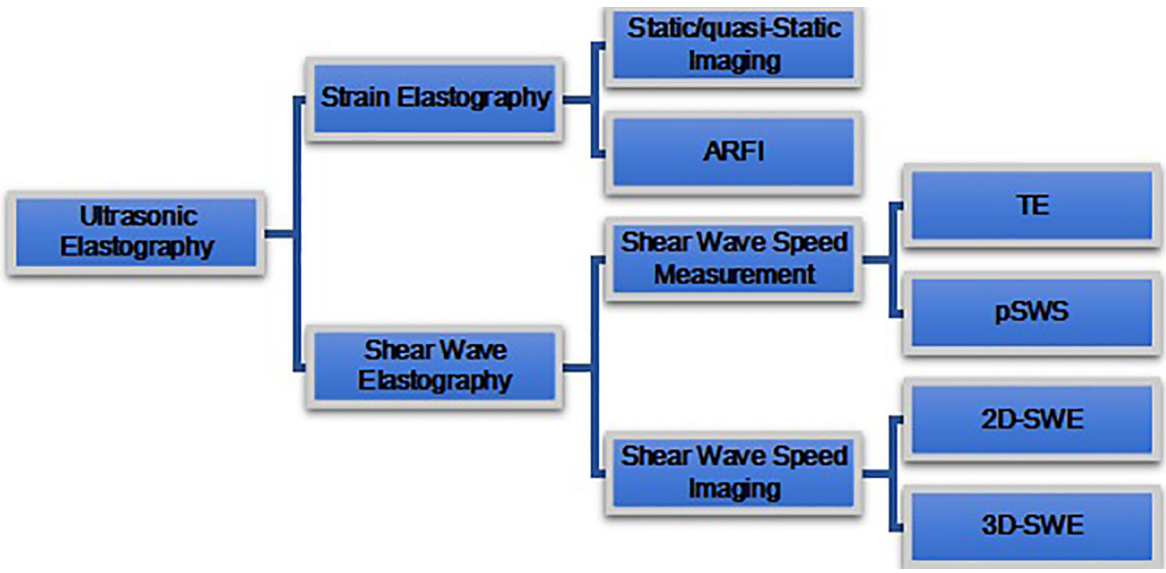

FIGURE 4 | Ultrasound elastography (UE) techniques. UE techniques can be classified by the type of excitation applied: 1) strain elastography (top) and 2) shear wave elastography (bottom). Excitation methods of strain elastography include constant force-induced displacement (static/quasi-static imaging) or acoustic energy-induced physiologic motion (ARFI). Excitation method of shear wave elastography where the shear waves are produced by a transducer. Shear wave elastography is classified as transient elastography (TE), point shear wave elastography (pSWE), two-dimensional shear wave elastography (2D-SWE), and three-dimensional shear wave elastography (3D-SWE), according to different measurement and imaging methods.

the tissue deformation generated by compression, which may be applied with a probe on the body surface for static/quasi-static imaging and may also be applied with acoustic radiation force for ARFI imaging. The tissue deformation is measured by US system and displayed as a color or gray map. On the screen of the US system, both the B-mode image and corresponding elastography image could be simultaneously displayed.

The parameters commonly used to indicate tissue hardness include elasticity score and strain ratio (SR). The elasticity score indicates the strain (with color or brightness) distribution within a selected area. The SR refers to the ratio of strain between area A (usually a mass) and area B (usually a normal surrounding tissue, fat, or muscle tissue) within the region of interest (ROI).

Advantages and Limitations

SE, especially static/quasi-static imaging, is suitable for superficial organs and thus is the most commonly used method for the evaluation of superficial LNs. The operation method of SE is simple, and the operation skills can be mastered in a short time of training. However, SE is a qualitative analysis technique, and it is not able to analyze tissue hardness quantitatively. The performance of static/quasi-static imaging

is not good at analyzing the deep LNs. Moreover, SE is user dependent and subjective (2, 3).

Shear Wave Speed Measurement

Techniques

Shear wave speed measurement technology is a method to generate shear waves and measure SWV. Based on the principle of fast propagation of shear wave speed in hard tissue and slow propagation in soft tissue, the hardness of tissue is indirectly reflected by measuring shear wave speed. Shear wave speed can be converted to Young's modulus by Young's model formula:

$$E = 3\rho C^2$$

where E represents stiffness (Young's modulus [kPa]), ρ is the density (kg/m^3, approximately equal to 1), and C is the shear wave speed (m/s).

The shear wave speed measurement techniques mainly include transient elastography (TE) and point SWE (pSWE). TE is the first shear wave speed measurement technology applied in clinical practice, but it is only used in the liver so far; therefore, this technique is not discussed in this review. The principle of pSWE is similar with ARFI: the probe applies an acoustic radiation force to the ROI of the tissue and generates transverse vibration shear waves. The receiver can detect the speed of shear wave in ROI, which is expressed by speed or by kPa value through Young's model formula.

Advantages and Limitations

pSWE can detect both deep organs (the liver, etc.) and superficial organs (the thyroid, etc.) (4–6), and therefore, this technique is suitable for both superficial and deep LNs. However, the ROI is with fixed size; it can only measure one part of a LN but may be too large if the LN is very small.

Shear Wave Speed Imaging

Techniques

The principles of shear wave speed imaging are that the US probe sends out the multipoint focused acoustic radiation force pulse, which makes the tissues at different depths along with the acoustic axis shift at almost the same time, producing plane shear wave, and then the image processing technology detects the SWV, forms color image, and calculates Young's modulus (elasticity index (EI)) (7). So compared with that of pSWE, the size of ROI in 2D-SWE can be adjustable. Some US diagnostic instruments are equipped with 3D probes with high-speed acquisition capability of mechanical scanning 2D-sensor sequences, which can conduct 3D reconstruction of tissue hardness.

Advantages and Limitations

The diagnosis of shear wave speed imaging is less influenced by the operator's experience and operation than SE, because it does not rely on freehand compression (8). It can display the conventional US images and elastic US images synchronously and measure SWV in real time. However, multicenter studies have shown that the repeatability of shear wave elastic imaging is affected by the size, location, depth, and other factors (9, 10).

CLINICAL APPLICATIONS OF ELASTOGRAPHY

Reactive Lymph Nodes (Inflammation)

Acute or chronic inflammation is the prime cause of LN enlargement (**Figure 5**). The elastographic architecture of LNs is kept in most inflammatory processes. Therefore, like in normal LNs, the cortex is also stiffer than the hilum in inflammatory LNs.

Strain Elastography

Both elasticity score and SR have been studied to evaluate the stiffness of reactive LN. Firstly, due to the lack of a unified classification method for US elastograms, different researchers classified US elastograms of LNs into a 4-point, 5-point, 6-point, 7-point, or 8-point rating scale. Secondly, some researchers compared the strain in target region with adjacent reference region to differentiate benign from malignant LNs.

Lyshchik classified US elastograms of LNs with a 4-point rating scale according to visibility, brightness compared with surrounding neck muscles, regularity, and definition of outline (11). Several studies classified elastograms of the LNs into five patterns according to relative distribution and ratio of soft or hard regions of the LN: pattern 1, absent or very small blue (hard) areas; pattern 2, total blue areas of less than 45%; pattern 3, total blue areas of greater than 45%; pattern 4, peripheral blue

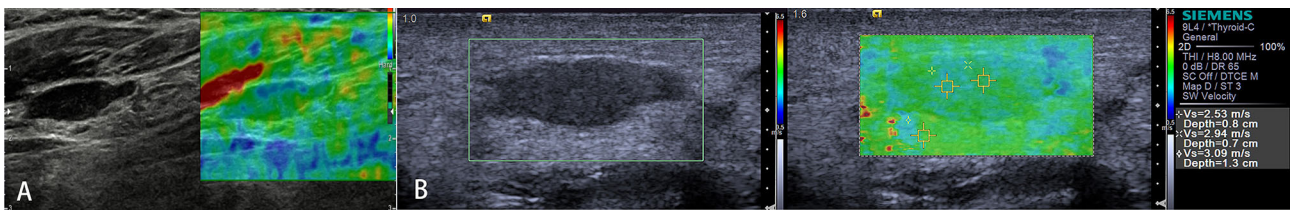

FIGURE 5 | Reactive lymph nodes. Both the strain elastography **(A)** and shear wave-based elastography **(B)** reveal uniform and symmetrical soft tissue (green).

area and central green (soft) area; and pattern 5, blue area with or without a green rim. Tan et al. found that 87.9% of benign LNs manifest pattern 1 or pattern 2 (3).

Besides, Lyshchik defined the surrounding neck muscles to LN SR as strain index; using strain index value of <1.5 in benign LN classification, SE showed 79% accuracy, 85% sensitivity, and 98% specificity (11). Acu et al. calculated each LN with mean strain index. With the use of strain index value of <1.7, SE differentiates benign LNs from malignant ones with 75% accuracy, 71.6% sensitivity, and 76.5% specificity (12). Özel et al. reported that elastography SRs were lower in benign LNs than malignant LNs (13). Many studies have shown that SE has potential diagnostic value in lymphadenopathy (**Table 1**); however, high user dependence is the limitation, especially using SR. Adjacent reference region was selected differently for SR measurement of LNs in different regions; in general, muscles as adjacent reference tissues were usable in cervical region, and fat tissue as an adjacent reference region may be a good choice in the axilla.

Shear Wave-Based Elastography

Compared with SE, shear wave-based elastography is regarded as potentially more objective. In most published researches, virtual touch tissue imaging (VTI) grade and SWV of ARFI imaging were used to evaluate reactive LNs, and the diagnostic performance of VTI is higher than that of SWV (19). In a study including 263 pediatric LNs, Bayramoglu et al. found that median elasticity and velocity values were higher in reactive LNs compared with normal LNs; with the use of the cutoff median elasticity and velocity values of >15 kPa and 2.24 m sn^{-1} for differentiating reactive LNs from normal LNs, sensitivity, specificity, positive predictive value (PPV), negative predictive value (NPV), and diagnostic accuracy were 27%, 96%, 82%, 74%, and 74% and 25%, 97%, 82%, 73%, and 74%, respectively. Many studies should be conducted on the evaluation of reactive LNs by shear wave-based elastography to explore the significance of SWE in the evaluation of reactive LNs and to analyze the potential factors affecting SWE imaging (24).

Malignant Lymph Nodes (Carcinoma)

Malignant tumor cells proliferate rapidly, causing internal pressure and increasing tissue stiffness in LNs. Therefore, the elastographic architecture of LNs changed compared with reactive LNs. Typically, the well-differentiated carcinoma initially infiltrates LNs in a circumscribed manner (focally stiffer and harder), whereas the undifferentiated carcinoma leads to a diffuse (mostly or completely stiffer and harder) infiltration (**Figure 6**).

Strain Elastography

Several pilot studies have evaluated the ability of SE to detect LN metastases in the cervical or axillary LNs (11, 14, 20–22, 27). Both elasticity score and SR have been studied, which showed that SE and conventional US may play complementary roles in

TABLE 1 | The diagnostic performance of ultrasound elastography in differentiating benign and malignant LNs.

Study	Study description	LN	SE (%)	SP (%)	PPV (%)	NPV (%)	Accuracy	Gold standard
Lo WC, *European Radiology* (14)	Qualitative (4 patterns)	131	66.7	57.1	52.2	71.0	–	Histology
Suzan Onol, *Cureus* (15)	Qualitative (4 scores)	70	94	70	–	–	86	Histology
Leyla Acu, *J Ultrasound Med* (12)	Qualitative (5 patterns)	220	82.1	56.2	45.1	87.8	64.1	Histopathology
Tsai WC, *Ultrasound in Medicine & Biology* (16)	Qualitative (5 patterns)	90	86	90	91	84	88	Surgical pathology
Xu Y, *Scientific Reports* (17)	Qualitative (5 patterns)	97	78	93	93	79	86	Surgical pathology
Müberra Pehlivan, *Braz J Otorhinolaryngol* (18)	Qualitative (5 patterns)	16	82.4	84.6	87	78	83.3	Histology
Zhang F, *Medicine (Baltimore)* (19)	Qualitative (6 patterns)	97	81.58	95.65	–	–	86.89	Histology
Lenghel LM, *Medical Ultrasonography* (20)	Qualitative (8 patterns)	69	66.7	96.7	–	–	84.6	Follow-up, histology
Lyshchik A, *Radiology* (11)	Quantitative (strain index ≥ 1.5)	141	85	98	–	–	92	Histology
Leyla Acu, *J Ultrasound Med* (12)	Quantitative (strain index ≥ 1.7)	220	71.6	76.5	57.1	86.0	75.0	Histopathology
Müberra Pehlivan, *Braz J Otorhinolaryngol* (18)	Quantitative (strain index ≥ 1.04)	16	100	84.62	–	–	95	Histology
Zhang F, *Medicine (Baltimore)* (19)	Quantitative (SWV ≥ 2.76 m)	97	57.89	86.96	–	–	68.85	Histology
Fujiwara T, *Ultrasound in Medicine & Biology* (21)	Quantitative (SWV ≥ 1.9 m/s)	42	95.0	81.8	–	–	88.0	Surgical pathology, Lymph node open biopsy
Meng W, *European Journal of Radiology* (22)	Quantitative (VTIQ value ≥ 2.595 m/s)	181	82.9	93.1	–	–	90.6	Surgical pathology, fine-needle aspiration
Azizi G, *Ultrasound in Medicine & Biology* (23)	Quantitative (VTIQ value ≥ 2.93 m/s)	270	92.59	75.49	48.54	97.60	78.9	Surgical pathology
Zuhal Bayramoglu, *Br J Radiol* (24)	Quantitative (elasticity > 17 kPa) (lymphoma *vs*. lymphadenitis)	117	96	100	100	99	99	Histology
Shuyi Luo, *Front Oncol* (25)	Qualitative SWE (4 scores)	121	96.7	100	100	96.8	98.3	Core needle biopsy, surgical pathology
Wei Lin Ng, *Acad Radiol* (26)	Qualitative SWE (4 scores)	107	96.0	56.1	–	–	81.3	Histopathology

LNs, lymph nodes; SE, sensitivity; SP, specificity; PPV, positive predictive value; NPV, negative predictive value; SWV, shear wave velocity; VTIQ, virtual touch tissue imaging quantification; SWE, shear wave elastography.

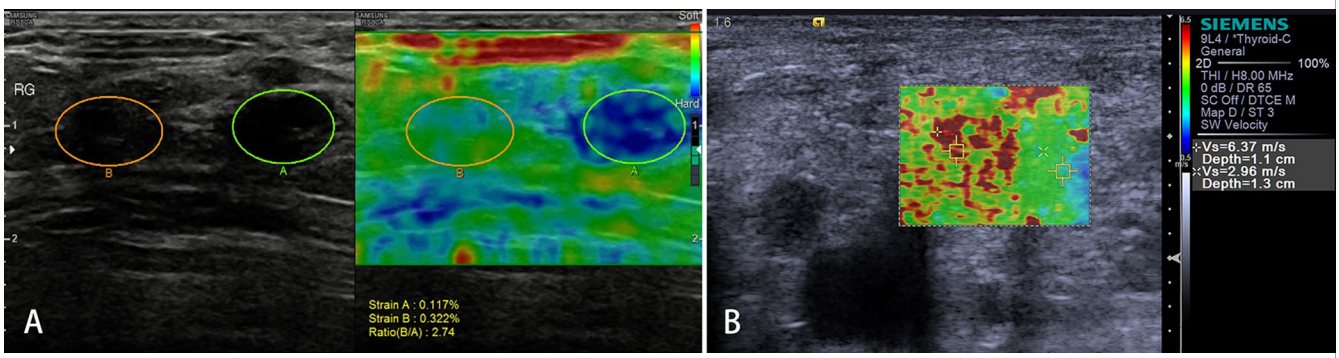

FIGURE 6 | Malignant lymph nodes (LNs) (carcinoma infiltration). The strain elastography reveals typically harder (blue) area in the LN than the surrounding tissues (green); strain ratio = 2.74 **(A)**. The shear wave-based virtual touch tissue imaging quantification reveals a harder (red) area in the LN, and the maximum shear wave velocity (6.37 m/s) is much higher than that of surrounding tissues (2.96 m/s) **(B)**.

differentiating malignant LNs and assessing the risk of metastatic LNs.

Firstly, suspected cervical LN metastases from hypopharyngeal and thyroid carcinomas have been recently investigated using SE (real-time elastography (RTE)) (11). An EI has been created by comparing the elasticity of the LN with the surrounding head and neck muscle tissue (muscle to LN SR). With the use of a ratio of >1.5 as an indicator of malignant infiltration, the sensitivity was 85% and the specificity was 98%, which are superior to the best B-mode criteria (11). These data have been reproduced by Tan et al. Moreover, inter-observer agreement with SE was very high (kappa 0.88–0.946) (3).

Secondly, some researchers qualitatively classified US elastograms of LNs into a 4-point, 5-point, 6-point, 7-point, or 8-point rating scale. Metastatic LNs were mostly evaluated to 3–4 points in a 4-point rating scale. Suzan (15) found that the sensitivity, specificity, and accuracy of RTE in differentiating benign LN from squamous cell carcinoma and malignant melanoma group were 91%, 70%, and 86%, respectively.

In a 5-point rating scale (3, 12, 16, 18), Tan et al. reported that 50 of malignant and 74.5% of metastatic LNs manifested pattern 3 or 4, while all primary malignant LNs manifested pattern 2 (3). In another study including 97 axillary LNs, using the criteria of score 1 and 2 as benign and scores 3, 4, and 5 as metastatic, the sensitivity, specificity, PPV, NPV, and accuracy were 78%, 93%, 93%, 79%, and 86%, respectively (16). Although qualitative strain methods based on elasticity score and SR have been widely studied all over the world for axillary and cervical LNs (17), SR >1.5 or hard composition over 50% can be a good indicator of malignancy. However, as compared with SWE, its dependence on operators cannot be overcome, and absolute quantitative elastic measurement cannot be provided; and for LNs with deep vertical distance and small volume, the judgment of RTE on LNs hardness is prone to false-positive results, which affects the accuracy of SE (16).

Shear Wave-Based Elastography

Clinically and theoretically, SWE seems to be an effective, quantitative tool for differential diagnosis of malignant and benign LNs in many researches, especially in small LNs (28). Based on previous researches, the maximum SWV (2.93 m/s) (23) and elastic value ratio (29) can be used as reliable indices to predict benign and malignant lymphatic nodes. Kılıç A et al. conducted a prospective study comparing conventional US with VTI quantification (VTIQ), and when using a cutoff value of 3.03 m/s, VTIQ differentiates malignant LNs from benign ones with 75% accuracy, 93% sensitivity, and 59% specificity (30).

Some researchers (25, 26) qualitatively classified SWE images of axillary LN (ALN) into 4-point patterns, which was similar to SWE patterns of breast lesions (31): color pattern 1, homogeneous pattern; color pattern 2, filling defect within LN; color pattern 3, homogeneous within LN with a localized colored area at the margin; and color pattern 4, filling defect within LN with a localized colored area at the margin (25). The benign ALNs usually manifest color pattern 1, while ALN metastases (ALNMs) usually manifest color patterns 2–4, and the sensitivity, specificity, PPV, NPV, and area under the receiver operating characteristic (ROC) curve (AUC) were 96.7%, 100%, 100%, 96.8%, and 98.3%, respectively (25). In addition, Luo et al. (25) and Lin et al. (26) directly compared the diagnostic performance of qualitative and quantitative SWE, and they found that qualitative SWE had better diagnostic performance than quantitative SWE in detecting ALNM.

However, a meta-analysis compared the diagnostic performance of qualitative elastography with quantitative elastography for ALNM in breast cancer and found that quantitative and qualitative elastography had similar diagnostic performance and good clinical utility (32). More studies with SWE should be conducted to get more reliable cutoff values of SWV and elastic value ratio in different sites.

Lymphoma

Lymphomas are a primary malignant tumor of LNs, lymphoid tissues outside LNs, and mononuclear macrophage system (**Figure 7**). Because of a highly heterogeneous group of lymphoproliferative malignancies, the biological behavior and pathological types of lymphomas are different, especially for non-Hodgkin's lymphoma. But the incidence of lymphomas

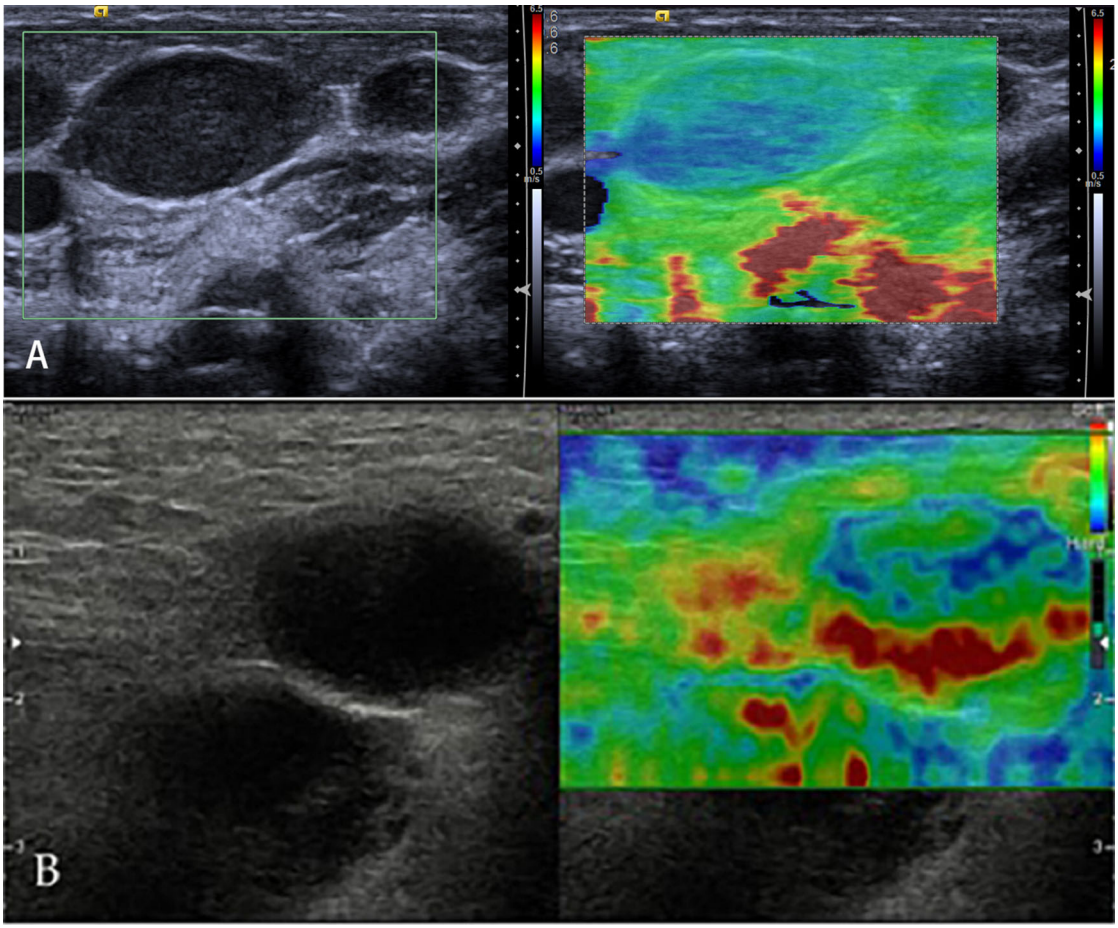

FIGURE 7 | Non-Hodgkin's lymphoma. The strain elastography reveals a focal harder (blue) area in the lymph node **(A)** and a diffuse harder (blue) area in the lymph node **(B)**.

represents approximately 4%, and newly diagnosed cancers increases each year; moreover, lymphomas are more commonly seen in developed countries, which may seriously endanger people's health (33). Knowledge of elastography in lymphoma is very limited. So far, different lymphomas cannot be differentiated. Initial experience suggests that focal LN infiltration (**Figure 7A**) is indicative of low-grade follicular lymphoma, whereas diffuse and homogenous LN infiltration is typically found in high-grade lymphoma (**Figure 7B**).

Strain Elastography

Few studies have reported on the evaluation of lymphoma with SE. With a 5-point rating scale of US elastograms of LNs, Acu et al. reported that most lymphoma manifested patterns 1 and 2 (16). Clinically and theoretically, the stiffness degree of lymphoma is different from that of metastatic and benign LNs (34). In most studies, the hardness of the lymphoma was low. Thus, when metastasis and lymphoma were considered as positive, reactive LNs were considered as negative in the differential diagnosis; and the sensitivity, specificity, and accuracy with a point rating scale of US elastograms were affected (35). With quantitative analysis of SE, elasticity parameter strain index showed high diagnostic accuracy for distinguishing lymphoma from lymphadenitis; the cutoff value of the strain index of the cervical LNs compared with sternocleidomastoid muscle has been reported to be 1.18 in a recent study (36). Though it is difficult to differentiate different lymphomas, the treatment effect evaluation with SE in Hodgkin's disease may be useful.

In the study on the efficacy of refractory and recurrent Hodgkin's disease, it has been shown that the hardness of some lymphoma nodules changes with the treatment effect. It indicates that SE could be reliable for therapy response monitoring of Hodgkin's lymphoma (37).

Shear Wave-Based Elastography

Currently, there are few studies on the evaluation of lymphoma by SWE. The number of enrolled lymphoma in these studies was small, including several case reports. Soo et al. qualitatively categorized shear speed map in a of total five SWE patterns in cervical LNs: pattern 1, absent or very small red (stiff) area; pattern 2, small scattered red areas, which mean total red area

less than 45%; pattern 3, large red area, equal or more than 45%; pattern 4, peripheral red area and central green (soft) area, suggesting central necrosis; and pattern 5, almost red area with or without a green rim. None of lymphoma manifested pattern 4 and pattern 5; and absolute values and ratio of both elasticity and speed were significantly lower in lymphomas than metastatic LNs (38). Based on a recent study in pediatric LN with quantitative evaluation of SWE, elasticity values higher than 17 kPa and velocity values higher than 2.45 m/s would be considered as lymphoma rather than lymphadenitis in an enlarged LN with at least a 91% diagnostic accuracy (24). Several case reports have evaluated uncommon different lymphomas with SWE. A report used SWE to evaluate primary B-cell lymphoma of the breast. The study showed that the mass of primary B-cell lymphoma on SWE was considerably stiff but softer than typical invasive ductal cancers. In the future, a prospective study with large-scale samples should be conducted to investigate quantitative or qualitative SWE features of primary B-cell lymphoma (39).

Other Lymphadenopathy

In the preliminary study of reactive and metastatic LNs, the AUC for combined evaluation is 0.97, which is much higher than that for B-mode US or elastography alone (28). The analysis of parameters can be used to quantitatively evaluate the characteristics of different LN diseases; it shows that LNs of tuberculosis (TB) are softer than metastatic LNs but harder than benign LNs (40). However, LNs of TB have a wide range of stiffness; the stiffness is related with internal structures, increased fibrous tissue and calcification can account for high stiffness, and liquefaction necrosis can decrease the stiffness. Cheng et al. found that only 50% LNs of TB can be correctly diagnosed by elastography (41).

In further studies, the combination of B-mode US and elastography may have important clinical value in differential diagnosis. Few researches have been done on relapsing or chronic lymphadenitis or rare benign diseases such as Kikuchi or Kimura disease (KD). The research shows that the LNs with KD show malignant signs in conventional US, but benign signs in SE; therefore, SE can help patients avoid unnecessary needle biopsy and inappropriate treatment (42). In a study of children's cervical LNs, the stiffness of the largest LNs in patients with bacterial cervical lymphadenitis (BCL) was significantly higher than that in patients with LN-first presentation of Kawasaki disease (NFKD) and healthy children, with a cutoff of 14.55 kPa; the sensitivity, specificity, and AUC were 89%, 76%, and 88.5%, respectively (43). So SWE is a potential method to differentiate early NFKD.

APPLICATIONS OF ENDOSCOPIC ULTRASOUND AND ENDOBRONCHIAL ULTRASOUND ELASTOGRAPHY

Endoscopic US (EUS) and endobronchial US (EBUS) are important tools to assess the digestive tract and surrounding organs, but the limited capacity to determine the exact pathological results is the major limitation. As a non-invasive technique, EUS and EBUS elastography have been proven to be able to provide complementary stiff information added to conventional EUS and EBUS imaging, becoming promising examination methods to differentiate benign from malignant LNs (44–46).

Differentiation of Benign and Malignant Lymph Nodes

Recently, an increasing number of literatures focused on the use of EUS and EBUS to diagnose mediastinal LNs and peritoneal lymphadenitis.

EUS elastography was originally used for the differential diagnosis of pancreatic lesions. Studies on the difference between benign and malignant pancreatic masses and LNs by SE showed that EUS elastography had more advantages than conventional US (47).

Similar to superficial LNs, physiological and reactive peritoneal LNs manifest homogeneous or scattered soft pattern with delineated vascular structures of LN hilum. And the LN medulla may manifest as slightly softer than the LN cortex. Malignant LNs are the most characterized by a homogeneous hard elastographic pattern, especially in diffuse metastatic infiltration; however, malignant LNs may display inhomogeneous but hard patterns because of incomplete metastatic infiltration and focal necrosis. More and more studies differentiated benign from malignant LNs with EUS; most of them were qualitative with elastographic histogram, using EUS–fine-needle aspiration biopsy (FNAB), histology, and/or surgical pathology as a reference standard.

Multiple studies have demonstrated that EUS and EBUS elastography can effectively identify the benign and malignant mediastinal and peritoneal LNs (**Table 2**) (47–51, 53–59). In addition, under the guidance of elastographic imaging, EUS-FNAB or EBUS-FNAB can improve the positive rate of diagnosis and avoid false-positive results.

With qualitative analysis of elastographic histogram, elasticity pattern and SR have been studied to evaluate the stiffness of LNs. Giovannini et al. firstly evaluated the ability of EUS elastography to differentiate benign from malignant LNs with elasticity pattern in 2006 (56). In this color-coded scale of elastographic patterns, yellow means normal tissue, green fibrosis, red fat, and blue malignant tissue. They conducted a multicenter study in 2009 and found improved specificity of 82.5% compared with 50% in the previous study (47). What is more, the sensitivity, specificity, PPV, NPV, and global accuracy of EUS elastography were 91.8%, 82.5%, 88.8%, 86.8%, and 88.1%, respectively, which were significantly better than the respective parameters of B-mode (56). In a study including 40 patients with a 4-point elasticity score, using the criteria of elasticity scores 1 and 2 as benign and elasticity scores 3 and 4 as malignant, the sensitivity, specificity, PPV, NPV, and diagnostic accuracy were 87.5%, 41.7%, 83.3%, 50%, and 60%, respectively (53).

Besides, some researchers qualitatively classified EBUS elastograms into three patterns (48, 50, 51): pattern 1, predominantly non-blue (green, yellow, and red); pattern 2, partly blue and non-blue (green, yellow, and red); and pattern

TABLE 2 | The diagnostic performance of EUS or EBUS elastography in differentiating benign and malignant LNs.

Study	Method	Study description	LN	SE (%)	SP (%)	PPV (%)	NPV (%)	Accuracy	Gold Standard
Knabe, *Surg Endosc* (46)	EUS	Qualitative (3 patterns)	40	100	64.1	75	–	–	Cytology, histology
Izumo, *Jpn J Clin Oncol* (48)	EBUS	Qualitative (3 patterns)	75	100	92.3	94.6	100	96.7	Histology
Korrungruang P, *Respirology* (49)	EBUS	Qualitative (3 patterns)	120	100	66.7	92.3	100	83	Histology, surgical pathology
Ching-Kai Lin, *Journal of the Formosan Medical Association* (50)	EBUS	Qualitative (3 patterns)	206	64.7	85.6	71.6	81.3	78.2	Histology, surgical pathology
Fournier C, *Bronchology Interv Pulmonol* (51)	EBUS	Qualitative (3 patterns)	217	87	68	80	77	80.7	Histology
He, *Journal of Central South University Medical Sciences* (52)	EBUS	Qualitative (4 patterns)	68	85.7	76.9	85.7	76.9	82.3	Cytology, histology, surgical pathology
Ahmed Youssef Altonbary, *Diagn Ther Endosc* (53)	EUS	Qualitative (4 patterns)	40	87.5	41.7	83.3	50	60	Cytology, histology
Giovannini, *WJG* (47)	EUS	Qualitative (5 patterns), multicenter	101	91.8	82.5	88.8	86.8	88.1	Cytology, histology
Xu, *Gastrointestinal Endoscopy* (54)	EUS	Meta-analysis	431	88	85	–	–	94.6	Cytology, surgical pathology
Korrungruang P, *Respirology* (49)	EBUS	Quantitative (SR ≥ 2.5)	120	100	70.8	93.2	100	85	Cytology, histology, surgical pathology
Hussein, *Arab Journal of Gastroenterology* (55)	EUS	Quantitative (SR ≥ 4.61)	126	89.8	83.3	82.5	90.2	–	Cytology, histology, surgical pathology
Ahmed Youssef Altonbary, *Diagn Ther Endosc* (53)	EUS	Quantitative (SR ≥ 6.7)	40	99.9	57.1	99.9	64	77.5	Cytology, histology

EUS, endoscopic ultrasound; EBUS, endobronchial ultrasound; LNs, lymph nodes; SE, sensitivity; SP, specificity; PPV, positive predictive value; NPV, negative predictive value; SR, strain ratio.

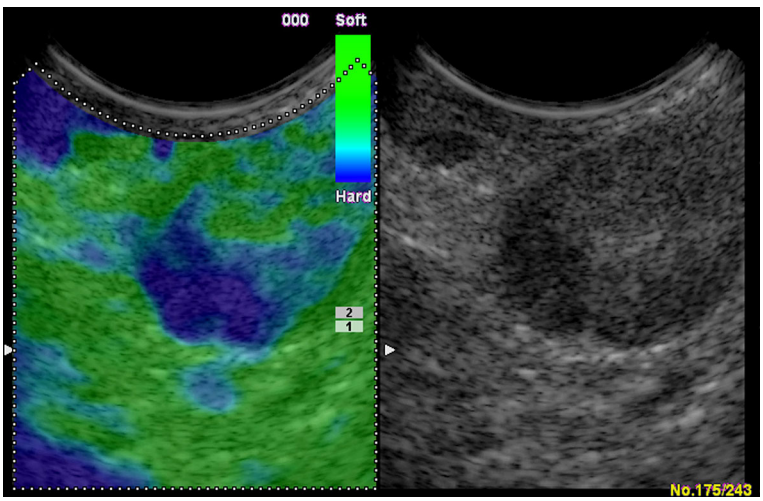

FIGURE 8 | Colorectal carcinoma with presacral circumscribed lymph node metastasis in endoscopic ultrasound. The strain elastography reveals a typically harder (blue) area in the lymph node.

3, predominantly blue. With the use of the criteria of pattern 1 elastogram as benign and pattern 3 as malignant for differentiating malignant and benign mediastinal LNs with EBUS elastography, the sensitivity, specificity, PPV, NPV, and diagnostic accuracy were 90.6%, 82.6%, 71.6%, 94.7%, and 85.2%, respectively. But the central necrosis within malignant LNs and the fibrotic component within benign LNs may influence the accuracy of elastographic evaluations. What is more, the definitions of elastography patterns were subjective and may be hard to repeat by other researchers.

When judging malignant LNs with SR, previous research showed that with the cutoff point of SR >2.5, EUS elastography can differentiate benign from atypical malignant mediastinal LN sensitively (56). Okasha et al. reported that there were 89.8% sensitivity and 83.3% specificity in differentiating malignant LNs from benign ones with endoscopic UE while using the SR cutoff value >4.61 (55). Altonbary et al. found that the sensitivity, specificity, PPV, NPV, and diagnostic accuracy for differentiating benign LNs from malignant LNs were 57.1%, 99.9%, 99.9%, 64%, and 77.5%, respectively, with the mean SR cutoff value >6.7 (53). These studies reported the SR was more accurate than conventional EUS or EBUS, and EUS elastography combined with other sonomorphologic features is a potentially useful prognostic index differentiating malignant from benign

TABLE 3 | Criteria on lymph node characterization using different ultrasound modes.

Lymphadenopathy More (most) likely	Reactive lymph nodes	Malignant infiltration	Lymphoma	Tuberculous lymphadenitis
B-mode	Preserved architecture, aspect ratio > 2, uniform cortex	Eccentric hypoechoic cortical thickening, aspect ratio < 2, boundary ambiguity, tissue edema around	Destroyed architecture, focal or global hypoechoic cortical thickening, usually without echogenic hilum, approximate sphere, pseudocystic appearance	Similar with malignant infiltration
Color Doppler	Lymphatic vascular structure	Peripheral or mixed vascularity, vascular distortion	Rich vascularity	Peripheral or mixed vascularity
Vascular resistance	Lower, RI < 0.8, PI < 1.6	Higher, RI > 0.8, PI > 1.6	Intermediate RI and PI	RI < 0.8, PI < 1.6
Strain elastography	1–2 points in 4-point rating elastography scale, SR in diffuse infiltration < 1.7	SR in diffuse infiltration > 1.7	Patterns 1 and 2 in five pattern elastographic score, dynamic changes occur after treatment	No data
Shear wave-based elastography	No data, most often normal architecture	Shear wave velocity > 3.03 m/s	Shear wave velocity > 2.45 m/s	No data

RI, resistive index; PI, pulsatility index; SR, strain ratio.

LNs (**Figure 8**). Besides, a meta-analysis found that the sensitivity and specificity of UE in differentiating benign and malignant LNs were 88% and 85%, respectively (54).

However, the SR was generally calculated by two selected target regions, which makes it hard to precisely represent the stiffness of the whole LN. Thus, some studies used software to semiquantitatively analyze the color distribution of LN elastogram. Nakajima and his colleagues analyzed 49 LNs with stiff area ratio; they found that the sensitivity and specificity were 81% and 85%, respectively, for predicting metastatic disease, using a cutoff value of 0.311 for stiff area ratios (57). Sun et al. used a software and transformed the elastographic image into gray scale, which varied form 0 (all red pixels) to 255 (all blue pixels). This method could calculate the mean gray value inside the target and reflect the stiffness of the targeted LN. They found that non-small cell lung cancer (NSCLC) showed a higher gray value than small cell lung cancer (SCLC) (201.33 versus 196.37) (58). Ma et al. found that the blue color proportion (BCP) of LNs containing benign diseases was higher than that of normal LNs containing lymphatic tissue (33.3%, 49.0%, and 42.9% *versus* 27.0%), which revealed that the LN stiffness would increase in some diseases with a higher density of cells and vessels, like granulomas and pulmonary infection. These LNs might show the features of metastatic LNs if assessed solely by EUS elastography. However, the BCP in malignant LNs was remarkably higher than benign LNs ($p < 0.001$, 57.1% versus 31.1%). The highest average BCP was shown in lung squamous cell carcinoma (71.6%) (59).

According to published studies on the qualitative EBUS elastography in differentiating benign from malignant LNs, Korrungruang et al. found that two methods had similar diagnostic performances (49), but Lin et al. considered that qualitative EBUS elastography may be more suitable for clinical practice (50).

In the future, more studies should be conducted to compare the qualitative and quantitative EUS elastography in differentiating benign from malignant LNs, in order to find a more suitable, accurate method for clinical practice.

CONCLUSION

UE is a promising method for measuring tissue hardness and has been widely used in differentiating reactive LNs, lymphoma, metastatic LNs, and other lymphadenopathy. Besides, EUS and EBUS elastography are non-invasive techniques and have been proven to be able to provide complementary stiff information for conventional EUS imaging; the positive rate of diagnosis of EUS-FNAB or EBUS-FNAB can be improved under the guidance of elastographic imaging. There are some studies that used elastography in cervical, axillary, mediastinal, and peritoneal LNs, but further studies with unbiased large-scale samples in different sites are still required. Also, the direct comparison between qualitative and quantitative elastography and new solutions for current elastographic limitations should be pursued. The current consensus for LNs diagnosis is that no single parameter has sufficient diagnostic performance, and the combination of UE and traditional US technology is conducive to the differential diagnosis of LNs (**Table 3**). In conclusion, UE can aid in the differentiation of benign and malignant LNs and has immense potential clinical values.

AUTHOR CONTRIBUTIONS

Conception and design: A-JY, X-WC, and CD. Drafting of the article: BW, QG, and YY. Critical revision of the article for important intellectual content: BW, QG, and J-YW. All authors contributed to the article and approved the submitted version.

FUNDING

This work was supported by the Science and Technology Department of Hunan Province under Grant No. 2020SK52705.

REFERENCES

1. Cosgrove D, Piscaglia F, Bamber J, Bojunga J, Correas JM, Gilja OH, et al. EFSUMB. EFSUMB Guidelines and Recommendations on the Clinical Use of Ultrasound Elastography. Part 2: Clinical Applications. *Ultraschall Med* (2013) 34(3):238–53. doi: 10.1055/s-0033-1335375
2. Bhatia KS, Cho CC, Yuen YH, Rasalkar DD, King AD, Ahuja AT. Real-Time Qualitative Ultrasound Elastography of Cervical Lymph Nodes in Routine Clinical Practice: Interobserver Agreement and Correlation With Malignancy. *Ultrasound Med Biol* (2010) 36(12):1990–7. doi: 10.1016/j.ultrasmedbio.2010.08.016
3. Tan R, Xiao Y, He Q. Ultrasound Elastography: Its Potential Role in Assessment of Cervical Lymphadenopathy. *Acad Radiol* (2010) 17(7):849–55. doi: 10.1016/j.acra.2010.03.014
4. Chen BD, Xu HX, Zhang YF, Liu BJ, Guo LH, Li DD, et al. The Diagnostic Performances of Conventional Strain Elastography (SE), Acoustic Radiation Force Impulse (ARFI) Imaging and Point Shear-Wave Speed (pSWS) Measurement for non-Calcified Thyroid Nodules. *Clin Hemorheol Microcirc* (2017) 65(3):259–73. doi: 10.3233/CH-16178
5. Dong Y, Wang WP, Xu Y, Cao J, Mao F, Dietrich CF. Point Shear Wave Speed Measurement in Differentiating Benign and Malignant Focal Liver Lesions. *Med Ultrasonography* (2017) 19(3):259–64. doi: 10.11152/mu-1142
6. Ozkan MB, Bilgici MC, Eren E, Caltepe G, Yilmaz G, Kara C, et al. Role of Point Shear Wave Elastography in the Determination of the Severity of Fibrosis in Pediatric Liver Diseases With Pathologic Correlations. *J Ultrasound Med: Off J Am Inst Ultrasound Med* (2017) 36(11):2337–44. doi: 10.1002/jum.14277
7. Bamber J, Cosgrove D, Dietrich CF, Fromageau J, Bojunga J, Calliada F, et al. EFSUMB Guidelines and Recommendations on the Clinical Use of Ultrasound Elastography. Part 1: Basic Principles and Technology. *Ultraschall der Med* (2013) 34(2):169–84. doi: 10.1055/s-0033-1335205
8. Bhatia KS, Lee YY, Yuen EH, Ahuja AT. Ultrasound Elastography in the Head and Neck. Part II. Accuracy for Malignancy. *Cancer imaging: Off Publ Int Cancer Imaging Soc* (2013) 13(2):260–76. doi: 10.1102/1470-7330.2013.0027
9. Yoon JH, Jung HK, Lee JT, Ko KH. Shear-Wave Elastography in the Diagnosis of Solid Breast Masses: What Leads to False-Negative or False-Positive Results? *Eur Radiol* (2013) 23(9):2432–40. doi: 10.1007/s00330-013-2854-6
10. Kim SJ, Ko KH, Jung HK, Kim H. Shear Wave Elastography: Is It a Valuable Additive Method to Conventional Ultrasound for the Diagnosis of Small (</=2 Cm) Breast Cancer? *Medicine* (2015) 94(42):e1540. doi: 10.1097/MD.0000000000001540
11. Lyshchik A, Higashi T, Asato R, Tanaka S, Ito J, Hiraoka M, et al. Cervical Lymph Node Metastases: Diagnosis at Sonoelastography–Initial Experience. *Radiology* (2007) 243(1):258–67. doi: 10.1148/radiol.2431052032
12. Leyla A, Suna Özhan O, Rusen A. Value of Ultrasound Elastography in the Differential Diagnosis of Cervical Lymph Nodes. *J Ultrasound Med* (2016) 35:2491–9. doi: 10.7863/ultra.15.09019
13. Özel D, Özel B. Evaluation of Diagnostic Value of Conventional and Color Doppler Ultrasound With Elastography Strain Ratios in Differentiation Between Benign and Malignant Lymph Nodes. *Pol J Radiol* (2018) 83:3236. doi: 10.5114/pjr.2018.73293
14. Lo WC, Cheng PW, Wang CT, Liao LJ. Real-Time Ultrasound Elastography: An Assessment of Enlarged Cervical Lymph Nodes. *Eur Radiol* (2013) 23(9):2351–7. doi: 10.1007/s00330-013-2861-7
15. Onol S, Ozkaya O. Diagnostic Value of Real-Time Elastography in Diagnosing Lymph Node Metastasis of Skin Cancer. *Cureus* (2020) Oct 1712(10):e10997. doi: 10.7759/cureus.10997
16. Tsai WC, Lin CK, Wei HK, Yu BL, Hung CF, Cheng SH, et al. Sonographic Elastography Improves the Sensitivity and Specificity of Axilla Sampling in Breast Cancer: A Prospective Study. *Ultrasound Med Biol* (2013) 39(6):941–9. doi: 10.1016/j.ultrasmedbio.2012.12.013
17. Xu Y, Bai X, Chen Y, Jiang L, Hu B, Hu B, et al. Application of Real-Time Elastography Ultrasound in the Diagnosis of Axillary Lymph Node Metastasis in Breast Cancer Patients. *Sci Rep* (2018) 8(1):10234. doi: 10.1038/s41598-018-28474-y
18. Pehlivan M, Gurbuz MK, Cingi C, Adapinar B, Değirmenci AN, Acikalin FM, et al. Diagnostic Role of Ultrasound Elastography on Lymph Node Metastases in Patients With Head and Neck Cancer. *Braz J Otorhinolaryngol* (2019) 85(3):297–302. doi: 10.1016/j.bjorl.2018.01.002
19. Zhang F, Zhao X, Ji X, Han R, Li P, Du M. Diagnostic Value of Acoustic Radiation Force Impulse Imaging for Assessing Superficial Lymph Nodes A Diagnostic Accuracy Study. *Med (Baltimore)* (2017) 96(43):e8125. doi: 10.1097/MD.0000000000008125
20. Lenghel LM, Bolboaca SD, Botar-Jid C, Baciut G, Dudea SM. The Value of a New Score for Sonoelastographic Differentiation Between Benign and Malignant Cervical Lymph Nodes. *Med Ultrasonography* (2012) 14(4):271–7.
21. Fujiwara T, Tomokuni J, Iwanaga K, Ooba S, Haji T. Acoustic Radiation Force Impulse Imaging for Reactive and Malignant/Metastatic Cervical Lymph Nodes. *Ultrasound Med Biol* (2013) 39(7):1178–83. doi: 10.1016/j.ultrasmedbio.2013.02.001
22. Meng W, Xing P, Chen Q, Wu C. Initial Experience of Acoustic Radiation Force Impulse Ultrasound Imaging of Cervical Lymph Nodes. *Eur J Radiol* (2013) 82(10):1788–92. doi: 10.1016/j.ejrad.2013.05.039
23. Azizi G, Keller JM, Mayo ML, Piper K, Puett D, Earp KM, et al. Shear Wave Elastography and Cervical Lymph Nodes: Predicting Malignancy. *Ultrasound Med Biol* (2016) 42(6):1273–81. doi: 10.1016/j.ultrasmedbio.2016.01.012
24. Bayramoglu Z, Caliskan E, Karakas Z, Karaman S, Tugcu D, Somer A, et al. Diagnostic Performances of Superb Microvascular Imaging, Shear Wave Elastography and Shape Index in Pediatric Lymph Nodes Categorization: A Comparative Study. *Br J Radiol* (2018) 91(1087):20180129. doi: 10.1259/bjr.20180129
25. Luo S, Yao G, Hong Z, Zhang S, Wang W, Zhang J, et al. Qualitative Classification of Shear Wave Elastography for Differential Diagnosis Between Benign and Metastatic Axillary Lymph Nodes in Breast Cancer. *Front Oncol* (2019) 9. doi: 10.3389/fonc.2019.00533
26. Ng WL, Omar N, Ab Mumin N, Ramli Hamid MT, Vijayananthan A, Rahmat K. Diagnostic Accuracy of Shear Wave Elastography as an Adjunct Tool in Detecting Axillary Lymph Nodes Metastasis. *Acad Radiol* (2021) S1076-6332(21):00138–0. doi: 10.1016/j.acra.2021.03.018
27. Ishibashi N, Yamagata K, Sasaki H, Seto K, Shinya Y, Ito H, et al. Real-Time Tissue Elastography for the Diagnosis of Lymph Node Metastasis in Oral Squamous Cell Carcinoma. *Ultrasound Med Biol* (2012) 38(3):389–95. doi: 10.1016/j.ultrasmedbio.2011.12.004
28. Desmots F, Fakhry N, Mancini J, Reyre A, Vidal V, Jacquier A, et al. Shear Wave Elastography in Head and Neck Lymph Node Assessment: Image Quality and Diagnostic Impact Compared With B-Mode and Doppler Ultrasonography. *Ultrasound Med Biol* (2016) 42(2):387–98. doi: 10.1016/j.ultrasmedbio.2015.10.019
29. Youk JH, Son EJ, Kim JA, Gweon HM. Pre-Operative Evaluation of Axillary Lymph Node Status in Patients With Suspected Breast Cancer Using Shear Wave Elastography. *Ultrasound Med Biol* (2017) 43(8):1581–6. doi: 10.1016/j.ultrasmedbio.2017.03.016
30. Klıç A, Çolakoğlu Er H. Virtual Touch Tissue Imaging Quantification Shear Wave Elastography for Determining Benign Verus Malignant Cervical Lymph Nodes: A Comparison With Conventional Ultrasound. *Diagn Interv Radiol* (2019) 25:114–21. doi: 10.5152/dir.2019.18406
31. Cong R, Li J, Guo S. A New Qualitative Pattern Classification of Shear Wave Elastograghy for Solid Breast Mass Evaluation. *Eur J Radiol* (2017) 87:111–9. doi: 10.1016/j.ejrad.2016.12.021
32. Huang XW, Huang QX, Huang H, Cheng MQ, Tong WJ, Xian MF, et al. Diagnostic Performance of Quantitative and Qualitative Elastography for Axillary Lymph Node Metastasis in Breast Cancer: A Systematic Review and Meta-Analysis. *Front Oncol* (2020) 10:552177. doi: 10.3389/fonc.2020.552177
33. Torre LA, Bray F, Siegel RL, Ferlay J, Lortet-Tieulent J, Jemal A. Global Cancer Statistics, 2012. *Cancer J Clin* (2015) 65(2):87–108. doi: 10.3322/caac.21262
34. Alam F, Naito K, Horiguchi J, Fukuda H, Tachikake T, Ito K. Accuracy of Sonographic Elastography in the Differential Diagnosis of Enlarged Cervical Lymph Nodes: Comparison With Conventional B-Mode Sonography. *AJR Am J Roentgenol* (2008) 191(2):604–10. doi: 10.2214/AJR.07.3401
35. Lenghel LM, Botar Jid C, Bolboaca SD, Ciortea C, Vasilescu D, Baciut G, et al. Comparative Study of Three Sonoelastographic Scores for Differentiation Between Benign and Malignant Cervical Lymph Nodes. *Eur J Radiol* (2015) 84(6):1075–82. doi: 10.1016/j.ejrad.2015.02.017
36. Turgut E, Celenk C, Tanrivermis Sayit A, Bekci T, Gunbey HP, Aslan K. Efciency of B-Mode Ultrasound and Strain Elastography in Differentiating Between Benign and Malignant Cervical Lymph Nodes. *Ultrasound Q* (2017) 33:201–7. doi: 10.1097/RUQ.0000000000000302

37. Squillaci E, Antonicoli M, Manenti G, Bolacchi F. Real-Time Ultrasound Elastography for Assessment of Response to Brentuximab Vedotin Treatment in Relapsed and Refractory Hodgkin Lymphoma. *Eur Rev Med Pharmacol Sci* (2016) 20(8):1628–35.
38. Chae SY, Jung HN, Ryoo I, Suh S. Differentiating Cervical Metastatic Lymphadenopathy and Lymphoma by Shear Wave Elastography. *Sci Rep* (2019) 9(1):12396. doi: 10.1038/s41598-019-48705-0
39. Youdong K, KYung Hee K, Hae KYoung J, HYun Ju L. Shear-Wave Elastography Features of Primary Non-Hodgkin's Lymphoma of the Breast: A Case Report and Literature Review. *J Clin Diagn Res* (2016) 10(12):TD01–3. doi: 10.7860/JCDR/2016/22612.9062
40. Fu Y, Shi YF, Yan K, Wang YJ, Yang W, Feng GS. Clinical Value of Real Time Elastography in Patients With Unexplained Cervical Lymphadenopathy: Quantitative Evaluation. *Asian Pac J Cancer Prev* (2014) 15(13):5487–92. doi: 10.7314/APJCP.2014.15.13.5487
41. Cheng KL, Choi YJ, Shim WH, Lee JH, Baek JH. Virtual Touch Tissue Imaging Quantification Shear Wave Elastography: Prospective Assessment of Cervical Lymph Nodes. *Ultrasound Med Biol* (2016) 42:378–86. doi: 10.1016/j.ultrasmedbio.2015.10.003
42. Baik J, Lee KH, Ryu J, Kim O, Yoon JH, Kim SH, et al. Role of Real-Time Elastography in the Evaluation of Cervical Lymph Nodes in Patients With Kikuchi Disease. *Ultrasound Med Biol* (2016) 42(9):2334–40. doi: 10.1016/j.ultrasmedbio.2016.05.009
43. Qin Q, Wang D, Xu L, Lan Y, Tong M. Evaluating Lymph Node Stiffness to Differentiate Bacterial Cervical Lymphadenitis and Lymph Node-First Presentation of Kawasaki Disease by Shear Wave Elastography. *J Ultrasound Med* (2020) 40(7):1371–80. doi: 10.1002/jum.15518
44. Saftoiu A, Vilmann P, Ciurea T, Popescu GL, Iordache A, Hassan H, et al. Dynamic Analysis of EUS Used for the Diffierentiation of Benign and Malignant Lymph Nodes. *Gastrointest Endosc* (2007) 66:291–300. doi: 10.1016/j.gie.2006.12.039
45. Barr RG, Nakashima K, Amy D, Cosgrove D, Farrokh A, Schafer F, et al. WFUMB Guidelines and Recommendations for Clinical Use of Ultrasound Elastography: Part 2: Breast. *Ultrasound Med Biol* (2015) 41:1148–60. doi: 10.1016/j.ultrasmedbio.2015.03.008
46. Knabe M, Günter E, Ell C, Pech O. Can EUS Elastography Improve Lymph Node Staging in Esophageal Cancer? *Surg Endosc* (2013) 27(4):1196–202. doi: 10.1007/s00464-012-2575-y
47. Giovannini M, Thomas B, Erwan B, Christian P, Fabrice C, Benjamin E, et al. Endoscopic Ultrasound Elastography for Evaluation of Lymph Nodes and Pancreatic Masses: A Multicenter Study. *World J Gastroenterol* (2009) 15 (13):1587–93. doi: 10.3748/wjg.15.1587
48. Izumo T, Sasada S, Chavez C, Matsumoto Y, Tsuchida T. Endobronchial Ultrasound Elastography in the Diagnosis of Mediastinal and Hilar Lymph Nodes. *Jpn J Clin Oncol* (2014) 44:956e62. doi: 10.1093/jjco/hyu105
49. Korrungruang P, Boonsarngsuk V. Diagnostic Value of Endobronchial Ultrasound Elastography for the Differentiation of Benign and Malignant Intrathoracic Lymph Nodes. *Respirology* (2017) 22(5):972–7. doi: 10.1111/resp.12979
50. Lin CK, Yu KL, Chang LY, Fan HJ, Wen YF, Ho CC. Differentiating Malignant and Benign Lymph Nodes Using Endobronchial Ultrasound Elastography. *J Formos Med Assoc* (2019) 118(1 Pt 3):436–43. doi: 10.1016/j.jfma.2018.06.021
51. Fournier C, Dhalluin X, Wallyn F, Machuron F, Bouchindhomme B, Copin MC, et al. Performance of Endobronchial Ultrasound Elastography in the Differentiation of Malignant and Benign Mediastinal Lymph Nodes: Results in Real-Life Practice. *J Bronchol Interv Pulmonol* (2019) 26(3):193–8. doi: 10.1097/LBR.0000000000000551
52. He H, Lu X, Ma H, Zhu J, Huang M. Value of Endobronchial Ultrasound Elastography in the Diagnosis of Mediastinal and Hilar Lymph Node Metastasis in Lung Cancer. *Zhong Nan Da Xue Xue Bao Yi Xue Ban* (2016) 41(1):30–6. doi: 10.11817/j.issn.1672-7347.2016.01.005
53. Altonbary AY, Hakim H, El-Shamy AM. Endoscopic Ultrasound Elastography for Evaluation of Lymph Nodes: A Single Center Experience. *Diagn Ther Endosc* (2018) 2018:7186341. doi: 10.1155/2018/7186341
54. Xu W, Shi J, Zeng X, Li X, Xie WF, Guo J, et al. EUS Elastography for the Differentiation of Benign and Malignant Lymph Nodes: A Meta-Analysis. *Gastrointestinal Endoscopy* (2011) 74(5):1001–9quiz 1115 e1001–1004. doi: 10.1016/j.gie.2011.07.026
55. Okasha H, Elkholy S, Sayed M, El-Sherbiny M, El-Hussieny R, El-Gemeie E, et al. Ultrasound, Endoscopic Ultrasound Elastography, and the Strain Ratio in Differentiating Benign From Malignant Lymph Nodes. *Arab J Gastroenterol* (2018) 19(1):7–15. doi: 10.1016/j.ajg.2018.01.001
56. Giovannini M, Hookey LC, Bories E, Pesenti C, Monges G, Delpero JR. Endoscopic Ultrasound Elastography: The Frst Step Towards Virtual Biopsy? Preliminary Results in 49 Patients. *Endoscopy* (2006) 38(4):344–8. doi: 10.1055/s-2006-925158
57. Nakajima T, Inage T, Sata Y, Morimoto J, Tagawa T, Suzuki H, et al. Elastography for Predicting and Localizing Nodal Metastases During Endobronchial Ultrasound. *Respiration* (2015) 90(6):499–506. doi: 10.1159/000441798
58. Sun J, Zheng X, Mao X, Wang L, Xiong H, Herth FJF, et al. Endobronchial Ultrasound Elastography for Evaluation of Intrathoracic Lymph Nodes: A Pilot Study. *Respiration* (2017) 93(5):327–38. doi: 10.1159/000464253
59. Ma H, An Z, Xia P, Cao J, Gao Q, Ren G, et al. Semi-Quantitative Analysis of EBUS Elastography as a Feasible Approach in Diagnosing Mediastinal and Hilar Lymph Nodes of Lung Cancer Patients. *Sci Rep* (2018) 8(1):3571. doi: 10.1038/s41598-018-22006-4

Conflict of Interest: The authors declare that the research was conducted in the absence of any commercial or financial relationships that could be construed as a potential conflict of interest.

frontiers in Oncology

ORIGINAL RESEARCH
published: 07 September 2021
doi: 10.3389/fonc.2021.709339

Preoperative Prediction of Microvascular Invasion in Patients With Hepatocellular Carcinoma Based on Radiomics Nomogram Using Contrast-Enhanced Ultrasound

Di Zhang[1], Qi Wei[2], Ge-Ge Wu[2], Xian-Ya Zhang[2], Wen-Wu Lu[1], Wen-Zhi Lv[3], Jin-Tang Liao[4], Xin-Wu Cui[2]*, Xue-Jun Ni[1]* and Christoph F. Dietrich[5]*

[1] Department of Medical Ultrasound, Affiliated Hospital of Nantong University, Nantong, China, [2] Department of Medical Ultrasound, Tongji Hospital, Tongji Medical College, Huazhong University of Science and Technology, Wuhan, China, [3] Department of Artificial Intelligence, Julei Technology Company, Wuhan, China, [4] Department of Diagnostic Ultrasound, Xiang Ya Hospital, Central South University, Changsha, China, [5] Department of Internal Medicine, Hirslanden Clinic, Bern, Switzerland

Purpose: This study aimed to develop a radiomics nomogram based on contrast-enhanced ultrasound (CEUS) for preoperatively assessing microvascular invasion (MVI) in hepatocellular carcinoma (HCC) patients.

Methods: A retrospective dataset of 313 HCC patients who underwent CEUS between September 20, 2016 and March 20, 2020 was enrolled in our study. The study population was randomly grouped as a primary dataset of 192 patients and a validation dataset of 121 patients. Radiomics features were extracted from the B-mode (BM), artery phase (AP), portal venous phase (PVP), and delay phase (DP) images of preoperatively acquired CEUS of each patient. After feature selection, the BM, AP, PVP, and DP radiomics scores (Rad-score) were constructed from the primary dataset. The four radiomics scores and clinical factors were used for multivariate logistic regression analysis, and a radiomics nomogram was then developed. We also built a preoperative clinical prediction model for comparison. The performance of the radiomics nomogram was evaluated *via* calibration, discrimination, and clinical usefulness.

Results: Multivariate analysis indicated that the PVP and DP Rad-score, tumor size, and AFP (alpha-fetoprotein) level were independent risk predictors associated with MVI. The radiomics nomogram incorporating these four predictors revealed a superior discrimination to the clinical model (based on tumor size and AFP level) in the primary dataset (AUC: 0.849 *vs*. 0.690; $p < 0.001$) and validation dataset (AUC: 0.788 *vs*. 0.661; $p = 0.008$), with a good calibration. Decision curve analysis also confirmed that the radiomics nomogram was clinically useful. Furthermore, the significant improvement of net reclassification index (NRI) and integrated discriminatory improvement (IDI) implied that the PVP and DP radiomics signatures may be very useful biomarkers for MVI prediction in HCC.

OPEN ACCESS

Edited by:
Lizhi Liu,
Sun Yat-Sen University Cancer Center (SYSUCC), China

Reviewed by:
Jianhua Zhou,
Sun Yat-Sen University Cancer Center (SYSUCC), China
Xulei Qin,
Stanford University, United States
Han Xiao,
Sun Yat-Sen University, China
Xiaofeng Tang,
Sun Yat-Sen University, China

***Correspondence:**
Jin-Tang Liao
liaojintang@hotmail.com
Xin-Wu Cui
cuixinwu@live.cn
Xue-Jun Ni
dyfnxj213@163.com

Specialty section:
This article was submitted to Cancer Imaging and Image-directed Interventions, a section of the journal Frontiers in Oncology

Received: *13 May 2021*
Accepted: *13 August 2021*
Published: *07 September 2021*

Citation:
Zhang D, Wei Q, Wu G-G, Zhang X-Y, Lu W-W, Lv W-Z, Liao J-T, Cui X-W, Ni X-J and Dietrich CF (2021) Preoperative Prediction of Microvascular Invasion in Patients With Hepatocellular Carcinoma Based on Radiomics Nomogram Using Contrast-Enhanced Ultrasound. Front. Oncol. 11:709339. doi: 10.3389/fonc.2021.709339

Conclusion: The CEUS-based radiomics nomogram showed a favorable predictive value for the preoperative identification of MVI in HCC patients and could guide a more appropriate surgical planning.

Keywords: microvascular invasion, hepatocellular carcinoma, contrast-enhanced ultrasound, radiomics, nomogram

INTRODUCTION

Hepatocellular carcinoma (HCC) is the most common primary hepatic malignancy and ranks third among all cancer-related deaths (1, 2). It has always been a major international health problem. Hepatectomy is recognized as the preferred treatment for primary HCC (3). However, recurrence occurs in 30%–50% of patients within 2 years after surgery, resulting in a lower overall survival rate (4). Therefore, it is very important to detect high-risk factors for early recurrence before surgery to enable the formulation of individualized treatment plans.

The definition of microvascular invasion (MVI) is the presence of microscopic metastatic hepatocellular carcinoma emboli within the smaller intrahepatic vessels (5). Some studies have confirmed that MVI is an essential determinant for predicting early recurrence and evaluating the long-term survival of HCC patients (6, 7). The presence of MVI is considered an aggressive pathological indicator (8). Larger resection margins are required for hepatectomy in high-risk patients with MVI (9). Accurate assessment of the presence of MVI before surgery can help surgeons choose appropriate surgical methods. Unfortunately, unlike macrovascular invasion, which can usually be detectable with preoperative imaging, MVI can only be determined according to postoperative pathological specimens (10). Preoperative biopsy is also unreliable due to sampling errors (11).

Imaging examination is an indispensable means of the preoperative evaluation of HCC, some studies have attempted to assess the relationship between preoperative imaging features and MVI status. Several recent reports have suggested that tumor size/number, non-smooth tumor margins, arterial peritumoral enhancement, higher mean kurtosis values, irregular circular enhancement, and radiological characteristics of the capsule may serve as predictors of MVI (12–15). Although these imaging features represent different rates of evaluation, the identification of imaging features mainly depends on the subjective judgment of the radiologist. The accuracy of diagnosis will be affected by the differences in the experience of radiologists. Therefore, a quantitative method is needed to identify MVI non-invasively and accurately before operation.

Radiomics is a process of converting images containing pathophysiology-related information into mineable high-dimensional data, enabling the quantification of diseases using unique imaging algorithms for the diagnosis, prediction, and prognostic evaluation at the molecular level (16–18). Previous studies have demonstrated the potential of radiomics to pre-operatively predict the status of MVI in patients with HCC (19–22). However, most of the radiomics signatures in these studies were based on computed tomography (CT) or magnetic resonance imaging (MRI). Compared with contrast-enhanced CT/MRI, contrast-enhanced ultrasound (CEUS) is a real-time imaging technology with no radiation and fewer limitations in liver examination (23–25). Zhou et al. reported that combined with the tumor number and tumor size, the washout rate of CEUS was significantly associated with the MVI status of HCC patients (26). To better interpret CEUS, we built a radiomics strategy.

Nomograms can be used for the multi-index joint diagnosis or prediction of disease onset or progression. Some studies have demonstrated that the nomograms incorporating clinical risk predictors such as serum α-fetoprotein level (AFP), tumor size, and platelet count (PLT) can be helpful in predicting preoperative MVI status for HCC (13, 27–29). To the best of our knowledge, there have been no previous studies to determine whether a nomogram containing CEUS radiomics would allow a superior prediction of the MVI status.

Thus, the aim of the present study was to develop and validate a radiomics nomogram that is based on the CEUS imaging and clinical risk factors for a preoperative prediction of the MVI status in patients with HCC.

MATERIALS AND METHODS

Patients

This retrospective study was approved by the Institutional Review Board who waived the requirement of informed consent. For the datasets, we assessed the Xiangya Hospital Central South University medical records database between September 2016 and March 2020 to identify patients with a histologically confirmed HCC who underwent surgical resection. The inclusion criteria were as follows: (1) pathologically confirmed primary HCC after hepatic resection; (2) MVI status was confirmed by hepatectomy and histopathological results; (3) CEUS examinations were performed within the two weeks before surgery; (4) solitary tumor; and (5) no previous liver surgery or other treatments had been performed for the suspected HCC lesion. The exclusion criteria included: (1) preoperative anticancer therapy (e.g., radiotherapy, radiofrequency ablation, or transcatheter arterial chemoembolization) before CEUS examination; (2) recurrent HCC; (3) the CEUS image quality of target tumor was unsatisfactory for evaluation; and (4) incomplete clinico-pathological data. The flow diagram of the study population is presented in **Supplementary Figure A1**.

Patients who met the inclusion criteria were randomly allocated to a primary dataset and a validation dataset. The

primary and validation datasets comprised 192 patients (166 men and 26 women; mean age, 55.1 ± 11.1 years; range, 27–83 years) and 121 patients (99 men and 22 women; mean age, 55.37 ± 12.1 years; range, 21–83 years), respectively.

Clinical and Pathologic Data

Baseline clinical information, including sex, age, tumor size, hepatitis, cholelithiasis, serum liver function as well as tumor markers, were derived from the medical records. Serological data including alanine aminotransferase (ALT), AFP, aspartate aminotransferase (AST), PLT, international normalized ratio (INR), albumin (ALB), total bilirubin (TBIL), and direct bilirubin (DBIL) were obtained a week before the surgery. We also collected postoperative pathological information, including the presence of MVI, pathologic differentiation of HCC (well, moderate, or poor according to the WHO histologic grade system), and the presence of liver cirrhosis. Positive MVI refers to cancer cell nests within the vascular lumen that can only be observed under the microscopy.

Contrast-Enhanced Ultrasound Examination

Image acquisition was performed within 2 weeks preoperatively. The CEUS images were acquired with the Aloka ARIETTA 70 (Aloka, Japan, C251 abdominal probe) ultrasound diagnostic instrument. All the CEUS examinations were performed by one of three experienced radiologists (each of whom had at least 15 years of hepatic CEUS experience).

First, the target tumor was detected and assessed by B-mode (BM) ultrasound, the transducer was fixed when the image showed the largest cross-section of the tumor, the maximum diameter measured was taken as the size of the tumor. Then, 2.4 mL of the second-generation ultrasound contrast agent (SonoVue, Bracco, Milan, Italy) was injected intravenously *via* the antecubital vein, followed by flushing with 5 mL of 0.9% normal saline solution. The timer was started immediately while the contrast agent was being injected. The target lesion was continuously observed on the largest cross-section, and each patient saved at least 4 minutes of digital movie clips on the hard disk. All the digital cine clips were recorded as digital imaging data and communications in medicine (DICOM) format and stored into the Picture Archiving and Communication Systems (PACS). Arterial phase (AP) images, portal venous phase (PVP) images, and delay phase (DP) images were obtained at 0–30 s, 31–120 s, and 121–240 s after intravenous injection of the contrast, respectively.

Tumor Segmentation and Radiomics Feature Extraction

Two board-certified radiologists (radiologist 1 and radiologist 2), both with more than 10 years of experience in abdominal CEUS interpretation and blinded to the pathological results and clinical data, independently reviewed the CEUS documents, including all the digital movie clips from this study. For each patient, four images were selected for analysis, including one of BM (before the start of CEUS), one of AP (approximately 25 s after contrast injection), one of PVP (approximately 60 s after contrast injection), and one of DP (approximately 180 s after contrast injection). All four images showed the largest cross-section of the tumor. The slice chosen for delineating the lesion was confirmed by the two radiologists in consensus. Regions of interest (ROI) were annotated manually around the target lesion margin on the selected BM, AP, PVP, and DP images using an open-source software (ITK-SNAP 3.8.0; http://www.itksnap.org) by radiologist 1. The histogram, morphology, intensity, laws, wavelet, and texture features were extracted by using an open-source software (Pyradiomics; http://pyradiomics.readthedocs.io/en/latest/index.html) through computing algorithms and stored as comma separated values (CSVs).

To evaluate the inter-observer and intra-observer reproducibility, 50 patients and their corresponding BM, AP, PVP, and DP images were randomly selected and independently delineated by the two radiologists (twice by radiologist 1 with an interval of 2 weeks and once by radiologist 2). After features extraction, the intraclass and interclass correlation coefficients (ICCs) were applied to assess the inter-observer and intra-observer reproducibility of the extracted features from the two radiologists. Features with an ICC < 0.80 were eliminated in the subsequent analyses.

Microvascular Invasion Status-Related Feature Selection and Radiomics Score Building

The Spearman rank-order correlation coefficient was implemented to evaluate the correlation and redundancy of radiomics features. The redundant features were eliminated with a Spearman rank-order correlation coefficient ≥ 0.8. Thereafter, the remaining features were selected by applying the minimum redundancy maximum relevance (mRMR) algorithm. Then, the key features related to the MVI status were selected by the least absolute shrinkage and selection operator (LASSO) logistic regression method using a five-fold cross validation after mRMR algorithm in the primary dataset. The LASSO algorithm was applied to weigh the linear combination of the selected features to generate a radiomics score (Rad-score). The formula for the BM, AP, PVP, and DP radiomics scores were established using the respective selected features. Then, the Mann-Whitney U test was applied in the primary and validation datasets to evaluate the potential association between the Rad-scores and MVI status.

Ultrasound Radiomics Nomogram Construction and Validation

To identify the clinical risk factor associated with the MVI status, we performed univariate analyses of the clinical parameters. Chi-square test was used on categorical variables and Student's t independent test was used on continuous variables. We further implemented a multivariable logistic regression analysis of the Rad-scores and independent clinical risk factors, variable selection was implemented with p-values below 0.05 as the preservation criteria to confirm the ultimate predictors for the MVI status. Then, a radiomics nomogram was constructed based

on the multivariable logistic regression analysis in the primary dataset. For comparison, we developed a clinical prediction model that only incorporated the independent clinical risk factors.

The calibration curve and Hosmer-Lemeshow test were performed to evaluate the calibration of the radiomics nomogram. The discrimination performance and the clinical usefulness of the nomogram were evaluated using receiver operating characteristic (ROC) curve analysis and Decision curve analysis (DCA), respectively. The difference between areas under the curve (AUCs) was compared by the DeLong test. For clinical use, the total score of each patient (defined as Nomo-score) was calculated according to the radiomics nomogram scoring method. Thereafter, the optimal cut-off value was assessed by maximizing the Youden index. The prediction performance of the optimal cut-off value of the total score was evaluated *via* the ROC, accuracy, sensitivity, specificity, positive and negative likelihood ratios as well as predictive values.

Statistical Analysis

All statistical analysis was conducted with the R software 3.6.1 (RStudio Inc.) and SPSS 24.0 software (SPSS Inc., Chicago, IL). Categorical variables were expressed as numbers or percentages, and continuous variables were expressed as mean ± SD or medians. The baseline clinical and pathologic data differences were compared by chi-square test for categorical variables and the Student's t test or Mann-Whitney U test for continuous variables as appropriate between the primary dataset and validation dataset. All two-sided p-values less than 0.05 were considered statistically significant. The packages of R3.6.1 that were used are presented in **Supplementary Table A1**.

RESULTS

Clinico-Pathological Information

The study flow chart is presented in **Figure 1**. The detailed clinico-pathological information of the two datasets is summarized in **Tables 1**, **2**. Positive MVI patients accounted for 41.1% (79/192) and 40.5% (49/121) of the primary and validation datasets, respectively. There was no significant difference between the two datasets in the presence of MVI (p = 0.909) or other clinicopathological characteristics. Univariate analysis revealed that the tumor size and AFP level were significantly different between the MVI positive and MVI negative groups in the primary dataset (**Table 2**). Thus, we constructed a clinical model for predicting the MVI status using multivariate logistic regression analysis based on the two clinical risk predictors.

Establishment of Ultrasound Radiomics Score

A set of 479 radiomics features were extracted from the BM, AP, PVP, and DP images of each patient. Favorable inter-observer and intra-observer reproducibility of feature extraction were achieved, with 90.2% (432) of the BM features, 89.4% (428) of the AP features, 93.1% (446) of the PVP features, and 82.5% (395) of the DP features had an intra-observer ICCs ≥ 0.80, and 90.2% (432) of the BM features, 93.5% (448) of the AP features, 92.5% (443) of the PVP features, and 95.4% (457) of the DP features had an inter-observer ICCs ≥ 0.80. For BM, six features were selected after mRMR algorithm and LASSO regression in the primary dataset for radiomics score construction (**Supplementary Figures A2A, B**). Similarly, two, eight, and nine radiomics features were finally selected as the potential predictors by mRMR algorithm and LASSO regression for the AP, PVP, and DP radiomics score construction, respectively (**Supplementary Figures A2C, D–H**). The calculation formulas of the BM, AP, PVP, and DP radiomics scores are provided in **Supplementary A1**. The BM, AP, PVP, and DP Rad-scores were all significantly higher in the MVI positive group in both the primary and validation datasets than those in the MVI negative group (**Table 2**). The performance of the four Rad-scores in distinguishing MVI-positive and MVI-negative patients are provided in **Supplementary Table 1**.

Modeling and Evaluation of the Radiomics Nomogram

The PVP Rad-score, DP Rad-score, AFP level, and tumor size were identified as independent risk predictors of the MVI status in HCC patients by the results of the multivariate logistic regression analysis (**Table 3**). Thus, we constructed a radiomics nomogram incorporating the above four independent risk predictors (**Figure 2A**). The Hosmer-Lemeshow test (P = 0.872 and 0.606 for the primary and validation datasets, respectively) and calibration curve revealed a good calibration of the radiomics nomogram for predicting the MVI status in the primary and validation datasets (**Figure 2B**).

The optimal threshold of the Nomo-score to identify the MVI status was identified to be 0.452 according to the Youden index, and the performance of using the radiomics nomogram to predict the MVI status with the recommended cut-off value are summarized in **Table 4**. An AUC of 0.849 (95% CI, 0.795–0.902) for the primary dataset and 0.788 (95% CI, 0.704–0.872) for the validation dataset demonstrated a good discrimination ability of the nomogram (**Figure 3**).

Moreover, the radiomics nomogram showed a superior discrimination to the clinical model in the primary dataset (AUC 0.849 *vs.* 0.690, P < 0.001) and validation dataset (AUC 0.788 *vs.* 0.661, P = 0.008) (**Table 3**). The DCA curve demonstrated that using the radiomics nomogram to predict the MVI status was more beneficial than using the clinical model when the threshold probability is between 0.1 and 0.8 (**Figure 4**). In addition, compared with the clinical prediction model which solely incorporated the independent clinical risk predictors, the utilization of the PVP and DP Rad-score significantly improves the prediction performance of the MVI status in terms of the NRI and IDI (**Table 5**). Besides, we further evaluated the performance of the radiomics nomogram in all patients. We classified the 313 patients into high- and low- risk subgroups

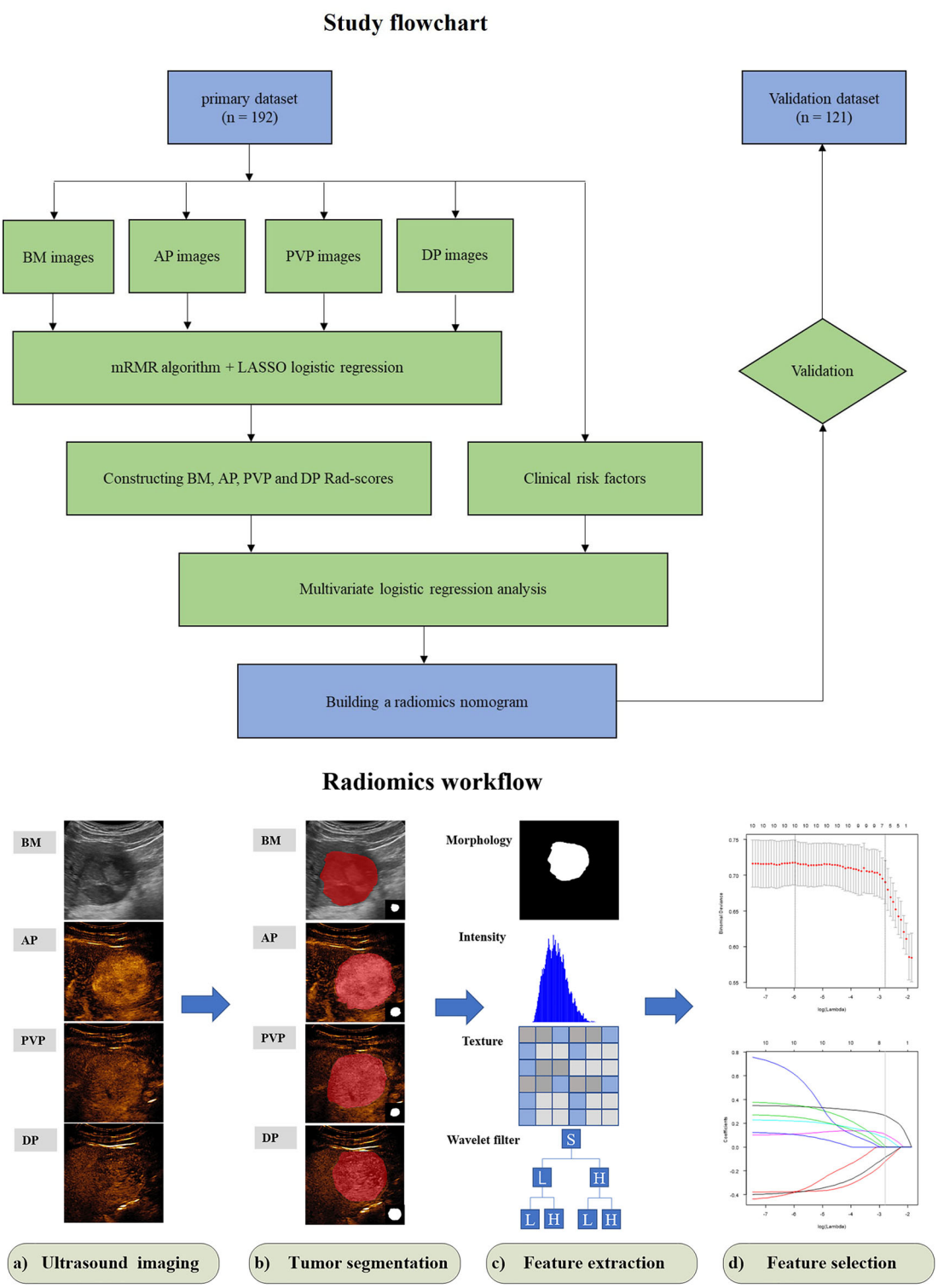

FIGURE 1 | Study flowchart of radiomics nomogram modeling for the MVI status prediction in patients with HCC and radiomics workflow. BM, B-mode; AP, arterial phase; PVP, portal venous phase; DP, delay phase; Rad-score, radiomics score; mRMR, minimum redundancy maximum relevance; LASSO, least absolute shrinkage and selection operator.

TABLE 1 | Clinicopathological characteristics in the primary and the validation datasets.

Characteristic	Primary dataset (n = 192)	Validation dataset (n = 121)	P-value
Gender			0.267
Male	166 (86.5)	99 (81.8)	
Female	26 (13.5)	22 (18.2)	
Age, mean ± SD, years	55.1 ± 11.0	55.37 ± 12.1	0.840
Tumor size			0.103
<5 cm	121 (63.0)	65 (53.7)	
≥5 cm	71 (37.0)	56 (46.3)	
MVI status			0.909
Positive	79 (41.1)	49 (40.5)	
Negative	113 (58.9)	72 (59.5)	
Pathologic grade			0.839
Well	30 (15.6)	22 (18.2)	
Moderately	123 (64.1)	75 (62.0)	
Poorly	39 (20.3)	24 (19.8)	
Cirrhosis			0.568
Positive	122 (63.5)	73 (60.3)	
Negative	70 (36.5)	48 (39.7)	
Cholelithiasis			0.993
Positive	38 (19.8)	24 (19.8)	
Negative	154 (80.2)	97 (80.2)	
Hepatitis			0.272
Positive	153 (79.7)	90 (74.4)	
Negative	39 (20.3)	31 (25.6)	
ALT (U/L)			0.808
≤40	109 (56.8)	67 (55.4)	
>40	83 (43.2)	54 (44.6)	
AST (U/L)			0.740
≤35	83 (43.2)	50 (41.3)	
>35	109 (56.8)	71 (58.7)	
AFP (μg/L)			0.203
≤20	74 (38.5)	58 (47.9)	
20–400	57 (29.7)	34 (28.1)	
≥400	61 (31.8)	29 (24.0)	
PLT (10^9/L)			0.674
<100	56 (29.2)	38 (31.4)	
≥100	136 (70.8)	83 (68.6)	
ALB (g/L)			0.469
<40	84 (43.75)	58 (47.9)	
≥40	108 (56.25)	63 (52.1)	
INR			0.748
≤1.2	149 (77.6)	92 (76.0)	
>1.2	43 (22.4)	29 (24.0)	
TBIL (μmol/L)			0.491
≤17.1	131 (68.2)	78 (64.5)	
>17.1	61 (31.8)	43 (35.5)	
DBIL (μmol/L)			0.640
≤6.8	102 (53.1)	61 (50.4)	
>6.8	90 (46.9)	60 (49.6)	
BM rad-score, median (interquartile range)	-4.06 (-7.04 to -1.12)	-3.69 (-6.43 to -1.44)	0.648
AP rad-score, median (interquartile range)	-3.54 (-4.30 to -2.89)	-3.48 (-4.00 to -2.58)	0.256
PVP rad-score, median (interquartile range)	-3.98 (-9.23 to 1.08)	-2.17 (-7.09 to 2.27)	0.115
DP rad-score, median (interquartile range)	-3.50 (-3.97 to -3.03)	-3.42 (-3.97 to -2.96)	0.336

ALT, alanine aminotransferase; AST, aspartate aminotransferase; AFP, α-fetoprotein; PLT, platelets count; ALB, albumin; INR, international normalized ratio; TBIL, total bilirubin; DBIL, direct bilirubin; BM, B-mode; AP, arterial phase; PVP, portal venous phase; DP, delay phase; Rad-score, radiomics score. Unless otherwise specified, data in parentheses are percentages.

according to whether the Nomo-score of each patient was above or below the optimal cut-off value (0.452). The results indicated that the high-risk group had a greater proportion of MVI positive in all patients (**Figure 5**). The radiomics nomogram also revealed a more favorable discriminatory ability than the clinical model in all 313 patients (AUC 0.825 *vs*. 0.678, P < 0.001).

DISCUSSION

In the current study, we developed and validated a radiomics nomogram that incorporated preoperative CEUS information for the individualized prediction of the MVI status in patients with HCC. The easy-to-use graphic tool might provide useful

TABLE 2 | Preoperative predictors for MVI in the primary and the validation datasets.

Characteristic	Primary dataset No. (%)			Validation dataset No. (%)		
	MVI (+)	MVI (-)	P value	MVI (+)	MVI (-)	P-value
Gender			0.467			0.600
male	70 (88.6)	96 (85.0)		39 (79.6)	60 (83.3)	
female	9 (11.4)	17 (15.0)		10 (20.4)	12 (16.7)	
Age, mean ± SD, years	54.0 ± 11.5	55.9 ± 10.6	0.224	53.8 ± 13.7	56.5 ± 10.8	0.232
Tumor size			<0.001			0.018
<5 cm	37 (46.8)	84 (74.3)		20 (40.8)	45 (62.5)	
≥5 cm	42 (53.2)	29 (25.7)		29 (59.2)	27 (37.5)	
Cirrhosis			0.503			0.093
Positive	48 (60.8)	74 (65.5)		34 (69.4)	39 (54.2)	
Negative	31 (39.2)	39 (34.5)		15 (30.6)	33 (45.8)	
Cholelithiasis			0.893			0.552
Positive	16 (20.3)	22 (19.5)		11 (22.4)	13 (18.1)	
Negative	63 (79.7)	91 (80.5)		38 (77.6)	59 (81.9)	
Hepatitis			0.282			0.132
Positive	60 (82.3)	93 (86.7)		40 (81.6)	50 (69.4)	
Negative	19 (17.7)	20 (13.3)		9 (18.4)	22 (30.6)	
ALT (U/L)			0.584			0.961
≤40	43 (54.4)	66 (58.4)		27 (55.1)	40 (55.6)	
>40	36 (45.6)	47 (41.6)		22 (44.9)	32 (44.4)	
AST (U/L)			0.733			0.222
≤35	33 (41.8)	50 (44.2)		17 (34.7)	33 (45.8)	
>35	46 (58.2)	63 (55.8)		32 (65.3)	39 (54.2)	
AFP (μg/L)			0.017			0.006
≤20	24 (30.4)	50 (44.2)		20 (40.8)	38 (52.8)	
20–400	21 (26.6)	36 (31.9)		10 (20.4)	24 (33.3)	
≥400	34 (43.0)	27 (23.9)		19 (38.8)	10 (13.9)	
PLT (10^9/L)			0.192			0.580
<100	19 (24.1)	37 (32.7)		14 (28.6)	24 (33.3)	
≥100	60 (75.9)	76 (67.3)		35 (71.4)	48 (66.7)	
ALB (g/L)			0.897			0.575
<40	35 (44.3)	49 (43.4)		25 (51.0)	33 (45.8)	
≥40	44 (55.7)	64 (56.6)		24 (49.0)	39 (54.2)	
INR			0.914			0.328
≤1.2	61 (77.2)	88 (77.9)		35 (71.4)	57 (79.2)	
>1.2	18 (22.8)	25 (22.1)		14 (28.6)	15 (20.8)	
TBIL (μmol/L)			0.108			0.001
≤17.1	59 (74.7)	72 (63.7)		23 (46.9)	55 (76.4)	
>17.1	20 (25.3)	41 (36.3)		26 (53.1)	17 (23.6)	
DBIL (μmol/L)			0.139			0.035
≤6.8	47 (59.5)	55 (48.7)		19 (38.8)	42 (58.3)	
>6.8	32 (40.5)	58 (51.3)		30 (61.2)	30 (41.7)	
BM rad-score, median (interquartile range)	-2.10 (-4.68 to 1.23)	-5.45 (-8.22 to -2.61)	<0.001	-2.24 (-4.80 to 2.01)	-4.72 (-7.20 to -2.25)	<0.001
AP rad-score, median (interquartile range)	-3.07 (-3.88 to -2.04)	-3.96 (-4.65 to -3.32)	<0.001	-2.85 (-3.64 to -2.15)	-3.68 (-4.39 to -3.20)	<0.001
PVP rad-score, median (interquartile range)	0.32 (-3.92 to 6.36)	-7.04 (-12.50 to -3.18)	<0.001	1.83 (-2.79 to 4.47)	-5.44 (-9.63 to -0.52)	<0.001
DP rad-score, median (interquartile range)	-3.13 (-3.52 to -2.82)	-3.75 (-4.22 to -3.28)	<0.001	-3.09 (-3.62 to -2.89)	-3.58 (-4.05 to -3.16)	0.001

ALT, alanine aminotransferase; AST, aspartate aminotransferase; AFP, α-fetoprotein; PLT, platelets count; ALB, albumin; INR, international normalized ratio; TBIL, total bilirubin; DBIL, direct bilirubin. BM, B-mode; AP, arterial phase; PVP, portal venous phase; DP, delay phase; Rad-score, radiomics score; Unless otherwise specified, data in parentheses are percentages.

information to facilitate clinical decision-making. Moreover, our study offers an alternative approach with no radiation while with a comparable performance compared to previous radiomics prediction models based on contrast-enhanced CT (19, 30).

The presence of MVI in patients with HCC is a key determinant associated with adverse tumor biology as well as poor outcomes (5, 31). Furthermore, MVI status has a negative influence on the recurrence and survival rate of HCC patients after transplantation or surgical resection (32, 33). In the Guidelines for Diagnosis and Treatment of Primary Liver Cancer in China (2017 Edition), MVI is an important factor that cannot be ignored in the selection of the treatment plan (34). Partial hepatectomy with a broader resection margin is recommended to improve the recurrence-free survival rate in HCC patients with MVI (21). Therefore, preoperative noninvasive and accurate identification of MVI is very helpful for the preoperative stratification of HCC patients.

In previous studies, some investigators attempted to predict the MVI status of HCC preoperatively by analyzing the clinical risk factors and combined imaging characteristics determined by radiologists (13, 35). However, the difference in the professional knowledge of operators cannot be ignored.

TABLE 3 | Variables and coefficients of the radiomics nomogram and clinical model.

Intercept and variable	Clinical model			Radiomics nomogram		
	β	Odds ratio (95% CI)	P-value	β	Odds ratio (95% CI)	P-value
Intercept	-1.263			4.744		
Tumor size (≥5 cm)	1.204	3.334 (1.775 to 6.263)	<0.001	-1.170	0.310 (0.116 to 0.833)	0.020
AFP (μg/L)						
≤20		Reference			Reference	
20–400	0.358	1.430 (0.669 to 3.062)	0.357	0.243	1.276 (0.523 to 3.111)	0.593
≥400	1.006	2.734 (1.313 to 5.695)	0.007	1.029	2.797 (1.164 to 6.726)	0.022
BM Rad-score	NA	NA	NA	NA	NA	NA
AP Rad-score	NA	NA	NA	NA	NA	NA
PVP Rad-score	NA	NA		0.214	1.239 (1.138 to 1.347)	<0.001
DP Rad-score	NA	NA		1.261	3.529 (1.687 to 7.382)	0.001
AUC						*P value
Primary dataset		0.690 (0.615 to 0.766)			0.849 (0.795 to 0.902)	<0.001
Validation dataset		0.661 (0.561 to 0.760)			0.788 (0.704 to 0.872)	0.008

**P value represents the difference of AUC between the radiomics nomogram and clinical model. AFP, α-fetoprotein; BM, B-mode; AP, arterial phase; PVP, portal venous phase; DP, delay phase; Rad-score, radiomics score; AUC, area under the receiver operating characteristic curve; NA, not available.*

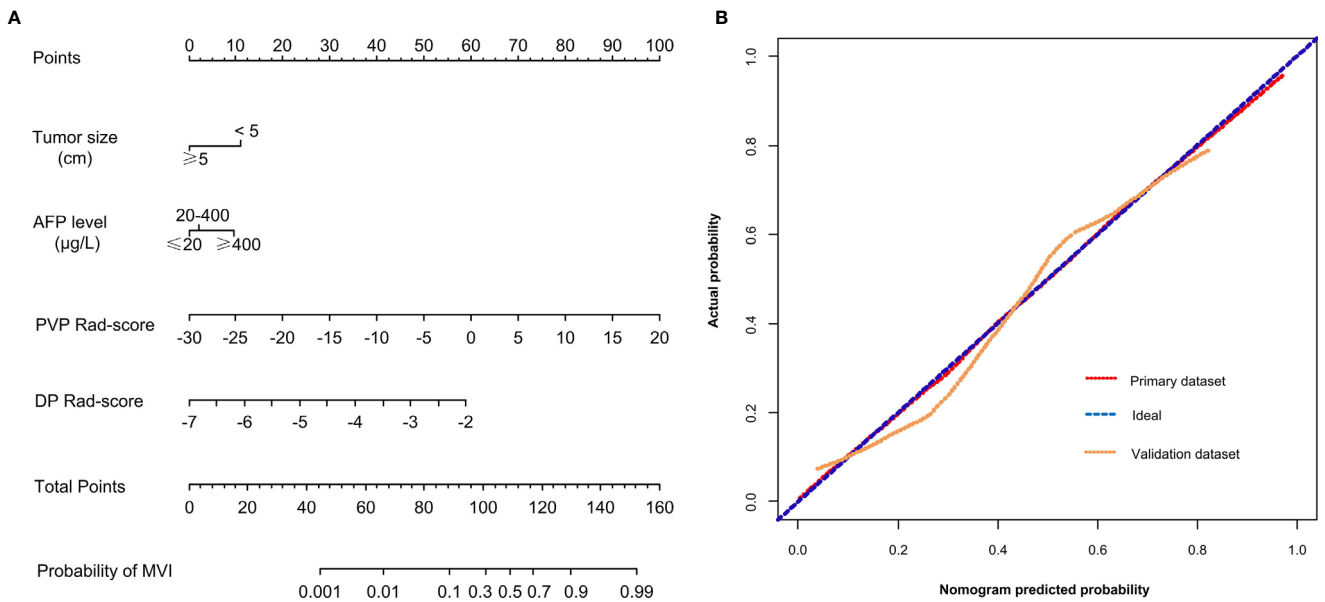

FIGURE 2 | **(A)** A radiomics nomogram combining the AFP level, tumor size, PVP Rad-score, and DP Rad-score. **(B)** Calibration curves of the radiomics nomogram in the primary and validation datasets. AFP, α-fetoprotein; PVP, portal venous phase; DP, delay phase; Rad-score, radiomics score.

Radiomics utilizes quantitative medical image features to predict tumor biological behavior, providing a new method for the prediction of the MVI status. Hu and his colleagues developed a radiomics strategy based on preoperative grayscale ultrasound images to predict the MVI status of patients with HCC (36). Dong et al. found that gross-tumoral region and peri-tumoral region radiomics signatures based on ultrasound images were also feasible for the preoperative prediction of the MVI status (37). However, their research was only based on grayscale ultrasound images, and did not include image features of other modes. CEUS, which contains imaging information of different aspects of a tumor, is widely used to observe and evaluate microcirculation blood perfusion of liver cancer (23, 38). Therefore, in the present study, we used radiomics strategy to quantitatively extracted multiphase CEUS imaging features to evaluate the overall information related to the MVI status that may be contained in tumors. It is worth noting that the radiomics scores of BM, AP, PVP, and DP were all significantly correlated with the MVI status in the univariate analysis. However, BM and AP radiomics scores were not incorporated in the final radiomics nomogram. We discovered that in the final multivariate logistic regression analysis, the strong discriminatory capacity of the PVP and DP Rad-scores diminished the value of BM and AP Rad-scores. In a previous study, the washout patterns of CEUS in the PVP and DP were considered to be significantly associated with the MVI status. High levels of MVI reduced tumor

TABLE 4 | Performance of the radiomics nomogram and clinical model for evaluating the preoperative MVI status.

Variable	Value (95% CI)			
	Clinical model		Radiomics nomogram	
	Primary dataset	Validation dataset	Primary dataset	Validation dataset
Cut-off value	0.362	0.362	0.452	0.452
AUC	0.690 (0.615 to 0.766)	0.661 (0.561 to 0.760)	0.849 (0.795 to 0.902)	0.788 (0.704 to 0.872)
Sensitivity, %	72.15 (61.99 to 82.28)	73.47 (61.22 to 85.71)	78.48 (69.62 to 87.34)	75.51 (63.27 to 87.76)
Specificity, %	56.64 (47.79 to 65.49)	52.78 (41.67 to 65.28)	78.76 (71.66 to 85.84)	70.83 (59.72 to 80.56)
PPV, %	53.77 (44.28 to 63.26)	51.43 (39.72 to 63.14)	72.09 (62.61 to 81.57)	63.79 (51.42 to 76.16)
NPV, %	74.42 (65.20 to 83.64)	74.51 (62.55 to 86.47)	83.96 (76.98 to 90.95)	80.95 (71.26 to 90.65)
PLR	1.66 (1.29 to 2.14)	1.56 (1.16 to 2.09)	3.70 (2.54 to 5.37)	2.59 (1.75 to 3.84)
NLR	0.49 (0.34 to 0.71)	0.50 (0.31 to 0.82)	0.27 (0.18 to 0.42)	0.35 (0.21 to 0.57)
Diagnostic accuracy, %	63.02 (55.77 to 69.86)	61.16 (51.87 to 69.88)	78.65 (72.17 to 84.22)	72.73 (63.88 to 80.43)

PPV, Positive predictive value; NPV, Negative predictive value; PLR, Positive likelihood ratio; NLR, Negative likelihood ratio; AUC, area under the receiver operating characteristic curve.

microvessel density, resulting in a reduced enhancement, that is, the smaller the density of the microvessels, the smaller the amount of contrast agent entering the tumor, which leads to the reduced enhancement on CEUS, promoting washout (26, 39). This might be the reason why our CEUS radiomics signature focused more on the PVP and DP Rad-scores.

As far as we know, our study is the first to utilize the radiomics nomogram to predict the preoperative MVI status of

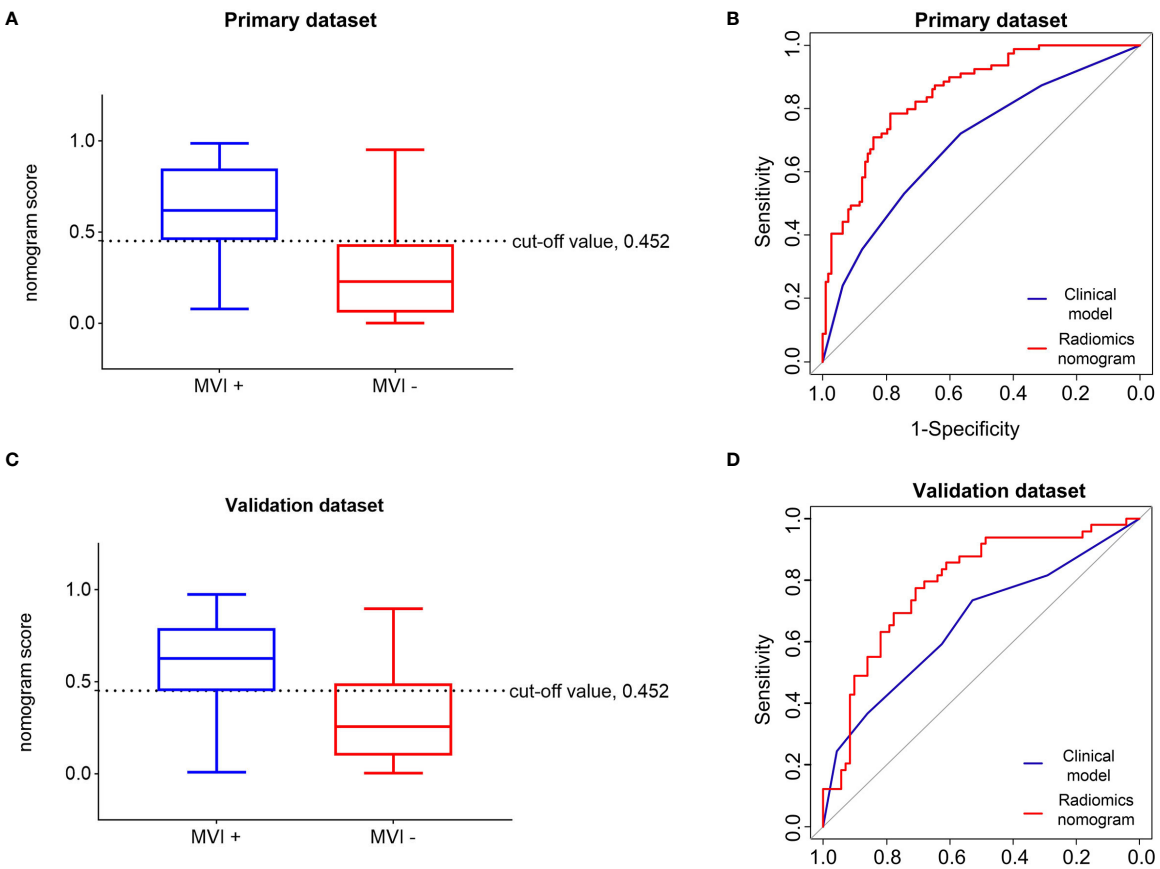

FIGURE 3 | Performance of the radiomics nomogram in predicting the MVI status of patients with hepatocellular carcinoma. Differential diagnosis of MVI+ and MVI– groups with the cut-off value of Nom-score of 0.452 in the primary **(A)** and validation **(C)** datasets. Receiver operating characteristic curves of the radiomics nomogram and clinical model in the primary **(B)** and validation **(D)** datasets. MVI+, patients with microvascular invasion; MVI–, patients without microvascular invasion.

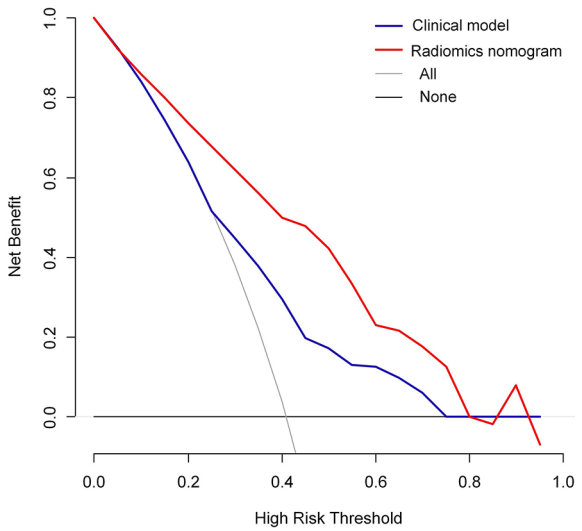

FIGURE 4 | Decision curve analysis (DCA) of the radiomics nomogram and clinical model in predicting the MVI status for hepatocellular carcinoma derived from the all 313 patients.

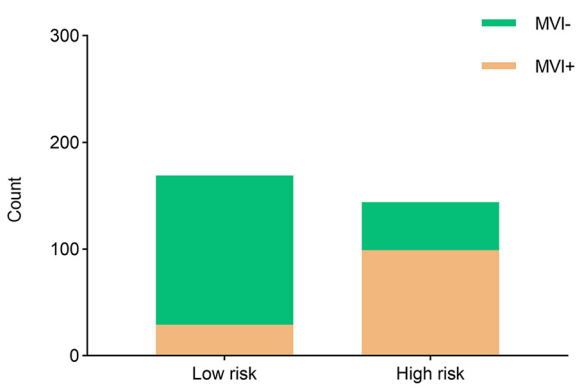

FIGURE 5 | The risk-classification performance of the radiomics nomogram in all 313 patients. MVI+, patients with microvascular invasion; MVI–, patients without microvascular invasion.

HCC patients based on CEUS imaging. In the current study, tumor size, AFP levels, PVP, and DP radiomics scores were the independent risk predictors associated with the MVI status, and the radiomics nomogram involved the above four factors achieving a favorable predictive value for the MVI status prediction (AUC of 0.849 for the primary dataset and 0.788 for the validation dataset). The predictive calibration curves of the radiomics nomogram in both the primary and validation datasets showed an agreement with the ideal curve. In addition, the significant improvement of NRI and IDI demonstrated that the PVP and DP radiomics signatures may be very useful biomarkers for MVI prediction. Decision curve analysis also proved that the radiomics nomogram can improve the prediction of the MVI status preoperatively. Our CEUS-based radiomics nomogram showed a better discrimination performance compared with nomograms that combined clinical risk factors and imaging features in previous studies (26, 40, 41). Moreover, it is worth noting that in previous studies, all imaging features were based on visual analysis and relied on the subjective evaluation of individual radiologists, while radiomics reflects the texture information of tumor and provides a quantitative analysis of the image features. The nomogram based on the radiomics score is more conducive to the objective evaluation of clinicians of the MVI status.

Our study revealed that a tumor size greater than 5 cm and a preoperative plasma AFP level above 400 μg/L were significant predictive factors associated with the MVI status. Some evidence has suggested that AFP plays an important role in regulating tumor growth and cell differentiation, and may stimulate the proliferation of hepatoma cells through the AFP receptors (42). HCC clones from the same parental cell line showed higher serum AFP levels in nude mice carrying tumor implants with a high metastatic potential than nude mice with low metastatic tumor implants (43). Some previous studies have reported that the preoperative AFP level in HCC patients with MVI were significantly higher, plasma AFP level can be used as an independent predictor to establish a preoperative MVI prediction model (13, 44). A previous study showed that when the diameter of HCC increased, the number of DNA ploidy transformed from diploid to aneuploid increased significantly, and the probability of invasion and metastasis increased (45). The pathological study of Adachi et al. revealed that through the histological examination of surgically resected specimens, portal vein invasion of hepatoma cells was significantly related to tumor size (46). Some studies have also reported that the incidence of MVI increased with an increasing tumor size in HCC (36, 47). The results of our study were consistent with those findings. In the present study, we also constructed a clinical model involving the preoperative AFP level and tumor size. The addition of PVP

TABLE 5 | Evaluation of the radiomics nomogram with respect to NRI and IDI.

Characteristic	Primary dataset			Validation dataset		
	Categorical NRI (95% CI)	Continuous NRI (95% CI)	IDI (95% CI)	Categorical NRI (95% CI)	Continuous NRI (95% CI)	IDI (95% CI)
Radiomics nomogram *vs.* clinical model	0.511 (0.344 to 0.678)	0.892 (0.636 to 1.148)	0.240 (0.178 to 0.302)	0.345 (0.132 to 0.557)	0.801 (0.478 to 1.125)	0.185 (0.108 to 0.262)
P-value	<0.0001	<0.0001	<0.0001	0.002	<0.0001	<0.0001

NRI, net reclassification improvement; IDI, index integrated discrimination improvement.

and DP radiomics signatures to the clinical predict model significantly improved the AUC of the clinical model (from 0.690 to 0.849, 0.661 to 0.788 in the primary dataset and validation dataset, respectively). Moreover, the DCA curve demonstrated that the radiomics nomogram improves the benefit more than the clinical predict model, which implied that radiomics signature added accessorial value to the clinical risk factors in the clinical application. For the clinical application of the radiomics nomogram, we analyzed the sensitivity, specificity, positive and negative likelihood ratios as well as predictive values in evaluating the risk of MVI positive. We displayed that the patients with a total Nomo-score of 0.452 or above were the subgroup of high-risk MVI. Therefore, this subgroup of HCC patients may be more suitable for a larger resection margin during liver resection.

The present study has several limitations. First, the radiomics signature was based on multi-phase CEUS images, and some information might still have been missed in comparison with the CEUS video. It is necessary to further research the association of the radiomics features and video-based CEUS signatures (such as time intensity curve parameters), which may improve the prediction performance of radiomics. Second, this was a retrospective study, so some selection bias and data imbalance may inevitably exist and have influenced our results. In addition, since our research took place in a single institution using one vendor machine, prospective and longitudinal cohort validation with a larger group of patients and multi-vendor machines are still needed to verify the reliability of the developed radiomics nomogram. Third, although all the US examinations were performed by experienced radiologists, there may be heterogeneity in the image quality due to the differences in radiologist manipulation.

CONCLUSION

In conclusion, our study developed a non-invasive predictive nomogram that incorporates the radiomics signature of multi-phase CEUS imaging and clinical risk factors, it may provide useful information for the preoperative assessment of the MVI status in patients with HCC and guide a more appropriate surgical planning.

DATA AVAILABILITY STATEMENT

The original contributions presented in the study are included in the article/**Supplementary Material**. Further inquiries can be directed to the corresponding authors.

ETHICS STATEMENT

The studies involving human participants were reviewed and approved by Ethics Committee of Huazhong University of Science and Technology Drug Clinical Trials. Written informed consent for participation was not required for this study in accordance with the national legislation and the institutional requirements.

AUTHOR CONTRIBUTIONS

DZ: Data curation, investigation, methodology, and writing the original draft. QW: Conceptualization, data curation, formal analysis, methodology, and validation. G-GW: Conceptualization and data curation. X-YZ: Formal analysis and visualization. W-WL: Data curation and formal analysis. W-ZL: Methodology, software, validation, and visualization. J-TL: Data curation, project administration, supervision, and writing – review. X-WC: Methodology, resources, supervision, and writing – review. X-JN: Project administration, resources, supervision, and writing – review. CD: Supervision and writing – review. All authors contributed to the article and approved the submitted version.

FUNDING

The authors are grateful of the support of National Natural Science Foundation of China (No. 82071953).

SUPPLEMENTARY MATERIAL

The Supplementary Material for this article can be found online at: https://www.frontiersin.org/articles/10.3389/fonc.2021.709339/full#supplementary-material

REFERENCES

1. Forner A, Reig M, Bruix J. Hepatocellular Carcinoma. *Lancet* (2018) 391:1301–14. doi: 10.1016/s0140-6736(18)30010-2
2. Heimbach JK, Kulik LM, Finn RS, Sirlin CB, Abecassis MM, Roberts LR, et al. AASLD Guidelines for the Treatment of Hepatocellular Carcinoma. *Hepatology* (2018) 67:358–80. doi: 10.1002/hep.29086
3. European Association for the Study of the Liver, Electronic address eee and European Association for the Study of the L. EASL Clinical Practice Guidelines: Management of Hepatocellular Carcinoma. *J Hepatol* (2018) 69:182–236. doi: 10.1016/j.jhep.2018.03.019
4. Chan AWH, Zhong J, Berhane S, Toyoda H, Cucchetti A, Shi K, et al. Development of Pre and Post-Operative Models to Predict Early Recurrence of Hepatocellular Carcinoma After Surgical Resection. *J Hepatol* (2018) 69:1284–93. doi: 10.1016/j.jhep.2018.08.027
5. Erstad DJ, Tanabe KK. Prognostic and Therapeutic Implications of Microvascular Invasion in Hepatocellular Carcinoma. *Ann Surg Oncol* (2019) 26:1474–93. doi: 10.1245/s10434-019-07227-9
6. Roayaie S, Blume IN, Thung SN, Guido M, Fiel MI, Hiotis S, et al. A System of Classifying Microvascular Invasion to Predict Outcome After Resection in Patients With Hepatocellular Carcinoma. *Gastroenterology* (2009) 137:850–5. doi: 10.1053/j.gastro.2009.06.003
7. Gouw AS, Balabaud C, Kusano H, Todo S, Ichida T, Kojiro M. Markers for Microvascular Invasion in Hepatocellular Carcinoma: Where do We Stand? *Liver Transpl* (2011) 17 Suppl 2:S72–80. doi: 10.1002/lt.22368
8. Lim KC, Chow PK, Allen JC, Chia GS, Lim M, Cheow PC, et al. Microvascular Invasion Is a Better Predictor of Tumor Recurrence and Overall Survival Following Surgical Resection for Hepatocellular Carcinoma Compared to the Milan Criteria. *Ann Surg* (2011) 254:108–13. doi: 10.1097/SLA.0b013e31821ad884

9. Hirokawa F, Hayashi M, Miyamoto Y, Asakuma M, Shimizu T, Komeda K, et al. Outcomes and Predictors of Microvascular Invasion of Solitary Hepatocellular Carcinoma. *Hepatol Res* (2014) 44:846–53. doi: 10.1111/hepr.12196
10. Zhang X, Li J, Shen F, Lau WY. Significance of Presence of Microvascular Invasion in Specimens Obtained After Surgical Treatment of Hepatocellular Carcinoma. *J Gastroenterol Hepatol* (2018) 33:347–54. doi: 10.1111/jgh.13843
11. Pawlik TM, Gleisner AL, Anders RA, Assumpcao L, Maley W, Choti MA. Preoperative Assessment of Hepatocellular Carcinoma Tumor Grade Using Needle Biopsy: Implications for Transplant Eligibility. *Ann Surg* (2007) 245:435–42. doi: 10.1097/01.sla.0000250420.73854.ad
12. Renzulli M, Brocchi S, Cucchetti A, Mazzotti F, Mosconi C, Sportoletti C, et al. Can Current Preoperative Imaging Be Used to Detect Microvascular Invasion of Hepatocellular Carcinoma? *Radiology* (2016) 279:432–42. doi: 10.1148/radiol.2015150998
13. Lei Z, Li J, Wu D, Xia Y, Wang Q, Si A, et al. Nomogram for Preoperative Estimation of Microvascular Invasion Risk in Hepatitis B Virus-Related Hepatocellular Carcinoma Within the Milan Criteria. *JAMA Surg* (2016) 151:356–63. doi: 10.1001/jamasurg.2015.4257
14. Wang WT, Yang L, Yang ZX, Hu XX, Ding Y, Yan X, et al. Assessment of Microvascular Invasion of Hepatocellular Carcinoma With Diffusion Kurtosis Imaging. *Radiology* (2018) 286:571–80. doi: 10.1148/radiol.2017170515
15. Lee S, Kim SH, Lee JE, Sinn DH, Park CK. Preoperative Gadoxetic Acid-Enhanced MRI for Predicting Microvascular Invasion in Patients With Single Hepatocellular Carcinoma. *J Hepatol* (2017) 67:526–34. doi: 10.1016/j.jhep.2017.04.024
16. Gillies RJ, Kinahan PE, Hricak H. Radiomics: Images Are More Than Pictures, They Are Data. *Radiology* (2016) 278:563–77. doi: 10.1148/radiol.2015151169
17. Lambin P, Leijenaar RTH, Deist TM, Peerlings J, de Jong EEC, van Timmeren J, et al. Radiomics: The Bridge Between Medical Imaging and Personalized Medicine. *Nat Rev Clin Oncol* (2017) 14:749–62. doi: 10.1038/nrclinonc.2017.141
18. Yin R, Jiang M, Lv WZ, Jiang F, Li J, Hu B, et al. Study Processes and Applications of Ultrasomics in Precision Medicine. *Front Oncol* (2020) 10:1736. doi: 10.3389/fonc.2020.01736
19. Ma X, Wei J, Gu D, Zhu Y, Feng B, Liang M, et al. Preoperative Radiomics Nomogram for Microvascular Invasion Prediction in Hepatocellular Carcinoma Using Contrast-Enhanced CT. *Eur Radiol* (2019) 29:3595–605. doi: 10.1007/s00330-018-5985-y
20. Xu X, Zhang H-L, Liu Q-P, Sun S-W, Zhang J, Zhu F-P, et al. Radiomic Analysis of Contrast-Enhanced CT Predicts Microvascular Invasion and Outcome in Hepatocellular Carcinoma. *J Hepatol* (2019) 70:1133–44. doi: 10.1016/j.jhep.2019.02.023
21. Yang L, Gu D, Wei J, Yang C, Rao S, Wang W, et al. A Radiomics Nomogram for Preoperative Prediction of Microvascular Invasion in Hepatocellular Carcinoma. *Liver Cancer* (2019) 8:373–86. doi: 10.1159/000494099
22. Ni M, Zhou X, Lv Q, Li Z, Gao Y, Tan Y, et al. Radiomics Models for Diagnosing Microvascular Invasion in Hepatocellular Carcinoma: Which Model Is the Best Model? *Cancer Imaging* (2019) 19:60. doi: 10.1186/s40644-019-0249-x
23. Dietrich CF, Potthoff A, Helmberger T, Ignee A, Willmann JK, Group CL-RW. [Contrast-Enhanced Ultrasound: Liver Imaging Reporting and Data System (CEUS LI-RADS)]. *Z. Gastroenterol* (2018) 56:499–506. doi: 10.1055/s-0043-124874
24. Wang W, Chen LD, Lu MD, Liu GJ, Shen SL, Xu ZF, et al. Contrast-Enhanced Ultrasound Features of Histologically Proven Focal Nodular Hyperplasia: Diagnostic Performance Compared With Contrast-Enhanced CT. *Eur Radiol* (2013) 23:2546–54. doi: 10.1007/s00330-013-2849-3
25. Wang JY, Feng SY, Yi AJ, Zhu D, Xu JW, Li J, et al. Comparison of Contrast-Enhanced Ultrasound Versus Contrast-Enhanced Magnetic Resonance Imaging for the Diagnosis of Focal Liver Lesions Using the Liver Imaging Reporting and Data System. *Ultrasound Med Biol* (2020) 46:1216–23. doi: 10.1016/j.ultrasmedbio.2020.01.023
26. Zhu W, Qing X, Yan F, Luo Y, Li Y, Zhou X. Can the Contrast-Enhanced Ultrasound Washout Rate Be Used to Predict Microvascular Invasion in Hepatocellular Carcinoma? *Ultrasound Med Biol* (2017) 43:1571–80. doi: 10.1016/j.ultrasmedbio.2017.04.003
27. Deng G, Yao L, Zeng F, Xiao L, Wang Z. Nomogram For Preoperative Prediction Of Microvascular Invasion Risk In Hepatocellular Carcinoma. *Cancer Manage Res* (2019) 11:9037–45. doi: 10.2147/CMAR.S216178
28. Wang L, Jin YX, Ji YZ, Mu Y, Zhang SC, Pan SY. Development and Validation of a Prediction Model for Microvascular Invasion in Hepatocellular Carcinoma. *World J Gastroenterol* (2020) 26:1647–59. doi: 10.3748/wjg.v26.i14.1647
29. Lin S, Ye F, Rong W, Song Y, Wu F, Liu Y, et al. Nomogram to Assist in Surgical Plan for Hepatocellular Carcinoma: A Prediction Model for Microvascular Invasion. *J Gastrointest Surg* (2019) 23:2372–82. doi: 10.1007/s11605-019-04140-0
30. Zhang X, Ruan S, Xiao W, Shao J, Tian W, Liu W, et al. Contrast-Enhanced CT Radiomics for Preoperative Evaluation of Microvascular Invasion in Hepatocellular Carcinoma: A Two-Center Study. *Clin Transl Med* (2020) 10:e111. doi: 10.1002/ctm2.111
31. Lauwers GY, Terris B, Balis UJ, Batts KP, Regimbeau JM, Chang Y, et al. Prognostic Histologic Indicators of Curatively Resected Hepatocellular Carcinomas: A Multi-Institutional Analysis of 425 Patients With Definition of a Histologic Prognostic Index. *Am J Surg Pathol* (2002) 26:25–34. doi: 10.1097/00000478-200201000-00003
32. Mazzaferro V, Llovet JM, Miceli R, Bhoori S, Schiavo M, Mariani L, et al. Predicting Survival After Liver Transplantation in Patients With Hepatocellular Carcinoma Beyond the Milan Criteria: A Retrospective, Exploratory Analysis. *Lancet Oncol* (2009) 10:35–43. doi: 10.1016/s1470-2045(08)70284-5
33. Rodriguez-Peralvarez M, Luong TV, Andreana L, Meyer T, Dhillon AP, Burroughs AK. A Systematic Review of Microvascular Invasion in Hepatocellular Carcinoma: Diagnostic and Prognostic Variability. *Ann Surg Oncol* (2013) 20:325–39. doi: 10.1245/s10434-012-2513-1
34. Zhou J, Sun HC, Wang Z, Cong WM, Wang JH, Zeng MS, et al. Guidelines for Diagnosis and Treatment of Primary Liver Cancer in China (2017 Edition). *Liver Cancer* (2018) 7:235–60. doi: 10.1159/000488035
35. Banerjee S, Wang DS, Kim HJ, Sirlin CB, Chan MG, Korn RL, et al. A Computed Tomography Radiogenomic Biomarker Predicts Microvascular Invasion and Clinical Outcomes in Hepatocellular Carcinoma. *Hepatology* (2015) 62:792–800. doi: 10.1002/hep.27877
36. Hu HT, Wang Z, Huang XW, Chen SL, Zheng X, Ruan SM, et al. Ultrasound-Based Radiomics Score: A Potential Biomarker for the Prediction of Microvascular Invasion in Hepatocellular Carcinoma. *Eur Radiol* (2019) 29:2890–901. doi: 10.1007/s00330-018-5797-0
37. Dong Y, Zhou L, Xia W, Zhao XY, Zhang Q, Jian JM, et al. Preoperative Prediction of Microvascular Invasion in Hepatocellular Carcinoma: Initial Application of a Radiomic Algorithm Based on Grayscale Ultrasound Images. *Front Oncol* (2020) 10:353. doi: 10.3389/fonc.2020.00353
38. Dietrich CF, Nolsoe CP, Barr RG, Berzigotti A, Burns PN, Cantisani V, et al. Guidelines and Good Clinical Practice Recommendations for Contrast-Enhanced Ultrasound (CEUS) in the Liver-Update 2020 WFUMB in Cooperation With EFSUMB, AFSUMB, AIUM, and FLAUS. *Ultrasound Med Biol* (2020) 46:2579–604. doi: 10.1016/j.ultrasmedbio.2020.04.030
39. Fan PL, Ding H, Mao F, Chen LL, Dong Y, Wang WP. Enhancement Patterns of Small Hepatocellular Carcinoma (</= 30 Mm) on Contrast-Enhanced Ultrasound: Correlation With Clinicopathologic Characteristics. *Eur J Radiol* (2020) 132:109341. doi: 10.1016/j.ejrad.2020.109341
40. Yang J, Zhu S, Yong J, Xia L, Qian X, Yang J, et al. A Nomogram for Preoperative Estimation of Microvascular Invasion Risk in Hepatocellular Carcinoma: Single-Center Analyses With Internal Validation. *Front Oncol* (2021) 11:616976. doi: 10.3389/fonc.2021.616976
41. Chou CT, Chen RC, Lin WC, Ko CJ, Chen CB, Chen YL. Prediction of Microvascular Invasion of Hepatocellular Carcinoma: Preoperative CT and Histopathologic Correlation. *AJR Am J Roentgenol* (2014) 203:W253–9. doi: 10.2214/ajr.13.10595
42. Peng SY, Chen WJ, Lai PL, Jeng YM, Sheu JC, Hsu HC. High Alpha-Fetoprotein Level Correlates With High Stage, Early Recurrence and Poor Prognosis of Hepatocellular Carcinoma: Significance of Hepatitis Virus Infection, Age, P53 and Beta-Catenin Mutations. *Int J Cancer* (2004) 112:44–50. doi: 10.1002/ijc.20279
43. Li Y, Tang ZY, Ye SL, Liu YK, Chen J, Xue Q, et al. Establishment of Cell Clones With Different Metastatic Potential From the Metastatic

Hepatocellular Carcinoma Cell Line MHCC97. *World J Gastroenterol* (2001) 7:630–6. doi: 10.3748/wjg.v7.i5.630
44. Liu C. Value of α-Fetoprotein in Association With Clinicopathological Features of Hepatocellular Carcinoma. *World J Gastroenterol* (2013) 19:1811–9. doi: 10.3748/wjg.v19.i11.1811
45. Lu XY, Xi T, Lau WY, Dong H, Xian ZH, Yu H, et al. Pathobiological Features of Small Hepatocellular Carcinoma: Correlation Between Tumor Size and Biological Behavior. *J Cancer Res Clin Oncol* (2011) 137:567–75. doi: 10.1007/s00432-010-0909-5
46. Adachi E, Maeda T, Kajiyama K, Kinukawa N, Matsumata T, Sugimachi K, et al. Factors Correlated With Portal Venous Invasion by Hepatocellular Carcinoma: Univariate and Multivariate Analyses of 232 Resected Cases Without Preoperative Treatments. *Cancer* (1996) 77:2022–31. doi: 10.1002/(sici)1097-0142(19960515)77:10<2022::Aid-cncr9>3.0.Co;2-s
47. Zhao WC, Fan LF, Yang N, Zhang HB, Chen BD, Yang GS. Preoperative Predictors of Microvascular Invasion in Multinodular Hepatocellular Carcinoma. *Eur J Surg Oncol* (2013) 39:858–64. doi: 10.1016/j.ejso.2013.04.003

Conflict of Interest: The authors declare that the research was conducted in the absence of any commercial or financial relationships that could be construed as a conflict of interest.

frontiers in Oncology

ORIGINAL RESEARCH
published: 08 September 2021
doi: 10.3389/fonc.2021.678617

Role of 3D Volumetric and Perfusion Imaging for Detecting Early Changes in Pancreatic Adenocarcinoma

Syed Rahmanuddin[1], Ronald Korn[2], Derek Cridebring[3], Erkut Borazanci[2], Jordyn Brase[1], William Boswell[1], Asma Jamil[1], Wenli Cai[4], Aqsa Sabir[1], Pejman Motarjem[1], Eugene Koay[5], Anirban Mitra[6], Ajay Goel[7], Joyce Ho[7], Vincent Chung[7] and Daniel D. Von Hoff[1,2,3]*

[1] National Medical Center & Beckman Research Institute, City of Hope Comprehensive Cancer Center, Duarte, CA, United States, [2] Virginia G Piper Cancer Center, Honor Health, Scottsdale, AZ, United States, [3] Molecular Medicine Division, Translational Genomics Research Institute (TGEN), Phoenix, AZ, United States, [4] Department of Radiology, Massachusetts General Hospital, Boston, MA, United States, [5] Department of Radiation Oncology, University of Texas MD Anderson Cancer Center, Houston, TX, United States, [6] Department of Pathology, University of Texas MD Anderson Cancer Center, Houston, TX, United States, [7] Molecular Diagnostic and Experimental Therapeutics, City of Hope Comprehensive Cancer Center, Monrovia, CA, United States

OPEN ACCESS

Edited by:
Ilja Ciernik, Städtische Klinikum Dessau, Germany

Reviewed by:
Sikandar Shaikh, Shadan Hospital and Institute of Medical Sciences, India
Jason Fleming, Moffitt Cancer Center, United States

***Correspondence:**
Syed Rahmanuddin
srahmanuddin@coh.org

Specialty section:
This article was submitted to Cancer Imaging and Image-directed Interventions, a section of the journal Frontiers in Oncology

Received: *10 March 2021*
Accepted: *13 August 2021*
Published: *08 September 2021*

Citation:
Rahmanuddin S, Korn R, Cridebring D, Borazanci E, Brase J, Boswell W, Jamil A, Cai W, Sabir A, Motarjem P, Koay E, Mitra A, Goel A, Ho J, Chung V and Von Hoff DD (2021) Role of 3D Volumetric and Perfusion Imaging for Detecting Early Changes in Pancreatic Adenocarcinoma. Front. Oncol. 11:678617. doi: 10.3389/fonc.2021.678617

Purpose: There is a major shortage of reliable early detection methods for pancreatic cancer in high-risk groups. The focus of this preliminary study was to use Time Intensity-Density Curve (TIDC) and Marley Equation analyses, in conjunction with 3D volumetric and perfusion imaging to demonstrate their potential as imaging biomarkers to assist in the early detection of Pancreatic Ductal Adenocarcinoma (PDAC).

Experimental Designs: A quantitative retrospective and prospective study was done by analyzing multi-phase Computed Tomography (CT) images of 28 patients undergoing treatment at different stages of pancreatic adenocarcinoma using advanced 3D imaging software to identify the perfusion and radio density of tumors.

Results: TIDC and the Marley Equation proved useful in quantifying tumor aggressiveness. Perfusion delays in the venous phase can be linked to Vascular Endothelial Growth Factor (VEGF)-related activity which represents the active part of the tumor. 3D volume analysis of the multiphase CT scan of the patient showed clear changes in arterial and venous perfusion indicating the aggressive state of the tumor.

Conclusion: TIDC and 3D volumetric analysis can play a significant role in defining the response of the tumor to treatment and identifying early-stage aggressiveness.

Keywords: 3D volumetric analysis, time intensity-density curve, perfusion analysis, pancreatic ductal adenocarcinoma, CT images

INTRODUCTION

Pancreatic cancer is one of the leading causes of cancer death globally (1). Due to conventional treatments having a minute impact on its natural progression, this disease is considered a major unresolved health problem. Metastases commonly develop in patients with pancreatic cancer resulting in high mortality (2). The average 5-year survival rate is less than 5% and death can occur to most patients 6 months after cancer diagnosis (1, 3). The incidence of pancreatic cancer is higher

in developed countries due, in part, to the differences in diet and lifestyle (1). Risk factors for pancreatic cancer include smoking cigarettes, a family history of pancreatic cancer, diabetes mellitus (Type I or Type II), obesity, consumption of a diet high in fat, alcohol use, and a lifestyle categorized by physical inactivity (4). One of the factors that contribute to the high rate of mortality stems from the nonspecific nature of early presenting symptoms. When the symptoms become severe enough for the individual to seek treatment, 80%–85% of patients present with the advanced unresectable form of this cancer (4). Although these symptoms are not specific and difficult to control, screening methods to identify the earlier stages of cancer can be addressed. Our primary focus for this preliminary study was to identify an approach that used the Time Intensity-Density Curve (TIDC) graphs to show its application in the early detection of pancreatic cancer. There are different types of pancreatic malignancies with Pancreatic Ductal Adenocarcinoma (PDAC) being the most common and severe, accounting for over 85% (4, 5). The cure involves a complete removal of the tumor through surgery; however only 10%–20% of PDAC patients are surgically eligible at the time of diagnosis (4).To compound this problem further, there is a lack of effective early detection tools for pancreatic cancer in high-risk populations (those with greater than 5% lifetime risk of pancreatic cancer) (4). Due to the lack of available early detection screening methods for pancreatic cancer, the fatality rates are greater, and the life expectancies from the time of diagnosis are lower as compared to other types of cancer (5, 6). Early screening methods for PDAC include Endoscopic Ultrasound (EUS) and Magnetic Resonance Imaging (MRI), which have not demonstrated improvement in the long-term survival (7) of patients. Despite the inability to enhance the long-term survival rates overall, these efforts in screening have paved the way for research in the creation of other modalities to detect pancreatic cancer. One of the current modalities is Computed Tomography (CT). CT exams are more accurate and robust in defining cancer characteristics while being the most common imaging modality available compared to EUS and MRI (7). **Table 1** provides a list of current diagnostic modalities and their respective advantages and limitations.

The International Cancer of the Pancreas (CAPS) Consortium recommends individuals who fall into a high-risk group to get screened for cancer beginning at age 50 using EUS or MRI, with annual surveillance if no pancreatic lesions are identified on baseline assessment (4, 8). Both modalities are sensitive and specific for detecting small lesions or early cancer without the risks of radiation exposure. However, EUS performs better in cases of small solid lesions and provides an opportunity for tissue diagnosis by FNA, while MRI Cholangiopancreatography (MRCP) with and without contrast is preferred for cystic lesions and often used as a secondary form of screening in cases where there is a high clinical suspicion for pancreatic cancer despite a negative CT (7).

This study evaluated the use of 3D quantitative volumetric and TIDC analysis for detecting PDAC characteristics. We believed that the switch from 2D to 3D imaging would negate some of the limitations identified with 2D imaging. Multi-phase multi-detector computed tomography (MDCT) is the first line modality of choice for the diagnosis of pancreatic cancer (9). These tests must be tailored to the location of the area to be screened and use the available tools to complete the process, which can be difficult Pancreas-specific screening and diagnostic protocols involve the use of images in the pre-contrast, early arterial (CT angiography), pancreatic, and portal venous phases. The early arterial phase is useful in delineating the aorta and superior mesenteric artery and the portal venous phase can assess venous involvement and liver metastases. There is conflicting data from researchers regarding the optimal phase for enhancement of pancreatic lesions. Some studies suggest a better visualization of PDAC as low-attenuation lesions during the arterial phase due to its hypo-vascularity (4), whereas others demonstrated better pancreatic enhancement and attenuation differences between the normal pancreas and tumor in the portal venous phase (4).

Pancreatic tumors are often hypo-vascular and ill-defined, with irregular texture and abnormal morphology (10). To better understand the long-term outcomes and prognostic factors associated with PDAC, multi-phase CT images of patients undergoing treatment for PDAC were analyzed using advanced 3D imaging software to characterize the perfusion and radio density of tumors at various stages. Our goals were to identify

TABLE 1 | Benefits and limitations of pancreatic cancer diagnostic modalities [i, ii].

Diagnostic modalities	Advantages	Limitations
MDCT	Most commonly available	Nephrotoxicity
89% sensitivity	Best validated	Radiation exposure
90% specificity	Cheapest	
MRI	Superior imaging	Expensive
89% sensitivity	Depicts local pancreatic disease	Less available
89% specificity	Iodine-free and no radiation	Contraindicated with some metal implants
EUS +/- FNA	Safe and less invasive	Less available in some countries
85% sensitivity[iii]	High sensitivity	Operator dependent
96% specificity[iii]	Able to detect small lesions	Inability to detect distant metastasis
	Able to take histological sample	

[i]*Adapted from Zhang L et al., World Journal of Gastroenterology. 2018; 24:2047-2060.*[6]

[ii]*CT, Computed tomography; MDCT, Multi-detector computed tomography; MRI, Magnetic resonance imaging; EUS, Endoscopic ultrasound; FNA, Fine needle aspiration; PET, Positron emission tomography.*

[iii]*Pooled sensitivity and specificity for EUS with FNA.*

imaging biomarkers to help detect pancreatic cancer early and define features of pancreatic cancer that correlate with disease severity and treatment response. The findings from this study might help define the mechanisms and growth patterns of PDAC while laying the groundwork for further research in early PDAC detection.

MATERIALS AND METHODS

Patient Population

A quantitative, retrospective, and prospective study was done using 41 adult patients with unresectable treatment naïve PDAC who were either enrolled in a clinical trial at Honor Health Cancer Center (Phoenix, AZ) or treated at City of Hope Comprehensive Cancer Center (Duarte, CA) as Standard of Care (SOC) non-study patients between 2015 and 2019.Consent was obtained from all clinical trial patients for the use of their images gathered from medical records for imaging analysis. As a result, there was limited control over the way the images were taken or its time frames. All patients were over the age of 18 and had been diagnosed with PDAC. We divided the participant sample into two groups, labeled Cohort 1 and Cohort 2.

Cohort 1 consisted of 22 patients enrolled in the clinical trial treated at Honor Health Cancer Center. Patients within this sample group received neo-adjuvant therapy (paricalcitol, paclitaxel protein bound, cisplatin, and gemcitabine) for up to 6 months with standard of care CT multiphase imaging. The original purpose for the Honor Health clinical trial was to see the resectability and CA 19-9 status within non-metastatic pancreatic cancer but we decided to use the preliminary imaging findings in this ongoing study and assess the volumetric response in Cohort 1 as well as Cohort 2. Patients with a positive metastatic disease were excluded from the study. Furthermore, patients whose tumors were deemed resectable after the completion of neo-adjuvant therapy were likewise removed from the study to receive SOC treatment due to changes in their condition.

Cohort 2 consisted of 19 patients treated at the City of Hope Comprehensive Cancer Center. Patients within this sample group received SOC therapy only and the CT multiphase imaging exam was performed at least every 3 months as a follow-up scan. Like Cohort 1, neo-adjuvant rules were not applied since most images were obtained retrospectively. Cohort 2 was divided based on the location where participants received care to ensure that variations in treatment, tools, or other variables did not affect the participants within their given groups. To make sure that there was uniformity in the participant samples (i.e., each patient in a participant group was exposed to similar variables as the other patients within the same participant group), we worked to increase the overall reliability of the data collected during the image acquisition process.

We submitted the complete requests for information in conjunction with the Health Insurance Portability and Accountability Act (HIPPA) authorization to obtain the records of all participants from the Honor Health and City of Hope Medical Records Departments. Following the receipt of the images, we then analyzed the scans to ensure that the images fit the necessary criteria. However, since we had no control over the image collection process, most of the data obtained could not be used due to issues with the imaging protocol. Additional exclusion criteria for these images included poor image quality, variations in time between images (e.g., too far apart or non-comparable to others within the sample set), and the use of non-standard practices in image collection. These variations, especially the latter, occurred more frequently than we anticipated, leaving the image sample size for TIDC at 28 patients out of the anticipated 41 participants from which scans were requested.

Image Acquisition

For the PDAC cohorts, we required multiphase CT images for collection at Honor Health and City of Hope. All images from Honor Health and City of Hope used the same standard protocol to acquire the participant CT scans for analysis. First, the images were obtained from the imaging conducted with multi-phase CT. Most of the acquired images were scanned on a GE scanner with a standard pancreatic protocol which included pre-injection, arterial, and portal venous phases (11). Second, to maximize the coherency and accuracy of the analysis, the images must have used the standard iodinated contrast agent Isovue 370. Patient files from both cohorts indicated that each participant received a dose of 150 cc + 40 cc of saline that was injected at a rate of 5 cc per second into the antecubital vein of the participant.

For scanning parameters, the areas of interest were defined as the region above the diaphragm to the inferior liver margin for arterial phase images. The region from above the diaphragm to the superior aspect of the iliac crest was used for both pre-contrast and venous phase images. Multi-phase scanning parameter used in the image collection process was at 120 kV with a 0.5 second rotation time. All images were reconstructed as follows: pre-contrast phase images were reconstructed into 3-mm slices and images from arterial or venous phases into 2-mm slices. Images were reviewed by experienced radiologists to ensure that the image quality was sufficient but 3D Qi has some high-resolution issue which can be fixed in future upgrades. Of the 28 participant images obtained, 24 were of ample quality for analysis. Initial images were reconstructed into 0.625 x 1.25 mm-slices for 3D post-processing and uploaded from the Picture Archiving and Communication System (PACS) to advanced imaging software (GE Advantage Workstation 3.2) for volumetric analysis.

3D Volumetric Analysis

A 3D imaging software application called GE AW 3.2 USA was used on the 28 PDAC patient CT images to conduct the volumetric analyses. This method of analysis refers to the total amount of a given substance, in this case, the pancreatic tumor, which was determined by measuring the volume that the tumor occupied (12–14). Similar analytical approaches had promising outcomes when exploring various medical conditions involving the pancreas and liver, providing adequate justification for its use

in the context of this study (12–17). To confirm the accuracy of this method, multiple series were registered and regions of interest were identified prior to receiving the requested study images to define volumetric tumor quantification. Edits to the regions of interest were performed when needed to ensure that volumetric analysis was as accurate as possible using the available tools (see **Figure 1**).

Images were imported to the Massachusetts General Hospital application called 3D Quantitative Imaging software (3DQI). The PDAC tumor was identified by a radiologist and radiology expert. All series were opened side by side to do a comparison for better visibility and quantitative assessment (See **Figure 2**). Elaboration on the perfusion imaging characteristics on multiphase CT was a major goal of this research. The standard CT protocol for the PDAC imaging requires non-contrast with arterial and venous phase imaging. This preliminary study was designed to observe changes occurring during the wash-in and wash-out rates seen in perfusion imaging. This application has been used successfully in hepatocellular carcinoma (HCC) (18–21). HCC shows a complete wash-out in the venous and late phase imaging but the PDAC tumor becomes more vascularized in the venous phase which indicates missing information that might be critical to how PDAC is defined.

Marley Equation

The Marley equation was created and first investigated in the Rahmanuddin lab to describe the difference in the enhancement patterns between the arterial and venous phases (see **Figure 3**). This equation uniquely defines the characteristics of each pixel and flow inside the tumor which is aggressive in nature and can potentially be useable in the early detection of pancreatic cancer. In comparison to HCC imaging, PDAC has unique characteristics which are seen in the late arterial or venous phase imaging. It is visible in the venous phase which indicates the prolonged time of tumor vascularization. The longer the venous phase wash-out rate, the higher the tumor aggression. Marley equation helps to define the gap between the arterial and venous phases which can estimate the accurate change in the time on perfusion imaging. Our previous preliminary results showed that using the Marley Equation can be beneficial in observing the differences more precisely. This equation might be helpful in relating imaging perfusion to Vascular Endothelial Growth Factors (VEGF). **Figure 3** provides a breakdown of the Marley equation, indicating how it was used in the assessment within the current study.

Time-Intensity-Density Curves

The potential in the application of TIDC, as a means of detecting tumor aggressiveness was seen using 3DQI software. Time-Density Curves for CT scans and Time-Intensity Curves for MRI scans provide a visual tool for the enhancement or reduction of a particular mass/lesion over time based on the intensity and density (22–25). Previous studies have demonstrated the utility of TIDC analysis in differentiating solid lesions in the pancreas using contrast-enhanced EUS (16), a first line diagnostic test (26–29). However, due to the limitations presented in the US examinations, compared to the test environment setting, and the associated concerns regarding accuracy across the application throughout treatment facilities in the United States, past researchers have noted the difficulties associated with standardizing these markers as a means of creating a unified evidence-based practice (EBP) for its use as a diagnostic modality (30–34).

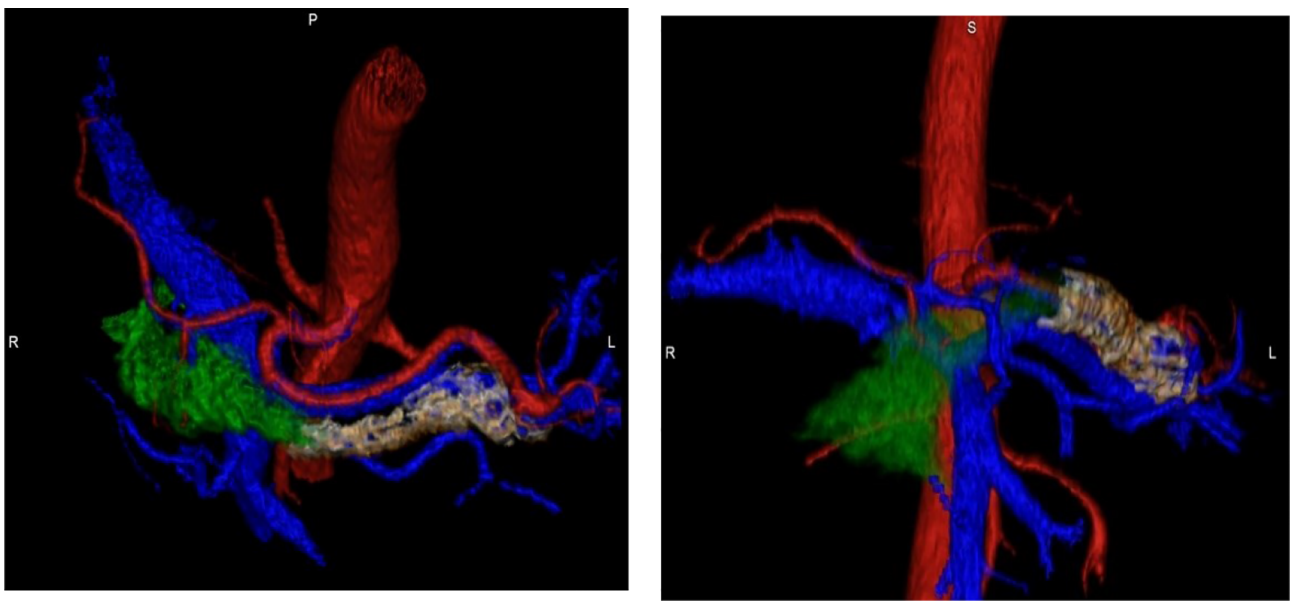

FIGURE 1 | Pancreatic Tumor Volumetric Mapping.

FIGURE 2 | 3D Qi Software.

Our focus was to identify an approach that used the TIDC to show how it can be applied in the early detection of pancreatic cancer. The identification of the TIDC patterns that correlate with PDAC responses to treatment would enable clinicians to better evaluate the severity of the disease, in addition to serving as a diagnostic screening modality. The TIDC model generated for the current study displayed information based on each pixel present in the multi-phase CT imaging within the tumors and tissues of interest in each participant. Through the integration of a computer-based software for pixel-by-pixel analysis, we were able to define the time-in and time-out quantitative numbers with a greater level of precision compared to past efforts (35–38). The artificial intelligence tool used was uniquely designed to differentiate the pixel-based change in contrast enhancement related to perfusion in multiphase imaging.

RESULTS

The Marley equation has proven that it is applicable in quantifying tumor aggressiveness. Using this equation, we were able to generate normal distribution histograms based on the minimum, maximum, and average tumor radio density, as measured in Hounsfield Units (HU). Tissue radio density refers to the opacity of the tissue as measured by how readily the different types of electromagnetic radiation passes through

Marley Equation:

$$Area\ under\ the\ normal\ distributions = \left| \int_{x_{venous_{min}}}^{x_{arterial_{max}}} [f(x_{venous}) - f(x_{arterial})]\, dx \right|$$

X is defined as the range of perfusion values in the arterial or venous phase.

The function f(x) represents $f(x) = \frac{1}{\sigma\sqrt{2\pi}} e^{-\frac{(x-\mu)^2}{2\sigma^2}}$ (σ *is variation &* π *is the average*)

FIGURE 3 | The Marley Equation.

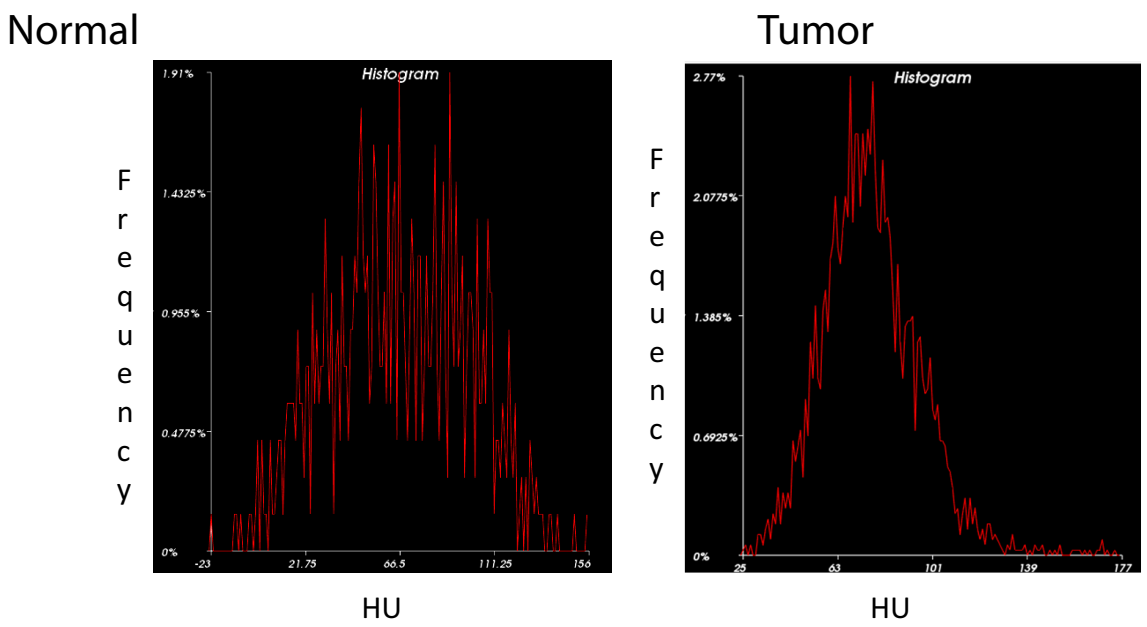

FIGURE 4 | Histogram Analysis of Normal Pancreas *vs*. PDAC. Histogram distribution of the normal pancreas *(left)* shows greater variation in density representative of its heterogeneous echotexture compared to a more homogenous pattern in PDAC *(right)*.

the tissue itself. HU is a common scale used in assessing CT scans and refers to a linear transformation of the radio density of various materials. The common HU reference point is distilled water at a standard pressure and room temperature set as zero. The tissue radio density on CT images, measured in HU, changed with respect to time. Specifically, analysis showed that the difference in tumor perfusion during the arterial and venous phases increases with respect to time. This change continuously increases during the later stages of the venous phase without changing the tumor dynamic contrast enhancement.

Our preliminary study highlighted the following major areas based on perfusion imaging. The Marley equation showed that perfusion changes play a major role in tumor kinetics (see **Figure 4**). PDAC tumor morphology is unique with normal heterogeneous features which have characteristics opposite to that of liver tumor morphology (4, 6, 19, 21). This is an important result due to the application of this equation showing a distinct contrast between the healthy pancreas and tumor.

TDIC analysis was performed on all patient images due to the limited availability of the multiphase standard imaging protocol. This was caused by missing scans including non-contrast images or series of the arterial or venous phases. However, 3D volumetric quantification was conducted on all images. Based on the pilot data, there are indications that perfusion in PDAC exhibits delays, showing a later response, as compared to a normal pancreatic tissue (see **Figure 5**). TIDC analysis shows that perfusion takes a longer time in the venous phase in PDAC imaging. These perfusion delays represent the active form of the tumor which might be significantly associated with tumor aggressiveness or VEGF-related activity. Longer perfusion time in the venous phase was directly correlated with the aggressiveness of the disease. This groundbreaking finding shows that TIDC analyses can observe PDAC in the venous phase manifesting in a manner opposite the normal pancreatic morphological TIDC which cleared the dynamic contrast in the late venous phase.

3D Volumetric Analysis

3D tumor volume was measured in patients diagnosed with PDAC receiving standard treatment with or without neoadjuvant therapy. A correlation of disease burden decreasing with clinical treatment was seen predominantly in Cohort 1. Changes in arterial and venous perfusion were related to tumor aggression. These findings have the potential for integration to create new screening tools which may serve as potential imaging biomarkers for the early detection of PDAC. Due to the small sample size, we were unable to produce statistical analyses, but the hypothesis is completely based on the perfusion characteristics on the follow-up imaging. Based on the findings, the PDAC volume measure decreases constantly over time which is seen with eight of the patients in Cohort 1 (see **Figure 6**), which indicates that the neoadjuvant population had a better control on the disease compared to the SOC of Cohort 2. The graphs indicated that 3D volume measurements might be a potential imaging biomarker to identify the disease progression or regression status. 3D volumetrics can provide more precise pixels based on the quantitative assessment on follow-up imaging for the those previously diagnosed with PDAC.

The average percent change in volume based on the images analyzed was explored (see **Figure 7**). Serial imaging in Cohort 1, who were receiving neoadjuvant therapy in addition to SOC

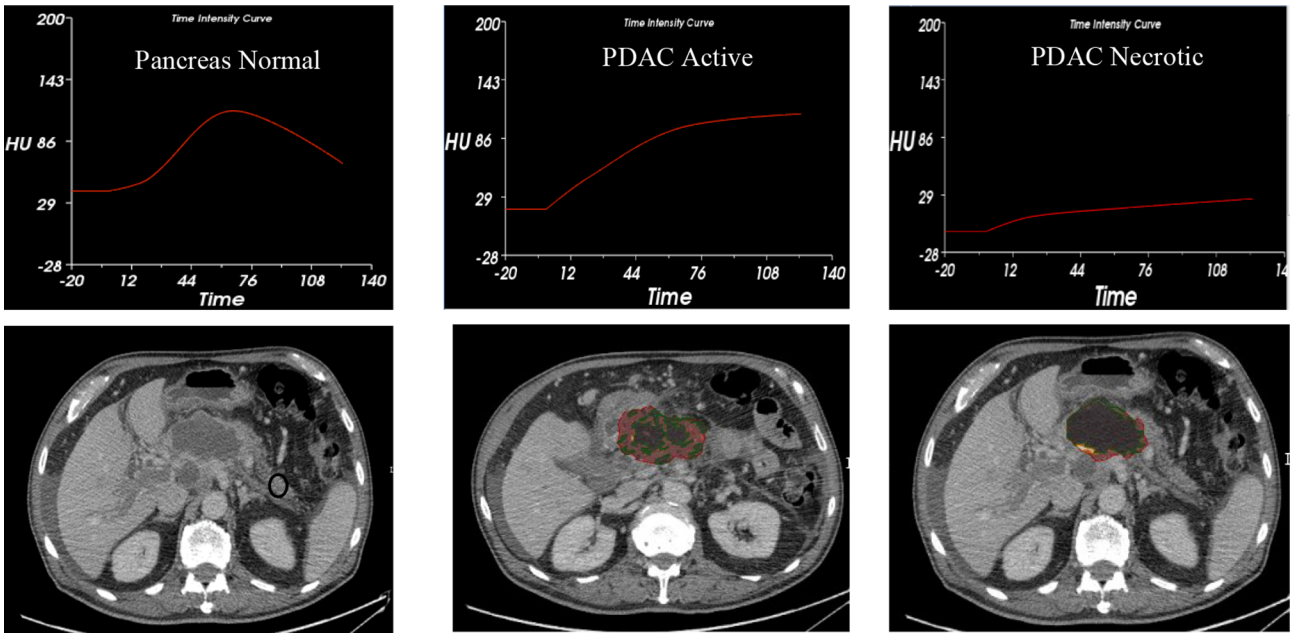

FIGURE 5 | Time Intensity/Density Curves.

treatment, showed steady decreases in tumor volume and venous vasculature. Imaging from Cohort 2, who were receiving standard therapy alone, displayed variable responses during treatment with an average decrease overall. This change does not display major differences compared to Cohort 1 but shows some change on the follow-up imaging. 3D volume could be a main indicator for the major and minor volumetric change compared to that of 2D analysis.

DISCUSSION

Pancreatic ductal adenocarcinoma (PDAC) accounts for over 85% of pancreatic malignancies (1). Despite the recent improvements to diagnostic imaging, conventional treatments, and newer targeted therapies, mortality remains high (4). The deep retroperitoneal location of the pancreas creates certain diagnostic uncertainties that limit current efforts in the early detection of pancreatic cancer (4). Multiphase CT is currently the standard modality for diagnostic testing (39–42). However, changes to tissue morphology that occur with PDAC make it difficult to define texture accurately with 2D CT imaging (39). This study evaluated the use of 3D quantitative volumetric and TIDC analysis for detecting PDAC treatment response.

The difference in tumor perfusion during the arterial and venous phases increased with respect to time. Results showed that volume- and perfusion-based imaging biomarkers could play a significant role in defining the aggressiveness of early-stage

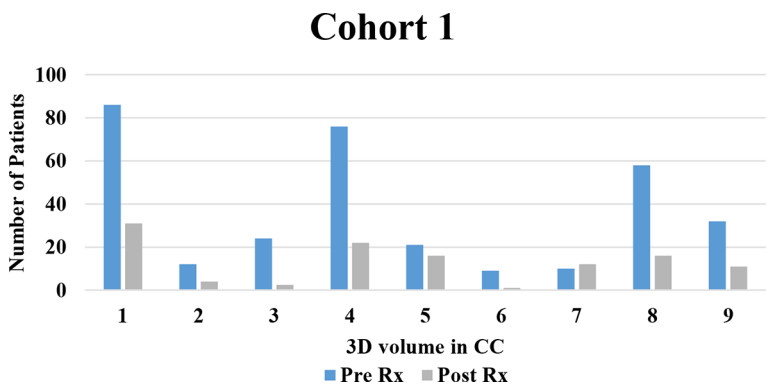

FIGURE 6 | Decreases in PDAC Volume.

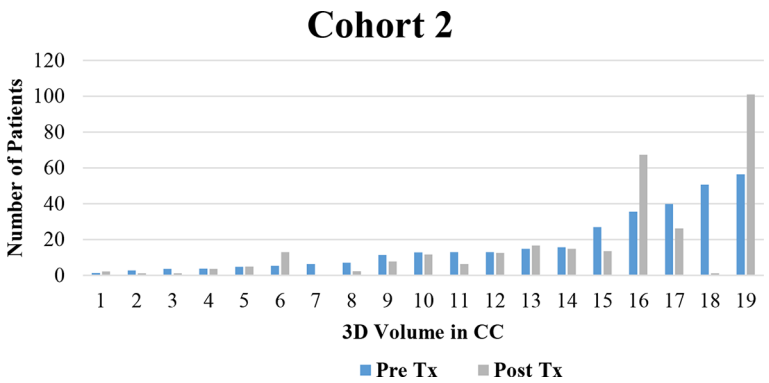

FIGURE 7 | Change in 3D volume which decreased over time.

tumors and response to therapy. Further studies to identify additional 3D imaging biomarkers for pancreatic cancer could collectively increase the precision of early diagnostic imaging (See **Figure 8**). Based on the results, it is predicted that the longer the time spent in the venous phase might relate to the tumor aggressiveness behavior. This methodology in conjunction with the Marly Equation might be useful for the early detection of pancreatic cancer by quantifying the exact changes in the perfusion imaging. The larger the change, the more aggressive the disease. It can also be useful for comparing TIDC standard venous phase perfusion rates to PDAC cases.

Tissue radiodensity on CT images, measured in HU, changed with respect to time. Clear documentation of these changes, albeit in a small sample size, suggests that there is potential for application in the creation of a screening tool that might be used to detect PDAC; however, more information is needed. Conclusive evidence that finds this result as accurate across a larger and more diverse sample population might point toward the use of this application in diagnostic modalities. Perfusion delays represented the active form of the tumor which might be associated with VEGF-related activity. Longer perfusion time in the venous phase was directly correlated with the aggressiveness of the disease which might reflect an increased angiogenesis. In cancer, VEGF has been identified as one of the main culprits behind rapid angiogenesis which deprives healthy cells of sufficient nutrients and promotes metastases (43). Even though PDAC displays a poor perfusion, it might still have a considerable VEGF-related activity (44). Many tumors require angiogenic processes that are therapeutically targetable (45). However, this dependency indicates the demand for nutrients and oxygen exchange which is satisfied by the metabolic burden of tumor cells instead of a measure of angiogenic dependence (45). Future projects with larger patient populations might provide more insight into the relationship of PDAC aggressiveness and angiogenesis.

This was a retrospective study, which means that contact from two medical facilities from which the participant data were obtained was not standardized. As a result, several potential participants were excluded from this study due to variability in the acquisition times of images during the treatment regimens. Patients at one facility receiving a certain type of treatment may

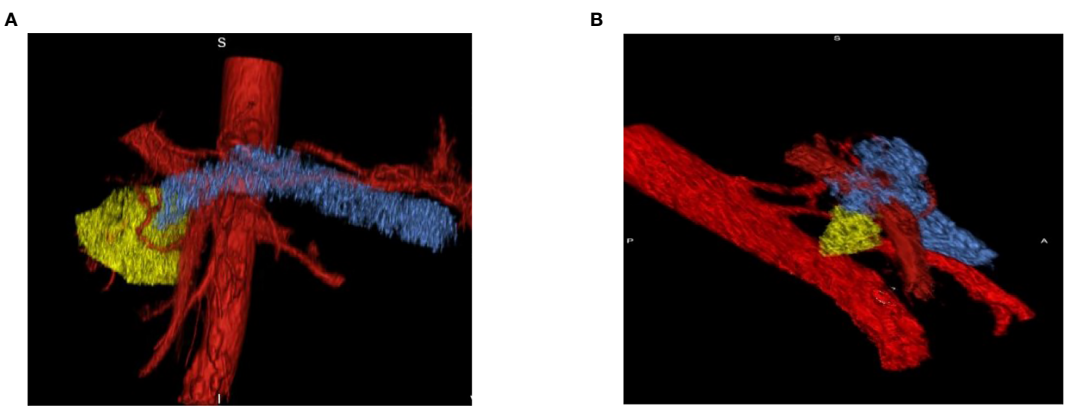

FIGURE 8 | Pre- and Post-Treatment Tumor. **(A)** Pre-treatment tumor surrounded by vessels which indicates the increase in perfusion effect in tumor progression. **(B)** Post-treatment tumor volume decreases on the follow-up scan which shows that decreases in perfusion lessens the aggressiveness of the tumor.

have images taken within a particular time frame after receiving treatment, while others may have images taken within a different time frame. This may cause imaging inconsistencies across the patient data that might not have been clearly documented, making it difficult to identify confounding variables and analysis less effective.

CONCLUSION

The clinical application of TIDC analysis is an emerging area of perfusion imaging. Previous studies have demonstrated the utility of TIDC analysis in differentiating pancreatic solid lesions using contrast-enhanced endoscopic ultrasound. However, technician-dependent ultrasound-based techniques have been shown, historically, to be difficult to standardize and can have limited accuracy. Variations in the way technicians complete their assigned imaging tasks can result in slightly different images. Similarly, differences in available imaging technologies within treatment facilities contribute to further variations in standardization. However, increased pushes for the integration of EBP within medical screening and diagnostic modalities could suggest that future efforts in this area could be better received, with a greater potential for application. Creating a unified standard set of protocols and procedures to assess multiphase CT scans is needed, regardless of instrumentation. Focus on the types of content to be included in the images, and the different views of the area should be increased in current screening methods. This information can then be translated into different diagnostic methods that can improve the effectiveness of early detection practices; however, the integration of EBP is only the first step.

TIDC analysis in six patients demonstrated a late venous perfusion delay, as compared to perfusion rates for a normal pancreas. It was hypothesized that the perfusion patterns in the late venous phase could be used to define the aggressiveness of pancreatic cancer. Our research was limited by the small sample size of the study. It was anticipated to collect and analyze data from all patient files; however, there was only enough uniformity in the imaging practices and time frames of six participants. This limitation is brought by a lack of imaging protocols with sufficient acquisition times suggesting an area in need for improvement. Several of these concerns can be decreased and possibly mitigated entirely with the integration of clear EBPs. The construction of TIDCs requires the availability of images taken from multiple phases over a longer period of time than that which is utilized most often in standard pancreatic imaging protocols. Among the study images obtained, the peak or maximum value of the curve was not visualized for pancreatic cancer images which suggests the need for extended acquisition times. It was suggested that the time-to-peak on TIDCs might provide important information about tumor aggressiveness. It might be helpful to define the precision-based imaging findings for the detection of the PDAC. Mostly patients who are diagnosed with cancer go the SOC protocol which provides the EBP clinical information.

Our preliminary results can be beneficial in acquiring more precise information for the tumor behavior using the perfusion imaging. Projects are currently underway that optimize imaging protocols for TIDC analysis in pancreatic cancer. With this study using a smaller population, we plan to take these new imaging techniques to a larger and more diverse population to test TIDC. Through the proliferation of research in this area, the creation of an early screening tool for pancreatic cancer becomes even more likely. Rahmanuddin lab is currently working on the discovery of several imaging biomarkers based on the perfusion imaging for PDAC.

Pancreatic cancer continues to have a high mortality due to the late detection and lack of effective screening methods. The novel radiomic biomarkers described here can be applied towards detecting variations in pancreatic cancer. A potential future screening tool for pancreatic cancer can involve a combination of standard imaging protocols, quantitative imaging biomarkers, and targeted molecular assays that allow the earlier detection of pancreatic cancer in high-risk patient populations. The completion of this study, combined with the efforts of other researchers in this and similar areas of research, serves as the first step in the creation of a screening tool of this nature. Using a smaller sample size, the potential effectiveness of TIDC in applications for screening was demonstrated.

DATA AVAILABILITY STATEMENT

The raw data supporting the conclusions of this article will be made available by the authors, without undue reservation.

AUTHOR CONTRIBUTIONS

All authors were involved in study design, manuscript writing, collection, and the final submission process. All authors contributed to the article and approved the submitted version.

REFERENCES

1. Veisani Y, Jenabi E, Khazaei S, Nematollahi S. Global Incidence and Mortality Rates in Pancreatic Cancer and the Association With the Human Development Index: Decomposition Approach. *Public Health* (2018) 156:87–91. doi: 10.1016/j.puhe.2017.12.015
2. Li D, Xie K, Wolff R, Abbruzzese JL. Pancreatic Cancer. *Lancet* (2004) 363 (9414):1049–57. doi: 10.1016/S0140-6736(04)15841-8
3. Ben Q, Xu M, Ning X, Liu J, Hong S, Huang W, et al. Diabetes Mellitus and Risk of Pancreatic Cancer: A Meta-Analysis of Cohort Studies. *Eur J Cancer* (2011) 47(13):1928–37. doi: 10.1016/j.ejca.2011.03.003
4. Vincent A, Herman J, Schulick R, Hruban R, Goggins M. Pancreatic Cancer. *Lancet* (2011) 378(9791):607–20. doi: 10.1016/S0140-6736(10) 62307-0
5. Ilic M, Ilic I. Epidemiology of Pancreatic Cancer. *World JWenal Gastroenterol* (2016) 22(44):9694–705. doi: 10.3748/wjg.v22.i44.9694

6. Zhang Q, Zeng L, Chen Y, Lian G, Qian C, Chen S, et al. Pancreatic Cancer Epidemiology, Detection, and Management. *Gastroenterol Res Pract* (2016) 2016:1–10. doi: 10.1155/2016/8962321
7. Zhang L, Sanagapalli S, Stoita A. Challenges in Diagnosis of Pancreatic Cancer. *World JWenal Gastroenterol* (2018) 24(19):2047–60. doi: 10.3748/wjg.v24.i19.2047
8. Canto M, Harinck F, Hruban R, Offerhaus G, Poley J, Jamel I, et al. International Cancer of the Pancreas Screening (CAPS) Consortium Summit on the Management of Patients With Increased Risk for Familial Pancreatic Cancer. *Gut* (2013) 62(3):339–47. doi: 10.1136/gutjnl-2012-303108
9. Choi B, Chung M, Han J, Han M, Yoon Y. Detection of Pancreatic Adenocarcinoma: Relative Value of Arterial and Late Phases of Spiral CT. *Abdominal Imaging* (1997) 22(2):199–203. doi: 10.1007/s002619900172
10. Crippa S, Partelli S, Bassi C, Beradi R, Capelli P, Scarpa A, et al. Long-Term Outcomes and Prognostic Factors in Neuroendocrine Carcinomas of the Pancreas: Morphology Matters. *Surgery* (2016) 159(3):862–71. doi: 10.1016/j.surg.2015.09.012
11. Graf O, Boland G, Warshaw A, Fernandez-del-Castillo C, Hahn P, Mueller P. Arterial Versus Portal Venous Helical CT for Revealing Pancreatic Adenocarcinoma: Conspicuity of Tumor and Critical Vascular Anatomy. *Am J Roentgenol* (1997) 169(1):119–23. doi: 10.2214/ajr.169.1.9207510
12. Phillip V, Zahel T, Danninger A, Erkan M, Dobritz M, Steiner J, et al. Volumetric Gain of the Human Pancreas After Left Partial Pancreatic Resection: A CT-Scan Based Retrospective Study. *Pancreatology* (2015) 15(5):542–7. doi: 10.1016/j.pan.2015.06.007
13. Baliyan V, Kordbacheh H, Parakh A, Kambadakone A. Response Assessment in Pancreatic Ductal Adenocarcinoma: Role of Imaging. *Abdominal Radiol* (2018) 43(2):435–44. doi: 10.1007/s00261-017-1434-7
14. Maignan A, Ouaissi M, Turrini O, Regenet N, Loundou A, Louis G, et al. Risk Factors of Exocrine and Endocrine Pancreatic Insufficiency After Pancreatic Resection: A Multi-Center Prospective Study. *JWenal Visceral Surg* (2018) 155(3):173–81. doi: 10.1016/j.jviscsurg.2017.10.007
15. Pandharipande P, Krinsky G, Rusinek H, Lee V. Perfusion Imaging of the Liver: Current Challenges and Future Goals. *Radiology* (2005) 234:661–73. doi: 10.1148/radiol.2343031362
16. Demir I, Jager C, Friess H, Ceyhan G. The Impact of Resection Margin Status on Pancreatic Cancer Associated Survival: A Meta-Analysis. *HPB* (2016) 18(supplement 1):e–130-131. doi: 10.1016/j.hpb.2016.02.307
17. Reichman T, Fiorello B, Carmody I, Bohorquez H, Cohen A, Seal J, et al. Using on-Site Liver 3-D Reconstruction and Volumetric Calculations in Split Liver Transplantation. *Hepatobiliary Pancreatic Dis Int* (2016) 15(6):587–92. doi: 10.1016/S1499-3872(16)60155-8
18. Nayak A, Kayal E, Arya M, Culli J, Krishan S, Agarwal S, et al. Computer-Aided Diagnosis of Cirrhosis and Hepatocellular Carcinoma Using Multi-Phase Abdomen CT. *Int J Comput Assist Radiol Surg* (2019) 14(8):1341–52. doi: 10.1007/s11548-019-01991-5
19. Roberts L, Sirlin C, Zaiem F, Almasri J, Prokop L, Heimbach J, et al. Imaging for the Diagnosis of Hepatocellular Carcinoma: A Systematic Review and Meta-Analysis. *Hepatology* (2018) 67(1):401–21. doi: 10.1002/hep.29487
20. Pickhardt P, Kitchin D, Lubner M, Ganeshan D, Bhalla S, Covey A. Primary Hepatic Angiosarcoma: Multi-Institutional Comprehensive Cancer Centre Review of Multiphasic CT and MR Imaging in 35 Patients. *Eur Radiol* (2015) 25(2):315–22. doi: 10.1007/s00330-014-3442-0
21. Lo E, Rucker A, Federle M. Hepatocellular Carcinoma and Intrahepatic Cholangiocarcinoma: Imaging for Diagnosis, Tumor Response to Treatment and Liver Response to Radiation. *Semin Radiat Oncol* (2018) 28(4):267–76. doi: 10.1016/j.semradonc.2018.06.010
22. Radiant Viewer. *Time-Intensity Curves (TIC)* (2016). Available at: https://www.radiantviewer.com/dicom-viewer-manual/time-intensity_curves_tic.htm.
23. Krix M. Time Intensity Curves. In: Baert A.L. (eds). *Encyclopedia Diagn Imaging*. Berlin, Heidelberg: Springer (2008). doi: 10.1007/978-3-540-35280-8_2488
24. Fellner C, Prantl L, Rennert J, Stroszczynski C, Jung E. Comparison of Time-Intensity Curve- (TIC-) Analysis of Contrast-Enhanced Ultrasounce (CEUS) and Dynamic Contrast-Enhanced (DCE) MRI for Postoperative Control of Microcirculation in Free Flaps – First Results and Critical Comments. *Clin Hemorheology Microcirculation* (2011) 48(1):187–98. doi: 10.3233/CH-2011-1399
25. Sherif H, Mahfouz A, Kambal A, Sayedin A, Mujeeb I. Relative Time-Intensity Curve: A New Method to Differentiate Benign and Malignant Lesions on Breast MRI. *Cancer Imaging* (2014) 14(supplement 1):26. doi: 10.1186/1470-7330-14-S1-P26
26. Yamamoto N, Kato H, Tomoda T, Matsumoto K, Sakakihara I, Noma Y, et al. Contrast-Enhanced Harmonic Endoscopic Ultrasonography With Time-Intensity Curve Analysis for Intraductal Papillary Mucinous Neoplasms of the Pancreas. *Endoscopy* (2016) 48(1):26–34. doi: 10.1055/s-0034-1393563
27. Choi T, Lee J, Kim J, Yu M, Han J, Choi B. Comparison of Multidetector CT and Gadobutrol-Enhanced MR Imaging for Evaluation of Small, Solid Pancreatic Lesions. *Korean J Radiol* (2016) 17(4):509–21. doi: 10.3348/kjr.2016.17.4.509
28. Granata V, Fusco R, Catalano O, Setola S, Castelguidone E, Piccirillo M, et al. Multidetector Computer Tomography in the Pancreatic Adenocarcinoma Assessment: An Update. *Infect Agents Cancer* (2016) 11:57. doi: 10.1186/s13027-016-0105-6
29. Garcia-Vazquez V, Marinetto E, Guerra P, Valdiviesco-Casique M, Calvo F, Alvarado-Vasquez E, et al. Assessment of Intraoperative 3D Imaging Alternatives for IOERT Dose Estimation. *Seitschrift fur Medizinishce Physik* (2017) 27(3):218–31. doi: 10.1016/j.zemedi.2016.07.002
30. Pomara C, Bello S, Grilli G, Guglielmi G, Turillazzi E. Multi-Phase Postmortem CT Angiography (MPMCTA): A New Axillary Approach Suitable in Fatal Thromboembolism. *La Radiologica Med* (2015) 120(7):670–3. doi: 10.1007/s11547-014-0467-z
31. Gupta V, Lantz J, Henriksson L, Engvall J, Karlsson M, Persson A, et al. Automated Three-Dimensional Tracking of the Left Ventricular Myocardium in Time-Resolved and Dose-Modulated Cardiac CT Images Using Deformable Image Registration. *JWenal Cardiovasc Computed Tomography* (2018) 12(2):139–48. doi: 10.1016/j.jcct.2018.01.005
32. Mokrane F, Dercle L, Myrignac O, Crubezy E, Rousseau H, Telmon N, et al. Towards a Multi-Phase Postmortem CT Angiography in Children: A Study on a Porcine Model. *Int J Legal Med* (2018) 132(5):1391–403. doi: 10.1007/s00414-018-1783-y
33. Mokrane F, Savall F, Dercle L, Crubezy E, Telmon N, Rousseau H, et al. Technical Note: A Preliminary Comparative Study Between Classical and Interventional Radiological Approaches for Multi-Phase Post-Mortem CT Angiography. *Forensic Sci Int* (2017) 271:23–32. doi: 10.1016/j.forsciint.2016.12.008
34. Ouchmich F, Angus V, Noblet V, Heitz F, Pessaux P. Liver Tissue Segmentation in Multiphase CT Scans Using Cascaded Convolutional Neural Networks. *Int J Comput Assist Radiol Surg* (2019) 14(8):1275–84. doi: 10.1007/s11548-019-01989-z
35. Putten J, Zinger S, Sommen F, With P, Prokop M, Hermans J. Quantitative CT Based Radiomics as Predictor of Resectability of Pancreatic Adenocarcinoma. *Med Imaging 2018: Computer-Aided Diagnosis* (2018) 10575O. doi: 10.1117/12.2291746
36. Ljosa V, Carpenter A. Introduction to the Quantitative Analysis of Two-Dimensional Fluorescence Microscopy Images for Cell-Based Screening. *PloS Comutational Biol* (2009) 5(12):e1000603. doi: 10.1371/journal.pcbi.1000603
37. Farag A, Lu L, Roth H, Liu J, Turkbey E, Summers R. Automatic Pancreas Segmentation Using Coarse-to-Fine Superpixel Labeling. *Deep Learn Convolutional Neural Networks Med Image Computing*. Edition 1. (2017). p.279–302. doi: 10.1007/978-3-319-42999-1_16
38. Farag A, Lu L, Roth H, Liu J, Turkbey E, Summer R. A Bottom-Up Approach for Pancreas Segmentation Using Cascaded Superpixels and (Deep) Image Patch Labeling. *IEEE Trans Image Process* (2016) 26(1):386–99. doi: 10.1109/TIP.2016.2624198
39. Salameh J, McInnes M, McGrath T, Salameh G, Schieda N. Diagnostic Accuracy of Dual-Energy CT for Evaluation of Renal Masses: Systematic Review and Meta-Analysis. *Am J Roentgenol* (2019) 212(4):W100–5. doi: 10.2214/AJR.18.20527
40. Sevcenco S, Spick C, Helbich T, Heinz G, Shariat S, Klingler H, et al. Malignancy Rates and Diagnostic Performance of the Bosniak Classification for the Diagnosis of Cystic Renal Lesions in Computed Tomography – a Systematic Review and Meta-Analysis. *Eur Radiol* (2017) 27(6):2239–47. doi: 10.1007/s00330-016-4631-9

41. Law R, Varayil J, Song L, Fidler J, Fletcher J, Barlow J, et al. Assessment of Multi-Modality Evaluations of Obscure Gastrointestinal Bleeding. *World JWenal Gastroenterol* (2017) 23(4):614–21. doi: 10.3748/wjg.v23.i4.614
42. Pepa R, Cerchione C, Pugliese N, Colicchio R, Salvatore P, Sirignano C, et al. Diagnostic-Driven Antifungal Approach in Neutropenic Patients at High Risk for Chronic Disseminated Candidiasis: Preliminary Observations on the Role of 1, 3-β-D-Glucan Antigenemia and Multiphasic Contrast-Enhanced Computed Tomography. *Supportive Care Cancer* (2018) 36(6):1691–4. doi: 10.1007/s00520-018-4138-9
43. Georgiadou D, Sergentanis TN, Sakellariou S, Filippakis GM, Zagouri F, Vlachodimitropoulos D, et al. VEGF and Id-1 in Pancreatic Adenocarcinoma: Prognostic Significance and Impact on Angiogenesis. *Eur J Surg Oncol* (2014) 40(10):1331–7. doi: 10.1016/j.ejso.2014.01.004
44. Longo V, Brunetti O, Gnoni A, Cascinu S, Gasparini G, Lorusso V, et al. Angiogenesis in Pancreatic Ductal Adenocarcinoma: A Controversial Issue. *Oncotarget* (2016) 7(36):58649–58. doi: 10.18632/oncotarget.10765
45. Goel H, Mercurio A. VEGF Targets the Tumour Cell. *Nat Rev Cancer* (2013) 13:871–82. doi: 10.1038/nrc3627

Conflict of Interest: The authors declare that the research was conducted in the absence of any commercial or financial relationships that could be construed as a potential conflict of interest.

frontiers in Oncology

ORIGINAL RESEARCH
published: 27 September 2021
doi: 10.3389/fonc.2021.710248

Computed Tomography-Based Radiomics for Preoperative Prediction of Tumor Deposits in Rectal Cancer

Yumei Jin[1,2†], Mou Li[1†], Yali Zhao[3], Chencui Huang[3], Siyun Liu[4], Shengmei Liu[1], Min Wu[5] and Bin Song[1*]*

[1] Department of Radiology, West China Hospital of Sichuan University, Chengdu, China, [2] Department of MRI, Qujing First People's Hospital, Qujing, China, [3] Department of Research Collaboration, R&D Center, Beijing Deepwise & League of PHD Technology Co., Ltd, Beijing, China, [4] Pharmaceutical Diagnostics, GE Healthcare, Beijing, China, [5] Huaxi MR Research Center (HMRRC), Department of Radiology, West China Hospital of Sichuan University, Chengdu, China

Objective: To develop and validate a computed tomography (CT)-based radiomics model for predicting tumor deposits (TDs) preoperatively in patients with rectal cancer (RC).

Methods: This retrospective study enrolled 254 patients with pathologically confirmed RC between December 2017 and December 2019. Patients were divided into a training set (n = 203) and a validation set (n = 51). A large number of radiomics features were extracted from the portal venous phase images of CT. After selecting features with L1-based method, we established Rad-score by using the logistic regression analysis. Furthermore, a combined model incorporating Rad-score and clinical factors was developed and visualized as the nomogram. The models were evaluated by the receiver operating characteristic curve (ROC) analysis and area under the ROC curve (AUC).

Results: One hundred and seventeen of 254 patients were eventually found to be TDs^+. Rad-score and clinical factors including carbohydrate antigen (CA) 19-9, CT-reported T stage (cT), and CT-reported peritumoral nodules (+/-) were significantly different between the TDs^+ and TDs^- groups (all $P < 0.001$). These factors were all included in the combined model by the logistic regression analysis (odds ratio = 2.378 for Rad-score, 2.253 for CA19-9, 2.281 for cT, and 4.485 for peritumoral nodules). This model showed good performance to predict TDs in the training and validation cohorts (AUC = 0.830 and 0.832, respectively). Furthermore, the combined model outperformed the clinical model incorporating CA19-9, cT, and peritumoral nodules (+/-) in both training and validation cohorts for predicting TDs preoperatively (AUC = 0.773 and 0.718, $P = 0.008$ and 0.039).

OPEN ACCESS

Edited by:
Changqiang Wu,
North Sichuan Medical College, China

Reviewed by:
Shaocheng Zhu,
Henan Provincial People's Hospital, China
Swapnil Ulhas Rane,
Advanced Centre for Treatment, Research and Education in Cancer, India

****Correspondence:***
Min Wu
wuminscu@scu.edu.cn
Bin Song
songlab_radiology@163.com

†These authors have contributed equally to this work and share first authorship

Specialty section:
This article was submitted to Cancer Imaging and Image-directed Interventions, a section of the journal Frontiers in Oncology

Received: *15 May 2021*
Accepted: *13 September 2021*
Published: *27 September 2021*

Citation:
Jin Y, Li M, Zhao Y, Huang C, Liu S, Liu S, Wu M and Song B (2021) Computed Tomography-Based Radiomics for Preoperative Prediction of Tumor Deposits in Rectal Cancer. Front. Oncol. 11:710248. doi: 10.3389/fonc.2021.710248

Conclusions: The combined model incorporating Rad-score and clinical factors could provide a preoperative prediction of TDs and help clinicians guide individualized treatment for RC patients.

Keywords: tumor deposits, rectal cancer, radiomics, computed tomography, preoperative prediction

INTRODUCTION

Rectal cancer (RC) is one of the most common cancers and a leading cause of cancer-related death worldwide (1, 2). Tumor deposits (TDs) in RC have been shown to be an important marker of poor prognosis (3–5). This adverse association persists even in those patients with lymph node metastasis (LNM), strongly suggesting that their effect on prognosis is separate and additive (3). Detecting TDs in advance is very important for assessing prognosis of RC patients.

TDs, also called extranodal TDs, peritumoral deposits, or satellite nodules, are defined as discrete tumor foci in the pericolic or perirectal fat, without histological evidence of residual lymph node or identifiable vascular or neural structures (6, 7). According to the eighth edition of the American Joint Committee on Cancer (AJCC) TNM staging system, any T lesions with negative regional LNM and positive TDs are classified as N1c (8). Positive TDs can elevate clinical stages of RC patients. For example, a stage I patient (T1-2N0) with TDs should be reclassified and treated as stage III (T1-2N1c). The early identification of TDs is important for evaluating the stage and treatment plan.

Rectal magnetic resonance imaging (MRI), computed tomography (CT), and endorectal ultrasound are the first-line examinations in RC. However, no imaging modality has been proved to be reliable to predict TDs (9–12). Currently, the diagnosis of TDs still depends on the pathology after surgery, which is not conducive to the early evaluation of tumor characteristics (9). In recent years, radiomics has attained ability of processing medical images and understanding information invisible to human eyes, and it has been widely used in tumor research. Chen et al. (11) and Yang et al. (12) established radiomics models based on ultrasound or MRI for predicting TDs. However, the sample sizes in these studies were small (TDs^+: 23-40). At present, there is still a lack of CT-based radiomics research in this field. Therefore, we aimed to evaluate predictive value of CT-based radiomics for TDs prediction in a bigger cohort of RC patients.

MATERIALS AND METHODS

Patients

This study was approved by the local Institutional Review Boards (No. 2019-1159, Date: 2019/12/26), and the need for written informed consent was waived.

The institutional database of medical records was searched for suitable patients between December 2017 and December 2019. A total of 254 patients with pathologically confirmed RC (mean age 59.2 years, age range 32-86 years) were finally enrolled according to the following criteria. The inclusion criteria: (1) Patients with pathologically confirmed RC; (2) Sufficient clinical data [e.g., carcinoembryonic antigen (CEA), carbohydrate antigen (CA) 19-9, and CA125]; (3) no prior therapy before surgery. The exclusion criteria: (1) CT scanning was not performed (n = 234); (2) Image quality was poor (n = 2); (3) Lack of tumor markers (n = 8); (4) Patients with other malignant tumors besides RC; (5) Patients receiving neoadjuvant chemoradiotherapy (nCRT) (n = 73). The flowchart of patient recruitment is shown in **Figure 1**. The baseline characteristics and pathological data of patients are listed in **Table 1**. The patients were divided into two groups, namely the training set (n = 203) and the validation set (n = 51), at a ratio of 8:2 according to the scanning date.

CT Examination

In our hospital, the chest-abdomen-pelvis contrast-enhanced CT is routinely used in patients with clinically suspected RC for evaluating the primary tumor and metastasis. In this study, CT scanning was performed on a 128-MDCT scanner (Somatom Definition AS+, Siemens Healthcare Sector, Forchheim, Germany) and a dual-source CT system (Somatom Definition Flash, Siemens Healthcare Sector, Forchheim, Germany). Both CT scanners used the same main parameters, as shown in **Supplementary Material**. The radiomics features were extracted from the portal venous phase images.

Reference Standard for Pathology

TDs were pathologically proven based on surgical specimens. Pathological confirmatory reports were acquired from medical records of the Department of Pathology. The numbers of LN and TDs were calculated and reported in the pathological reports.

CT Evaluation

Two experienced radiologists (10 and 5 years' experience in the diagnosis of RC) were assigned to review CT images, without any patient identification and clinicopathological information. Because of limited ability of CT to distinguish T1 from T2 lesions, T1 and T2 lesions were classified as one group (T1-2 group). The nodules with diameter > 3 mm within the lymphatic drainage space of RC on CT images were defined as peritumoral nodules. The inter-observer reliability of CT-reported T stage (cT) and peritumoral nodules (+/-) was evaluated by a weighted kappa statistics test. Then any disagreement between the two readers was solved by discussion during the image interpretation. The results of cT and peritumoral nodules (+/-) are shown in **Table 1**.

Feature Extraction and Model Building

The tumoral and peritumoral regions in all patients were separately drawn slice by slice to obtain intra- and peritumoral

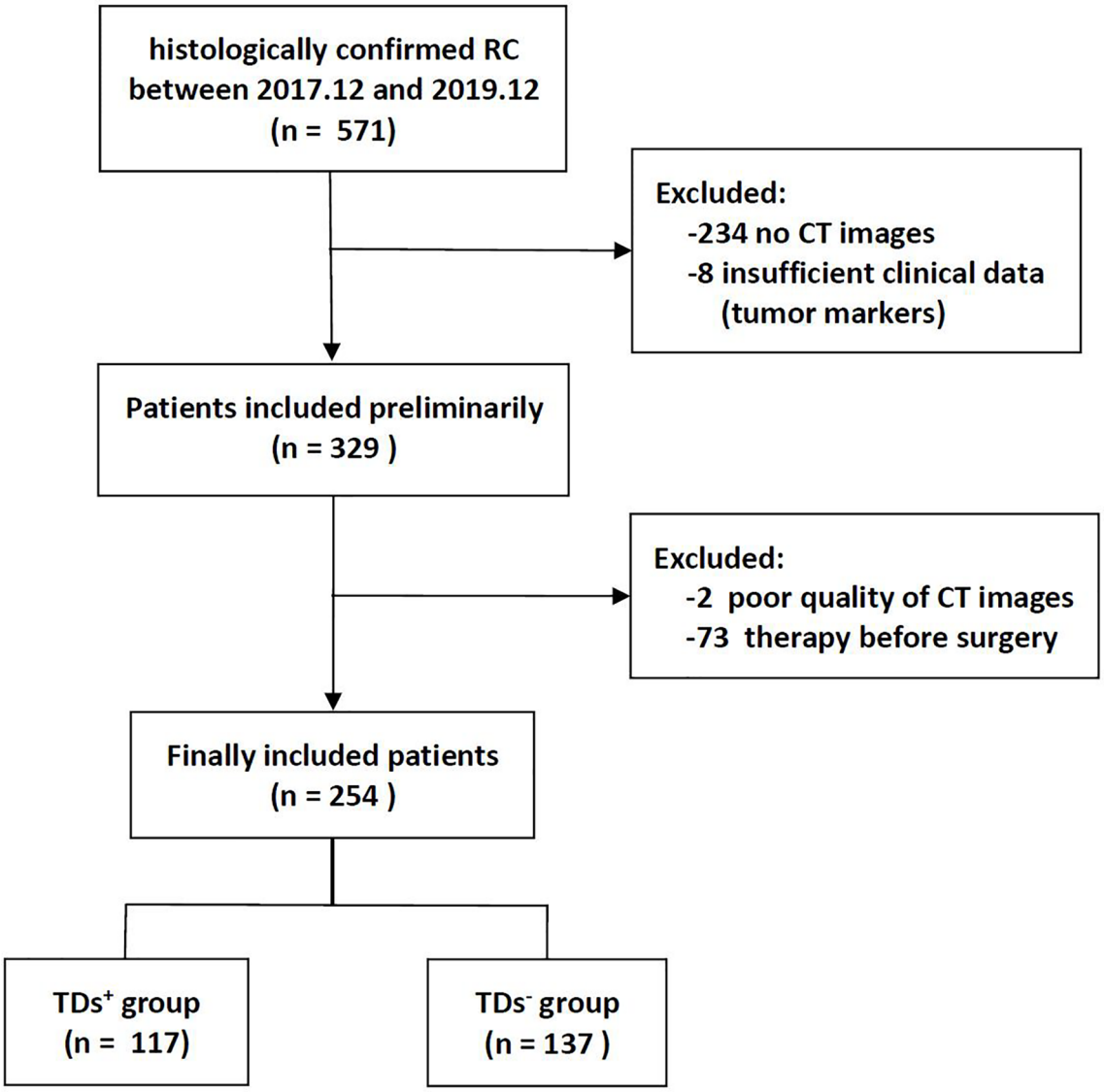

FIGURE 1 | Flowchart of patients' recruitment pathway.

features (**Figure 2**). The radiologists selected 20 patients randomly for evaluating feature stability. For the intra-class correlation analysis, one radiologist drew volumes of interest (VOI) twice (one month apart). The inter-observer correlation coefficient was calculated by comparing VOIs of radiologist 1 (first time) and radiologist 2. It is commonly admitted that intra- and inter-class correlation coefficient (ICC) < 0.5 indicates poor reliability, 0.5 - 0.75: moderate reliability, and > 0.75: good or excellent reliability (13). Thus, the features with ICC ≤ 0.75 were excluded.

The CT images were resampled to a pixel spacing of 1.0 mm in three anatomical directions. High-pass and low-pass wavelet filters, Laplacian of Gaussian (LoG) filters with different σ parameters, and the other image transformation methods such as square, square root, logarithm, exponential, gradient, lbp2d, and lbp3 were employed to pre-process original images. Then, we extracted radiomics features (i.e., the first-order, shape, and texture features) by using PyRadiomics (14). The texture features included the following types: the gray-level co-occurrence matrix (GLCM), the gray-level run-length matrix (GLRLM), the gray-level size zone matrix (GLSZM), and the gray-level dependence matrix (GLDM). Finally, a total of 2107 features were extracted from original and filtered images. To eliminate the differences in the value scales, all features were normalized by the z-score analysis. Redundant features were randomly removed by correlation analysis with a threshold of 0.5. Then different feature-selection and machine-learning methods were combined to form 84 classifiers, as shown in **Supplementary Material**. The optimal parameters of radiomics were adjusted to output the best classifier (Rad-score).

TABLE 1 | Baseline characteristics of the study population.

Characteristics	TD positive (n = 117)	TD negative (n = 137)	*P* value	training cohort (n = 203)	validation cohort (n = 51)	*P* value
Age (mean ± SD,years)	59 ± 13	60 ± 11	0.553	59 ± 11	59 ± 14	0.682
Gender (men/women)	62/55	89/48	0.056	112/91	39/12	**0.006**
Volume (median,cm^3)	15.1	12.0	**0.042**	14.0	13.0	0.829
Location			0.078			0.157
upper	61	56		89	28	
middle-lower	56	81		114	23	
cT stage (T1-2/T3/T4)	11/84/22	57/70/10	**<0.001**	53/127/23	15/27/9	0.753
Peritumoral nodules (+/-)[1]	103/14	73/64	**<0.001**	140/63	36/15	0.822
CEA (+/-)	61/56	48/89	**0.006**	87/116	22/29	0.971
CA19-9 (+/-)	44/73	22/115	**<0.001**	50/153	16/35	0.326
CA125 (+/-)	11/106	6/131	0.110	13/190	4/47	0.713
Rad-score	0.60 ± 0.19	0.42 ± 0.20	**<0.001**	0.49 ± 0.21	0.53 ± 0.21	0.343
pT stage (T1/2/3/4)	0/7/91/19	7/37/86/7	**<0.001**	6/34/145/18	1/10/32/8	0.533
pN stage (N0/1/2)	0/69/48	80/43/14	**<0.001**	64/90/49	16/22/13	0.897
Histologic grade (1/2/3)	0/86/31	3/114/20	**0.008**	1/158/44	2/42/7	0.085

[1]*Peritumoral nodule was defined as any nodule (diameter > 3mm) within the lymphatic drainage space of rectal cancer on CT images. P values less than 0.05 are shown in bold.*

The Rad-score and clinical factors were assessed by the univariate logistic regression analysis. The features revealed as statistically significant were then involved into the multivariate logistic regression analysis for constructing the combined model. A nomogram was generated for the model visualization, graphical evaluation of variable importance, and the calculation of predictive accuracy. The Hosmer-Lemeshow test was performed to assess the goodness-of-fit of the nomogram. A calibration curve, obtained by plotting the actual TDs^+ probability against the nomogram-predicted probability of TDs^+, was used to assess the calibration of the nomogram (15). Decision curve first introduced in 2006 by Vickers et al. (16) was used to evaluate clinical utility of the nomogram. The receiver operating characteristic curve (ROC) analysis was performed to assess the predictive performance of the models.

Statistical Analysis

Student's *t* test, non-parametric test, chi-squared test, and Fisher's exact test (where appropriate) were used to analyze differences of baseline characteristics in **Table 1**. The area under the ROC curve (AUC) was compared by Delong's test. The software used in this study included SPSS 21.0 software (IBM), Python 3.6, Stata 15.0, and Medcalc 15.2.2. The confidence level was set at $P < 0.05$.

RESULTS

Patients' Characteristics

A total of 254 patients were enrolled in this study, in which 117 patients were TDs^+. As shown in **Table 1**, there were significant differences in volume ($P = 0.042$), cT ($P < 0.001$), peritumoral nodules (+/-) ($P < 0.001$), CEA ($P = 0.006$), CA19-9 ($P < 0.001$), and pathological factors [i.e., T stage ($P < 0.001$), N stage ($P < 0.001$), and grade ($P = 0.008$)] between the TDs^+ and TDs^- groups. Between the training and validation cohorts, there was a significant difference in gender. The weighted kappa coefficients of cT and peritumoral nodules (+/-) between two radiologists were 0.656 [95% confidence interval (CI): 0.570-0.741] and 0.679 (95% CI: 0.584-0.774) in the whole cohort, which showed substantial consistency according to the generally accepted knowledge: 0.41-0.60, moderate, 0.61-0.80, substantial, and 0.81-1.00, almost perfect (17).

Feature Selection and Model Building

For the consistency test of VOIs, 1490 tumoral and 1605 peritumoral features had good reliability with ICC > 0.75. Rad-score involving 10 peritumoral and 3 tumoral features was finally established by the logistic regression analysis. The 13 features and their coefficients are shown in **Supplementary Material**. Rad-score had statistical difference between the TDs^+ and TD^- groups (0.60 ± 0.19 *vs* 0.42 ± 0.20, $P < 0.001$).

A clinical model was composed of three factors selected by the logistic regression analysis, namely CA19-9, cT, and peritumoral nodules (+/-). The combined model was built by adding Rad-score to the clinical model [odds ratio (OR) = 2.378 for Rad-score, 2.281 for cT, 4.485 for peritumoral nodules (+/-), and 2.253 for CA19-9], as summarized in **Table 2**. Although volume and CEA were significantly different between the TDs^+ and TDs^- groups, they were both excluded by the multivariate logistic regression analysis (**Table 2**).

A nomogram was generated for visualizing the combined model (**Figure 3**). In the nomogram, the point for each variable on the corresponding axis can be added to determine the risk of TDs^+. Higher total score was associated with greater risk of TDs^+. The combined model had a good fit according to the Hosmer-Lemeshow test ($P = 0.642 > 0.05$). The calibration curve of the nomogram demonstrated a good agreement between the predicted probability and actual observed probability (**Figure 4A**), because the solid line was close to the reference line (dotted line). However, this model underestimated actual risk of TDs^+ (the range of the threshold probability: 30%-75%) and overestimated risk when threshold probability > 75%. The decision curve was performed to assess clinical usefulness of the combined model (**Figure 4B**), showing that the combined model

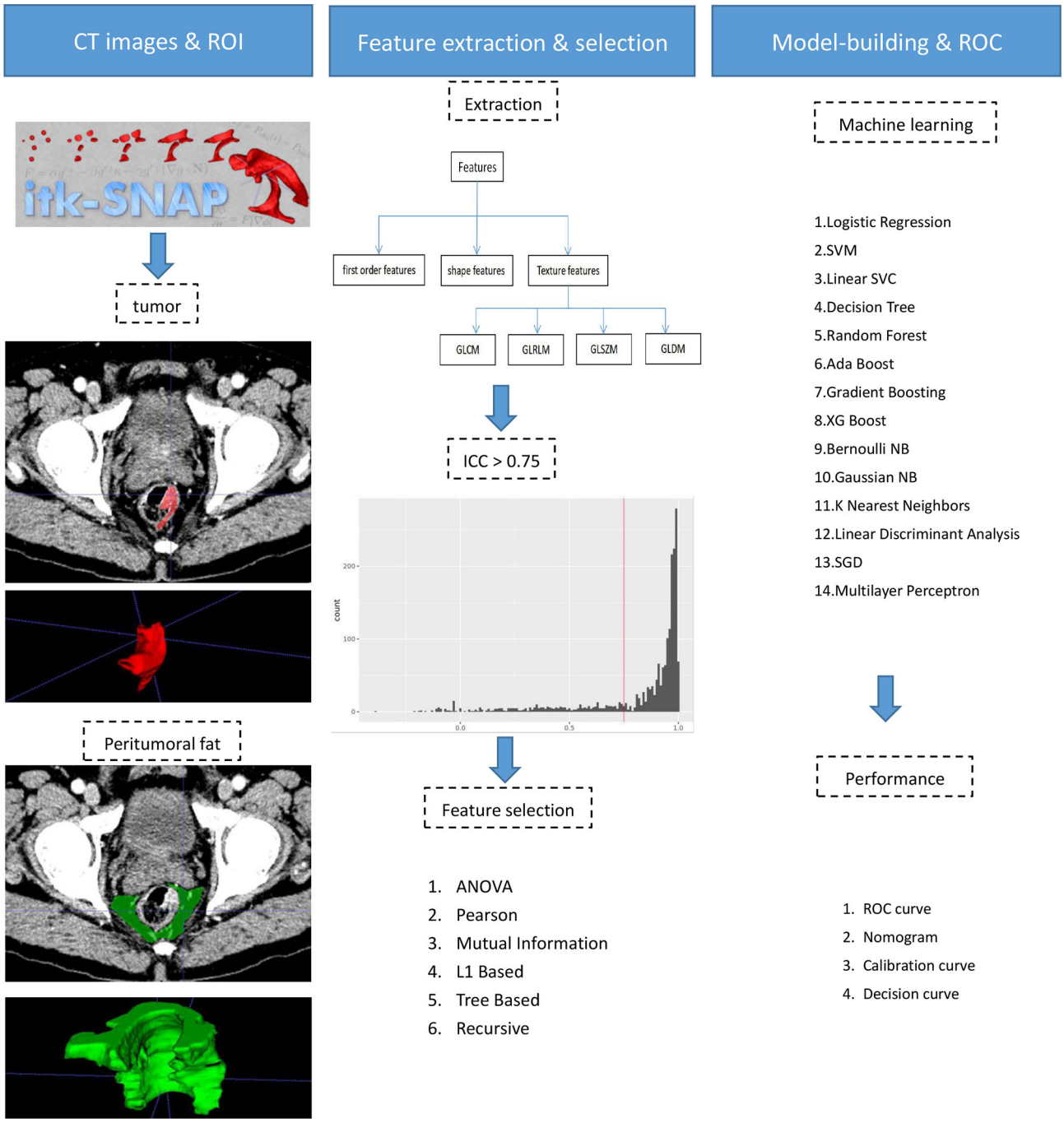

FIGURE 2 | Radiomics workflow.

obtained more benefit than "treat all", "treat none", Rad-score, and the clinical model, when the threshold probability was between 18% and 70%.

Model Comparisons

The AUCs of the clinical model were 0.773 (95%CI: 0.709-0.829) in the training cohort and 0.718 (95%CI: 0.575-0.835) in the validation cohort. Rad-score had similar AUCs with the clinical model (0.747, 95%CI: 0.681-0.805 and 0.717, 95%CI: 0.574-0.835). Improved predictive value was achieved by adding Rad-score to the clinical model. In detail, the AUCs of the combined model were higher than those of the clinical model in the training and validation cohorts (0.830 and 0.832; $P = 0.008$ and 0.039). As shown in **Table 3** and **Figure 5**.

TABLE 2 | Risk factors selected by the logistic regression analysis.

Variables	Univariate		Multivariate	
	OR	*P*-value	OR	*P*-value[1]
Age	0.996	0.745		
Gender	0.624	0.098		
Volume	1.000	0.918		
Location	2.216	**0.006**	0.677	0.267
cT stage	3.496	**<0.001**	2.281	**0.009**
Peritumoral nodules (+/-)	6.009	**<0.001**	4.485	**<0.001**
CEA	1.725	0.057		
CA19-9	2.928	**0.002**	2.253	**0.045**
CA125	2.779	0.098		
Rad-score	2.771	**<0.001**	2.378	**<0.001**

[1]*If P > 0.1, variables were excluded from the combined model. P values less than 0.05 are shown in bold.*

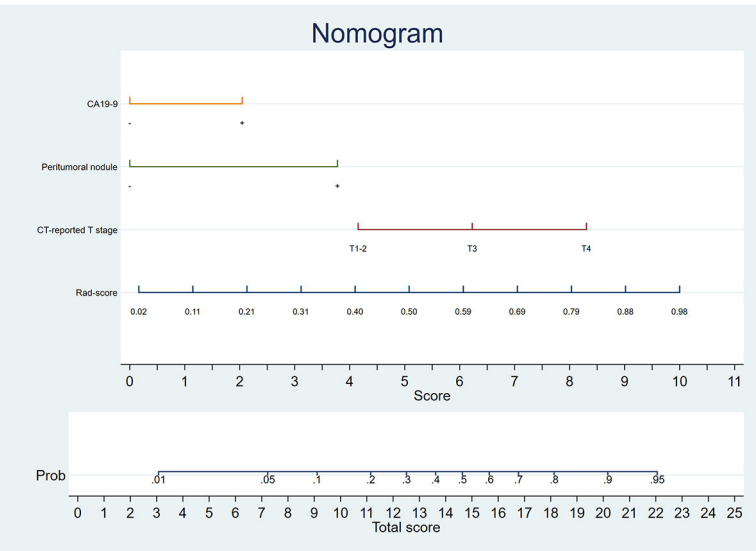

FIGURE 3 | Nomogram developed in the training cohort.

Subgroup Analyses

The results of subgroup analyses were listed in **Table 4**. In our study, there were 35 patients with N1c in the TDs$^+$ group. The values of the combined model were significantly different between the N1c group and the rest TDs$^+$ (n = 82) (0.55 ± 0.27 *vs* 0.69 ± 0.19, $P = 0.002$). However, the clinical model had no significant difference between them ($P = 0.113$). For differentiating N1c from TDs$^-$ patients, the combined model had an AUC of 0.741 (95%CI: 0.669-0.805), which was not significantly higher than that of the clinical model (0.711, 95% CI: 0.637-0.778; $P = 0.326$). In the rest TDs$^+$ group, the combined model outperformed the clinical model in identifying TDs$^+$ from TDs$^-$ patients (AUC = 0.864 *vs* 0.781, $P < 0.001$).

In TDs$^+$ group, there were 77 patients with 1-2 TDs and 40 patients with ≥ 3 TDs. The group with ≥ 3 TDs had higher values of both combined and clinical models than the 1-2 TDs group ($P = 0.015$ for combined model, and 0.08 for the clinical model). Moreover, the combined model outperformed the clinical model in both 1-2 and ≥ 3 TDs$^+$ groups when differentiating TDs$^+$ from TDs$^-$ patients (both $P = 0.005$).

The patients with peritumoral nodules on imaging were all classified as clinical stage III in this study. The combined model had moderate diagnostic performance (AUC = 0.771, 95%CI: 0.701-0.831) in the stage III patients. As for patients without peritumoral nodules on imaging, the combined model also showed moderate diagnostic performance with an AUC of 0.751. As for patients with different pathological T stages, the combined model had similar AUCs between the T1-2 and T3-4 groups (0.740 and 0.789).

DISCUSSION

In this study, a combined model incorporating Rad-score, CA19-9, cT, and peritumoral nodules (+/-) was established based on CT in a bigger cohort (compared with the previous studies),

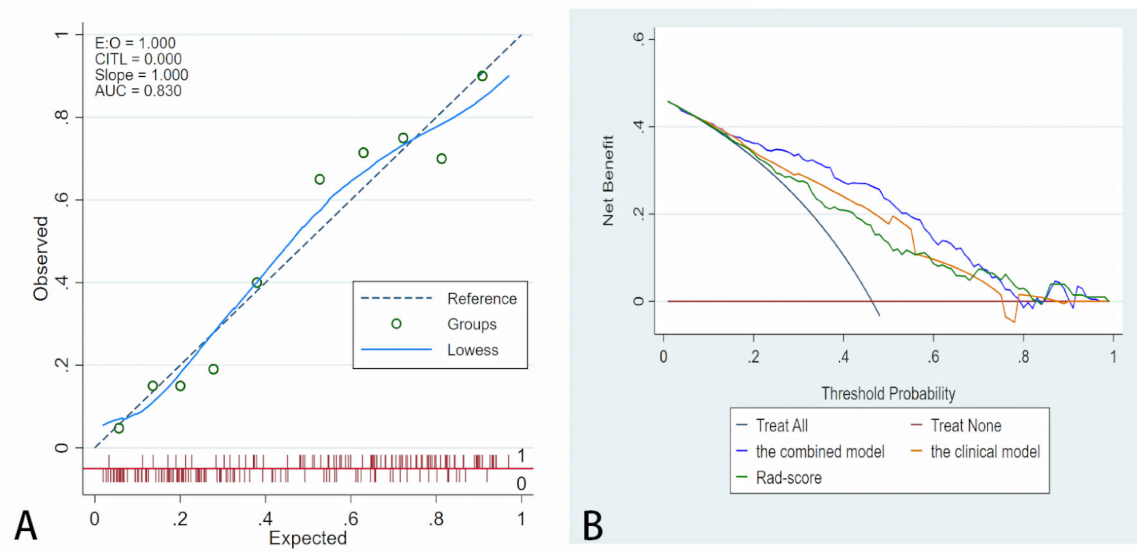

FIGURE 4 | Fit and usefulness evaluation of the nomogram. **(A)** Calibration curve of the nomogram. The calibration curve depicts the calibration of the model in terms of the agreement between the predicted risk of TDs (x axis) and observed outcomes of TDs (y axis). The blue solid line represents the performance of the nomogram (Note: a closer fit to the diagonal dotted line represents a better prediction). **(B)** The decision curve demonstrates that the model obtains more benefit than "treat all", "treat none", Rad-score, and the clinical model, when the threshold probability is in the range of 18% to 70%.

TABLE 3 | ROC analyses of the models in the training and validation cohorts.

Model	The training cohort			*P* value	The validation cohort			*P* value
	AUC	SEN (%)	SPE (%)		AUC	SEN	SPE	
Rad-score	0.747 (95%CI: 0.681-0.805)	77.7	59.6	**0.001**	0.717 (95%CI: 0.574-0.835)	91.3	60.7	0.054
Clinical model	0.773 (95%CI: 0.709-0.829)	80.9	63.3	**0.008**	0.718 (95%CI: 0.575-0.835)	82.6	60.7	**0.039**
Combined model	0.830 (95%CI: 0.771-0.879)	80.9	76.2		0.832 (95%CI: 0.701-0.922)	78.3	71.4	

P values: compared with the combined model. P values less than 0.05 are shown in bold.

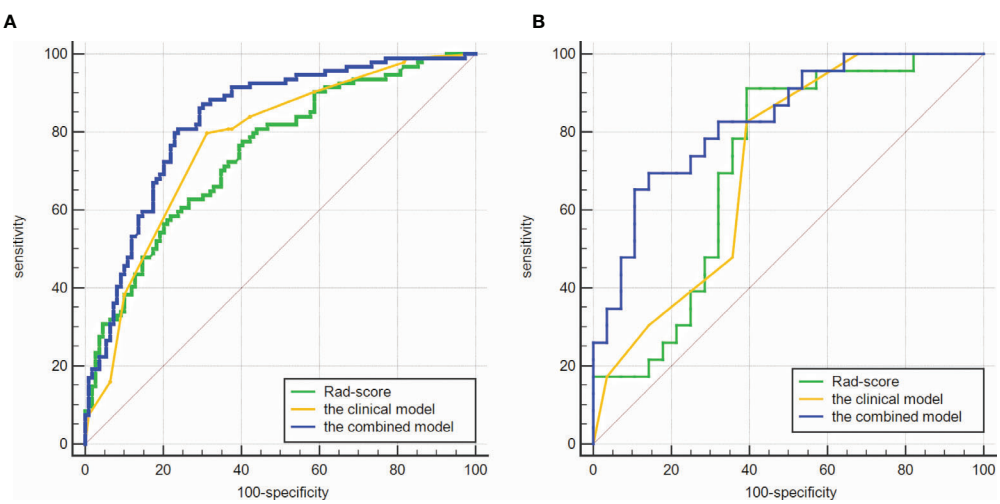

FIGURE 5 | Comparisons of ROC curves. **(A)** in the training cohort. **(B)** in the validation cohort. The combined models had higher AUCs (0.830 and 0.832) than the clinical model (0.773 and 0.718).

TABLE 4 | Subgroup analyses of the models in the whole cohort.

Subgroups	The clinical model				The combined model				*P*
	value	AUC	SEN	SPE	value	AUC	SEN	SPE	
TD+									
N1c (n = 35)	0.56 ± 0.21	0.711 (95%CI: 0.637-0.778)	74.3%	67.2%	0.55 ± 0.27	0.741 (95%CI: 0.669-0.805)	80.0%	59.9%	0.326
TDs^+ except N1c (n = 82)	0.62 ± 0.18	0.781 (95%CI: 0.721-0.834)	82.9%	67.2%	0.69 ± 0.19	0.864 (95%CI: 0.812-0.907)	87.8%	74.5%	**<0.001**
Number of TDs									
1-2 (n = 77)	0.58 ± 0.21	0.732 (95%CI: 0.668-0.790)	75.3%	67.2%	0.62 ± 0.24	0.800 (95%CI: 0.740-0.852)	84.4%	66.4%	**0.005**
≥3 (n = 40)	0.64 ± 0.16	0.814 (95%CI: 0.749-0.869)	90.0%	67.2%	0.72 ± 0.19	0.880(95%CI: 0.823-0.924)	90.0%	75.9%	**0.005**
Pathological T stage									
T1-2		0.519 (95%CI: 0.375-0.661)	57.1%	52.3%		0.740 (95%CI: 0.598-0.853)	57.1%	97.7%	**0.028**
T3-4		0.732 (95%CI: 0.665-0.791)	86.4%	55.9%		0.789(95%CI: 0.726-0.843)	80.9%	65.6%	**0.033**
Peritumoral nodules on CT									
+ (n = 176)		0.661 (95%CI: 0.586-0.730)	91.3%	38.4%		0.771 (95%CI: 0.701-0.831)	85.4%	57.5%	**0.003**
- (n = 78)		0.667 (95%CI: 0.552-0.770)	85.7%	42.2%		0.751 (95%CI: 0.640-0.842)	57.1%	82.8%	0.263
Clinical stage									
II (n = 49)		0.550 (95%CI: 0.401-0.692)	41.7%	73.0%		0.721 (95%CI: 0.574-0.839)	50.0%	89.2%	0.180
III (n = 176)		0.661 (95%CI: 0.586-0.730)	91.3%	38.4%		0.771 (95%CI: 0.701-0.831)	85.4%	57.5%	**0.003**

P value: comparison between the clinical model and combined model. P values less than 0.05 are shown in bold.

showing potential to predict TDs in RC. This combined model outperformed the clinical model in predicting TDs (AUC = 0.830 *vs* 0.773, $P = 0.008$ in the training cohort; 0.832 *vs* 0.718, $P = 0.039$ in the validation cohort), indicating that adding Rad-score to the clinical factors improved the predictive value.

TDs are an important prognostic factor in RC. A meta-analysis reported that a total of 21 included studies all found a significantly worse prognosis in patients with TDs (3). Goldstein et al. (18) found that when patients with differing numbers of LNM were assessed separately, those with TDs still demonstrated a worse prognosis. For example, with one positive node 5-year survival was 62% with no TDs detected *versus* 44% with TDs. When six or more LNs were involved 5-year survival was 16% without TDs *versus* 3% with TDs. This result strongly suggests that the effect of TDs on prognosis is separate from that of LNM. Thus, preoperative prediction of TDs is of great significance to assess the prognosis of patients with LNM or without LNM (N1c). The selection of treatment strategies mostly depends on cancer staging. According to the eighth edition of the AJCC TNM staging system, the presence of TDs without LNM causes patients to be classified as N1c, and these patients are staged as III. That is, once TDs are present, nCRT is recommended. If TDs status is absent pretherapeutically, the treatment plan may be misguided.

Traditional imaging techniques, such as CT, MRI, and US, that depend on the naked eye cannot reliably assess the condition of TDs. Recently, radiomics has appeared as a potent tool for constructing decision-support models. Researchers have started to use radiomics to predict TDs in RC. Chen et al. (11) developed a ultrasound radiomics model with an AUC of 0.795 in a cohort of 127 patients (TDs^+: n = 40). Yang et al. (12) established a MRI-based radiomics model in 139 RC patients (TDs^+: n = 23), which had an AUC of 0.820. Our results showed a comparable AUC with the previous studies in a bigger cohort (254 patients; TDs^+: n = 117). We included T stage in the combined model, which was consistent with Yang et al. (12). Different from Yang et al. (12) [two-dimensional (2D) region of interest (ROI)], we established the model based on 3D ROI, namely VOI. 2D ROI did not cover the whole lesion, and thus some information of tumor heterogeneity may be lost.

In this study, "peritumoral nodule" was defined as any nodule (diameter > 3 mm) within the lymphatic drainage space of RC, involving LNM and TDs. The CT-reported factors (i.e., cT and peritumoral nodule) were reviewed by two experienced radiologists, and thus reliable data were acquired. The volume in the TDs^+ group was larger than that of the TDs^- group (median: 15.1 *vs* 12.0 cm^3), which was consistent with the conclusion of Wei et al. (19). Although elevated CEA was found in the TDs^+ group, CEA was not included in the combined model. Peritumoral features accounted for the majority of features in Rad-score (10/13, 76.9%), suggesting the important role of environment around the rectum in the formation of TDs (20).

Although AJCC has not correlated a higher number of TDs with staging, which is unlike LNs (e.g., N1: 1 to 3 regional LNs, N2: ≥ 4 regional LNs) (8). Several authors have found a significant relationship between an increasing number and worsening of prognosis (18, 21, 22). For example, in patients with ≥ 3 TDs, none was alive at 5-year follow up. It is worthy of note that this is significantly worse than patients who had similar number of LNM (in fact even those with ≥ 6 positive LNs had a 5-year survival of 11%). In our study, the group with ≥ 3 TDs had higher value of the combined model than the 1-2 TDs group ($P = 0.015$), indicating that the combined model was helpful for predicting the number of TDs. Moreover, the N1c group had lower value of the combined model than the rest TDs^+ group ($P = 0.002$), suggesting possibility of the combined model for predicting N1c. In the future, a large multicenter study is certainly needed to confirm these observations.

The patients with peritumoral nodules on imaging were all classified as clinical stage III in this study. The combined model had moderate diagnostic performance in the stage II and III patients, indicating the good stability of the model. There were 78 patients without peritumoral nodules on imaging, in which 14 patients were TDs^+. Because of the small sample size, the

diagnostic performance of the combined model (AUC = 0.751) was not accurate here. More cases are needed to verify this result.

Our study had several limitations. First, the selection bias existed due to the retrospective design. Second, prospective and external validation was not performed. Third, because it is impossible to achieve one-to-one correspondence between pathological and radiological peritumoral nodules in this study, we delineated the whole peritumoral area in the lymphatic drainage space of RC. Finally, we excluded nodules with diameter < 3 mm on imaging, while there was still a risk of TDs in these small nodules (23).

In conclusion, the CT-based radiomics model is helpful for the preoperative prediction of TDs in RC patients.

DATA AVAILABILITY STATEMENT

The original contributions presented in the study are included in the article/**Supplementary Material**. Further inquiries can be directed to the corresponding authors.

ETHICS STATEMENT

The studies involving human participants were reviewed and approved by West China Hospital of Sichuan University Biomedical Research Ethics Committee. Written informed consent for participation was not required for this study in accordance with the national legislation and the institutional requirements.

AUTHOR CONTRIBUTIONS

BS and MW conceived of the presented idea. YJ and SML collected the data. ML, YZ, and CH analyzed the data. ML drafted the manuscript. SYL improved the quality of English. All authors contributed to the article and approved the submitted version.

SUPPLEMENTARY MATERIAL

The Supplementary Material for this article can be found online at: https://www.frontiersin.org/articles/10.3389/fonc.2021.710248/full#supplementary-material

REFERENCES

1. Mattiuzzi C, Sanchis-Gomar F, Lippi G. Concise Update on Colorectal Cancer Epidemiology. *Ann Transl Med* (2019) 7(21):609. doi: 10.21037/atm.2019.07.91
2. Bray F, Ferlay J, Soerjomataram I, Siegel RL, Torre LA, Jemal A. Global Cancer Statistics 2018: GLOBOCAN Estimates of Incidence and Mortality Worldwide for 36 Cancers in 185 Countries. *CA Cancer J Clin* (2018) 68 (6):394–424. doi: 10.3322/caac.21492
3. Lord AC, D'Souza N, Pucher PH, Moran BJ, Abulafi AM, Wotherspoon A, et al. Significance of Extranodal Tumour Deposits in Colorectal Cancer: A Systematic Review and Meta-Analysis. *Eur J Cancer* (2017) 82:92–102. doi: 10.1016/j.ejca.2017.05.027
4. Lin Q, Wei Y, Ren L, Zhong Y, Qin C, Zheng P, et al. Tumor Deposit is a Poor Prognostic Indicator in Patients Who Underwent Simultaneous Resection for Synchronous Colorectal Liver Metastases. *Onco Targets Ther* (2015) 8:233–40. doi: 10.2147/OTT.S71414
5. Ueno H, Hashiguchi Y, Shimazaki H, Shinto E, Kajiwara Y, Nakanishi K, et al. Peritumoral Deposits as an Adverse Prognostic Indicator of Colorectal Cancer. *Am J Surg* (2014) 207(1):70–7. doi: 10.1016/j.amjsurg.2013.04.009
6. Washington MK, Berlin J, Branton P, Burgart LJ, Carter DK, Fitzgibbons PL, et al. Members of the Cancer Committee, College of American Pathologists. Protocol for the Examination of Specimens From Patients With Primary Carcinoma of the Colon and Rectum. *Arch Pathol Lab Med* (2009) 133 (10):1539–51. doi: 10.1043/1543-2165-133.10.1539
7. Pricolo VE, Steingrimsson J, McDuffie TJ, McHale JM, McMillen B, Shparber M. Tumor Deposits in Stage III Colon Cancer: Correlation With Other Histopathologic Variables, Prognostic Value, and Risk Stratification-Time to Consider "N2c". *Am J Clin Oncol* (2020) 43(2):133–8. doi: 10.1097/COC.0000000000000645
8. Amin MB, Greene FL, Edge SB, Compton CC, Gershenwald JE, Brookland RK, et al. The Eighth Edition AJCC Cancer Staging Manual: Continuing to Build a Bridge From a Population-Based to a More "Personalized" Approach to Cancer Staging. *CA Cancer J Clin* (2017) 67(2):93–9. doi: 10.3322/caac.21388
9. Hoshino N, Murakami K, Hida K, Sakamoto T, Sakai Y. Diagnostic Accuracy of Magnetic Resonance Imaging and Computed Tomography for Lateral Lymph Node Metastasis in Rectal Cancer: A Systematic Review and Meta-Analysis. *Int J Clin Oncol* (2019) 24(1):46–52. doi: 10.1007/s10147-018-1349-5
10. Li XT, Sun YS, Tang L, Cao K, Zhang XY. Evaluating Local Lymph Node Metastasis With Magnetic Resonance Imaging, Endoluminal Ultrasound and Computed Tomography in Rectal Cancer: A Meta-Analysis. *Colorectal Dis* (2015) 17(6):O129–35. doi: 10.1111/codi.12909
11. Chen LD, Li W, Xian MF, Zheng X, Lin Y, Liu BX, et al. Preoperative Prediction of Tumour Deposits in Rectal Cancer by an Artificial Neural Network-Based US Radiomics Model. *Eur Radiol* (2020) 30(4):1969–79. doi: 10.1007/s00330-019-06558-1
12. Yang YS, Feng F, Qiu YJ, Zheng GH, Ge YQ, Wang YT. High-Resolution MRI-Based Radiomics Analysis to Predict Lymph Node Metastasis and Tumor Deposits Respectively in Rectal Cancer. *Abdom Radiol (NY)* (2021) 46(3):873–84. doi: 10.1007/s00261-020-02733-x
13. Benchoufi M, Matzner-Lober E, Molinari N, Jannot AS, Soyer P. Interobserver Agreement Issues in Radiology. *Diagn Interv Imaging* (2020) 101(10):639–41. doi: 10.1016/j.diii.2020.09.001
14. van Griethuysen JJM, Fedorov A, Parmar C, Hosny A, Aucoin N, Narayan V, et al. Computational Radiomics System to Decode the Radiographic Phenotype. *Cancer Res* (2017) 77(21):e104–7. doi: 10.1158/0008-5472.CAN-17-0339
15. Alba AC, Agoritsas T, Walsh M, Hanna S, Iorio A, Devereaux PJ, et al. Discrimination and Calibration of Clinical Prediction Models: Users' Guides to the Medical Literature. *JAMA* (2017) 318(14):1377–84. doi: 10.1001/jama.2017.12126
16. Vickers AJ, Elkin EB. Decision Curve Analysis: A Novel Method for Evaluating Prediction Models. *Med Decis Making* (2006) 26(6):565–74. doi: 10.1177/0272989X06295361
17. Roldán-Nofuentes JA, Amro RM. Combination of the Weighted Kappa Coefficients of Two Binary Diagnostic Tests. *J Biopharm Stat* (2018) 28 (5):909–26. doi: 10.1080/10543406.2017.1402781
18. Goldstein NS, Turner JR. Pericolonic Tumor Deposits in Patients With T3N +MO Colon Adenocarcinomas: Markers of Reduced Disease Free Survival and Intra-Abdominal Metastases and Their Implications for TNM Classification. *Cancer* (2000) 88(10):2228–38. doi: 10.1002/(sici)1097-0142(20000515)88:10<2228::aid-cncr5>3.0.co;2-1
19. Wei XL, Qiu MZ, Zhou YX, He MM, Luo HY, Wang FH, et al. The Clinicopathologic Relevance and Prognostic Value of Tumor Deposits and the Applicability of N1c Category in Rectal Cancer With Preoperative Radiotherapy. *Oncotarget* (2016) 7(46):75094–103. doi: 10.18632/oncotarget.12058
20. Nagtegaal ID, Knijn N, Hugen N, Marshall HC, Sugihara K, Tot T, et al. Tumor Deposits in Colorectal Cancer: Improving the Value of Modern

Staging-A Systematic Review and Meta-Analysis. *J Clin Oncol* (2017) 35 (10):1119–27. doi: 10.1200/JCO.2016.68.9091
21. Puppa G, Maisonneuve P, Sonzogni A, Masullo M, Capelli P, Chilosi M, et al. Pathological Assessment of Pericolonic Tumor Deposits in Advanced Colonic Carcinoma: Relevance to Prognosis and Tumor Staging. *Mod Pathol* (2007) 20 (8):843–55. doi: 10.1038/modpathol.3800791
22. Shimada Y, Takii Y. Clinical Impact of Mesorectal Extranodal Cancer Tissue in Rectal Cancer: Detailed Pathological Assessment Using Whole-Mount Sections. *Dis Colon Rectum* (2010) 53(5):771–8. doi: 10.1007/DCR.0b013e3181cf7fd8
23. Horne J, Bateman AC, Carr NJ, Ryder I. Lymph Node Revealing Solutions in Colorectal Cancer: Should They be Used Routinely? *J Clin Pathol* (2014) 67 (5):383–8. doi: 10.1136/jclinpath-2013-202146

Conflict of Interest: Authors YZ and CH were employed by the company Beijing Deepwise & League of PHD Technology Co., Ltd. Author SYL was employed by the company GE Healthcare (Beijing).

The remaining authors declare that the research was conducted in the absence of any commercial or financial relationships that could be construed as a potential conflict of interest.

Publisher's Note: All claims expressed in this article are solely those of the authors and do not necessarily represent those of their affiliated organizations, or those of the publisher, the editors and the reviewers. Any product that may be evaluated in this article, or claim that may be made by its manufacturer, is not guaranteed or endorsed by the publisher.

frontiers in Oncology

REVIEW
published: 11 November 2021
doi: 10.3389/fonc.2021.758958

Fibroblast-Activated Protein Inhibitor PET/CT: Cancer Diagnosis and Management

Serkan Kuyumcu[1], *Yasemin Sanli*[1] *and Rathan M. Subramaniam*[2,3]*

[1] Department of Nuclear Medicine, Istanbul Faculty of Medicine, Istanbul University, Istanbul, Turkey, [2] Otago Medical School, University of Otago, Dunedin, New Zealand, [3] Department of Radiology, Duke University, Durham, NC, United States

Fibroblast activation protein (FAP), overexpressed on cancer-associated fibroblasts (CAFs), is a novel target for molecular imaging of various tumors. Recently, the development of several small-molecule FAP inhibitors for radiolabeling with ^{68}Ga has resulted in the emergence of studies evaluating its clinical role in cancer imaging. Preliminary findings have demonstrated that, in contrast to radiotracers taking advantage of cancer-specific targets such as PSMA and DOTATATE, FAPs as a target are the most promising that can compete with ^{18}FDG in terms of widespread indications. They also have the potential to overcome the shortcomings of ^{18}FDG, particularly false-positive uptake due to inflammatory or infectious processes, low sensitivity in certain cancer types, and radiotherapy planning. In addition, the attractive theranostic properties may facilitate the treatment of many refractory cancers. This review summarizes the current FAP variants and related clinical studies, focusing on radiopharmacy, dosimetry, and diagnostic and theranostic applications.

Keywords: PET, cancer-associated fibroblast, fibroblast activation protein, theranostic, 68Ga-FAPI04, FAPI

OPEN ACCESS

Edited by:
Vikas Prasad,
Universitätsklinikum Ulm, Germany

Reviewed by:
Francesco Ceci,
Università di Torino, Italy
Murat Fani Bozkurt,
Hacettepe University, Turkey

***Correspondence:**
Rathan M. Subramaniam
rathan.subramaniam@otago.ac.nz

Specialty section:
This article was submitted to Cancer Imaging and Image-directed Interventions, a section of the journal Frontiers in Oncology

Received: *15 August 2021*
Accepted: *18 October 2021*
Published: *11 November 2021*

Citation:
Kuyumcu S, Sanli Y and Subramaniam RM (2021) Fibroblast-Activated Protein Inhibitor PET/CT: Cancer Diagnosis and Management. Front. Oncol. 11:758958. doi: 10.3389/fonc.2021.758958

INTRODUCTION

Historically, cancer imaging has focused on morphological anatomy, as opposed to molecular imaging, which targets physiological activity in a specific tissue by utilizing modalities that use certain probes to overcome the poorly reflected biology of cancer by anatomical imaging. In this regard, the association between glycolysis and cancer cell metabolism has well been translated into PET imaging in cancer, and ^{18}F-FDG PET/CT has revolutionized cancer imaging and gained widespread acceptance for managing various malignancies. More than 40 years of success of ^{18}F-FDG has also led to the successful integration of specific radiotracers such as ^{68}Ga-labeled somatostatin analogs and prostate-specific membrane antigens (PSMA) into clinical practice (1) in the last decade, resulting in an exponentially decreasing timeframe for widespread acceptance. Similarly, the recent emergence of radiolabeled fibroblast activation protein (FAP) inhibitors (FAPI) with pan-cancer targeting features hints at relatively rapid adoption. FAPs are overexpressed by cancer-associated fibroblasts (CAFs) found in the tumor stroma of various cancers, and several radiolabeled FAPI variants have already been introduced as promising targets for PET/CT imaging (2–6). The excellent imaging contrast, low activity in normal organs, and theranostic potential are encouraging; however, activated fibroblasts in benign conditions with inflammatory and wound-

healing processes can also express FAPs. This review summarizes the pathophysiology of FAPs and clinical implications of FAP-targeted PET/CT data in malignant diseases focusing on radiopharmaceuticals and dosimetry. In this regard, a search of PubMed, MEDLINE, and Scopus databases with one or more combinations of the following terms: "FAPI", "FAPI PET", "cancer-associated fibroblast", "fibroblast activation protein", and "fibroblast activation protein inhibitor" was performed. All papers in English were evaluated and were included if they fell within the scope of this review.

PHYSIOLOGY AND PATHOLOGY

FAP is a type II transmembrane serine protease expressed in activated tumor stroma and inflamed tissues during wound healing (7). Overexpression has been seen in most epithelial cancers, especially in tumors with a high degree of desmoplasia (8). FAP is not overexpressed by tumor cells themselves; it is overexpressed by CAFs that are responsible for tumor growth, aggressiveness, and migration, which consist of a high tumor volume within the tumor stroma (9); thus, a high expression of FAP on CAFs may be considered a factor of aggressiveness of tumor behavior and poor prognostication (10). The tumor microenvironment (TME) plays a crucial role in the survival, proliferation, and spread of tumor cells (11). FAP is overexpressed on the cancer-related fibroblast cell membrane and TME stromal cells. On the other hand, FAP is barely expressed in healthy adult tissues, except uterine stroma, particularly in the proliferative phase, pancreatic alpha cells, human placenta, and some dermal fibroblasts (12). Because of minimal expression in normal tissue, labeled FAP *via* radiopharmaceuticals is seen as a promising target in diagnosis as well as therapy in oncology (13).

RADIOPHARMACEUTICALS AND DOSIMETRY

It has been over 30 years since Garin-Chesa et al. proposed the surface glycoprotein of reactive stromal fibroblasts as potential antibody targets in human epithelial cancer (14). Consecutive attempts for imaging FAPs (15) acknowledged the disadvantages and challenges of the initial compounds, leading to the introduction of small-molecule FAP inhibitors with more favorable characteristics, particularly increased selectivity and affinity (16, 17). The preliminary human applications using the early FAP inhibitor, namely FAPI02, demonstrated high tumor specificity but declining uptake over time. Consequently, Lindner et al. (18) evaluated a group of novel tracers derived from FAPI02 to improve tumor uptake and retention and accordingly proposed FAPI04 as a more suitable tracer with the potential for theranostic applications. A dosimetry study including 50 patients with various cancers by Giesel et al. also confirmed the higher tumor retention time of ^{68}Ga-FAPI04 than ^{68}Ga-FAPI02. The estimated effective doses for ^{68}Ga-FAPI04 and ^{68}Ga-FAPI02 PET/CT were reported as 1.80E−2 mSv/MBq and 1.64E−2 mSv/MBq, respectively, which is similar to that of clinically established PET imaging procedures. These values are comparable or lower than the effective dose of PET/CT imaging with ^{18}F-FDG (1.9E−2 mSv/MBq) (19), ^{68}Ga-labeled somatostatin analogs (2.1E−2 mSv/MBq) (20), and ^{68}Ga-PSMA (1.71E−2–2.3E−2 mSv/MBq) (21).

Further research on FAPI molecules has been conducted to improve the therapeutic efficacy through higher-dose delivery. Higher tumor-to-organ/blood ratios achieved with FAPI21 and FAPI46, as reported by Loktev et al. (3), were promising; however, due to increased uptake of FAPI21 in the oral mucosa, thyroid, and salivary glands, FAPI46 was presumed more favorable. Accordingly, clinical imaging studies with ^{68}Ga-FAPI46 in a cohort of 69 patients by Ferdinandus et al. (22) and six patients by Koerber et al. (20) have demonstrated encouraging results. Another novel FAP inhibitor with a different structure based on the squaric acid motif, DOTA.SA.FAPi has also been introduced (23). Human studies also confirmed high target-to-background ratios achieved with colorectal cancer xenograft mouse model in a cohort of 54 patients (24). The mean effective dose equivalent was 1.64E−2 mSv/MBq, similar to other FAPI PET studies.

Most FAP inhibitors have been labeled using the DOTA derivatives; nevertheless, NOTA chelators have also been studied. A FAP inhibitor, FAPI74, which allows labeling with ^{18}F and ^{68}Ga, has also been studied in a cohort of 10 patients (4). High contrast imaging and low radiation burden using ^{18}F-FAPI74 were reported (effective dose rate of 1.4E−2 mSv/MBq). Wang et al. (6) also introduced a NOTA-FAPI, Al^{18}F-NOTA-FAPI, with comparable affinity with several other FAPI probes. They reported successful imaging of 10 cancer patients and calculated the whole-body effective dose of 1.24E−02 mSv/MBq. Another FAPI molecule that allows ^{18}F labeling is the glycosylated FAP inhibitor (^{18}FFGlc-FAPI). Toms et al. (25) evaluated ^{18}FFGlc-FAPI in the preclinical setting and proposed it as a candidate that can take advantage of extended PET imaging provided by the longer physical half-life of ^{18}F and higher tumor retention of Glc-FAPI. The only non-PET radiotracer is reported by Linder et al. (23). The authors have studied novel FAPI variants for labeling using the theranostic pair, ^{99m}Tc, and ^{188}Re. FAPI34 was labeled with ^{99m}Tc, and SPECT scans of two patients were comparable with PET imaging with ^{68}Ga-FAPI46.

Despite the enthusiasm that FAPI agents have gained in cancer imaging, the experience on targeted radionuclide applications is mainly restricted to a small number of cases. Thus, data on effective dose rates for therapeutic radionuclides is far limited. In the clinical setting, two metastatic breast cancer patients tolerated treatments very well with ^{177}Lu-DOTA.SA.FAPi (26) and ^{90}Y-FAPI04[18], and preliminary results indicated that the treatment was safe. Linder et al. (23) and Kratochwil et al. (27) have treated two patients with ^{90}Y-FAPI46 and one with ^{153}Sm-FAPI46; however, no dosimetric results were reported. Despite the preliminary patient reports on FAP-targeted radionuclide treatments, the data on dosimetry of

normal organs is still lacking. Recently, Kuyumcu et al. (28) reported estimated radiation-absorbed doses to normal organs using low-dose ^{177}Lu-FAPI04. The estimated radiation dose to critical organs was significantly low compared with clinically established targeted radionuclide therapies, particularly ^{177}Lu-DOTATATE and ^{177}Lu-PSMA. Bone marrow was the dose-limiting organ, and the authors concluded that up to 50 GBq of cumulative activity could be tolerated. These results are expected regarding the high image contrast; however, the relatively short tumor retention time requires dose increase to achieve tumoricidal effects. Therefore, further research is necessary to optimize the therapeutic efficacy and determine the safety of high-dose radionuclide treatments. Baum et al. (29) reported comparable estimated radiation dose to critical organs using ^{177}Lu-labeled FAP-2286; however, a higher radiation dose to tumoral lesions was achieved, justifying further investigation.

FIBROBLAST ACTIVATION PROTEIN-TARGETED IMAGING IN ONCOLOGY

Early clinical trials have evaluated patient groups with various cancers. In 2018, the first PET imaging of FAPs in three patients was reported by Loktev et al. (30) as a proof-of-concept study. Tracer uptake with a high tumor-to-background ratio was noted in breast, lung, and pancreatic cancers. Consequently, Kratochwil et al. (31) from the same team reported the remarkable ^{68}Ga-FAPI PET/CT results of 80 cancer patients with 28 different tumor types. The uptake values highly varied between different tumor types as well as individuals. The highest uptake of ^{68}Ga-FAPI (SUV_{max} >12) was detected in sarcoma, esophageal, breast, cholangiocarcinoma, and lung cancer patients, while pheochromocytoma, renal cell, differentiated thyroid, and gastric cancers were the lowest (SUV_{max} <6). The low background activity resulted in excellent image contrast despite the intratumoral and interindividual variability even with low tumor activity. In a preliminary study, Giesel et al. (2) evaluated different FAPI variants in a cohort of 50 cancer patients. Similarly, high ^{68}Ga-FAPI uptake was observed in esophageal, pancreatic, head and neck, nonsmall cell lung, and colon cancers in contrast to low or no uptake in dedifferentiated thyroid cancer. The authors have demonstrated the first comparative evaluation of ^{68}Ga-FAPI PET/CT imaging with ^{18}FDG PET/CT in six patients as distinct from other preliminary studies.

Chen et al. (32) compared ^{68}Ga-FAPI04 PET/CT with ^{18}FDG PET/CT in a larger cohort of 75 patients. ^{68}Ga-FAPI04 PET/CT was superior to ^{18}FDG PET/CT in newly diagnosed 54 patients with 12 tumor types. Similarly, ^{68}Ga-FAPI04 was superior in 21 patients with eight cancer types who underwent PET/CT for restaging. The uptake of ^{68}Ga-FAPI04 was significantly higher and resulted in high contrast images with the highest uptake in sarcoma, pancreatic, liver, and esophageal cancers. Ten patients with high FAPI04 uptake were negative on ^{18}FDG PET/CT, particularly hepatocellular, gastric, and pancreatic cancers. The sensitivity of ^{68}Ga-FAPI04 PET/CT was significantly higher than ^{18}FDG in detecting bone, visceral, and lymph node metastases; however, the specificity was lower. Therefore, false positivity also applies to ^{68}Ga-FAPI04 as a potential diagnostic pitfall and requires careful evaluation. However, ^{68}Ga-FAPI04 PET/CT outperformed ^{18}FDG PET/CT in patients with liver metastasis and peritoneal carcinomatosis. Another comparative study by Chen et al. (33) evaluated 68 cancer patients with inconclusive ^{18}FDG-PET/CT findings. Fifty-nine of the patients had histopathologically confirmed malignant disease, and most of the FDG-negative or inconclusive patients, mainly gastric and liver cancers, presented significantly increased 68Ga-FAPI04 uptake. Higher uptake was also noted with peritoneal carcinomatosis, liver, and skeletal metastases. On the other hand, despite high ^{18}FDG uptake in the metastatic brain lesions, the tumor-to-background ratio on ^{68}Ga-FAPI04 PET/CT was higher due to lack of background activity. The authors have highlighted the complementary role of ^{68}Ga-FAPI04 imaging in patients with inconclusive ^{18}FDG PET/CT findings.

The encouraging results of studies investigating various cancers have led to the emergence of ^{68}Ga-FAPI PET studies in specific cancer types. Head and neck cancers are among the most investigated cancers as a target of FAP-directed PET imaging. In a cohort of 45 patients with nasopharyngeal cancers, ^{68}Ga-FAPI04 PET/CT was superior to ^{18}FDG PET/CT in detecting primary tumors, lymph nodes, and metastatic disease, resulting in management changes in 18% of the patients (34). Qin et al. (35) compared ^{68}Ga-FAPI04 with ^{18}FDG PET/MR in 15 patients with nasopharyngeal carcinoma. ^{68}Ga-FAPI04 uptake in the primary tumors was lower than ^{18}FDG uptake, although not statistically different. On the other hand, lower ^{68}Ga-FAPI04 uptake in the metastatic lymph nodes was statistically significant; however, ^{68}Ga-FAPI04 imaging outperformed ^{18}FDG in detecting unknown distant metastases and improved primary tumor delineation for differentiation of skull-base and intracranial invasion. Another study (36) evaluated 14 patients with head and neck cancers and compared ^{68}Ga-FAPI04 PET/CT with ^{18}FDG-PET/CT for differentiating between healthy and tumor tissue. In a cohort of 12 patients with adenoid cystic carcinomas, Röhrich et al. (37) reported that ^{68}Ga-FAPI PET/CT increased staging accuracy. ^{68}Ga-FAPI04 PET/CT was also proposed as a feasible imaging method in 10 patients with oral squamous cell carcinoma by Linz et al. (38), although they did not reach a firm conclusion.

Another cancer group of interest for FAP-targeted imaging is the gastrointestinal malignancies. The advantages of ^{68}Ga-FAPI04 over ^{18}F-FDG PET/CT in the imaging of esophageal cancer were reported as single-case studies (39, 40) and two small cohort studies which investigated the potential of ^{68}Ga-FAPI04 PET/CT on target volume delineation for radiotherapy planning. Overexpression of FAPs in gastric carcinomas has also been demonstrated (41–43). Quin et al. investigated 20 gastric cancer patients and described the superiority of ^{68}Ga-FAPI04 PET/MR over ^{18}F-FDG PET/CT in visualizing the primary tumors and most metastatic lesions (44). Pang et al. (45) evaluated ^{68}Ga-FAPI04 PET/CT of 20 patients with gastric carcinoma and reported higher detection rates and mean SUV_{max} than 18FDG

PET/CT. The authors have also evaluated patients with duodenal (n = 2) and colorectal cancers (n = 13). The duodenal adenocarcinomas were ^{18}FDG negative and demonstrated ^{68}Ga-FAPI04 uptake. On the other hand, ^{68}Ga-FAPI04 and ^{18}FDG PET/CT detected all primary lesions in colorectal cancer patients; however, significantly higher SUV_{max} and higher tumor-to-background contrast resulted in more precise tumor delineation. In an investigation into lower gastrointestinal tract tumors, Koerber et al. (20) evaluated the role of FAPI PET/CT in colon, sigmoid, rectal, and anal cancers. The authors concluded that primary and metastatic tumors could be accurately detected by ^{68}Ga-FAPI PET/CT changing TNM status and disease management. Peritoneal carcinomatosis patients (n = 46) were evaluated by Zhao et al. (46), and the authors reported sensitivity of ^{68}Ga-FAPI04 PET/CT superior to ^{18}F-FDG PET/CT in detecting diffuse or nodular type disease. They also noted that significantly higher tracer uptake was mainly observed in peritoneal carcinomatosis from gastric cancer.

The characteristics of FDG uptake in primary liver malignancies are unpredictable, particularly in hepatocellular carcinoma (HCC) due to factors such as low metabolism and physiological liver activity (47). In a cohort of 17 patients, Shi et al. reported higher ^{68}Ga-FAPI04 uptake in malignant liver nodules than in benign nodules (48). The authors have also evaluated hepatocellular carcinoma (n = 14) and intrahepatic cholangiocarcinoma (n = 3) patients in another study (49) and concluded the superiority of ^{68}Ga-FAPI04 PET/CT over ^{18}F-FDG PET/CT in the detection of primary hepatic malignancies. Guo et al. (50) confirmed the superiority of ^{68}Ga-FAPI04 PET/CT in 20 patients with hepatocellular carcinoma and 12 patients with intracellular cholangiocarcinoma with a sensitivity equivalent to that of contrast-enhanced CT and MRI. They also reported two patients with benign nodules that were ^{68}Ga-FAPI negative and highlighted its potential in differentiating benign from malignant lesions. Similarly, the ability of dynamic ^{68}Ga-FAPI04 PET/CT in differentiating HCC from non-HCC lesions has also been demonstrated in a brief report (51). ^{68}Ga-FAPI04 PET/CT was compared with contrast-enhanced CT in 19 pancreatic ductal adenocarcinoma patients, and ^{68}Ga-FAPI04 PET/CT results changed TNM staging in 10 patients. However, the authors have noted challenges of differentiating pancreatitis from adenocarcinoma (52). In another study, Liermann et al. (53) compared ^{68}Ga-FAPI04 PET/CT with ceCT in seven recurrent pancreatic patients for radiotherapy planning. However, both studies did not use ^{18}F-FDG PET/CT for comparison.

In a study by Komek et al. (54), the authors compared the ^{68}Ga-FAPI04 with ^{18}F-FDG PET/CT of 20 breast cancer patients and concluded that ^{68}Ga-FAPI04 was superior to ^{18}F-FDG in detecting the primary tumor and the metastatic lesions with high sensitivity and tumor-to-background ratio. In a study by Dendl et al. (55), investigating patients with various gynecological malignancies, 14 patients had breast cancer, and the authors have reported strong to moderate FAP expression in the stroma of breast carcinomas. FAP expression in ovarian (n = 9), cervical (n = 4), endometrial (n = 2), and tubal cancers (n = 1) in addition to one patient with uterine leiomyosarcoma was also investigated. High tracer uptake and low background activity in gynecological tumors resulted in excellent image contrast compared with ^{18}F-FDG, and the authors recommended further research on clinical applications.

Koerber et al. (56) evaluated the role of ^{68}Ga-FAPI imaging in a cohort of 15 patients diagnosed with various sarcoma subtypes. The excellent tumor-to-background ratio was achieved in primary tumors and metastases, including low-grade sarcomas, where ^{18}F-FDG PET/CT has limitations. Accordingly, ^{68}Ga-FAPI PET/CT was highlighted as a promising probe with the potential for the theranostic approach. Kessler et al. (57) evaluated 47 patients with bone or soft tissue sarcomas and measured a significant association between tracer uptake and histopathological FAP expression. High sensitivity and PPV of FAPI PET resulted in upstaging in eight (13%) patients and management change in 13 (30%) patients compared with FDG-PET.

^{18}F-FDG PET/CT has a limited role in diagnosing malignant brain tumors and is particularly useful in distinguishing recurrent tumors from radiation necrosis. On the other hand, lack of background activity in FAP-targeted imaging provides high image contrast, and this advantage over FDG PET has been addressed in various reports, particularly for brain metastases. Regarding primary brain tumors, two studies have evaluated FAP-targeted imaging for glioblastomas. Windisch et al. (58) has studied 14 glioblastoma patients in the setting of radiotherapy planning. A diagnostic study by Rohrich et al. (59) in 18 glioma patients evaluated FAP-specific imaging as a promising new tool to differentiate between low-grade and high-grade diseases. In this regard, PET imaging of FAPs may potentially be used as a noninvasive probe for predicting malignant progression of IDH-mutant WHO grade II gliomas to grades III and IV over time, which may have severe therapeutic consequences.

^{18}F-FDG PET/CT has a well-established impact on high-grade lymphoma management; however, its role in indolent, low-grade disease is controversial. Recently, Jin et al. (60) investigated 11 Hodgkin lymphoma and 62 non-Hodgkin lymphoma patients, and increased radiotracer uptake was observed in Hodgkin lymphoma. Indolent lymphomas showed mild uptake in contrast to aggressive non-Hodgkin lymphomas with high uptake, which resulted in a positive association between the corresponding clinical classification of non-Hodgkin lymphomas.

In a recent meta-analysis, Sollini et al. (61) evaluated 23 studies that included 17 oncologic and six non-oncologic articles to evaluate the potential role of ^{68}Ga-FAPI imaging. They found that the superiority of ^{68}Ga-FAPI over ^{18}F-FDG was observed especially in abdominal cancers in detecting either the primary tumor or the nodal and distant metastases. They demonstrated estimated pooled sensitivity and specificity of patient-based ^{68}Ga-FAPI imaging were 0.99 (95% CI, 0.97–1.00; I^2 = 0.00%; p = 0.75) and 0.87 (95% CI, 0.62–1.00; I^2 = 0.00%; p = 0.51) with negligible heterogeneity, respectively. On the contrary, the lesion-based analysis revealed high heterogeneity in sensitivity and specificity.

Meanwhile, pooled sensitivity for the primary tumor and distant metastases was found 1.00 (95% CI, 0.98–1.00; I^2 = 0.00%; p = 0.51) and 0.93 (95% CI, 0.88–0.97; I^2 = 0.00%; p = 0.41) with negligible heterogeneity, respectively, whereas pooled sensitivity and specificity of nodal metastases had high heterogeneity (I^2 = 89.18% and I^2 = 95.74). Consequently, FAPI PET was demonstrated as a promising radiopharmaceutical, especially in some malignancies with low FDG uptake in the primary tumor or its metastasis. **Table 1** summarizes the studies evaluating FAP-targeted imaging and **Figure 1** illustrates intraindividual comparison of ^{18}FDG and ^{68}Ga-FAPI04 PET/CT in various cancer entities.

TABLE 1 | Summary of studies evaluating FAP-targeted imaging of various cancer types.

Reference	Malignant disease	*n*	Study outcome
Loktev et al. (30)	Various types of cancer	8	FAPI allows rapid and quality imaging and labeling with therapeutic isotopes in tumors with high stromal content.
Kratochwil et al. (31)	Various types of cancer	80	The highly selective tumor uptake of FAPI may reveal new applications for noninvasive tumor characterization, staging imaging, or radioligand therapy.
Giesel et al. (2)	Various types of cancer	50	FAPI-targeted PET does not require any diet or fasting; it has better image quality than ^{18}F-FDG, and acquisition can be obtained earlier.
Chen et al. (32)	Various types of cancer	75	^{68}Ga-FAPI PET/CT showed superior diagnostic efficiency compared with 18F-FDG PET/CT, particularly in the diagnosis of liver metastases, peritoneal carcinomatosis, and brain tumors.
Chen et al. (33)	Various types of cancer	68	In patients with inconclusive ^{18}F-FDG PET/CT findings, ^{68}Ga-FAPI may have a complementary role in differentiating malignant lesions, locating the primary site of unknown malignancy.
Zhao et al. (34)	Nasopharyngeal carcinoma	45	^{68}Ga-FAPI PET/CT can diagnose primary and metastatic nasopharyngeal carcinoma and supplement MRI for T staging and radiotherapy planning.
Qin et al. (35)	Nasopharyngeal carcinoma	15	^{68}Ga-FAPI shows better diagnostic performance than ^{18}F-FDG in patients with nasopharyngeal carcinoma.
Syed et al. (36)	Head and neck cancer	14	A novel approach of tumor detection, contouring, and targeted radiotherapy of head and neck cancers using ^{68}Ga-FAPI PET.
Röhrich et al. (37)	Adenoid cystic carcinoma	12	^{68}Ga-FAPI PET/CT is a promising imaging modality for adenoid cystic carcinomas, increasing the accuracy of staging exams and radiotherapy planning volumes compared with conventional CT and MRI.
Linz et al. (38)	Oral cavity squamous cell carcinoma	10	Compared with ^{18}F-FDG and cervical MRI, ^{68}Ga-FAPI can reduce patient morbidity, minimizing the number of neck dissections due to false-positive cervical lymph nodes.
Qin et al. (44)	Gastric carcinomas	20	^{68}Ga-FAPI PET/MR showed better diagnostic performance than ^{18}F-FDG PET/CT in visualizing the primary and metastatic lesions of gastric cancer.
Pang et al. (45)	Gastric, duodenal, and colorectal cancers	35	^{68}Ga-FAPI PET/CT showed superior diagnostic performance. To compare the diagnostic efficacy of 68Ga FAPI PET/CT and ^{18}F-FDG PET/CT in primary and metastatic cancers of the gastrointestinal tract.
Koerber et al. (20)	Colon, sigmoid, rectal, and anal cancers	22	^{68}Ga-FAPI PET/CT imaging of lower gastrointestinal tract primary and metastatic tumors resulted in changes in TNM staging and treatment management.
Zhao et al. (46)	Peritoneal carcinomatosis	46	^{68}Ga-FAPI04 PET/CT showed superior diagnostic performance compared with ^{18}F-FDG PET/CT to detect peritoneal carcinomatosis, particularly in gastric cancer.
Shi et al. (48)	Liver malignancies	17	^{68}Ga-FAPI04 has demonstrated high sensitivity, particularly in the detection of poorly differentiated hepatic malignancies.
Shi et al. (49)	Liver malignancies	20	^{68}Ga-FAPI PET/CT has superior potential for imaging of hepatic tumors compared with ^{18}F-FDG PET/CT.
Guo et al. (50)	Liver malignancies	34	The sensitivity of ^{68}Ga-FAPI04 PET/CT in detecting primary and metastatic liver lesions is equivalent to that of contrast-enhanced CT and MRI and better than ^{18}F-FDG PET/CT.
Geist et al. (51)	Hepatic lesions	8	Dynamic ^{68}Ga-FAPI PET scan allows differentiation between hepatocellular carcinoma and non-HCC lesions
Röhrich et al. (52)	Pancreatic ductal adenocarcinomas	19	^{68}Ga-FAPI PET/CT allowed restaging in half of the patients with PDAC and the majority of patients with recurrent disease compared with standard-of-care imaging.
Liermann et al. (53)	Pancreatic cancer	7	FAPI PET/CT seems to be a superior imaging modality to contrast-enhanced CT, which is the current gold standard in pancreatic cancer with the potential as a tool for automatic target volume definition before radiotherapy.
Kömek et al. (54)	Breast cancer	20	^{68}Ga-FAPI04 PET/CT is superior to 18F-FDG PET/CT in detecting primary tumors and metastases in breast cancer patients.
Dendl et al. (55)	Gynecological malignancies	31	^{68}Ga FAPI PET/CT seems to be a more promising imaging modality for staging and follow-up of gynecological tumors compared with ^{18}F-FDG PET/CT
Koerber et al. (56)	Several types of sarcoma	15	^{68}Ga-FAPI PET/CT has a high potential for clinical use in patients diagnosed with sarcoma as a staging probe and tumor characterization.
Kessler et al. (57)	Bone and soft tissue sarcomas	47	There is a correlation between tumoral FAPI uptake intensity and histopathological FAP expression in sarcoma patients, and FAPI PET has a high sensitivity.
Windish et al. (58)	Glioblastoma	14	For target volume delineation, ^{68}Ga-FAPI PET outperformed MRI in detecting gross tumor volumes.
Röhrich et al. (59)	Gliomas	18	Using FAP-specific PET imaging may allow a noninvasive distinction between low-grade IDH-mutant and high-grade gliomas.
Jin et al. (60)	Different subtypes of lymphomas	73	^{68}Ga-FAPI imaging may be an alternative method for detecting FAP expression in lymphoma lesions and characterizing lymphoma profiles.
Sollini et al. (61)	Various types of cancer	482	68Ga-FAPI PET appears to be a suitable method for the detection of primary lesions and distant metastases of malignancies that are not particularly suitable for 18F-FDG PET imaging.

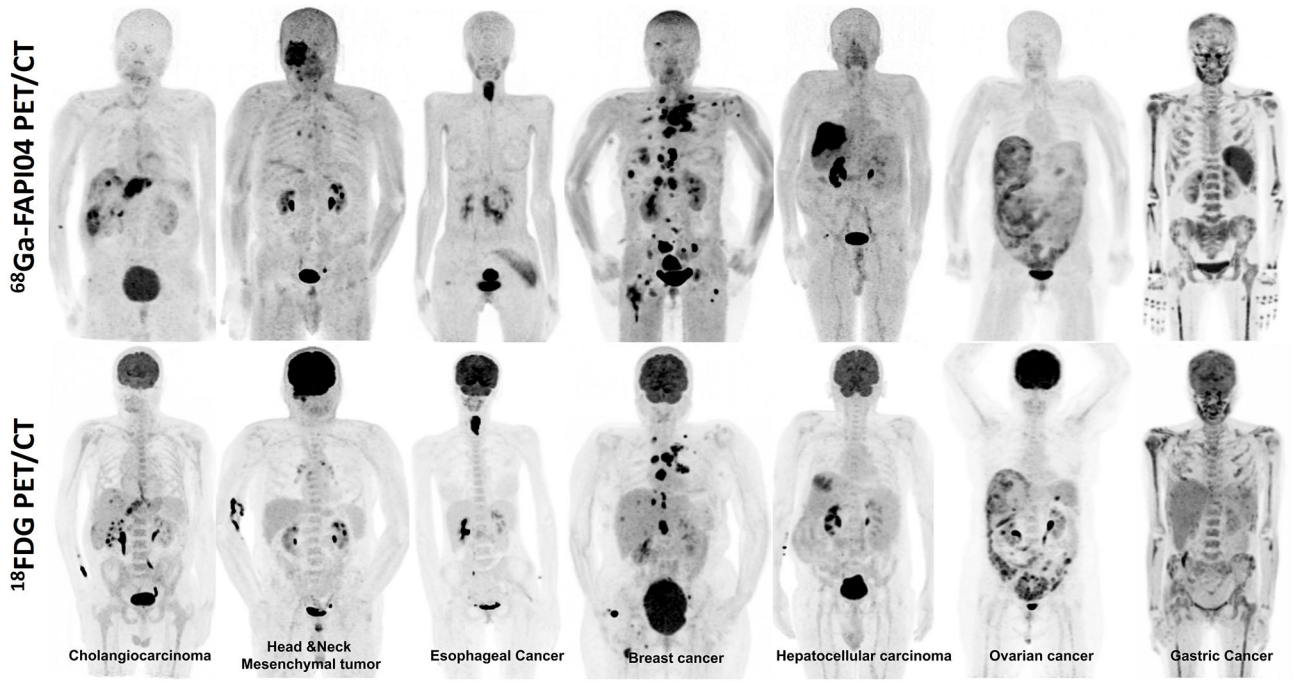

FIGURE 1 | Intraindividual comparison of ^{18}F-FDG and ^{68}Ga-FAPI04 PET maximum-intensity projection images of seven patients with various histopathologically proven tumors. The uptake of ^{68}Ga-FAPI04 is superior or equal to ^{18}F-FDG in the metastatic lesions.

RADIOTHERAPY PLANNING

Radiotherapy can be used as neoadjuvant or adjuvant therapy in many tumors. Accurate tumor delineation is the most critical part of therapy planning because it directly affects therapy response. Although computed tomography (CT) is the most commonly used modality, numerous studies in literature showed that 18F-FDG PET/CT could be used for delineating metabolic tumor volume to predict tumor response and tumor delineation for radiotherapy planning (62, 63). On the other hand, there is no consensus on the optimal method with ^{18}F-FDG PET/CT imaging because of false-positivity/negativity-like infection/inflammation or masking of the FDG uptake due to tumor location. For this reason, FAPI PET/CT can be a useful alternative radiopharmaceutical to ^{18}F-FDG in radiotherapy planning.

Currently, a limited number of articles are available related to radiotherapy planning in the literature. In one of these, Zhao et al. compared the usefulness of ^{68}Ga-FAPI with ^{18}F-FDG PET/CT imaging in evaluating gross tumor volume (GTV) delineation in 21 locally advanced esophageal cancer patients (64). They showed that ^{68}Ga-FAPI had significantly higher radiotracer uptake than ^{18}F-FDG, especially when the primary tumor was in the middle or lower thoracic esophagus. Moreover, the authors showed that ^{68}Ga-FAPI PET/CT had a higher success rate than ^{18}F-FDG PET/CT for detecting metastatic lymph nodes. In addition to this study, Ristau et al. also evaluated the impact of primary staging with ^{68}Ga-FAPI PET/CT on radiotherapy planning in esophageal cancer patients (65). They showed that primary tumors demonstrated high FAPI uptake with excellent tumor-to-background ratios that resulted in accurate target volume delineation.

Syed et al. compared GTV between ^{68}Ga-FAPI PET/CT and conventional radiologic imaging methods such as contrast-enhanced CT and MRI in head and neck cancer in 14 patients (36). Of these, two patients had taken additive radiotherapy after surgical resection for macroscopic residual tumors, whereas the rest of the 12 patients received radiotherapy in the definitive setting with a prior biopsy for histopathological confirmation. They have used four different thresholds (three-, five-, seven-, and tenfold increased uptake) of FAPI uptake in the primary tumor and normal tissue. Eventually, the authors showed that primary tumors had high FAPI avidity, while low background uptakes were shown in healthy tissues in the head and neck region. GTV was found to have significant disparities between all threshold levels of FAPI-GTV to CT-GTV. Also, Röhrich et al. compared the clinical potential of conventional imaging and ^{68}Ga-FAPI PET/CT for staging and radiotherapy planning in a total of 12 (seven primary, five recurrent) adenoid cystic carcinoma patients in the head and neck region (37). They demonstrated that ^{68}Ga-FAPI PET/CT led to upstaging in two of 12 patients and to the detection of additional metastases in three patients and thus staging was altered in 42% of patients with ^{68}Ga-FAPI PET/CT. Moreover, they showed that when compared with conventional imaging, the accuracy of target volume delineation for radiotherapy improved with FAPI PET. In addition, in a pilot study, 13 glioblastoma patients who were candidates for radiotherapy were evaluated with

FAPI PET compared with MRI (58). FAP-specific GTV was created using a five-, seven-, and tenfold threshold of increased uptake compared with normal tissue, and MRI-specific GTV was created based on T1-weighted images. They demonstrated that FAP-specific GTV were significantly different from the MRI-GTV for FAP fivefold threshold but not with FAP seven- and tenfold thresholds. FAP-specific PET target volume delineation was not found covered by MRI-GTVs in this study. All of these studies need to be supported by further studies with larger sample sizes.

THERANOSTICS

FAP-targeted diagnostic imaging has so far shown promising potential for a broad spectrum of cancers. However, taking theranostic properties and low tracer uptake in nontarget organs into account, the possibility of radionuclide treatments of cancers that are currently not in the scope of nuclear medicine is most appealing. The knowledge of theranostic applications using therapeutic radionuclides such as ^{177}Lu, ^{90}Y, and ^{225}Ac in metastatic neuroendocrine and prostate cancers will likely accelerate new research data on FAP-targeted radionuclide treatments. Still, the therapeutic applications are limited. The first reported FAP-targeted radionuclide treatment using ^{90}Y-FAPI04 was administered to a metastatic breast cancer patient by Lindner et al. (18). The posttreatment bremsstrahlung images were in line with ^{68}Ga-FAPI04 PET images, and the treatment was well tolerated with no adverse effects observed. A significant reduction in pain medication proved the potential efficacy of the treatment. Dendl et al. (55) reported temporary stable disease in patients with metastatic breast and colon cancer after receiving four cycles of ^{90}Y-FAPI04 treatment. Another progressive metastatic breast cancer patient was reported by Ballal et al. (26). The authors used a novel FAP agent based on the squaric acid motif with improved structural features and administered the patient with 3.2 GBq of ^{177}Lu-DOTA.SA.FAPi on compassionate grounds. The primary tumor and the metastatic brain lesion received 1.48E mGy/MBq and 3.46 mGy/MBq absorbed dose. Jokar et al. (66) also reported a metastatic breast carcinoma patient who had failed conventional treatments and received two cycles of ^{177}Lu-FAPI46. Kratochwil et al. (27) treated a metastatic sarcoma patient using ^{153}Sm and ^{90}Y, reaching a cumulative dose of 20 GBq ^{153}Sm-FAPI46 and 8GBq ^{90}Y-FAPI46 in three cycles. The authors reported 8 months of stable disease, encouraging further studies. So far, two comprehensive studies of FAP-targeting radionuclide treatment have been reported. Baum et al. (29) studied FAP-2286 and administered ^{177}Lu-labeled FAP-2286 to 10 patients with pancreas, breast, ovarian, and rectal cancers. Although a treatment response was not achieved, the authors concluded the reasonable toxicity profile with well-tolerated adverse effects. Assadi et al. (67) have administered ^{177}Lu-FAPI46 to 21 patients with various cancers and reported stable disease in 12 of the patients, emphasizing the tolerability and safety of the treatment. The results of both studies agreed that current results warranted further investigation. In summary, the preliminary studies (**Table 2**) have reported low estimated radiation dose to nontarget organs compared with well-established radionuclide therapies such as PSMA and DOTATATE. The tumor retention time of FAP inhibitor compounds has evolved since their first introduction; however, dose-escalation studies to achieve tumoricidal effects and optimize the therapeutic efficacy for different tumors require further research.

LIMITATIONS

Although there is emerging FAP-targeted PET/CT data available for cancer imaging, activated fibroblasts, particularly in tissue-remodeling processes, can also express FAPs. As a result, circumstances such as the differentiation of chronic inflammatory or wound-healing processes and malignancy limit the specificity of FAPI PET imaging for certain cancer entities such as pancreatic cancer (52). On the other hand, this allows its use in non-oncological diseases; however, other than the case reports, FAPI PET imaging of nonmalignant conditions has focused on cardiovascular (69–71) and rheumatological (68, 72, 73) diseases. Eventually, clinical adoption of FAPI PET requires understanding the limitations of FAPI PET, its use in

TABLE 2 | Summary of studies evaluating FAP-targeted radionuclide treatments.

Reference	Malignancy	*n*	Radiopharmaceutical	Administered dose	Tumor absorbed dose	Cycles	Response
Lindner et al. (18)	Breast	1	^{90}Y-FAPI04	2.9 GBq	n/a	1	Reduction in pain medication
Ballal et al. (26)	Breast	1	^{177}Lu-DOTA.SA.FAPi	3.2 GBq	1.48 and 3.46 mGy/MBq	1	Decrease in the intensity of headaches. No adverse effects
Kratochwil et al. (27)	Sarcoma	1	^{153}Sm-FAPI46 and ^{90}Y-FAPI46	20 GBq ^{153}Sm- and 8 GBq ^{90}Y-FAPI46 (*cumulative*)	n/a	3	Stable disease for 8 months
Baum et al. (29)	Various	10	^{177}Lu-FAP-2286	5.8 ± 2.0 GBq (*mean*)	3 ± 2.7 Gy/GBq (*mean*)	2 (*mean*)	PD (*n* = 10), SD (*n* = 1); well tolerated, no adverse symptoms
Dendl et al. (55)	Breast and colon	1	^{90}Y-FAPI	n/a	n/a	4	PD
Jokar et al. (66)	Breast	1	^{177}Lu-FAPI46	3.7 GBq (*per cycle*)	n/a	2	n/a
Assadi et al. (68)	Various	21	^{177}Lu-FAPI46	3.7GBq (*mean*)	n/a	2 (*mean*)	SD (*n* = 12) and PD (*n* = 6)

SD, stable disease; PD, progressive disease; n/a, not available.

cancer-specific and non-oncological applications, which can be achieved in the long term.

CONCLUSION

In diagnostic oncology, targeting increased glucose uptake as a hallmark of cancer-associated metabolic changes by ^{18}FDG PET/CT is unrivaled. Its capability in detecting metabolic changes even in the absence of anatomical changes has led to high sensitivity; however, increased glycolysis is also common in various nonmalignant diseases and physiological processes, which causes low specificity. Several PET radiotracers have been developed in the last decades; however, they targeted specific cancer types. FAPIs have the potential to compete with FDG for diagnosis, staging, treatment planning, and therapy response assessment in many human solid tumors. In addition, it has the potential to be a theranostic modality for these tumors and likely transform the therapeutic options available, outside standard treatments, to millions of patients, in the future.

AUTHOR CONTRIBUTIONS

SK and YS: data collection and extraction and manuscript writing. RS: content planning, study design, and manuscript editing. All authors contributed to the article and approved the submitted version.

REFERENCES

1. Marin JFG, Nunes RF, Coutinho AM, Zaniboni EC, Costa LB, Barbosa FG, et al. Theranostics in Nuclear Medicine: Emerging and Re-Emerging Integrated Imaging and Therapies in the Era of Precision Oncology. *RadioGraphics* (2020) 40(6):1715–40. doi: 10.1148/rg.2020200021
2. Giesel FL, Kratochwil C, Lindner T, Marschalek MM, Loktev A, Lehnert W, et al. (68)Ga-FAPI PET/CT: Biodistribution and Preliminary Dosimetry Estimate of 2 DOTA-Containing FAP-Targeting Agents in Patients With Various Cancers. *J Nucl Med* (2019) 60(3):386–92. doi: 10.2967/jnumed.118.215913
3. Loktev A, Lindner T, Burger EM, Altmann A, Giesel F, Kratochwil C, et al. Development of Fibroblast Activation Protein-Targeted Radiotracers With Improved Tumor Retention. *J Nucl Med* (2019) 60(10):1421–9. doi: 10.2967/jnumed.118.224469
4. Giesel FL, Adeberg S, Syed M, et al. FAPI-74 PET/CT Using Either (18)F-AlF or Cold-Kit (68)Ga Labeling: Biodistribution, Radiation Dosimetry, and Tumor Delineation in Lung Cancer Patients. *J Nucl Med* (2021) 62(2):201–7. doi: 10.2967/jnumed.120.245084
5. Lindner T, Altmann A, Kramer S, Kleist C, Loktev A, Kratochwil C, et al. Design and Development of (99m)Tc-Labeled FAPI Tracers for SPECT Imaging and (188)Re Therapy. *J Nucl Med* (2020) 61(10):1507–13. doi: 10.2967/jnumed.119.239731
6. Wang S, Zhou X, Xu X, Ding J, Liu S, Hou X, et al. Clinical Translational Evaluation of Al(18)F-NOTA-FAPI for Fibroblast Activation Protein-Targeted Tumour Imaging. *Eur J Nucl Med Mol Imaging* (2021). doi: 10.1007/s00259-021-05470-5
7. Fearon DT. The Carcinoma-Associated Fibroblast Expressing Fibroblast Activation Protein and Escape From Immune Surveillance. *Cancer Immunol Res* (2014) 2(3):187–93. doi: 10.1158/2326-6066.CIR-14-0002
8. Liu F, Qi L, Liu B, Liu J, Zhang H, Che D, et al. Fibroblast Activation Protein Overexpression and Clinical Implications in Solid Tumors: A Meta-Analysis. *PLoS One* (2015) 10(3):e0116683. doi: 10.1371/journal.pone.0116683
9. Kalluri R. The Biology and Function of Fibroblasts in Cancer. *Nat Rev Cancer* (2016) 16(9):582–98. doi: 10.1038/nrc.2016.73
10. Sharma P, Singh SS, Gayana S. Fibroblast Activation Protein Inhibitor PET/CT: A Promising Molecular Imaging Tool. *Clin Nucl Med* (2021) 46(3):e141–e50. doi: 10.1097/RLU.0000000000003489
11. Balkwill FR, Capasso M, Hagemann T. The Tumor Microenvironment at a Glance. *J Cell Sci* (2012) 125(Pt 23):5591–6. doi: 10.1242/jcs.116392
12. Šimková A, Bušek P, Šedo A, Konvalinka J. Molecular Recognition of Fibroblast Activation Protein for Diagnostic and Therapeutic Applications. *Biochim Biophys Acta Proteins Proteom* (2020) 1868(7):140409. doi: 10.1016/j.bbapap.2020.140409
13. Hamson EJ, Keane FM, Tholen S, Schilling O, Gorrell MD. Understanding Fibroblast Activation Protein (FAP): Substrates, Activities, Expression and Targeting for Cancer Therapy. *Proteomics Clin Appl* (2014) 8(5-6):454–63. doi: 10.1002/prca.201300095
14. Garin-Chesa P, Old LJ, Rettig WJ. Cell Surface Glycoprotein of Reactive Stromal Fibroblasts as a Potential Antibody Target in Human Epithelial Cancers. *Proc Natl Acad Sci USA* (1990) 87(18):7235–9. doi: 10.1073/pnas.87.18.7235
15. Welt S, Divgi CR, Scott AM, Garin-Chesa P, Finn RD, Graham M, et al. Antibody Targeting in Metastatic Colon Cancer: A Phase I Study of Monoclonal Antibody F19 Against a Cell-Surface Protein of Reactive Tumor Stromal Fibroblasts. *J Clin Oncol* (1994) 12(6):1193–203. doi: 10.1200/JCO.1994.12.6.1193
16. Jansen K, Heirbaut L, Cheng JD, Joossens J, Ryabtsova O, Cos P, et al. Selective Inhibitors of Fibroblast Activation Protein (FAP) With a (4-Quinolinoyl)-Glycyl-2-Cyanopyrrolidine Scaffold. *ACS Med Chem Lett* (2013) 4(5):491–6. doi: 10.1021/ml300410d
17. Tsai TY, Yeh TK, Chen X, Hsu T, Jao Y-C, Huang C-H, et al. Substituted 4-Carboxymethylpyroglutamic Acid Diamides as Potent and Selective Inhibitors of Fibroblast Activation Protein. *J Med Chem* (2010) 53 (18):6572–83. doi: 10.1021/jm1002556
18. Lindner T, Loktev A, Altmann A, Giesel F, Kratochwil C, Debus J, et al. Development of Quinoline-Based Theranostic Ligands for the Targeting of Fibroblast Activation Protein. *J Nucl Med* (2018) 59(9):1415–22. doi: 10.2967/jnumed.118.210443
19. Boellaard R, Delgado-Bolton R, Oyen WJ, Giammarile F, Tatsch K, Eschner W, et al. FDG PET/CT: EANM Procedure Guidelines for Tumour Imaging: Version 2.0. *Eur J Nucl Med Mol Imaging* (2015) 42(2):328–54. doi: 10.1007/s00259-014-2961-x
20. Koerber SA, Staudinger F, Kratochwil C, Adeberg S, Haefner MF, Ungerechts G, et al. The Role of (68)Ga-FAPI PET/CT for Patients With Malignancies of the Lower Gastrointestinal Tract: First Clinical Experience. *J Nucl Med* (2020) 61(9):1331–6. doi: 10.2967/jnumed.119.237016
21. Fendler WP, Eiber M, Beheshti M, Bomanji J, Ceci F, Cho S, et al. (68)Ga-PSMA PET/CT: Joint EANM and SNMMI Procedure Guideline for Prostate Cancer Imaging: Version 1.0. *Eur J Nucl Med Mol Imaging* (2017) 44(6):1014–24. doi: 10.1007/s00259-017-3670-z
22. Ferdinandus J, Kessler L, Hirmas N, Trajkovic-Arsic M, Hamacher R, Umutlu L, et al. Equivalent Tumor Detection for Early and Late FAPI-46 PET Acquisition. *Eur J Nucl Med Mol Imaging* (2021), 1–7. doi: 10.1007/s00259-021-05266-7
23. Moon ES, Elvas F, Vliegen G, De Lombaerde S, Vangestel C, De Bruycker S, et al. Targeting Fibroblast Activation Protein (FAP): Next Generation PET Radiotracers Using Squaramide Coupled Bifunctional DOTA and DATA(5m) Chelators. *EJNMMI Radiopharm Chem* (2020) 5(1):1–20. doi: 10.1186/s41181-020-00102-z
24. Ballal S, Yadav MP, Moon ES, Kramer VS, Roesch F, Kumari S, et al. Biodistribution, Pharmacokinetics, Dosimetry of [(68)Ga]Ga-DOTA.SA.FAPi, and the Head-to-Head Comparison With [(18)F]F-FDG PET/CT in Patients With Various Cancers. *Eur J Nucl Med Mol Imaging* (2021) 48(6):1915–31. doi: 10.1007/s00259-020-05132-y
25. Toms J, Kogler J, Maschauer S, Daniel C, Schmidkonz C, Kuwert T, et al. Targeting Fibroblast Activation Protein: Radiosynthesis and Preclinical Evaluation of an (18)F-Labeled FAP Inhibitor. *J Nucl Med* (2020) 61 (12):1806–13. doi: 10.2967/jnumed.120.242958

26. Ballal S, Yadav MP, Kramer V, Moon ES, Roesch F, Tripathi M, et al. A Theranostic Approach of [(68)Ga]Ga-DOTA.SA.FAPi PET/CT-Guided [(177)Lu]Lu-DOTA.SA.FAPi Radionuclide Therapy in an End-Stage Breast Cancer Patient: New Frontier in Targeted Radionuclide Therapy. *Eur J Nucl Med Mol Imaging* (2021) 48(3):942–4. doi: 10.1007/s00259-020-04990-w
27. Kratochwil C, Giesel FL, Rathke H, Fink R, Dendl K, Debus J, et al. [(153)Sm] Samarium-Labeled FAPI-46 Radioligand Therapy in a Patient With Lung Metastases of a Sarcoma. *Eur J Nucl Med Mol Imaging* (2021), 1–3. doi: 10.1007/s00259-021-05273-8
28. Kuyumcu S, Kovan B, Sanli Y, Buyukkaya F, Simsek DH, Özkan ZG, et al. Safety of Fibroblast Activation Protein-Targeted Radionuclide Therapy by a Low-Dose Dosimetric Approach Using 177lu-Fapi04. *Clin Nucl Med* (2021) 46(8):641–6. doi: 10.1097/RLU.0000000000003667
29. Baum RP, Schuchardt C, Singh A, Chantadisai M, Robiller FC, Zhang J, et al. Feasibility, Biodistribution and Preliminary Dosimetry in Peptide-Targeted Radionuclide Therapy (PTRT) of Diverse Adenocarcinomas Using (177)Lu-FAP-2286: First-In-Human Results. *J Nucl Med* (In Press). doi: 10.2967/jnumed.120.259192
30. Loktev A, Lindner T, Mier W, Debus J, Altmann A, Jäger D, et al. A Tumor-Imaging Method Targeting Cancer-Associated Fibroblasts. *J Nucl Med* (2018) 59(9):1423–9. doi: 10.2967/jnumed.118.210435
31. Kratochwil C, Flechsig P, Lindner T, Abderrahim L, Altmann A, Mier W, et al. (68)Ga-FAPI PET/CT: Tracer Uptake in 28 Different Kinds of Cancer. *J Nucl Med* (2019) 60(6):801–5. doi: 10.2967/jnumed.119.227967
32. Chen H, Pang Y, Wu J, Zhao L, Hao B, Wu J, et al. Comparison of [(68)Ga]Ga-DOTA-FAPI-04 and [(18)F] FDG PET/CT for the Diagnosis of Primary and Metastatic Lesions in Patients With Various Types of Cancer. *Eur J Nucl Med Mol Imaging* (2020) 47(8):1820–32. doi: 10.1007/s00259-020-04769-z
33. Chen H, Zhao L, Ruan D, Pang Y, Hao B, Dai Y, et al. Usefulness of [(68)Ga]Ga-DOTA-FAPI-04 PET/CT in Patients Presenting With Inconclusive [(18)F]FDG PET/CT Findings. *Eur J Nucl Med Mol Imaging* (2021) 48(1):73–86. doi: 10.1007/s00259-020-04940-6
34. Zhao L, Pang Y, Zheng H, Han C, Gu J, Sun L, et al. Clinical Utility of [(68)Ga]Ga-Labeled Fibroblast Activation Protein Inhibitor (FAPI) Positron Emission Tomography/Computed Tomography for Primary Staging and Recurrence Detection in Nasopharyngeal Carcinoma. *Eur J Nucl Med Mol Imaging* (2021) 1–12. doi: 10.1007/s00259-021-05336-w
35. Qin C, Liu F, Huang J, Ruan W, Liu Q, Gai Y, et al. A Head-to-Head Comparison of (68)Ga-DOTA-FAPI-04 and (18)F-FDG PET/MR in Patients With Nasopharyngeal Carcinoma: A Prospective Study. *Eur J Nucl Med Mol Imaging* (2021), 1–10. doi: 10.1007/s00259-021-05255-w
36. Syed M, Flechsig P, Liermann J, Windisch P, Staudinger F, Akbaba S, et al. Fibroblast Activation Protein Inhibitor (FAPI) PET for Diagnostics and Advanced Targeted Radiotherapy in Head and Neck Cancers. *Eur J Nucl Med Mol Imaging* (2020) 47(12):2836–45. doi: 10.1007/s00259-020-04859-y
37. Rohrich M, Syed M, Liew DP, Giesel FL, Liermann J, Choyke PL, et al. (68)Ga-FAPI-PET/CT Improves Diagnostic Staging and Radiotherapy Planning of Adenoid Cystic Carcinomas - Imaging Analysis and Histological Validation. *Radiother Oncol* (2021) 160:192–201. doi: 10.1016/j.radonc.2021.04.016
38. Linz C, Brands RC, Kertels O, Dierks A, Brumberg J, Gerhard-Hartmann E, et al. Targeting Fibroblast Activation Protein in Newly Diagnosed Squamous Cell Carcinoma of the Oral Cavity - Initial Experience and Comparison to [(18)F]FDG PET/CT and MRI. *Eur J Nucl Med Mol Imaging* (2021) 1–10. doi: 10.1007/s00259-021-05422-z
39. Zhao L, Chen S, Lin L, Sun L, Wu H, Lin Q, et al. [(68)Ga]Ga-DOTA-FAPI-04 Improves Tumor Staging and Monitors Early Response to Chemoradiotherapy in a Patient With Esophageal Cancer. *Eur J Nucl Med Mol Imaging* (2020) 47(13):3188–9. doi: 10.1007/s00259-020-04818-7
40. Liu Q, Shi S, Xu X, Yu X, Song S. The Superiority of [(68)Ga]-FAPI-04 Over [(18)F]-FDG PET/CT in Imaging Metastatic Esophageal Squamous Cell Carcinoma. *Eur J Nucl Med Mol Imaging* (2021) 48(4):1248–9. doi: 10.1007/s00259-020-04997-3
41. Pang Y, Huang H, Fu L, Zhao L, Chen H. 68Ga-FAPI PET/CT Detects Gastric Signet-Ring Cell Carcinoma in a Patient Previously Treated for Prostate Cancer. *Clin Nucl Med* (2020) 45(8):632–5. doi: 10.1097/RLU.0000000000003099
42. Fan C, Guo W, Su G, Chen B, Chen H. Widespread Metastatic Gastric Signet-Ring Cell Carcinoma Shown by 68Ga-FAPI PET/CT. *Clin Nucl Med* (2021) 46(2):e78–e9. doi: 10.1097/RLU.0000000000003245
43. Lin R, Lin Z, Zhang J, Yao S, Miao W. Increased 68ga-FAPI-04 Uptake in Schmorl Node in a Patient With Gastric Cancer. *Clin Nucl Med* (2021) 46(8):700–2. doi: 10.1097/RLU.0000000000003623
44. Qin C, Shao F, Gai Y, Liu Q, Ruan W, Liu F, et al. (68)Ga-DOTA-FAPI-04 PET/MR in the Evaluation of Gastric Carcinomas: Comparison With (18)F-FDG PET/CT. *J Nucl Med* (2021). doi: 10.2967/jnumed.120.258467
45. Pang Y, Zhao L, Luo Z, Hao B, Wu H, Lin Q, et al. Comparison of (68)Ga-FAPI and (18)F-FDG Uptake in Gastric, Duodenal, and Colorectal Cancers. *Radiology* (2021) 298(2):393–402. doi: 10.1148/radiol.2020203275
46. Zhao L, Pang Y, Luo Z, Fu K, Yang T, Zhao L, et al. Role of [(68)Ga]Ga-DOTA-FAPI-04 PET/CT in the Evaluation of Peritoneal Carcinomatosis and Comparison With [(18)F]-FDG PET/CT. *Eur J Nucl Med Mol Imaging* (2021) 48(6):1944–55. doi: 10.1007/s00259-020-05146-6
47. Kuyumcu S, Has-Simsek D, Iliaz R, Sanli Y, Buyukkaya F, Akyuz F, et al. Evidence of Prostate-Specific Membrane Antigen Expression in Hepatocellular Carcinoma Using 68ga-PSMA PET/CT. *Clin Nucl Med* (2019) 44(9):702–6. doi: 10.1097/RLU.0000000000002701
48. Shi X, Xing H, Yang X, Li F, Yao S, Zhang H, et al. Fibroblast Imaging of Hepatic Carcinoma With (68)Ga-FAPI-04 PET/CT: A Pilot Study in Patients With Suspected Hepatic Nodules. *Eur J Nucl Med Mol Imaging* (2021) 48(1):196–203. doi: 10.1007/s00259-020-04882-z
49. Shi X, Xing H, Yang X, Li F, Yao S, Congwei J, et al. Comparison of PET Imaging of Activated Fibroblasts and (18)F-FDG for Diagnosis of Primary Hepatic Tumours: A Prospective Pilot Study. *Eur J Nucl Med Mol Imaging* (2021) 48(5):1593–603. doi: 10.1007/s00259-020-05070-9
50. Guo W, Pang Y, Yao L, Zhao L, Fan C, Ke J, et al. Imaging Fibroblast Activation Protein in Liver Cancer: A Single-Center *Post Hoc* Retrospective Analysis to Compare [(68)Ga]Ga-FAPI-04 PET/CT Versus MRI and [(18)F]-FDG PET/CT. *Eur J Nucl Med Mol Imaging* (2021) 48(5):1604–17. doi: 10.1007/s00259-020-05095-0
51. Geist BK, Xing H, Wang J, Shi X, Zhao H, Hacker M, et al. A Methodological Investigation of Healthy Tissue, Hepatocellular Carcinoma, and Other Lesions With Dynamic (68)Ga-FAPI-04 PET/CT Imaging. *EJNMMI Phys* (2021) 8(1):8. doi: 10.1186/s40658-021-00353-y
52. Rohrich M, Naumann P, Giesel FL, Choyke PL, Staudinger F, Wefers A, et al. Impact of (68)Ga-FAPI PET/CT Imaging on the Therapeutic Management of Primary and Recurrent Pancreatic Ductal Adenocarcinomas. *J Nucl Med* (2021) 62(6):779–86. doi: 10.2967/jnumed.120.253062
53. Liermann J, Syed M, Ben-Josef E, Schubert K, Schlampp I, Sprengel SD, et al. Impact of FAPI-PET/CT on Target Volume Definition in Radiation Therapy of Locally Recurrent Pancreatic Cancer. *Cancers (Basel)* (2021) 13(4):796. doi: 10.3390/cancers13040796
54. Komek H, Can C, Guzel Y, Oruç Z, Gündoğan C, Yildirim ÖA, et al. (68)Ga-FAPI-04 PET/CT, a New Step in Breast Cancer Imaging: A Comparative Pilot Study With the (18)F-FDG PET/CT. *Ann Nucl Med* (2021) 35(6):744–52. doi: 10.1007/s12149-021-01616-5
55. Dendl K, Koerber SA, Finck R, Mokoala KM, Staudinger F, Schillings L, et al. (68)Ga-FAPI-PET/CT in Patients With Various Gynecological Malignancies. *Eur J Nucl Med Mol Imaging* (2021) 48(5):4089–100. doi: 10.1007/s00259-021-05378-0
56. Koerber SA, Finck R, Dendl K, Uhl M, Lindner T, Kratochwil C, et al. Novel FAP Ligands Enable Improved Imaging Contrast in Sarcoma Patients Due to FAPI-PET/CT. *Eur J Nucl Med Mol Imaging* (2021) 48(5):3918–24. doi: 10.1007/s00259-021-05374-4
57. Kessler L, Ferdinandus J, Hirmas N, Bauer S, Dirksen U, Zarrad F, et al. Ga-68-FAPI as Diagnostic Tool in Sarcoma: Data From the FAPI-PET Prospective Observational Trial. *J Nucl Med* 2021:jnumed.121.262096. doi: 10.2967/jnumed.121.262096
58. Windisch P, Rohrich M, Regnery S, Tonndorf-Martini E, Held T, Lang K, et al. Fibroblast Activation Protein (FAP) Specific PET for Advanced Target Volume Delineation in Glioblastoma. *Radiother Oncol* (2020) 150:159–63. doi: 10.1016/j.radonc.2020.06.040
59. Rohrich M, Loktev A, Wefers AK, Altmann A, Paech D, Adeberg S, et al. IDH-Wildtype Glioblastomas and Grade III/IV IDH-Mutant Gliomas Show Elevated Tracer Uptake in Fibroblast Activation Protein-Specific PET/CT. *Eur J Nucl Med Mol Imaging* (2019) 46(12):2569–80. doi: 10.1007/s00259-019-04444-y
60. Jin X, Wei M, Wang S, Wang G, Lai Y, Shi Y, et al. Detecting Fibroblast Activation Proteins in Lymphoma Using (68)Ga-FAPI PET/CT. *J Nucl Med* (2021). doi: 10.2967/jnumed.121.262134

61. Sollini M, Kirienko M, Gelardi F, Fiz F, Gozzi N, Chiti A. State-Of-the-Art of FAPI-PET Imaging: A Systematic Review and Meta-Analysis. *Eur J Nucl Med Mol Imaging* (2021). doi: 10.21203/rs.3.rs-543400/v1
62. Gardin I. Methods to Delineate Tumour for Radiotherapy by Fluorodeoxyglucose Positron Emission Tomography. *Cancer Radiother* (2020) 24(5):418–22. doi: 10.1016/j.canrad.2020.04.008
63. Im HJ, Bradshaw T, Solaiyappan M, Cho SY. Current Methods to Define Metabolic Tumor Volume in Positron Emission Tomography: Which One is Better? *Nucl Med Mol Imaging* (2018) 52(1):5–15. doi: 10.1007/s13139-017-0493-6
64. Zhao L, Chen S, Chen S, Pang Y, Dai Y, Hu S, et al. (68)Ga-Fibroblast Activation Protein Inhibitor PET/CT on Gross Tumour Volume Delineation for Radiotherapy Planning of Oesophageal Cancer. *Radiother Oncol* (2021) 158:55–61. doi: 10.1016/j.radonc.2021.02.015
65. Ristau J, Giesel FL, Haefner MF, Staudinger F, Lindner T, Merkel A, et al. Impact of Primary Staging With Fibroblast Activation Protein Specific Enzyme Inhibitor (FAPI)-PET/CT on Radio-Oncologic Treatment Planning of Patients With Esophageal Cancer. *Mol Imaging Biol* (2020) 22(6):1495–500. doi: 10.1007/s11307-020-01548-y
66. Jokar N, Velikyan I, Ahmadzadehfar H, Rekabpour SJ, Jafari E, Ting HH, et al. Theranostic Approach in Breast Cancer: A Treasured Tailor for Future Oncology. *Clin Nucl Med* (2021) 46(8):e410–e20.
67. Assadi M, Rekabpour SJ, Jafari E, Divband G, Nikkholgh B, Amini H, et al. Feasibility and Therapeutic Potential of 177Lu-Fibroblast Activation Protein Inhibitor-46 for Patients With Relapsed or Refractory Cancers: A Preliminary Study. *Clin Nucl Med* (2021) 46(11):e523–30. doi: 10.1097/RLU.0000000000003810
68. Schmidkonz C, Rauber S, Atzinger A, Katus HA, Haberkorn U, Leuschner F, et al. Disentangling Inflammatory From Fibrotic Disease Activity by Fibroblast Activation Protein Imaging. *Ann Rheum Dis* (2020) 79(11):1485–91. doi: 10.1136/annrheumdis-2020-217408
69. Finke D, Heckmann MB, Herpel E, Katus HA, Haberkorn U, Leuschner F, et al. Early Detection of Checkpoint Inhibitor-Associated Myocarditis Using 68ga-FAPI PET/CT. *Front Cardiovasc Med* (2021) 8(54). doi: 10.3389/fcvm.2021.614997
70. Heckmann MB, Reinhardt F, Finke D, Nekolla S, Kessler L, Ferdinandus J, et al. Relationship Between Cardiac Fibroblast Activation Protein Activity by Positron Emission Tomography and Cardiovascular Disease. *Circ Cardiovasc Imaging* (2020) 13(9):e010628. doi: 10.1161/CIRCIMAGING.120.010628
71. Siebermair J, Köhler MI, Kupusovic J, Tascilar K, Müller A-T, Atzinger A, et al. Cardiac Fibroblast Activation Detected by Ga-68 FAPI PET Imaging as a Potential Novel Biomarker of Cardiac Injury/Remodeling. *J Nucl Cardiol* (2021) 28(3):812–21. doi: 10.1007/s12350-020-02307-w
72. Bergmann C, Distler JHW, Treutlein C, Peng L, Zhang W, Li F. 68Ga-FAPI-04 PET-CT for Molecular Assessment of Fibroblast Activation and Risk Evaluation in Systemic Sclerosis-Associated Interstitial Lung Disease: A Single-Centre, Pilot Study. *Lancet Rheumatol* (2021) 3(3):e185–94. doi: 10.1016/S2665-9913(20)30421-5
73. Luo Y, Pan Q, Yang H, Peng L, Zhang W, Li F. Fibroblast Activation Protein-Targeted PET/CT With (68)Ga-FAPI for Imaging IgG4-Related Disease: Comparison to (18)F-FDG PET/Ct. *J Nucl Med* (2021) 62(2):266–71. doi: 10.2967/jnumed.120.244723

Conflict of Interest: The authors declare that the research was conducted in the absence of any commercial or financial relationships that could be construed as a potential conflict of interest.

Publisher's Note: All claims expressed in this article are solely those of the authors and do not necessarily represent those of their affiliated organizations, or those of the publisher, the editors and the reviewers. Any product that may be evaluated in this article, or claim that may be made by its manufacturer, is not guaranteed or endorsed by the publisher.

frontiers | Frontiers in Oncology

ORIGINAL RESEARCH
published: 01 April 2022
doi: 10.3389/fonc.2022.738299

Efficacy and Safety of Thermal Ablation for Treating Lymph Node Metastasis From Papillary Thyroid Carcinoma: A Systematic Review and Meta-Analysis

Zheng Ding[1†], Juan Chen[1†], Zhiguang Chen[2], Xiaoke Zeng[2], Pengchao Zheng[2], Xuemei Wang[2], Xinwu Cui[3] and Liang Sang[2*]*

[1] The First Affiliated Hospital of China Medical University, Shenyang, China, [2] Department of Ultrasound, The First Hospital of China Medical University, Shenyang, China, [3] Departmant of Medical Ultrasound, Tongji Hospital, Tongji Medical College, Huazhong University of Science and Technology, Wuhan, China

Objective: To evaluate the efficacy and safety of thermal ablation, including radiofrequency ablation (RFA), microwave ablation (MVA), and laser ablation (LA), for treating lymph node metastasis (LNM) from papillary thyroid carcinoma (PTC).

Design and Methods: PubMed and EMBASE were searched for studies reporting the efficacy and safety of thermal ablation for treating LNM in PTC. After selecting the relevant literature (including 11 papers, 208 patients, 412 lymph nodes), the QUADAS-2 tool was used to evaluate its quality. Then, both the fixed-effects and random-effects models combined with subgroup analysis were used to calculate data on volume changes in metastatic lymph nodes and changes in serum thyroglobulin (Tg) levels. We pooled the proportion of major and overall complication rates and complete disappearance rates and used subgroup forest plots and funnel plots for visual representation. Because of publication bias, we also performed a trim-and-filled model for correction. The rate of recurrence and distant metastasis with ablated details were pooled.

Results: In the 11 articles (208 patients and 412 diseased lymph nodes), all thermal ablation methods showed effectiveness in reducing lymph node volume ($P = 0.02$) and serum Tg levels ($P < 0.01$) which showed no between-group difference. The pooled proportion of major complications was 0%(95% CI: -0.14; 0.15, $P = 1$) and the overall complication rate was 5% (95% CI: -0.09; 0.20, $P = 1$), which revealed no significant difference among modalities. The pooled proportion of the complete disappearance rate was 82% (95% CI: 0.43; 0.96, $P < 0.01$) and the data with statistical significance which contains RFA and LA showed complete disappearance rate was 59% and 81% respectively.

OPEN ACCESS

Edited by:
Po-Hsiang Tsui,
Chang Gung University, Taiwan

Reviewed by:
Paolo Piero Limone,
Hospital Mauritian Turin, Italy
Yukun Luo,
People's Liberation Army General Hospital, China

****Correspondence:***
Xinwu Cui
cuixinwu@live.cn
Liang Sang
13889167622@163.com

[†]These authors have contributed equally to this work

Specialty section:
This article was submitted to Cancer Imaging and Image-directed Interventions, a section of the journal Frontiers in Oncology

Received: *08 July 2021*
Accepted: *08 March 2022*
Published: *01 April 2022*

Citation:
Ding Z, Chen J, Chen Z, Zeng X, Zheng P, Wang X, Cui X and Sang L (2022) Efficacy and Safety of Thermal Ablation for Treating Lymph Node Metastasis From Papillary Thyroid Carcinoma: A Systematic Review and Meta-Analysis. Front. Oncol. 12:738299. doi: 10.3389/fonc.2022.738299

Conclusion: All thermal ablation methods, including RFA, MWA, and LA, were effective and safe for treating LNM in PTC and were especially suitable for nonsurgical patients. Besides, subgroup analysis showed no significant difference, except for LA is better than RFA in complete disappearance rate.

Keywords: thermal ablation, radiofrequency ablation, microwave ablation, laser ablation, lymph node metastasis, papillary thyroid carcinoma

INTRODUCTION

Thyroid cancer has become the most common endocrine malignancy, and its incidence has increased faster than that of many other malignant tumors in many other countries in recent decades. Despite the sharp rise in the incidence, the mortality rate of thyroid cancer has remained stable. Papillary thyroid carcinoma (PTC) is the most common subtype of thyroid cancer. It is a typically indolent disease with a high cure rate; however, related lymph node metastasis (LNM) is frequently observed after resection of the PTC (1, 2). Surgery and/or radioactive iodine therapy is currently the preferred treatment, but due to many factors, a considerable proportion of patients cannot undergo surgery or radioactive iodine therapy, such as those who have had many previous surgeries, an inaccessible tumor position or small size, and poor nutritional status (3).

In many cases related to neck diseases, thermal ablation, including radiofrequency ablation (RFA), microwave ablation (MWA), and laser ablation (LA), have performed well. Complications of surgical treatment include nerve injury (the superior laryngeal nerve and recurrent laryngeal nerve), thyroid dysfunction, significant blood loss, and slow recovery. Compared to surgical treatment, thermal ablation is a relatively safe and economical treatment due to its low complication rate and cost (4–8). Therefore, it can be used to treat more patients with related diseases and be applied repeatedly instead of performing many surgeries over time to deal with newly discovered PTC lymph node metastases.

Recent studies come from many regions and hospitals that have shown the safety and effectiveness of thermal ablation for treating PTC and LNM from PTC (9–22). Our purpose is to verify the efficacy and safety of thermal ablation for patients with metastatic lymph nodes from PTC, and the results obtained through this verification can provide a certain degree of guidance for clinical practice.

MATERIALS AND METHODS

Literature Search Strategy

We searched the PubMed and EMBASE databases to find published articles on the review topic. We used the following search terms: [("Metastatic" AND "Lymph nodes") AND (thyroid) AND ("carcinoma" OR "cancer" OR "malignancy") AND ("radiofrequency ablation" OR "RFA" OR "laser ablation" OR "LA" OR "microwave ablation" OR "MWA" OR "thermal ablation")]. The search was updated until 28 February 2021, with English language only. Then, we applied a rigorous screening of the articles. After deleting duplicates, we reviewed their abstracts to obtain relevant articles. Finally, the full-text review was carried out, and studies with sample sizes that were too small were excluded.

Inclusion Criteria

(a) Both retrospective and prospective studies were included. (b) The study population was patients with LNM of PTC who had undergone thyroidectomy, and the diagnosis was confirmed by ultrasound-guided fine-needle aspiration biopsy (FNAB). (c) Patients received only one modality of LA, RFA, or MWA. (d) Detailed data were reported, including the number, size, and volume of affected lymph nodes at the initial diagnosis and follow-up, the rate of recurrence and distant metastasis, complications, and serum Tg level.

Exclusion Criteria

(a) Cases that were given more than one treatment. (b) Lack of a detailed description of the lymph nodes and patient numbers, effective rate, recurrence rate, metastasis rate, and complications. (c) There was only a primary lesion without lymph node metastasis. (d) The follow-up was less than six months.

Data Extraction

We extracted the following data from the 11 studies into the data form: (a) First author, affiliation, year of publication, study design; (b) The number, age, and sex ratio of the cases; (c) Ablation treatment, the type, size, and volume of metastatic lymph nodes, ablation time and energy, changes of lymph nodes during follow-up (1 month, 3 months, 6 months, 12 months, 18 months, and 24 months); (d) The incidence of complications, local recurrence rate, distant metastasis rate, the proportion of complete disappearance of lymph node metastasis, the average volume reduction rate, the Tg level.

Complications: There were two kinds of complications: major complications and minor complications. Major complications may lead to permanent sequelae or death, while minor complications do not cause sequelae and can be corrected in a short time (23, 24). For example, hypothyroidism and irreversible voice changes are regarded as major complications, while bleeding, fever, cough, and temporary hoarseness are minor complications.

In the included studies, "no cancer seeding", "lymph nodes undetectable", "complete remission", "nodes were negative", "completely disappeared" mean complete disappearance; "remained detectable", "partial response", "nodes positive", and

"scar-like" implied that they had not disappeared completely. FNAB detects local recurrence in the ablated lymph nodes' central and marginal areas; "no regeneration" represents no local recurrence. Words such as "local control" refer to the absence of distant metastases.

Data Synthesis and Statistical Analysis

We conducted a meta-analysis on the extracted data to obtain the average volume reduction rate and subgroup analysis of the reduction rate of Tg levels in serum at same time. Then, we analyzed and described the proportion of complete disappearance, local recurrence rate, distant metastasis rate, and incidence of complications of metastatic lymph nodes of primary PTC after the main treatment. To calculate and guarantee the objectivity of the data, the fixed-effects model and random-effects model were both adopted (25). Also, we conducted between-group difference by analyzing part with sufficient data. After that, we calculated heterogeneity using the inconsistency index I^2 (I^2 > 25% suggests low heterogeneity; I^2 > 50%, moderate; and I^2 > 75%, high) with the Q statistic and P value (26). When P > 0.05 and I^2 < 50%, we chose the fixed-effects model; in contrast, we used the Hartung-Knapp-Sidik-Jonkman random-effects model to avoid false-positives when there was high heterogeneity and low quality of the studies, with P ≤ 0.05 and I^2 > 50% (27–29).

For the pooled estimated outcome, we used the correlation analysis method to calculate the major complication rate and overall complication rate, as well as the complete disappearance rate, with forest plots and subgroup plots. We also drew 2 funnel plots to show the publication bias of the overall complication rate and complete disappearance rate. Considering that the number of included documents was greater than 10, we used Peter's examination to evaluate the publication bias. After deleting invalid data, both the major complication rate and disappearance rate were corrected using the trim and fill method, and a funnel plot was used to show the publication bias (30, 31). Peter's linear regression asymmetry test was used to test the statistical significance (32, 33) (P < 0.01 means a significant bias).

Quality assessment of the statistical analyses was calculated by RevMan 5.4 software, and other statistical analyses were calculated by R studio 1.4 (R version 3.6.2) with the "meta" and "metafor" packages.

RESULTS

Literature Search

The search process is shown in **Figure 1**. We searched 1449 papers, of which 11 papers, 208 cases, and 412 lymph nodes were finally selected after applying the inclusion/exclusion criteria. After removing 675 duplicated records, we excluded 743 studies, including those not in the field of interest (684), case reports (36), and review articles (23). The full-text screening was conducted on the remaining 31 studies, and only 11 met the inclusion criteria. Although the publication date of the articles was not restricted, the selected studies were all published after 2009, with a certain degree of timeliness and adaptability.

Literature Quality

The data were extracted by one author and verified by another to ensure accuracy and validity.

With the help of the built-in tailored questionnaire system and criteria provided by the Quality Assessment of Diagnostic Accuracy Studies-2 (QUADAS-2), as well as the image generation tool of Review Manager 5.4 software (34, 35), the two reviewers independently evaluated the methodological quality of the 11 included studies. The outcome is shown below (**Figure 2**).

Characteristics of the Included Studies

The detailed features of the 11 included studies (3, 4, and 4 studies treated with RFA, MWA, and LA, respectively) are shown in **Table 1**; 9 studies were retrospective, and 2 were prospective. After a preliminary study of the demographic characteristics of the patients, we found that the mean ages of these patients ranged between 37.2 and 63.2 years, and approximately 64.0% (133/208) of the patients were women. Among the 11 studies, 3 were European (44 cases), and the remaining 8 were Asian (164 cases). The mean follow-up time after the treatment was greater than 8.4 months.

Changes in the Lymph Nodes Volume After LA, RFA and MWA

The overall pooled estimates for the standardized mean difference (SMD) of tumor volume (the unit is mm^3) from baseline or before thermal ablation to the last follow-up after therapy (6 studies involved) are summarized in **Figure 3A** with corresponding forest plots. Using the random-effects model, RFA, MWA, and LA all induced a statistically significant reduction in nodule volume after

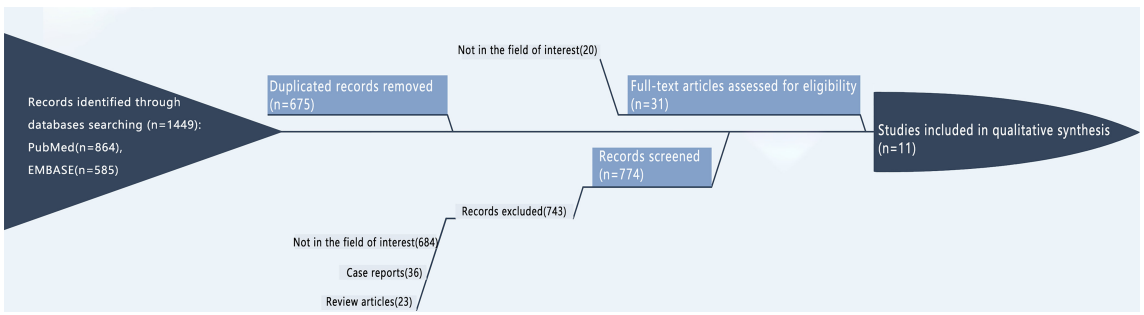

FIGURE 1 | Flow diagram of study screening.

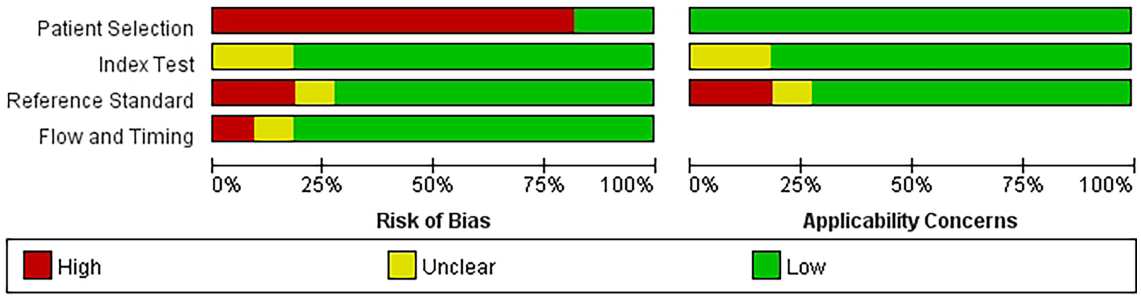

FIGURE 2 | Quality Assessment of Diagnostic Accuracy Studies-2.

ablation (I^2 = 64%, τ^2 = 0.3438, P = 0.02). Pooled SMD is 1.53 (95% Confidence interval(CI): -2.24; -0.82). **Figure 3B** also shows a great reduction rate (the unit is %) of lymph node volume change (I^2 = 71%, τ^2 = 0.1439, P < 0.01). We used both the fixed-effects model and the random-effects model to calculate the pooled reduction rate, which was 0.94 (95% CI: 0.92; 0.96) and 0.93 (95% CI: 0.87; 0.97), respectively.

Changes in the Serum Tg Level After LA, RFA and MWA

Figure 4A indicates that the serum Tg level (8 studies involved) showed a statistically significant decrease after thermal ablation (I^2 = 79%, t^2 = 0.4953, P < 0.01). The pooled SMD is -1.41 (95% CI: -2.08; -0.73) and no difference between groups. From the funnel diagram in **Figure 4B**, it can be seen that the points are evenly distributed, but there is great heterogeneity, which cannot be avoided.

Frequencies of Complete Disappearance and Effective Rate After LA, RFA and MWA

The comparison between frequencies of complete disappearance (7 studies involved) is shown in **Figure 5A** (I^2 = 72%, τ^2 = 4.9612, P < 0.01) (correlation coefficient(COR) = 0.72, 95% CI: 0.66; 0.76; COR = 0.82, 95% CI: 0.43; 0.96) and **Figure 5B**. The outcome of subgroup analysis showed complete disappear rate which LA is higher than

TABLE 1 | Characteristics of the included studies.

First author	Affiliation (study period)	Year	Design	Type of thermal ablation	No. Patients	No. MLN	Age mean±SD	male/ female	follow-up (months) mean±SD
Guang et al. (9)	Chinese PLA General Hospital,China (2013~2014)	2017	retrospective	RFA	33	54	43.7±10.7 (22~67)	11/22	21±4 (12-24)
Lim et al. (22)	Department of Radiology, Seoul Soonchunhyang University Hospital, Yongsan-Gu Seoul, Korea (2008~2012)	2015	retrospective	RFA	39	61	52.8± 16.7 (21–92)	14/25	26.4±13.7
Wang et al. (10)	Zhejiang Cancer Hospital, Hangzhou, China (2013~2014)	2014	retrospective	RFA	8	20	43.6±9.3 (30~58)	1/7	9.4±5.1 (6-20)
Zhou et al. (11)	Rui Jin Hospital of Shanghai Jiao Tong University,China (2017~2018)	2019	retrospective	MWA	14	21	45.1±12.1 (30~64)	3/11	8.4±4.1 (3-18)
Teng et al. (12)	China-Japan Union Hospital of Jilin University,China (2014~2015)	2018	retrospective	MWA	11	24	40.36 ±10.52 (31~59)	3/8	32 (no details)
Cao et al. (18)	China-Japan Friendship Hospital, Beijing, China (2015~2018)	2020	retrospective	MWA	14	38	46.9 ±11.9 (28-73)	3/11	23.6±9.3 (12-36)
Han et al. (19)	Chinese People's Liberation Army General Hospital (2015~2020)	2020	retrospective	MWA	37	98	43.58 ±13.77 (14-74)	17/20	11.09 ±9.21
Papini et al. (14)	Italian thyroid center (2009~2010)	2013	prospective	LA	5	8	53.6±18.3	1/4	12 (no details)
Mauri et al. (13)	A public hospital (2010~2012)	2013	retrospective	LA	15	24	62±14 (32~80)	8/7	12 (no details)
Mauri et al. (15)	Division of Interventional Radiology, European Institute of Oncology, Milan, Italy. (2010~2013)	2016	retrospective	LA	24	46	63.2±13.2 (32~80)	11/13	30±11 (12-45)
Guo et al.* (16)	The First Affiliated Hospital of Guangxi Medical University (2016~2017)	2020	prospective	LA	8	18	37.2±15.94 (18~72)	3/5	12 (no details)

**Paper from Guo et al. have been deleted benign nodes data.*

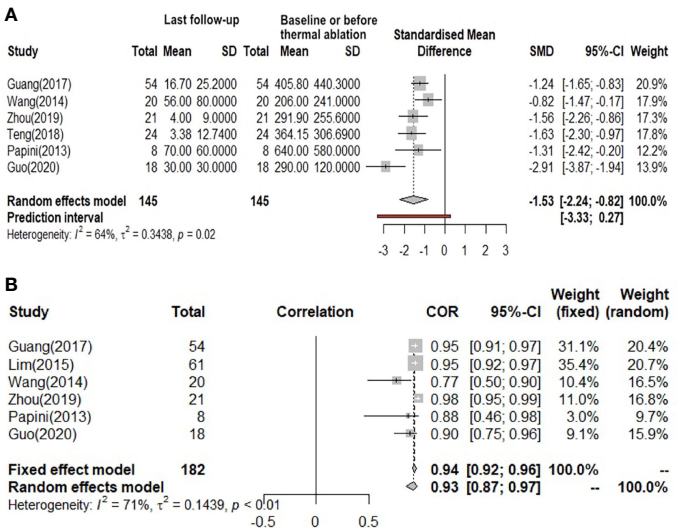

FIGURE 3 | **(A)** Before and after changes in the volume of lymph nodes. **(B)** The reduction rate of lymph nodes volume.

RFA, while MWA cannot entail in the conclusion because of its statistical significance. Since the number of data points was less than 10, we used Peters' test to calculate publication bias. After using the trim and filled model for correction, the outcome is presented in the form of forest plots, with low publication bias (**Figure 5B**) (36). Wang (2014) and Mauri (2013) have effective rates of 0.75 and 0.73, and Han did not report this data, but all of the other studies have an effective rate of 100%. So, the overall effective rate is 97.67% (210/215). In the analysis, we can see that the effective rate is very high, while the complete disappearance rate is relatively low.

Frequencies of Recurrence and Distant Metastasis After LA, RFA and MWA

After resection of the primary tumor, a series of ablation treatments for metastatic lymph nodes was performed. Theoretically, there is still a certain probability of local recurrence and distant metastasis. In these 11 studies (**Table 2**), six had no local recurrence or distant metastasis. Other studies had a small number of local recurrences or distant metastases. However, they were all effectively controlled after further LA, RFA, or MWA treatment. Regarding the ablation time and energy, 7 studies mentioned times ranging from 12 s to 1200 s, and 6 studies mentioned energies ranging from 70 J to 36000 J. Guo (16) thought that the ablation approach should be adjusted for the individual nodes, and we think this may be the reason for the wide variation in ablation time and energy.

Frequencies of Complications From LA, RFA and MWA

The major complication rate and overall complication rate are compared in **Figure 6** and **Figure 7A**, in which we can see I^2 =

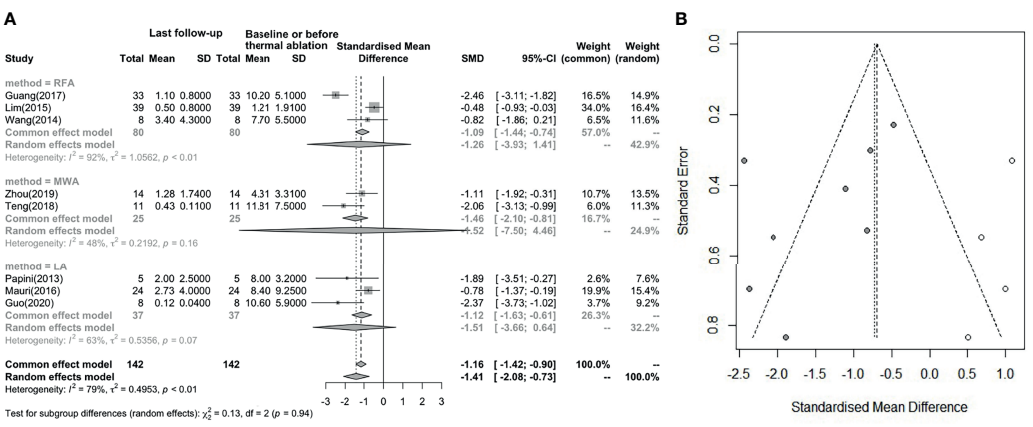

FIGURE 4 | **(A)** Before and after changes in serum Tg level. **(B)** Revised funnel plots of changing in serum Tg level.

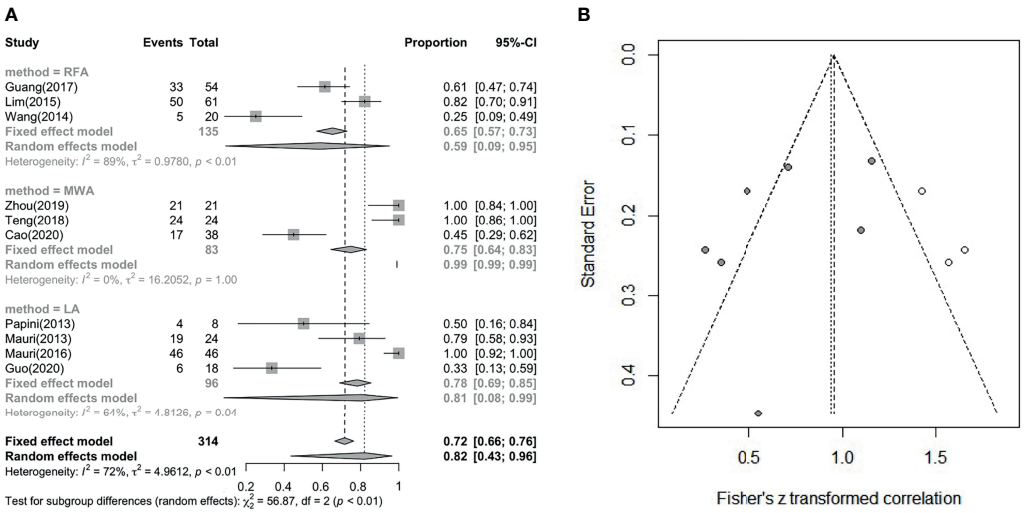

FIGURE 5 | **(A)** Pooled complete disappearance rate. **(B)** Revised funnel plots of complete disappearance rate.

0%, P = 1.00, showing that there is no statistically significant difference (P > 0.05), although the heterogeneity is low (**Figure 7B**). Therefore, there was no difference between the two complication ratios. On the other hand, the incidence of the major complication rate was 1/208 (0.48%), and the overall complication rate was 11/208 (5.29%). The incidence of complications remains low, and the safety of the treatment is guaranteed and there is no subgroup difference.

DISCUSSION

This meta-analysis showed that US-guided thermal ablation is a valid therapeutic method for LNM of PTC. RFA, MWA and LA all resulted in a significant reduction in metastatic lymph nodes (P = 0.02), and the reduction rate was 93%-94% (P < 0.01). In addition, during the follow-up process ranging from 6 to 24 months, the patient's diseased lymph node size was effectively controlled, and the serum Tg level was also effectively improved (P < 0.01), this is similar with a latest meta-analysis (37). However, we performed a pooled summary analysis of the main complications and overall complications, and a detailed subgroup analysis of the complete disappearance rate was performed. In the pooled analyses of the complete disappearance rate, the effective rate, and the major and overall complications (including major and minor complications), we found that there were few complications after thermal ablation (P = 1 not statistically significant). Almost all complications were minor and disappeared over time. Furthermore, almost all subgroup analysis showed no significant difference among thermal ablation methods, only except for LA is better than RFA in complete disappearance rate. In addition, we carried out the bias correction of the funnel plot for each forest plot, so that the bias of the article cases can be more clearly reflected. We use statistical analysis to specify each P value, and the results are more reliable and have certain clinical significance.

TABLE 2 | Recurrence rate and distant metastasis situation associated with ablated time and energy.

Author	Local recurrence	Distant metastasis	Ablated time (s)	Ablated energy (J)
Guo (2020) (16)	0	0	Depend on individual nodes	Depend on individual nodes
Teng (2018) (12)	0	0	75.63 ± 45.44 (12-174)	1512.5 ± 908.8 (240-3480)
Zhou (2019) (11)	0	0	93.9 ± 56.9 (30-190)	NA
Cao (2020) (18)	0	0	NA	NA
Han (2020)* (19)	0	0	206.55 ± 193.59	NA
Guang (2017)* (9)	0	1	140.7 ± 88.4 (24-447)	426.7 ± 279.8 (70-1320)
Wang (2014)* (10)	0	1	162 (30-360)	NA
Papini (2013) (14)	0	2	NA	942 ± 342 (573-1574)
Mauri (2013) (13)	5	3	NA	1200-4200
Mauri (2016) (15)	4	3	300-600	1200-4200
Lim (2015) (22)	0	0	243.5 ± 264.7 (33-1200)	3936.4 ± 5960.9 (370-36000)

Han (2020): Patients with local recurrence or distant metastasis during follow-up were excluded.*
Guang (2017):During the 12-month follow-up, distant metastasis was found in one patient, and was successfully ablated later.*
Wang (2014): Two new cervical recurrent lymph nodes occurred in one case, which was finally ablated.*

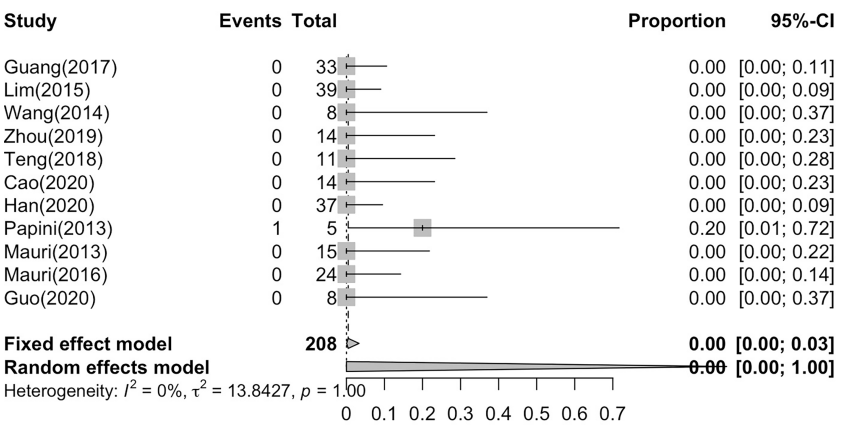

FIGURE 6 | Pooled major complication rate.

In some other documents, these three thermal ablation treatments were compared with surgical treatments for different thyroid diseases, and they all showed effectiveness and safety at different levels, including lower complication rates and only minor side effects. Therefore, they are considered to be better alternatives to surgical treatment (6–8, 38–40). In all of the analyses performed, statistically significant data showed the effectiveness of all three thermal ablation methods. Although there were some metastases and complications in some literature reports, all of them returned to normal after intervention during the follow-up process, so they were classified as minor complications. In addition, in this meta-analysis, no case reported life-threatening or irreversible complications, so thermal ablation is suitable for treating LNM of PTC. These findings are consistent with previous research findings, many literatures have shown the effectiveness and safety of the three thermal ablation methods for various types of thyroid nodules and lymph nodes (41, 42). In the ablation of thyroid nodules, some literatures have compared RFA with LA and found that RFA is faster than LA which led to a conclusion that regeneration is less but requires higher energy (43, 44). There is also literature comparing RFA and MWA, suggesting that RFA may have a better long-term effect in reducing nodule volume (45).

Based on the results of this systematic review and meta-analysis, we still feel very encouraging and confident for clinicians to perform promising and innovative treatment methods for patients who cannot tolerate surgery or explicitly refuse surgery. This ought to improve patient outcomes and allow them to avoid the physical and mental trauma caused by multiple surgeries. During the execution of thermal ablation therapy, patients received local anesthesia, and injected an isolation fluid around the lymph nodes to prevent thermal injury to important anatomy such as peripheral blood vessels and nerves (16, 18). This also ensures the effectiveness and safety of the treatment. In addition, percutaneous TA treatment has good feasibility and reproducibility, it can be performed many times until the desired therapeutic effect is achieved, and without increased technical difficulties due to the previous treatments. This is undoubtedly a gratifying gospel for patients with multiple recurrence of lymph nodes.

When summarizing the heterogeneity of all studies (46, 47), we found that the heterogeneity of the major complication rate and overall complication rate were 0 (but not statistically significant), but the rest of the outcomes showed the characteristics of medium-to-high heterogeneity (I^2 > 50%). Although we used both fixed-effects and random-effects models, subgroup analysis should also be used to obtain each characteristic of the three thermal treatments. However, since there are relatively few studies reporting on each modality at present, the cases we have obtained are relatively limited. We hope that we can obtain more comprehensive information on thermal ablation in the future.

The present meta-analysis also has several limitations. First, the sample size of the studies was limited, and most were retrospective, which may have affected the accuracy of the results. Second, after summarizing the data of these three thermal ablation methods (RFA, MWA, LA), we found that doctors use different ablation strategies for different patients (including the time, frequency, and energy of ablation). Therefore, a multicenter and large sample study is needed to determine a more standardized and unified ablation strategy. In addition, our research regards the situation of last control as the final result, so detailed analysis during long-term follow-up was not conducted. For clinical guidance, we can conclude that the use of thermal ablation has a good therapeutic effect on LNM of PTC. It can reduce the volume of the lymph nodes to a large extent, but it requires additional long-term follow-up to pay attention to the disease factors.

In general, by analyzing the three thermal ablation treatments, we found that thermal ablation is safe and efficacious and will be an option for treatment with great potential for LNM in the future. However, its limitations include a lack of standardized procedures and the requirement for experienced doctors, and longer-term follow-up periods are necessary.

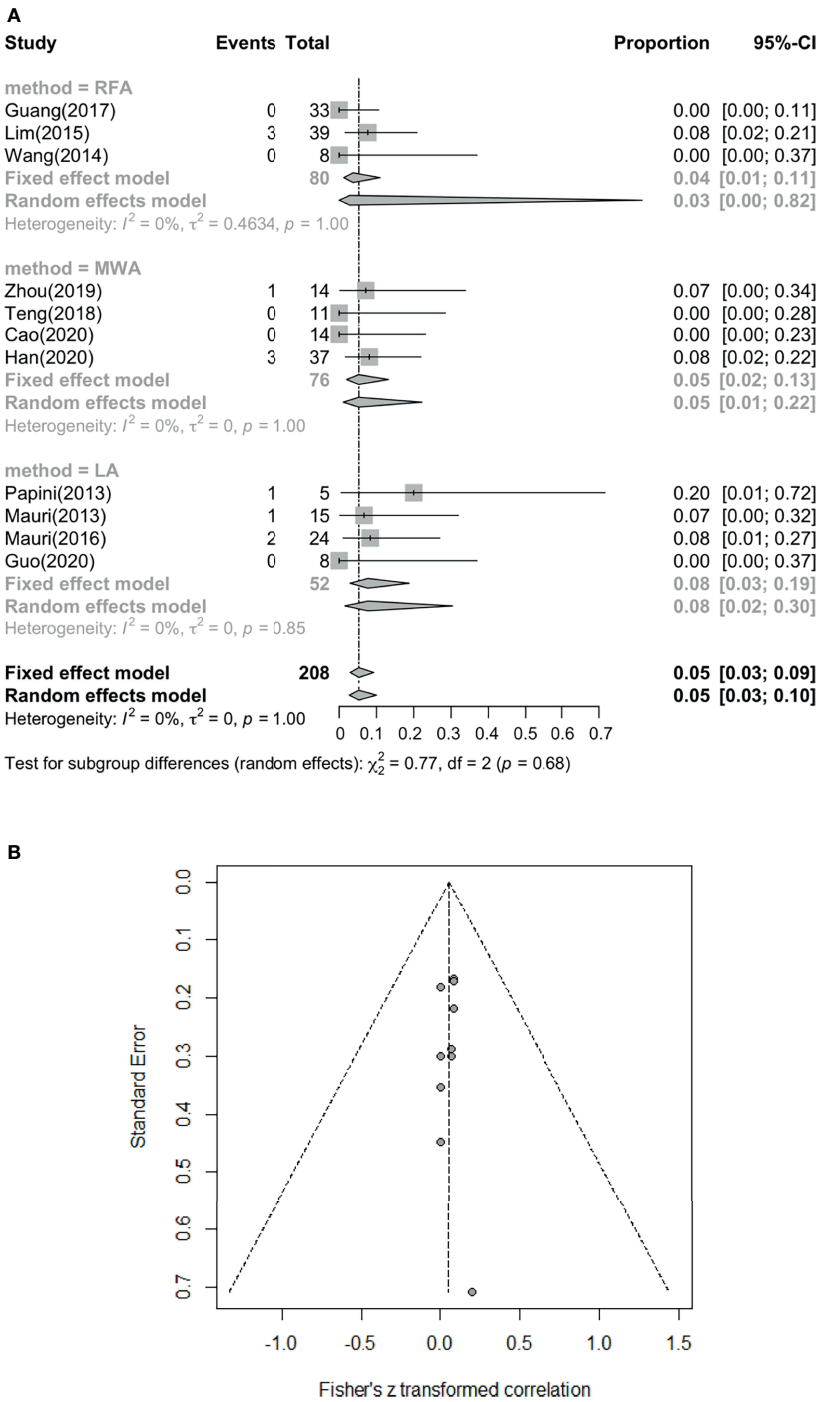

FIGURE 7 | **(A)** Pooled overall complication rate. **(B)** Funnel plots of overall complication rate.

DATA AVAILABILITY STATEMENT

The original contributions presented in the study are included in the article/supplementary material. Further inquiries can be directed to the corresponding authors.

AUTHOR CONTRIBUTIONS

Guarantors of integrity of entire study: ZD, JC, XC, and LS. Literature research: ZD, JC, XC, and LS. Study concepts/study design: all authors. Contributed to acquisition of data: ZD and

JC. Contributed reagents/materials/analysis tools: ZD and JC. Manuscript drafting or manuscript revision: all authors. Statistical analysis: all authors. All authors contributed to the article and approved the submitted version.

ACKNOWLEDGMENTS

We appreciate Dr. Gaoxing Zheng from Zhongshan First Hospital Affiliated to Fudan University for his time and advice to debugging our code.

REFERENCES

1. Morris LG, Sikora AG, Tosteson TD, Davies L. The Increasing Incidence of Thyroid Cancer: The Influence of Access to Care. *Thyroid* (2013) 23(7):885–91. doi: 10.1089/thy.2013.0045
2. Lee KE, Chung IY, Kang E, Koo do H, Kim KH, Kim SW, et al. Ipsilateral and Contralateral Central Lymph Node Metastasis in Papillary Thyroid Cancer: Patterns and Predictive Factors of Nodal Metastasis. *Head Neck* (2013) 35 (5):672–6. doi: 10.1002/hed.23016
3. Dupuy DE, Goldberg SN. Image-Guided Radiofrequency Tumor Ablation: Challenges and Opportunities–Part II. *J Vasc Interv Radiol* (2001) 12 (10):1135–48. doi: 10.1016/s1051-0443(07)61670-4
4. Wyse G, Hong H, Murphy K. Percutaneous Thermal Ablation in the Head and Neck: Current Role and Future Applications. *Neuroimaging Clin N Am* (2009) 19(2):161–8. doi: 10.1016/j.nic.2009.01.004. Table of Contents.
5. Shen K, Xue S, Xie Y, Wang H, Li J, Sun Y, et al. Comparison of Thermal Ablation and Routine Surgery for the Treatment of Papillary Thyroid Microcarcinoma: A Systematic Review and Meta-Analysis. *Int J Hyperthermia* (2020) 37(1):913–24. doi: 10.1080/02656736.2020.1777331
6. Che Y, Jin S, Shi C, Wang L, Zhang X, Li Y, et al. Treatment of Benign Thyroid Nodules: Comparison of Surgery With Radiofrequency Ablation. *AJNR Am J Neuroradiol* (2015) 36(7):1321–5. doi: 10.3174/ajnr.A4276
7. Zhang M, Tufano RP, Russell JO, Zhang Y, Zhang Y, Qiao Z, et al. Ultrasound- Guided Radiofrequency Ablation Versus Surgery for Low-Risk Papillary Thyroid Microcarcinoma: Results of Over 5 Years' Follow-Up. *Thyroid* (2020) 30(3):408–17. doi: 10.1089/thy.2019.0147
8. Zhou W, Ni X, Xu S, Zhang L, Chen Y, Zhan W. Ultrasound-Guided Laser Ablation Versus Surgery for Solitary Papillary Thyroid Microcarcinoma: A Retrospective Study. *Int J Hyperthermia* (2019) 36(1):897–904. doi: 10.1080/02656736.2019.1649475
9. Guang Y, Luo Y, Zhang Y, Zhang M, Li N, Zhang Y, et al. Efficacy and Safety of Percutaneous Ultrasound Guided Radiofrequency Ablation for Treating Cervical Metastatic Lymph Nodes From Papillary Thyroid Carcinoma. *J Cancer Res Clin Oncol* (2017) 143(8):1555–62. doi: 10.1007/s00432-017-2386-6
10. Wang L, Ge M, Xu D, Chen L, Qian C, Shi K, et al. Ultrasonography-Guided Percutaneous Radiofrequency Ablation for Cervical Lymph Node Metastasis From Thyroid Carcinoma. *J Cancer Res Ther* (2014) 10 Suppl:C144– 9. doi: 10.4103/0973-1482.145844
11. Zhou W, Chen Y, Zhang L, Ni X, Xu S, Zhan W. Percutaneous Microwave Ablation of Metastatic Lymph Nodes From Papillary Thyroid Carcinoma: Preliminary Results. *World J Surg* (2019) 43(4):1029–37. doi: 10.1007/s00268-018-04879-8
12. Teng D, Ding L, Wang Y, Liu C, Xia Y, Wang H. Safety and Efficiency of Ultrasound-Guided Low Power Microwave Ablation in the Treatment of Cervical Metastatic Lymph Node From Papillary Thyroid Carcinoma: A Mean of 32 Months Follow-Up Study. *Endocrine* (2018) 62(3):648–54. doi: 10.1007/s12020-018-1711-4
13. Mauri G, Cova L, Tondolo T, Ierace T, Baroli A, Di Mauro E, et al. Percutaneous Laser Ablation of Metastatic Lymph Nodes in the Neck From Papillary Thyroid Carcinoma: Preliminary Results. *J Clin Endocrinol Metab* (2013) 98(7):E1203–7. doi: 10.1210/jc.2013-1140
14. Papini E, Bizzarri G, Bianchini A, Valle D, Misischi I, Guglielmi R, et al. Percutaneous Ultrasound-Guided Laser Ablation is Effective for Treating Selected Nodal Metastases in Papillary Thyroid Cancer. *J Clin Endocrinol Metab* (2013) 98(1):E92–7. doi: 10.1210/jc.2012-2991
15. Mauri G, Cova L, Ierace T, Baroli A, Di Mauro E, Pacella CM, et al. Treatment of Metastatic Lymph Nodes in the Neck From Papillary Thyroid Carcinoma With Percutaneous Laser Ablation. *Cardiovasc Intervent Radiol* (2016) 39 (7):1023–30. doi: 10.1007/s00270-016-1313-6
16. Guo Y, Li Z, Wang S, Liao X, Li C. Single-Fiber Laser Ablation in Treating Selected Metastatic Lymph Nodes of Papillary Thyroid Carcinoma and Benign Cold Thyroid Nodules-Preliminary Results. *Lasers Surg Med* (2020) 52(5):408– 418. doi: 10.1002/lsm.23150
17. Spartalis E, Karagiannis SP, Plakopitis N, Theodori MA, Athanasiadis DI, Schizas D, et al. Percutaneous Laser Ablation of Cervical Metastatic Lymph Nodes in Papillary Thyroid Carcinoma: Clinical Efficacy and Anatomical Considerations. *Expert Rev Med Devices* (2020) 29:1–7. doi: 10.1080/17434440.2021.1864323
18. Cao XJ, Wei Y, Zhao ZL, Peng LL, Li Y, Yu MA. Efficacy and Safety of Microwave Ablation for Cervical Metastatic Lymph Nodes Arising Post Resection of Papillary Thyroid Carcinoma: A Retrospective Study. *Int J Hyperthermia* (2020) 37(1):450–5. doi: 10.1080/02656736.2020.1759829
19. Han ZY, Dou JP, Cheng ZG, Liu FY, Yu J, Yu XL, et al. Efficacy and Safety of Percutaneous Ultrasound-Guided Microwave Ablation for Cervical Metastatic Lymph Nodes From Papillary Thyroid Carcinoma. *Int J Hyperthermia* (2020) 37(1):971–5. doi: 10.1080/02656736.2020.1805128
20. Tong M, Li S, Li Y, Li Y, Feng Y, Che Y. Efficacy and Safety of Radiofrequency, Microwave and Laser Ablation for Treating Papillary Thyroid Microcarcinoma: A Systematic Review and Meta-Analysis. *Int J Hyperthermia* (2019) 36(1):1278–86. doi: 10.1080/02656736.2019.1700559
21. Choi Y, Jung SL. Efficacy and Safety of Thermal Ablation Techniques for the Treatment of Primary Papillary Thyroid Microcarcinoma: A Systematic Review and Meta-Analysis. *Thyroid* (2020) 30(5):720–31. doi: 10.1089/thy.2019.0707
22. Lim HK, Baek JH, Lee JH, Kim WB, Kim TY, Shong YK, et al. Efficacy and Safety of Radiofrequency Ablation for Treating Locoregional Recurrence From Papillary Thyroid Cancer. *Eur Radiol* (2015) 25(1):163–70. doi: 10.1007/s00330-014-3405-5
23. Saad WE, Wallace MJ, Wojak JC, Kundu S, Cardella JF. Quality Improvement Guidelines for Percutaneous Transhepatic Cholangiography, Biliary Drainage, and Percutaneous Cholecystostomy. *J Vasc Interv Radiol* (2010) 21(6):789–95. doi: 10.1016/j.jvir.2010.01.012
24. Rolston JD, Englot DJ, Cornes S, Chang EF. Major and Minor Complications in Extraoperative Electrocorticography: A Review of a National Database. *Epilepsy Res* (2016) 122:26–9. doi: 10.1016/j.eplepsyres.2016.02.004
25. Harrer M, Cuijpers P, Furukawa TA, Ebert DD. *Doing Meta-Analysis With R: A Hands-on Guide (1st Ed.)*. Boca Raton: Chapman and Hall/CRC (2021). Available at: https://doi.org/10.1201/9781003107347.
26. Higgins JP, Thompson SG, Deeks JJ, Altman DG. Measuring Inconsistency in Meta-Analyses. *BMJ* (2003) 327(7414):557–60. doi: 10.1136/bmj.327.7414.557
27. Wiksten A, Rücker G, Schwarzer G. Hartung-Knapp Method is Not Always Conservative Compared With Fixed-Effect Meta-Analysis. *Stat Med* (2016) 35 (15):2503–15. doi: 10.1002/sim.6879
28. Makambi KH. The Effect of the Heterogeneity Variance Estimator on Some Tests of Treatment Efficacy. *J Biopharm Stat* (2004) 14(2):439–49. doi: 10.1081/BIP-120037191
29. IntHout J, Ioannidis JP, Borm GF. The Hartung-Knapp-Sidik-Jonkman Method for Random Effects Meta-Analysis Is Straightforward and Considerably Outperforms the Standard Dersimonian-Laird Method. *BMC Med Res Methodol* (2014) 14:25. doi: 10.1186/1471-2288-14-25
30. Duval S, Tweedie R. Trim and Fill: A Simple Funnel-Plot-Based Method of Testing and Adjusting for Publication Bias in Meta-Analysis. *Biometrics* (2000) 56(2):455–63. doi: 10.1111/j.0006-341x.2000.00455.x
31. Rothstein HR, Sutton AJ, Borenstein M. Publication Bias in Meta-Analysis. *Publ Bias Meta-Analysis: Prevention Assess Adjustments* (2005), 1–7. doi: 10.1002/0470870168.ch1
32. Egger M, Davey Smith G, Schneider M, Minder C. Bias in Meta-Analysis Detected by a Simple, Graphical Test. *BMJ* (1997) 315(7109):629–34. doi: 10.1136/bmj.315.7109.629
33. Sterne JA, Sutton AJ, Ioannidis JP, Terrin N, Jones DR, Lau J, et al. Recommendations for Examining and Interpreting Funnel Plot Asymmetry in Meta-Analyses of Randomised Controlled Trials. *BMJ* (2011) 343:d4002. doi: 10.1136/bmj.d4002

34. Whiting PF, Rutjes AW, Westwood ME, Mallett S, Deeks JJ, Reitsma JB, et al. QUADAS-2: A Revised Tool for the Quality Assessment of Diagnostic Accuracy Studies. *Ann Intern Med* (2011) 155(8):529–36. doi: 10.7326/0003-4819-155-8-201110180-00009
35. Ma LL, Wang YY, Yang ZH, Huang D, Weng H, Zeng XT. Methodological Quality (Risk of Bias) Assessment Tools for Primary and Secondary Medical Studies: What are They and Which is Better? *Mil Med Res* (2020) 7(1):7. doi: 10.1186/s40779-020-00238-8
36. Duval S. The Trim and Fill Method[. *Publ Bias Meta-Analysis: Prevention Assess Adjustments* (2005), 127–44. doi: 10.1002/0470870168.ch8
37. Qiu Y, Xing Z, He Y, Liu J, Yang Q, Luo Y. Ultrasound-Guided Thermal Ablation for Cervical Lymph Node Metastasis From Thyroid Carcinoma: A Meta-Analysis of Clinical Efficacy and Safety. (2021). doi: 10.1007/s10103-021-03428-5
38. Ha EJ, Baek JH, Lee JH. The Efficacy and Complications of Radiofrequency Ablation of Thyroid Nodules. *Curr Opin Endocrinol Diabetes Obes* (2011) 18 (5):310–4. doi: 10.1097/MED.0b013e32834a9168
39. Li J, Liu Y, Liu J, Qian L. Ultrasound-Guided Percutaneous Microwave Ablation Versus Surgery for Papillary Thyroid Microcarcinoma. *Int J Hyperthermia* (2018) 34(5):653–9. doi: 10.1080/02656736.2018.1453092
40. Zhang J, Yan L, Diao Z, Chen H, Cheng J. Potential Threat of Tracheal Diverticulum to Thermal Ablation Treatment of Thyroid Nodule. *Advanced Ultrasound Diagnosis Ther* (2019) 3(1):6–11. doi: 10.37015/AUDT.2019.190802
41. Cui T, Jin C, Jiao D, Teng D, Sui G. Safety and Efficacy of Microwave Ablation for Benign Thyroid Nodules and Papillary Thyroid Microcarcinomas: A Systematic Review and Meta-Analysis. *Eur J Radiol* (2019) 118:58–64. doi: 10.1016/j.ejrad.2019.06.027
42. Ben Hamou AB, Ghanassia E, Espiard S, Abi Rached H, Jannin A, Correas JM, et al. Safety and Efficacy of Thermal Ablation (Radiofrequency and Laser): Should We Treat All Types of Thyroid Nodules? †. *Int J Hyperthermia* (2019) 36(1):666–76. doi: 10.1080/02656736.2019.1627432
43. Mauri G, Cova L, Monaco CG, Sconfienza LM, Corbetta S, Benedini S, et al. Benign Thyroid Nodules Treatment Using Percutaneous Laser Ablation (PLA) and Radiofrequency Ablation (RFA). *Int J Hyperthermia* (2017) 33 (3):295–9. doi: 10.1080/02656736.2016.1244707
44. Cho SJ, Baek JH, Chung SR, Choi YJ, Lee JH. Long-Term Results of Thermal Ablation of Benign Thyroid Nodules: A Systematic Review and Meta-Analysis. *Endocrinol Metab (Seoul)* (2020) 35(2):339–50. doi: 10.3803/EnM.2020.35.2.339
45. Guo DM, Chen Z, Zhai YX, Su HH. Comparison of Radiofrequency Ablation and Microwave Ablation for Benign Thyroid Nodules: A Systematic Review and Meta-Analysis. *Clin Endocrinol (Oxf)* (2021) 95(1):187–96. doi: 10.1111/cen.14438
46. Higgins JP, Thompson SG. Quantifying Heterogeneity in a Meta-Analysis. *Stat Med* (2002) 21(11):1539–58. doi: 10.1002/sim.1186
47. Huedo-Medina TB, Sánchez-Meca J, Marín-Martínez F, Botella J. Assessing Heterogeneity in Meta-Analysis: Q Statistic or I2 Index? *Psychol Methods* (2006) 11(2):193–206. doi: 10.1037/1082-989X.11.2.193

Conflict of Interest: The authors declare that the research was conducted in the absence of any commercial or financial relationships that could be construed as a potential conflict of interest.

frontiers | Frontiers in Oncology

ORIGINAL RESEARCH
published: 17 May 2022
doi: 10.3389/fonc.2022.828850

The Efficacy and Safety of Transarterial Chemoembolization Plus Iodine 125 Seed Implantation in the Treatment of Hepatocellular Carcinoma With Oligometastases: A Case Series Reports

Weihua Zhang[1,2†], *Linxia Wu*[1†], *Lei Chen*[1,2†], *Yanqiao Ren*[1,2], *Tao Sun*[1,2], *Bo Sun*[1,2], *Licheng Zhu*[1,2], *Yiming Liu*[1,2*] *and Chuansheng Zheng*[1,2*]

[1] *Department of Radiology, Union Hospital, Tongji Medical College, Huazhong University of Science and Technology, Wuhan, China,* [2] *Department of Interventional Radiology, Union Hospital, Tongji Medical College, Huazhong University of Science and Technology, Wuhan, China*

Background: Patients with different primary tumor oligometastases can obtain survival benefits from external radiotherapy. The study was conducted to explore the efficacy and safety of transarterial chemoembolization (TACE) plus iodine 125 seed (TACE-I) implantation for hepatocellular carcinoma (HCC) oligometastases.

Methods: 187 patients who received TACE-I in our institution were retrospectively reviewed from January 2014 to December 2018. Thirty-two patients were included in the analysis. The primary endpoints of the study were overall survival (OS) and progression-free survival (PFS). The secondary endpoints of the study were tumor response and PFS of the metastatic sites.

Results: The median OS (mOS) of patients was 18 months, and the median PFS (mPFS) was 7 months. The objective response rate (ORR) and disease control rate (DCR) of patients three months after receiving TACE-I were 34.4% and 71.9%, respectively. The ORR and DCR of patients for metastatic sites were 50% and 81.3%, respectively. The mPFS of patients for metastatic sites was 14 months. The univariable and multivariable regression analyses indicated that the ECOG score was an independent predictor for mOS and mPFS. The number of iodine seeds and ECOG scores were independent predictors for mPFS for metastatic sites. After patients received TACE-I, the most

OPEN ACCESS

Edited by:
Giuseppe Esposito, MedStar Georgetown University Hospital, United States

Reviewed by:
Fujun Zhang, Sun Yat-sen University Cancer Center (SYSUCC), China
Xu-Hua Duan, First Affiliated Hospital of Zhengzhou University, China

***Correspondence:**
Yiming Liu
lymtongji@163.com
Chuansheng Zheng
hqzcsxh@sina.com

†These authors have contributed equally to this work

Specialty section:
This article was submitted to Cancer Imaging and Image-directed Interventions, a section of the journal Frontiers in Oncology

Received: *04 December 2021*
Accepted: *29 March 2022*
Published: *17 May 2022*

Citation:
Zhang W, Wu L, Chen L, Ren Y, Sun T, Sun B, Zhu L, Liu Y and Zheng C (2022) The Efficacy and Safety of Transarterial Chemoembolization Plus Iodine 125 Seed Implantation in the Treatment of Hepatocellular Carcinoma With Oligometastases: A Case Series Report. Front. Oncol. 12:828850. doi: 10.3389/fonc.2022.828850

common adverse events were abdominal pain, fever, and appetite. The adverse events of patients were relieved after receiving symptomatic treatments.

Conclusion: Iodine 125 seed implantation may be an effective and safe treatment for patients with hepatocellular carcinoma with oligometastasis, thereby providing a new selective option for these patients.

Keywords: hepatocellular carcinoma, oligometastasis, transarterial chemoembolization, iodine 125, efficacy, safety

INTRODUCTION

Liver cancer is one of the most common and fatal cancers (1). There are 905677 new cases of liver cancer worldwide in 2020 (2). Of these patients, approximately 90% are diagnosed with hepatocellular carcinoma (HCC) (3). Radical treatments, such as transplantation, liver resection or ablation, are recommended as the first-line treatments for patients with early HCC because they can improve the 5-year survival rate of patients (4). However, approximately 80% of patients are diagnosed with intermediate to advanced HCC because the symptoms of patients with early HCC are not obvious (5). Previous studies have shown that patients with early HCC have potential tumor metastasis, which is one of the reasons why patients with early-stage tumors still have tumor recurrence after surgery (6). HCC patients with invasion of distant organs are considered to be in an advanced stage (4). For patients with advanced HCC, Atezolizumab plus Bevacizumab therapy is recommended as a strong first-line treatment because the median overall survival of patients after Atezolizumab plus Bevacizumab therapy is 19.2 months, which is longer for patients treated with sorafenib or lenvatinib alone (7–9).

Recently, patients with tumor metastases to three organs with no more than five tumors or HCC metastases to a single organ with no more than 3 tumors were considered that they had tumors oligomestases (10). These patients have not been considered at an advanced stage because their survival times can be extended if they receive suitable treatments (11–15). Oligomestases are considered the transitional state from the intermediate to advanced stage. For these patients, the guideline does not provide exact treatments (4). However, some randomized controlled studies have shown that HCC patients with oligometastases may obtain survival benefits from external radiotherapy (16–19).

The results of external radiotherapy in the treatment of HCC patients with oligometastases are encouraging, but no study has focused internal radiotherapy on treating HCC patients with oligometastases. Iodine 125 seed implantation is an internal radiotherapy. The seeds are implanted into the tumor under the guidance of CT or ultrasound. After being implanted, the seeds emit rays to the tumor cells, which alter the DNA to kill the tumor cells (20, 21). Previous studies have shown that patients with HCC obtain survival benefits from iodine 125 seed implantation, especially when combined with transarterial chemoembolization (TACE) (22–24). However, it remains unknown whether patients with oligometastases obtain survival benefits from TACE plus iodine 125 seed implantation (TACE-I). The present study was conducted to explore the efficacy and safety of TACE-I in the treatment of HCC patients with oligometastases.

Abbreviations: HCC, Hepatocellular Carcinoma; TACE-I, Transarterial chemoembolization plus iodine 125 seed implantation; OS, Overall Survival; PFS, Progression-free Survival; ORR, Objective Response Rate; DCR, Disease Control Rate; ECOG, Eastern Cooperative Oncology Group; mRECIST, modified Respond Evaluation Criteria in Solid Tumors; EASL, European Association for the Study of the Liver.

MATERIALS AND METHODS

Patient Selection

From January 2014 to December 2018, a total of 187 HCC patients who received TACE-I were retrospectively reviewed. Thirty-two patients were included in the study based on the inclusion criteria and exclusion criteria. The study was conducted in accordance with the Declaration of Helsinki, and it was approved by the Ethics Committee Board of Tongji Medical College, Huazhong University of Science and Technology. Informed consent from the patients was waived by the board because the study was a retrospective study.

The inclusion criteria were as follows: (1) patients were diagnosed with HCC according to the EASL guidelines by imaging or biopsy (4); (2) patients received TACE-I treatment; (3) patients without portal vein tumor thrombus.

The exclusion criteria were as follows: (1) patients with no oligometastases; (2) patients received TACE or iodine 125 seed implantation before included in the study; (3) patients with Child-pugh C; (4) patients with ECOG score larger than 2; (5) patients with platelet count less than $60^{\times}10^{\wedge}9$/L; and (6) patients lost to follow-up (**Figure 1**).

TACE Procedure

TACE was performed for the treatment of intrahepatic tumors. First, a 5F catheter was introduced to the femoral artery by the Seldinger method, and it was then placed into the celiac trunk. Celiac angiography was conducted to relocate the tumor. A 5F catheter or 3F microcatheter was then introduced into the tumor feeding artery. Finally, lipiodol (10-20 ml), epirubicin (20-40 mg) and subsequent absorbable gelatin sponge particles with diameters ranging from 350 to 560 μm were injected into the tumor feeding artery.

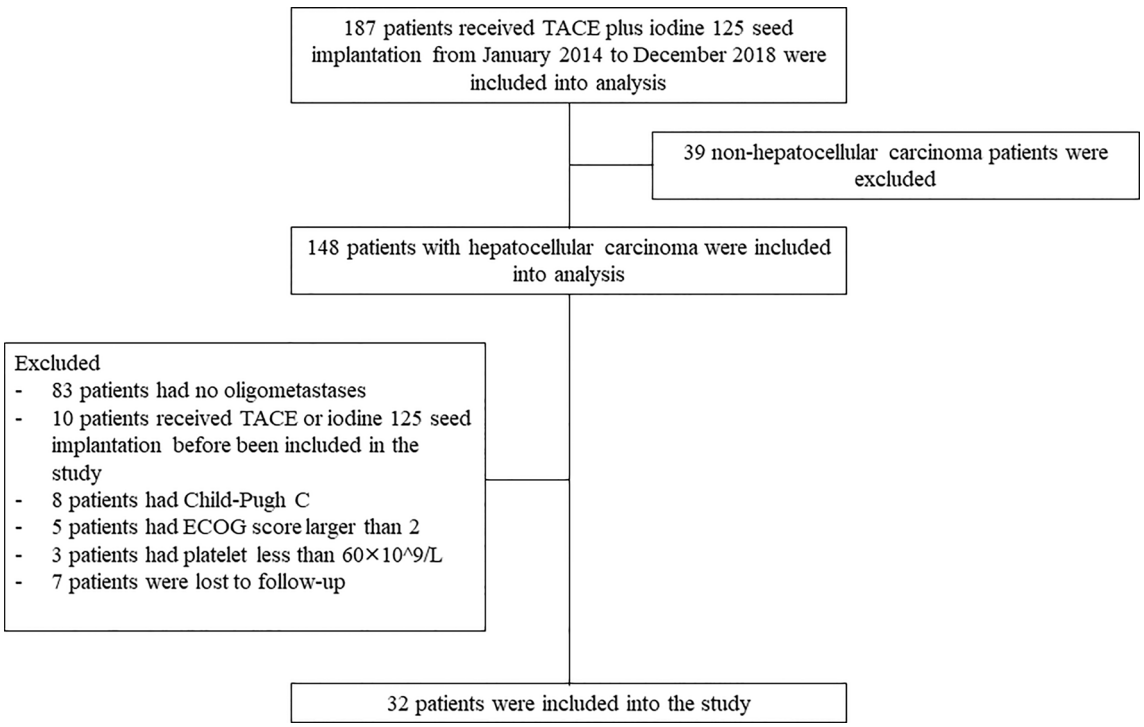

FIGURE 1 | The flowchart of patient selection.

Iodine 125 Seed Implantation Procedure

Three to seven days after the TACE protocol, iodine 125 seed implantation was performed for the treatment of extrahepatic tumors. Iodine 125 seeds, which were enclosed in NiTinol capsules, were purchased from the Institute of Atomic Energy, Beijing. Before the implantation of iodine 125 seeds, patients received a computed tomography (CT) scan, and the images were then transmitted to the treatment-planning system (TPS). The number of iodine 125 seeds was determined by TPS in accordance with the minimum peripheral dose (90–165 Gy). Under the guidance of CT and ultrasound, the iodine seeds were implanted into the tumor at intervals of 1 to 1.5 cm by 18 G needles and a turntable implantation gun (XinKe Pharmaceutical Ltd., Shanghai, China) (**Figure 2**).

Study Endpoints

The primary endpoints of the study were overall survival (OS) and progression-free survival (PFS). The secondary endpoints were PFS of the metastatic sites and disease control rate (DCR). OS was defined as the interval from the time of initial TACE to

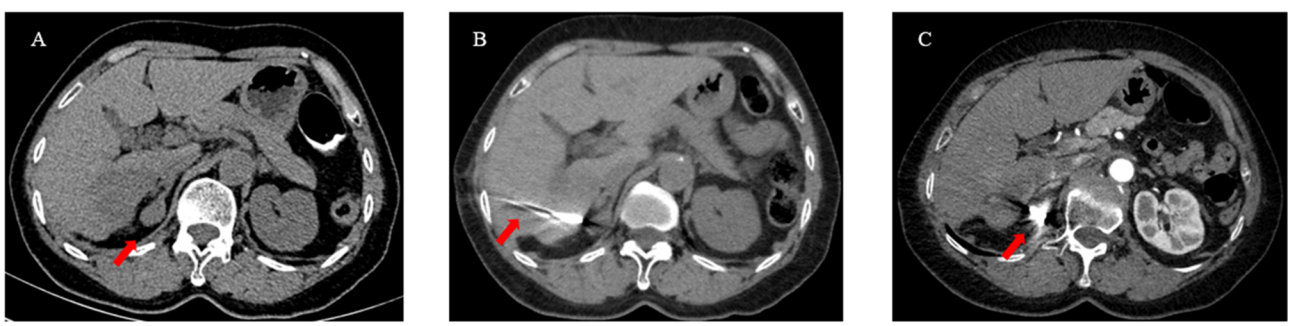

FIGURE 2 | A 63-year-old woman with HCC oligometastases. **(A)** The CT scan showed HCC oligometastasis (red arrow) in the right adrenal gland; **(B)** Under the guidance of CT, iodine 125 seeds were implanted into the metastatic by a 18G needle and turntable implantation gun (red arrow); **(C)** The CT scan showed that the Iodine 125 seeds were evenly distributed (red arrow).

the time of patient death or the end of the study. PFS was defined as the interval from the time patients received the first treatment of iodine 125 seed implantation to the time of overall tumor progression or the end of the study. The PFS of the metastatic sites was defined as the interval from the time of the initial iodine 125 seed implantation to the time of metastatic site progression or the end of the study. The DCR was defined as the ratio of patients with tumor complete response (CR), partial response (PR) or stable disease (SD) to all patients. The ORR was defined as the ratio of patients with tumor complete response (CR) or partial response (PR) to all patients. PFS and DCR were evaluated based on the modified Respond Evaluation Criteria in Solid Tumors (mRECIST) (25).

Follow Up

All patients who received TACE or iodine 125 seed implantation in the institution were followed. Patients were diagnosed with HCC oligometastases based on PET-CT, enhanced CT, enhanced MRI or whole body bone imaging. In the study, patients were required to undergo CT, MRI, ultrasound or laboratory examination every month after the initial iodine 125 seed implantation and then once every two or three months. The tumor response was evaluated by two radiologists (one with 15 years of experience and another with 8 years of experience) and one interventional radiologist (with 32 years of experience). The patients were recommended to receive another TACE or iodine 125 seed implantation if the imaging of the patients showed primary tumors, metastatic site progression or remaining tumors. The end time of the study was June 2021.

Statistical Analysis

The continuous variables were compared by the paired sample t test. The Kaplan–Meier method was used to plot the survival curves. Cox regression analysis was used to evaluate the variables that may influence the outcomes. The variables with P less than 0.05 in the univariable regression analysis were included in the multivariable regression analysis. A nested graph was used to show the changes in liver function before TACE-I and after TACE-I. All P values were two-tailed, and a P value less than 0.05 was considered statistically significant. All statistical analyses were conducted by SPSS. 26.0 (IBM Corp., Armonk, NY, USA).

RESULTS

Patient Characteristics

A total of 187 patients received TACE plus iodine 125 seed implantation from January 2014 to December 2018. Based on the inclusion criteria and exclusion criteria, 32 patients were included in the study. Among them, 5 patients received sorafenib and 2 patients received apatinib before been included into the study. 26 patients had single organ metastases, and 6 patients had multiple organ metastases. Single primary tumor was present in 14 patients, and multiple tumors were present in 18 patients. Eight patients received TACE once, and 24 patients received TACE multiple times. 25 patients received one iodine 125 seed implantation, and 7 patients received multiple iodine seed implantations (**Table 1**).

Survival Outcomes and Tumor Response

The median OS of patients with TACE-I was 18 months (95% CI: 13.9-22.1 months) (**Figure 3A**). The median PFS of patients was 7 months (95% CI: 2.8-11.2 months) (**Figure 3B**), and the median PFS of the metastatic sites was 14 months (95% CI: 10.8-17.2 months) (**Figure 3C**). The overall DCR three months after the treatment was 71.9%, and the DCR of metastatic sites was 81.3% (**Table 2**).

TABLE 1 | The baseline characteristics of patients with TACE-I.

Characteristics	TACE+Iodine 125 seed implantation
Age (years)	57.5 ± 12.5
ALT (U/L)	44 ± 32.5
AST (U/L)	43.8 ± 30.3
Leukocyte (*10^9/L)	5.1 ± 2.4
Neutrophils (*10^9/L)	4.3 ± 0.5
Lymphocytes (*10^9/L)	1.3 ± 0.6
Erythrocyte (*10^{12}/L)	4.3 ± 0.5
Platelet (*10^9/L)	146.3 ± 61.5
Primary tumor size (cm)	5.8 ± 2.8
Metastatic tumor size (cm)	3 ± 1.5
Number of iodine seeds	29.4 ± 20.8
Gender	
Male	27
Female	5
HBV	
Yes	20
No	12
Cirrhosis	
Yes	24
No	8
Primary tumor number	
1	15
≥2	17
Metastatic tumor number	
1	15
2	15
3	2
Metastatic sites	
Single organ metastases	26
Multiple organs metastases	6
AFP level	
>200	15
<200	17
TACE session	
1	8
≥2	24
Iodine 125 seeds implantation session	
1	25
≥2	7
Child-Pugh	
A	23
B	9
ECOG	
0	9
1	13
2	10

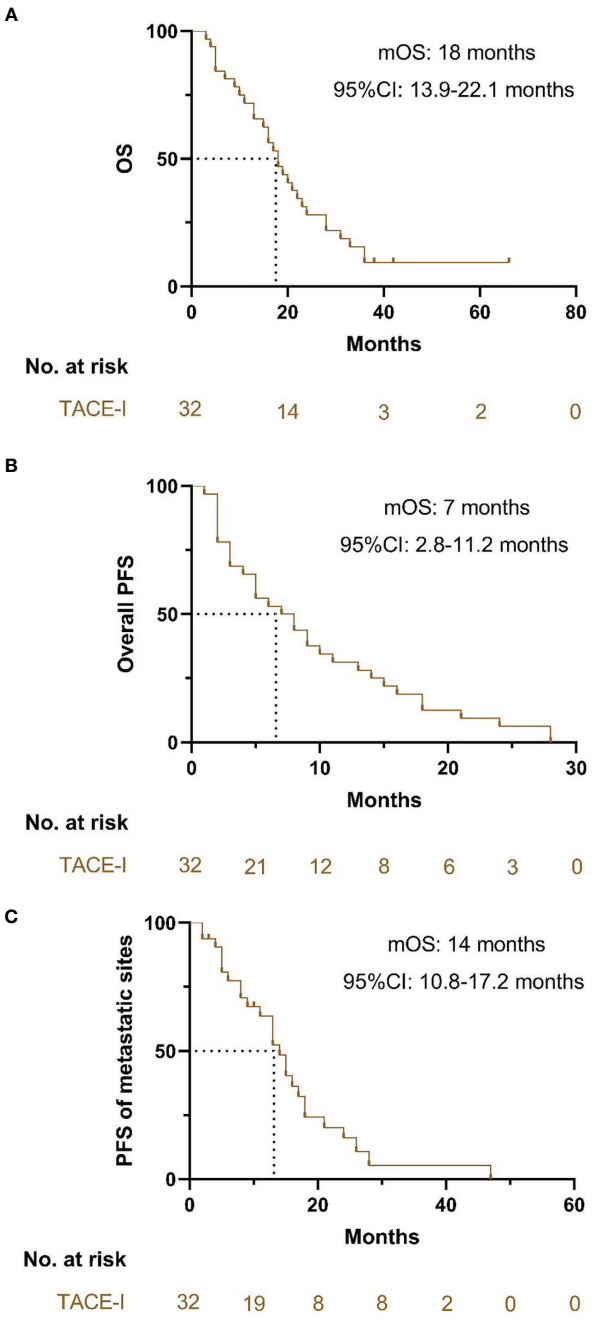

FIGURE 3 | Kaplan-Meier curves for OS, PFS and PFS of metastatic sites. **(A)** Kaplan-Meier curves for OS; **(B)** Kaplan-Meier curves for PFS; **(C)** Kaplan-Meier curves for PFS of the metastatic sites.

Predictors for OS PFS and PFS of Metastatic Sites

In the Cox regression analysis for OS, the univariable regression analysis showed that primary tumor size (HR: 1.223, 95% CI: 1.058-1.413, P=0.006) and ECOG (1 vs. 0: HR: 12.857, 95% CI: 2.664-62.043, P=0.001; 2 vs. 0: HR: 70.286, 95% CI: 11.547-427.833, P<0.001) were predictors for OS. In the multivariable regression analysis, only ECOG (1 vs. 0: HR: 13.024, 95% CI: 2.687-63.114, P=0.001) was an independent predictor for OS (**Table 3**).

In the Cox regression analysis for PFS, the univariable regression analysis showed that age (HR: 0.969, 95% CI: 0.939-0.999, P=0.046), metastatic sites (HR: 0.366, 95% CI: 0.136-0.985, P=0.047) and ECOG (2 vs. 0: HR: 10.693, 95% CI: 3.135-36.466, P<0.001) were predictors for PFS. In the multivariable regression analysis, the results showed that ECOG (2 vs. 0: HR: 9.038, 95% CI: 2.300-35.521, P=0.002) was an independent predictor for PFS. (**Table 4**)

In the Cox regression analysis for PFS of the metastatic sites, the univariable regression analysis showed that age (HR: 0.953, 95%CI: 0.918-0.989, P=0.011), number of iodine 125 seeds (HR: 1.023, 95%CI: 1.002-1.044, P=0.035) and ECOG (2 vs. 0: HR: 8.214, 95%CI: 2.152-31.345, P=0.002) were independent predictors for PFS of the metastatic sites. In the multivariable regression analysis, the results showed that the number of iodine 125 seeds (HR: 1.042, 95% CI: 1.014-1.071, P=0.004) and ECOG (2 vs. 0: HR: 15.365, 95% CI: 3.137-75.272, P=0.001) were independent predictors for PFS of metastatic sites (**Table 5**).

TABLE 2 | The tumor response for overall tumor burden and metastatic sites.

Tumor response	Overall	Metastatic sites
Complete response	2 (6.3%)	4 (12.5%)
Partial response	9 (28.1%)	12 (37.5%)
Stable disease	12 (37.5%)	10 (31.3%)
Progressive disease	9 (28.1%)	6 (18.7%)
ORR	34.4%	50%
DCR	71.9%	81.3%

Change of Liver Function and Blood Index

In the present study, the liver function and blood index before treatment and one month after treatment were evaluated. There was no statistically significant difference in alanine aminotransferase (ALT), aspartate aminotransferase (AST), leukocyte count, neutrophil count or platelet count. However, the lymphocyte count in the patients one month after receiving the treatments was lower than that in the patients before receiving the treatments (**Figure 4**).

Adverse Event Analyses

In the present study, nine adverse events of patients after receiving the treatments were reported. The most common adverse event was postembolism syndrome, including fever (53%), abdominal pain (75%), nausea (56.3%), vomiting (21.9%) and poor appetite (78.1%). There were 4 patients with headache, 5 patients with leukopenia, 3 patients with bleeding and 2 patients with radiation pneumonia. For grade III or IV adverse events, 2 patients had severe fever, 5 patients had severe abdominal pain, 1 patient had severe nausea, 1 patient had severe vomiting and 3 patients had a severely poor appetite. The adverse events were alleviated after the patients received symptomatic treatments (**Table 6**).

TABLE 3 | Univariable regression analysis and multivariable regression analysis for OS.

Characteristics	Univariable analysis		Multivariable analysis	
	HR (95%CI)	P value	HR (95%CI)	P value
Age (years)	0.979 (0.950,1.008)	0.150		
ALT (U/L)	1.010 (0.999,1.021)	0.074		
AST (U/L)	0.999 (0.988,1.009)	0.798		
Leukocyte	1.182 (0.973,1.436)	0.093		
Neutrophils	1.289 (0.989,1.679)	0.060		
Lymphocytes	0.823 (0.438,1.546)	0.544		
Erythrocyte (◊10^{12}/L)	1.590 (0.692,3.649)	0.274		
Platelet	1.006 (0.999,1.013)	0.075		
Primary tumor size (cm)	1.223 (1.058,1.413)	0.006	0.973 (0.812,1.166)	0.768
Metastatic tumor size (cm)	1.218 (0.988,1.502)	0.065		
Number of iodine seeds	1.012 (0.996,1.028)	0.146		
Gender				
Male	Ref			
Female	0.576 (0.199,1.668)	0.309		
HBV				
Yes	Ref			
No	0.890 (0.413,1.919)	0.766		
Cirrhosis				
Yes	Ref			
No	0.764 (0.309,1.885)	0.559		
Primary tumor number				
1	Ref			
≥2	1.370 (0.635,2.958)	0.423		
Metastatic tumor number				
1	Ref			
2	0.795 (0.371,1.702)	0.555		
3	0.893 (0.198,4.033)	0.883		
Metastatic sites				
Single organ metastases	Ref			
Multiple organs metastases	0.649 (0.258,1.634)	0.359		
AFP level				
>200	Ref			
<200				
TACE session				
1	Ref			
≥2	0.851 (0.408,1.776)	0.668		
Iodine 125 seeds implantation session				
1	Ref			
≥2	0.598 (0.240,1.490)	0.270		
Child-Pugh				
A	Ref			
B	1.417 (0.643,3.121)	0.387		
ECOG				
0	Ref		Ref	
1	12.857 (2.664,62.043)	0.001	13.024 (2.687,63.114)	0.001
2	70.286 (11.547,427.833)	<0.001	49.989 (7.630,327.484)	<0.001

DISCUSSION

Iodine 125 seeds alone or combined with TACE have been used in the treatment of different stages of HCC with encouraging results (22, 23). Patients with oligometastases are considered to have a transition state between an intermediate stage and an advanced stage. High-quality studies have demonstrated that these patients may obtain survival benefits from external radiotherapy (12, 17, 18). However, it remains unclear whether these patients obtain survival benefits from internal radiotherapy. The present study was conducted to explore the efficacy of TACE plus iodine 125 seed implantation in patients with HCC oligometastases.

The main findings of the present study were that patients with HCC oligometastases obtain survival benefits from TACE-I and can tolerate the treatments. In the present study, the mOS of patients was 18 months, and the mPFS of patients was 7 months. In addition, the mPFS of metastatic sites was 14 months. The mOS and mPFS of the patients in the present study were longer than the mOS and mPFS of patients with advanced HCC in previous high-quality studies. Recently, atezolizumab plus bevacizumab has been recommended as a strong first-line treatment for patients with advanced HCC instead of sorafenib and lenvatinib (weak first-line treatment) because the mOS of patients with advanced HCC who received

TABLE 4 | Univariable regression analysis and multivariable regression analysis for PFS.

Characteristics	Univariable analysis		Multivariable analysis	
	HR (95%CI)	P value	HR (95%CI)	P value
Age (years)	0.969 (0.939,0.999)	0.046	0.998 (0.964,1.033)	0.144
ALT (U/L)	1.004 (0.994,1.014)	0.437		
AST (U/L)	0.998 (0.988,1.008)	0.713		
Leukocyte	1.126 (0.935,1.356)	0.210		
Neutrophils	1.002 (0.996,1.009)	0.506		
Lymphocytes	0.797 (0.436,1.457)	0.461		
Erythrocyte (◊10^{12}/L)	1.205 (0.550,2.639)	0.641		
Platelet	1.002 (0.996,1.009)	0.506		
Primary tumor size (cm)	1.174 (0.997,1.383)	0.054		
Metastatic tumor size (cm)	1.136 (0.879,1.470)	0.330		
Number of iodine seeds	1.015 (0.997,1.034)	0.108		
Gender				
Male	Ref			
Female	0.385 (0.131,1.134)	0.083		
HBV				
Yes	Ref			
No	0.721 (0.340,1.530)	0.394		
Cirrhosis				
Yes	Ref			
No	0.736 (0.311,1.741)	0.485		
Primary tumor number				
1	Ref			
≥2	1.597 (0.753,3.386)	0.222		
Metastatic tumor number				
1	Ref			
2	1.141 (0.538,2.419)	0.732		
3	1.487 (0.328,6.741)	0.607		
Metastatic sites				
Single organ metastases	Ref		Ref	
Multiple organs metastases	0.366 (0.136,0.985)	0.047	0.458 (0.160,1.306)	0.144
AFP level				
>200	Ref			
<200	0.694 (0.333,1.445)	0.329		
TACE session				
1	Ref			
≥2	0.500 (0.217,1.152)	0.104		
Iodine 125 seeds implantation session				
1	Ref			
≥2	0.428 (0.166,1.099)	0.078		
Child-Pugh				
A	Ref			
B	1.328 (0.605,2.915)	0.479		
ECOG				
0	Ref		Ref	
1	1.315 (0.522,3.317)	0.561	1.361 (0.527,3.510)	0.524
2	10.693 (3.135,36.466)	<0.001	9.038 (2.300,35.521)	0.002

the combination treatment was 19.2 months and the mPFS was 6.8 months (3, 7, 9). The mOS and mPFS of the present study were similar to the results from the IMbrave 150 study (7). However, the patients included in the present study and the IMbrave study were different. It remains unclear whether patients with HCC oligometastases obtain survival benefits from immunotherapy plus tyrosine kinase inhibitors, and more studies are required to explore this treatment. Chen JB et al. studied 40 HCC patients with pulmonary oligometastases who received sorafenib plus regional therapies (radiofrequency ablation, iodine 125 seeds and resection) (26); they reported that the mOS was 18.37 months, which was similar to the mOS in the present study, and the median time to progression was shorter than the mPFS in the present study. The differences may be due to the inclusion of patients with macrovascular invasion in their study, which may influence the tumor response. In the present study, the overall ORR and DCR were higher than those in previous studies (14, 27, 28), indicating that the combination treatment may limit tumor progression. Additionally, we evaluated the metastatic tumor responses after the treatment. The mPFS, ORR and DCR of metastatic sites were longer than the overall mPFS in the present study and the mPFS in previous studies, demonstrated that iodine 125 seeds control metastatic tumors.

TABLE 5 | Univariable regression analysis and multivariable regression analysis for PFS of metastatic sites.

Characteristics	Univariable analysis		Multivariable analysis	
	HR (95%CI)	P value	HR (95%CI)	P value
Age (years)	0.953 (0.918,0.989)	0.011	0.970 (0.938,1.004)	0.082
ALT (U/L)	1.006 (0.995,1.018)	0.273		
AST (U/L)	0.999 (0.988,1.010)	0.851		
Leukocyte	0.979 (0.771,1.243)	0.860		
Neutrophils	0.948 (0.659,1.362)	0.772		
Lymphocytes	0.715 (0.336,1.521)	0.383		
Erythrocyte (◊10^{12}/L)	1.010 (0.436,2.337)	0.982		
Platelet	1.003 (0.996,1.010)	0.409		
Primary tumor size (cm)	1.126 (0.936,1.354)	0.207		
Metastatic tumor size (cm)	1.151 (0.863,1.534)	0.338		
Number of iodine 125 seeds	1.023 (1.002,1.044)	0.035	1.042 (1.014,1.071)	0.004
Gender				
Male	Ref			
Female	0.646 (0.236,1.772)	0.396		
HBV				
Yes	Ref			
No	1.431 (0.645,3.176)	0.378		
Cirrhosis				
Yes	Ref			
No	0.772 (0.299,1.994)	0.593		
Primary tumor number				
1	Ref			
≥2	1.980 (0.840,4.663)	0.118		
Metastatic tumor number				
1	Ref			
2	1.134 (0.487,2.642)	0.771		
3	3.353 (0.697,16.118)	0.131		
Metastatic sites				
Single organ metastases	Ref			
Multiple organs metastases	0.563 (0.204,1.550)	0.266		
AFP level				
>200	Ref			
<200	0.712 (0.323,.1.570)	0.400		
TACE session				
1	Ref			
≥2	0.512 (0.197,1.330)			
Iodine 125 seeds implantation session				
1	Ref			
≥2	0.377 (0.126,1.123)	0.080		
Child-Pugh				
A	Ref			
B	1.315 (0.537,3.221)	0.549		
ECOG				
0	Ref		Ref	
1	1.825 (0.644,5.166)	0.258	1.282 (0.443,3.707)	0.647
2	8.214 (2.152,31.345)	0.002	15.365 (3.137,75.272)	0.001

After exclusion of potential variables that might influence the results, the Cox regression analysis showed that higher ECOG scores were independent worse predictors for OS, PFS and PFS of metastatic sites. Thus, for patients with HCC oligometastases, lower ECOG scores of patients with HCC oligometastases before they receive TACE-I might result in more survival benefits.

In the evaluation of the safety of patients included in the study, a total of nine adverse events were reported. Most of the patients had mild adverse events, but some patients were reported to have severe adverse events (grades III or IV). The adverse events of patients were alleviated after they received symptomatic treatments. Moreover, the dynamic changes in liver functions and blood indices were evaluated. Only lymphocyte counts of patients one month after the treatment were significantly lower than those before the treatment. For future follow-up, the lymphocyte count was within the normal range. In the study, 2 patients had radiation pneumonia after they receiving iodine 125 seeds implantation. It might be that there were 5 patients with HCC metastasized to lung. And the iodine 125 seeds were implanted in the tumors located in lung, which lead to radiation pneumonia. The results of the adverse event analyses showed that patients with HCC oligometastases may tolerate TACE-I.

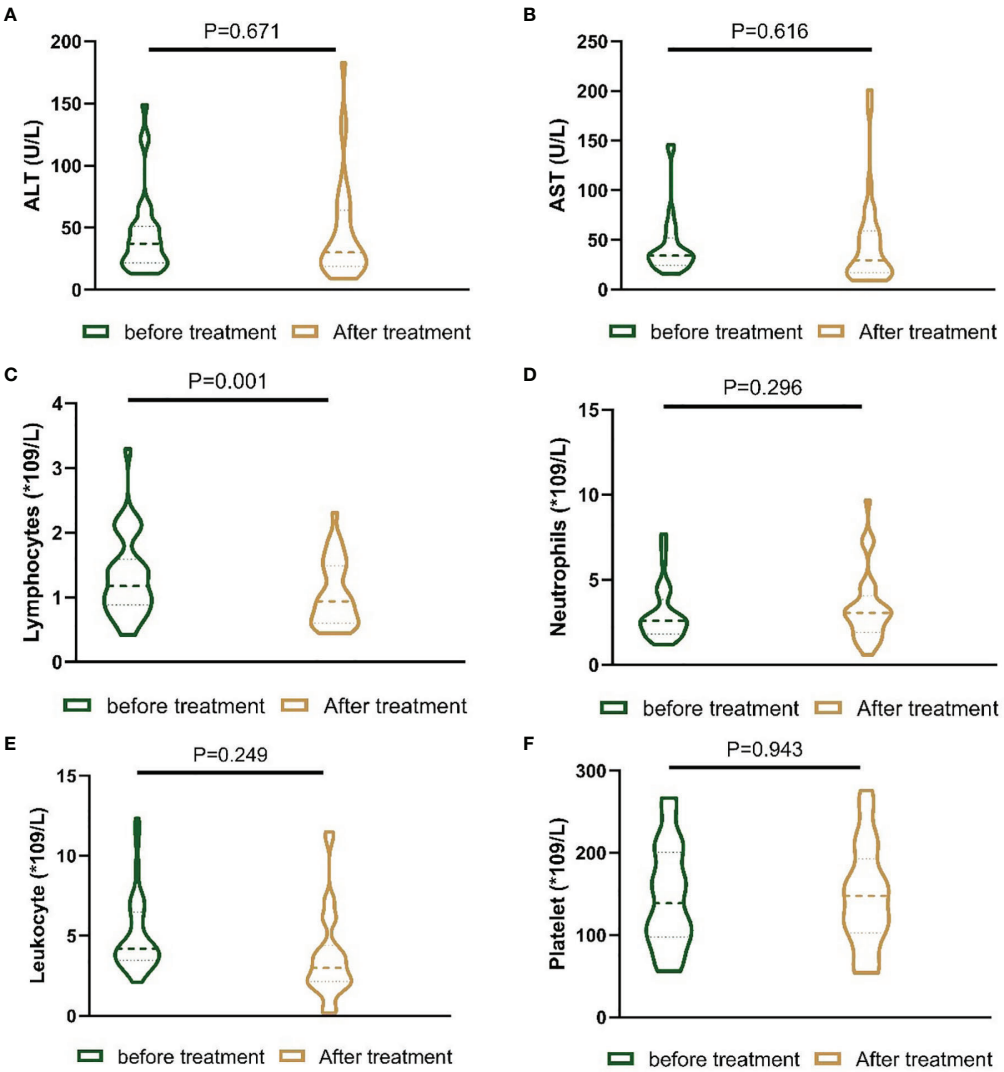

FIGURE 4 | Nested figures for changing of liver function and blood index of patients before the treatment and one month after the treatment. **(A)** Change of ALT; **(B)** change of AST; **(C)** change of lymphocytes; **(D)** change of neutrophils; **(E)** change of leukocyte; **(F)** change of platelet.

TABLE 6 | Adverse events of patients after receiving the treatments.

Adverse events	All grades (N, %)	III or IV grades (N, %)
Postembolism syndrome		
Fever	17 (53.1)	2 (6.3)
Abdominal pain	24 (75)	5 (15.6)
Headache	4 (12.5)	0 (0)
Nausea	18 (56.3)	1 (3.1)
Vomit	7 (21.9)	1 (3.1)
Poor appetite	25 (78.1)	3 (9.4)
Iodine 125 seeds implantation related adverse events		
Leukopenia	5 (15.6)	0 (0)
Bleeding	3 (9.4)	0 (0)
Radiation pneumonia	2 (6.3)	0 (0)

There present study had several limitations. First, the study was a retrospective study, which led to inevitable selection bias. Second, the sample size was small, which may lead to a low level of evidence. Thus, future prospective studies or large sample retrospective studies are needed to confirm the conclusion of the present study.

CONCLUSION

TACE-I may be effective and safe in the treatment of patients with hepatocellular carcinoma oligometastases, thereby providing new evidence for clinics to select suitable treatment for these patients.

DATA AVAILABILITY STATEMENT

The raw data supporting the conclusions of this article will be made available by the authors, without undue reservation.

ETHICS STATEMENT

The studies involving human participants were reviewed and approved by Ethics Committee Board of Tongji Medical College, Huazhong University of Science and Technology. Written informed consent for participation was not required for this study in accordance with the national legislation and the institutional requirements.

AUTHOR CONTRIBUTIONS

WZ, LW, and LC collected the patients' data. LC, LW, and WZ drafted the manuscript. CZ, YL, BS, and TS revised the manuscript. WZ, LC, LZ, and YR analyzed and interpreted the data. LW and WZ made substantial contributions to the conception of the work. YL and CZ made substantial contributions to the design of the work and have revised the manuscript substantively. All authors read and approved the final manuscript.

FUNDING

This study was supported by National Natural Science Foundation of China (No. 81873919 and 81801810).

REFERENCES

1. Siegel RL, Miller KD, Fuchs HE, Jemal A. Cancer Statistics, 2021. *CA. Cancer J Clin* (2021) 71:7–33. doi: 10.3322/caac.21654
2. Sung H, Ferlay J, Siegel RL, Laversanne M, Soerjomataram I, Jemal A, et al. Global Cancer Statistics 2020: GLOBOCAN Estimates of Incidence and Mortality Worldwide for 36 Cancers in 185 Countries. *CA Cancer J Clin* (2021) 71(3):209–49. doi: 10.3322/caac.21660
3. Llovet JM, Kelley RK, Villanueva A, Singal AG, Pikarsky E, Roayaie S, et al. Hepatocellular Carcinoma. *Nat Rev Dis Primers* (2021) 7(1):6. doi: 10.1038/s41572-020-00240-3
4. EASL Clinical Practice Guidelines: Management of Hepatocellular Carcinoma. *J Hepatol* (2018) 69:182–236. doi: 10.1016/j.jhep.2018.03.019
5. Llovet JM, De Baere T, Kulik L, Haber PK, Greten TF, Meyer T, et al. Locoregional Therapies in the Era of Molecular and Immune Treatments for Hepatocellular Carcinoma. *Nat Rev Gastroenterol Hepatol.* (2021) 18:293–313.
6. Hanahan D, Weinberg RA. Hallmarks of Cancer: The Next Generation. *Cell* (2011) 144:646–74. doi: 10.1016/j.cell.2011.02.013
7. Finn RS, Qin S, Ikeda M, Galle PR, Ducreux M, Kim TY, et al. Atezolizumab Plus Bevacizumab in Unresectable Hepatocellular Carcinoma. *N Engl J Med* (2020) 382:1894–905. doi: 10.1056/NEJMoa1915745
8. Kudo M, Finn RS, Qin S, Han KH, Ikeda K, Piscaglia F, et al. Lenvatinib Versus Sorafenib in First-Line Treatment of Patients With Unresectable Hepatocellular Carcinoma: A Randomised Phase 3 Non-Inferiority Trial. *Lancet* (2018) 391(10126):1163–73. doi: 10.1016/S0140-6736(18)30207-1
9. Llovet JM, Ricci S, Mazzaferro V, Hilgard P, Gane E, Blanc JF, et al. Sorafenib in Advanced Hepatocellular Carcinoma. *N Engl J Med* (2008) 359(4):378–90. doi: 10.1056/NEJMoa0708857
10. Gutiontov SI, Pitroda SP, Weichselbaum RR. Oligometastasis: Past, Present, Future. *Int J Radiat Oncol Biol Phys* (2020) 108:530–8. doi: 10.1016/j.ijrobp.2020.02.019
11. Hellman S, Weichselbaum RR. Oligometastases. *J Clin Oncol* (1995) 13:8–10. doi: 10.1200/JCO.1995.13.1.8
12. Lehrer EJ, Singh R, Wang M, Chinchilli VM, Trifiletti DM, Ost P, et al. Safety and Survival Rates Associated With Ablative Stereotactic Radiotherapy for Patients With Oligometastatic Cancer: A Systematic Review and Meta-Analysis. *JAMA Oncol* (2021) 7(1):92–106. doi: 10.1001/jamaoncol.2020.6146
13. Klein EA. Seeing and Not Believing: Oligometastases and the Future of Metastatic Prostate Cancer. *Eur Urol* (2015) 67:864–5. doi: 10.1016/j.eururo.2014.09.035
14. Yen CJ, Kudo M, Lim HY, Hsu CH, Vogel A, Brandi G, et al. Efficacy and Safety of Ramucirumab in Asian and Non-Asian Patients With Advanced Hepatocellular Carcinoma and Elevated Alpha-Fetoprotein: Pooled Individual Data Analysis of Two Randomized Studies. *Liver Sancer* (2020) 9 (4):440–54. doi: 10.1159/000506946
15. Divisi D, Barone M, Zaccagna G, Gabriele F, Crisci R. Surgical Approach in the Oligometastatic Patient. *Ann Trans Med* (2018) 6:94. doi: 10.21037/atm.2018.01.19
16. Siva S, Bressel M, Murphy DG, Shaw M, Chander S, Violet J, et al. Stereotactic Abative Body Radiotherapy (SABR) for Oligometastatic Prostate Cancer: A Prospective Clinical Trial. *Eur Urol* (2018) 74(4):455–62. doi: 10.1016/j.eururo.2018.06.004
17. Chalkidou A, Macmillan T, Grzeda MT, Peacock J, Summers J, Eddy S, et al. Stereotactic Ablative Body Radiotherapy in Patients With Oligometastatic Cancers: A Prospective, Registry-Based, Single-Arm, Observational, Evaluation Study. *Lancet Oncol* (2021) 22:98–106. doi: 10.1016/S1470-2045(20)30537-4
18. Bowden P, See AW, Frydenberg M, Haxhimolla H, Costello AJ, Moon D, et al. Fractionated Stereotactic Body Radiotherapy for Up to Five Prostate Cancer Oligometastases: Interim Outcomes of a Prospective Clinical Trial. *Int J Sancer* (2020) 146(1):161–8. doi: 10.1002/ijc.32509
19. All S, Garant A, Hannan R. Stereotactic Ablative Radiation (SAbR) for Oligometastatic RCC. *Semin Radiat Oncol* (2021) 31:227–34. doi: 10.1016/j.semradonc.2021.02.002
20. Qin QH, Huang BS, Tan QX, Yang WP, Lian B, Wei CY. Radiobiological Effect Induced by Different Activities of (125)I Seed Brachytherapy in a Hepatocellular Carcinoma Model. *Int J Clin Exp Med* (2014) 7:5260–7.
21. Demaria S, Ng B, Devitt ML, Babb JS, Kawashima N, Liebes L, et al. Ionizing Radiation Inhibition of Distant Untreated Tumors (Abscopal Effect) Is Immune Mediated. *Int J Radiat Oncol Biol Phys* (2004) 58(3):862–70. doi: 10.1016/j.ijrobp.2003.09.012
22. Chen L, Sun T, Kan X, Chen S, Ren Y, Cao Y, et al. Transarterial Chemoembolization Combined With Iodine-125 Seed Implantation for Patients With Hepatocellular Carcinoma: A Retrospective Controlled Study. *J Int Med Res* (2020) 48(10):300060520944309. doi: 10.1177/0300060520944309
23. Huang M, Lin Q, Wang H, Chen J, Bai M, Wang L, et al. Survival Benefit of Chemoembolization Plus Iodine125 Seed Implantation in Unresectable Hepatitis B-Related Hepatocellular Carcinoma With PVTT: A Retrospective Matched Cohort Study. *Eur Radiol* (2016) 26(10):3428–36. doi: 10.1007/s00330-015-4198-x
24. Chen L, Kan X, Sun T, Ren Y, Cao Y, Yan L, et al. Transarterial Chemoembolization Combined With Iodine 125 Seeds Versus Transarterial Chemoembolization Combined With Radiofrequency Ablation in the Treatment of Early- and Intermediate-Stage Hepatocellular Carcinoma. *BMC Gastroenterol* (2020) 20(1):205. doi: 10.1186/s12876-020-01355-3
25. Lencioni R, Llovet JM. Modified RECIST (mRECIST) Assessment for Hepatocellular Carcinoma. *Semin Liver Dis* (2010) 30:52–60. doi: 10.1055/s-0030-1247132
26. Chen J, Lu S, Zhang Y, Xu L, Chen J, Wang J, et al. Sorafenib Monotherapy Versus Sorafenib Combined With Regional Therapies for Hepatocellular Carcinoma Patients With Pulmonary Oligometastases: A Propensity Score-Matched Analysis. *J Cancer* (2018) 9(10):1745–53. doi: 10.7150/jca.24568
27. Ikeda K, Kudo M, Kawazoe S, Osaki Y, Ikeda M, Okusaka T, et al. Phase 2 Study of Lenvatinib in Patients With Advanced Hepatocellular Carcinoma. *J Gastroenterol* (2017) 52:512–9. doi: 10.1007/s00535-016-1263-4

28. He W, Liao L, Hu D, Li B, Wang C, Qiu J, et al. Apatinib Versus Sorafenib in Patients With Advanced Hepatocellular Carcinoma: A Preliminary Study. *Ann Trans Med* (2020) 8(16):1000. doi: 10.21037/atm-20-5298

Conflict of Interest: The authors declare that the research was conducted in the absence of any commercial or financial relationships that could be construed as a potential conflict of interest.

Publisher's Note: All claims expressed in this article are solely those of the authors and do not necessarily represent those of their affiliated organizations, or those of the publisher, the editors and the reviewers. Any product that may be evaluated in this article, or claim that may be made by its manufacturer, is not guaranteed or endorsed by the publisher.

frontiers | Frontiers in Oncology

TYPE Original Research
PUBLISHED 22 July 2022
DOI 10.3389/fonc.2022.894246

OPEN ACCESS

EDITED BY
Zaver Bhujwalla,
Johns Hopkins Medicine, United States

REVIEWED BY
Yiming Liu,
Huazhong University of Science and Technology, China
Feng Duan,
First Affiliated Hospital of Chinese PLA General Hospital, China

*CORRESPONDENCE
Po-Hsiang Tsui
tsuiph@mail.cgu.edu.tw
Chih-Horng Wu
chw1020@ntuh.gov.tw

†These authors have contributed equally to this work

SPECIALTY SECTION
This article was submitted to Cancer Imaging and Image-directed Interventions, a section of the journal Frontiers in Oncology

RECEIVED 11 March 2022
ACCEPTED 27 June 2022
PUBLISHED 22 July 2022

CITATION
Wang C-Y, Zhou Z, Chang Y-H, Ho M-C, Lu C-M, Wu C-H and Tsui P-H (2022) Ultrasound single-phase CBE imaging for monitoring radiofrequency ablation of the liver tumor: A preliminary clinical validation. *Front. Oncol.* 12:894246. doi: 10.3389/fonc.2022.894246

Ultrasound single-phase CBE imaging for monitoring radiofrequency ablation of the liver tumor: A preliminary clinical validation

Chiao-Yin Wang[1†], Zhuhuang Zhou[2†], Yu-Hsuan Chang[3], Ming-Chih Ho[4,5,6], Chiu-Min Lu[3], Chih-Horng Wu[3,7*] and Po-Hsiang Tsui[1,8,9*]

[1]Department of Medical Imaging and Radiological Sciences, College of Medicine, Chang Gung University, Taoyuan, Taiwan, [2]Department of Biomedical Engineering, Faculty of Environment and Life, Beijing University of Technology, Beijing, China, [3]Department of Medical Imaging, National Taiwan University Hospital, Taipei, Taiwan, [4]Departments of Surgery, National Taiwan University Hospital and College of Medicine, National Taiwan University, Taipei, Taiwan, [5]Center for Functional Image and Interventional Image, National Taiwan University, Taipei, Taiwan, [6]Department of Surgery, National Taiwan University Hospital Hsin-Chu Biomedical Park Branch, Hsin-Chu, Taiwan, [7]Department of Radiology, College of Medicine, National Taiwan University, Taipei, Taiwan, [8]Division of Pediatric Gastroenterology, Department of Pediatrics, Chang Gung Memorial Hospital at Linkou, Taoyuan, Taiwan, [9]Department of Biomedical Engineering, Chang Gung University, Taoyuan, Taiwan

Radiofrequency ablation (RFA) is an alternative treatment for early-stage hepatocellular carcinoma (HCC). The production of gas bubbles by RFA indicates threshold temperature of tissue necrosis and results in changes in backscattered energy (CBE) when ultrasound monitors RFA. In this study, ultrasound single-phase CBE imaging was used as a means of monitoring RFA of the liver tumor by analyzing the backscattering of ultrasound from gas bubbles in the liver. A total of 19 HCC patients were enrolled in the study. An ultrasound system was used during RFA to monitor the ablation process and acquire raw image data consisting of backscattered signals for single-phase CBE imaging. On the basis of single-phase CBE imaging, the area corresponding to the range of gas bubbles was compared with the tumor sizes and ablation zones estimated from computed tomography. During RFA, ultrasound single-phase CBE imaging enabled improved visualization of gas bubbles. Measured gas bubble areas by CBE were related to tumor size (the Spearman correlation coefficient r_s = 0.86; $p < 0.05$); less dependent on the ablation zone. Approximately 95% of the data fell within the limits of agreement in Bland-Altman plots, and 58% of the data fell within the 95% CI. This study suggests that single-phase CBE imaging provides information about liver tumor size because of the abundant vessels in liver tumors that promote the generation of gas bubbles, which serve as natural contrast agents in RFAs to enhance ultrasound backscattering. Ultrasound single-phase CBE imaging may allow clinicians to determine if

the required minimum RFA efficacy level is reached by assessing gas bubbles in the liver tumors.

KEYWORDS

ultrasound, radiofrequency ablation, CBE imaging, liver tumor, HCC (hepatic cellular carcinoma)

Introduction

The most common form of liver cancer is hepatocellular carcinoma (HCC) (1, 2). Surgical resection and liver transplantation are the two main treatment options for HCC, depending on whether the patient is a suitable transplant candidate (3). HCC patients who are ineligible for surgery or liver transplantation may choose to undergo radiofrequency ablation (RFA) or microwave ablation (MWA), alternative therapies with a minimal invasiveness (3). RFA and MWA have similar therapeutic effects, complication rates, and rates of residual foci of untreated disease; however, RFA can be applied to tumor ablation with fewer sessions (4) and was recommended for safe and effective first-line treatment of early-stage HCC (5–7).

Physicians typically use computed tomography (CT) or ultrasound imaging guidance to place a needle electrode into a liver tumor (8, 9). A contrast-enhanced CT could further be used to monitor the progress of RFA and to assess its efficacy (10). Compared to CT, ultrasound provides a more portable method of guiding needle electrode insertion without radiation concerns. Notably, ultrasound can be difficult to detect the ablation zone for the following reasons: RFA heats up the tissue nearly to boiling point, resulting in gas bubbles which degrade image quality and obscure the ablation zone (11, 12). This is because gas bubbles are acoustically strong scatterers that contribute significant backscattered echoes when interacting with ultrasound. However, studies have shown that the areas of gas bubbles under high-temperature RFA correlates with those being treated by RFA (13–16), implying that the quantitative information obtained from temperature distribution and gas bubbles may be helpful in achieving ultrasound-guided RFA with intraoperative feedback of ablation zone measurements. Therefore, ultrasound monitoring of gas bubbles is critically meaningful and of potential during RFA in spite of not being widely used in clinical applications yet.

Echo time shift, changes in the backscattered energy (CBE), statistics of backscattered signals, and nonlinear parameters of the medium are commonly seen acoustic parameters that assist in the estimation of ultrasound temperature (17). Due to its recent improvements in technical developments and characteristics as described below, CBE may have greater potential in monitoring RFA of liver tumors. The CBE method was initially developed for noninvasive thermometry (18). The underlying mechanism for the temperature dependence of CBE is explained by thermal effects on the scatterers' backscatter coefficients (19, 20). The accurate estimation and imaging of CBE require corrections for temperature-related signal motion effects (i.e., echo time shift); however, motion compensation is not necessary if CBE imaging is positioned solely to visualize thermal distribution (21). In order to use uncompensated CBE to monitor nonuniform heating with an improved contrast resolution and lower computational complexity, integrated CBE imaging (ICBE) utilizing sliding window processing and a polynomial approximation has also been proposed (22). As CBE artifacts are prevalent at the location of the RFA electrode, a recent study proposed ultrasound single-phase CBE imaging based on positive CBE values; an *in vitro* validation demonstrated that single-phase CBE imaging suppressed artifacts and was more accurate in estimating the ablation zone (23). Moreover, RFA-induced gas bubbles may be used as natural contrast agents in CBE imaging, as changes in the level of backscattered signals are susceptible to tissue-air interfaces due to their large difference in acoustic impedance. Therefore, ultrasound single-phase CBE imaging could be a feasible strategy for intraoperative monitoring of clinical RFA for liver tumors.

This study aims to evaluate the effectiveness of ultrasound single-phase CBE imaging in monitoring RFA treatment of liver tumors for HCC patients. To clarify the clinical relevance and position of ultrasound CBE, the range of gas bubbles measured by the proposed method is compared with the tumor size and the ablation zone.

Materials and methods

Subjects

The Institute Review Board (IRB) of National Taiwan University Hospital (NTUH) approved this study (IRB number: 201804053RINC). Subjects signed informed consents

and experiments were conducted in accordance with approved protocols. In total, 19 patients (age: 62.3 ± 11.5 years, range: 42 to 88 years) with newly diagnosed HCC with the Milan criteria who are scheduled for RFA treatments have been recruited, and their demographic information is shown in **Table 1**.

Experimental procedures

Refer to **Figure 1** for experimental procedures. For each patient, CT-guided RFA using iodized oil (Lipiodol, Andre Guerbet, Aulnay-sous-Bois, France) was performed as described in the previous study (24). The tumor size was measured firstly. Depending on the size of the tumor, approximately 2 to 5 mL of iodized oil was applied. An abdominal angiography was conducted, and the infused iodized oil was observed through fluoroscopy until the tumor staining was determined. Afterwards, the patient was transferred to a CT room (Ingenuity 128 CT, Philips, Amsterdam, Netherlands), placed supine, and underwent anesthesia. A commercially available RFA system (Cool-tip, Covidien, Mansfield, MA, USA; BigTip & V-tip, RF Medical, Seoul, Korea; VIVA RF generator, STARmed, Goyang, Korea; LeVeen, Boston Scientific, Natick, MA, USA) was used in the study. Several CT scans were performed to confirm the position of the RFA needle using a 21-gauge Chiba needle. Using a needle electrode (2 cm or 3 cm active tip), tumor ablations were performed until the ablation zones cover the entire tumor.

During the RFA procedure, an ultrasound scanner (Model 2000, Terason, Burlington, MA, USA) and convex array transducer (Model 10L5, Terason) were used to monitor the ablation by an experienced radiologist. The ultrasound transducer was placed axially along the RF electrode and held in a freehand fashion without movement in order to ensure that the needle tip would be clearly visible in the B-scan. The raw data consisted of 256 scan lines of ultrasound backscattered signals at the sampling rate of 12 MHz which were acquired every minute until the RFA was completed. After this, the patient was scanned with a contrast-enhanced CT and the application IntelliSpace Portal (Philips), which is part of the workstation, was used to determine the ablation zone, as shown in **Figure 2**.

It should be noted that the inflammatory response will cause peripheral rim enhancement in hepatic artery phase CT images. Therefore, to minimize the effect of inflammation, porto-venous phase images were used to measure tumor sizes and ablation zones. Moreover, CT and contrast-enhanced ultrasound (CEUS) images can be applied to post-RFA evaluations. However, the CEUS images have relatively lower spatial resolution; comparatively, CT images are still regarded as the gold standard for measuring tumors and ablation zones.

TABLE 1 Demographic data of the patients and RFA parameters used in the study.

Characteristics	
No. of participants	19
Age, years	
Mean ± standard deviation (range)	62.1 ± 12.1 (42.0 – 88.0)
Median	64.0
Tumor size (mm^2)	
Mean ± standard deviation (range)	159.4 ± 78.4 (71.1 – 427.4)
Median	144.0
Heating conditions	
Power range, watt	
Min – max	56 – 140
Last tip temperature, °C	
Mean ± standard deviation (range)	79.8 ± 9.1 (52 – 92)
Median	82.0
Heating time, minute	
Mean ± standard deviation (range)	10.2 ± 1.7 (6 – 12)
Median	11

Ultrasound single-phase CBE imaging

Raw data from the image was then used for ultrasound single-phase CBE imaging. In contrast to conventional CBE imaging which derives its information from the ratio of backscattered energy at each temperature relative to the reference at each pixel (20, 21), single-phase CBE imaging is based on a window-to-window computational scheme which reduces the effects of speckle motion and simplifies the algorithm for practical applications (23). It is illustrated in **Figure 3** and briefly described below how the detailed algorithm described in the previous study (23) operates.

Each raw data set was processed to form an envelope image using an analytic expression for the backscattered signal, and the corresponding B-mode image was constructed using logarithm-compressed envelope images with a dynamic range of 40 dB. Initially, a window is positioned at the upper-left corner of the uncompressed envelope image R_k at each time point ($k = 0, 1, 2, \ldots$ min; R_0 is the preablation data) for acquiring local envelope data $\hat{R_k}$. The regional CBE value (denoted by η_s) is calculated using equation (1) and assigned as the new pixel corresponding to the window location.

$$\eta_s = 10 \cdot log_{10}\left(\frac{E\left[\hat{R}_k^2\right]}{E\left[\hat{R}_0^2\right]}\right). \quad (1)$$

where $E[\cdot]$ denote the statistical mean. Let the window move throughout R_k and R_0 in steps of a certain number of pixels corresponding to a window overlap ratio (WOR) for calculating regional CBE values. After data interpolation, a CBE image with the same size as the original image can be obtained. It should be

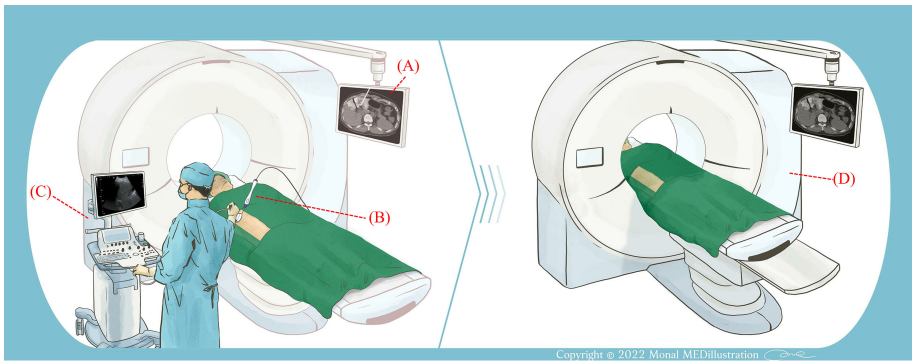

FIGURE 1
Illustration of the experimental procedure. **(A)** CT was used to measure the size of the liver tumor and guide the placement of the RF needle electrode. **(B)** After determining the electrode position, the RFA system was activated and ablation was performed. **(C)** An ultrasound system was used to monitor RFA. The ultrasound transducer was held in a freehand fashion. **(D)** Following RFA, the patient received a contrast injection and CT scans were performed to examine the ablation area.

noted that both positive and negative pixels (denoted by $CBE|_{\eta_s}>0$ and $CBE|_{\eta_s}<0$, respectively) simultaneously exist in a CBE image. Single-phase CBE imaging was defined as $CBE|_{\eta_s}>0$ parametric imaging, which was achieved by adjusting negative values in CBE image 0. Using a technique known as temporal compounding, we were able to collect sufficient information about backscattering from gas bubbles and improve the visualization of ablation zones (25); that is, $CBE|_{\eta_s}>0$ maps acquired at various time points are used for summing and averaging to obtain the temporal compounding $CBE|_{\eta_s}>0$ imaging. Polynomial approximation of the temporal compounding $CBE|_{\eta_s}>0$ image (denoted by $\overline{CBE}|_{\eta_s>0}$) was subsequently applied to visualize temperature distributions and heat conduction behaviors.

In the computational settings, the order of performing polynomial approximation was set to 12, based on empirical data previously obtained (23). The WOR was set to 50%, and the side of the sliding window was three times the pulse length of the ultrasound transducer (6.9 mm).

Data analysis and statistical analysis

In the analysis of $\overline{CBE}|_{\eta_s>0}$ images, the areas within the contours of −1 to −6 dB were segmented to qualitatively measure the regions of shading change within the single-phase CBE image (denoted by $S_{\overline{CBE}|_{\eta_s>0}}$ with mm^2 as the unit). The values of $S_{\overline{CBE}|_{\eta_s>0}}$ were compared with those of tumor sizes and ablation

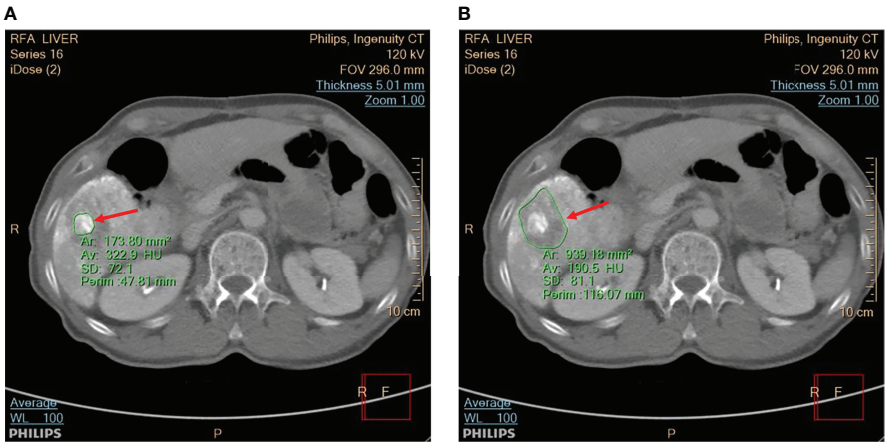

FIGURE 2
The CT scan was utilized to view **(A)** the tumor and **(B)** the ablation zone, as indicated by red arrows. The application IntelliSpace Portal (Philips) was utilized to measure the tumor size and ablation zone size, as shown in the CT images segmented by green contour lines.

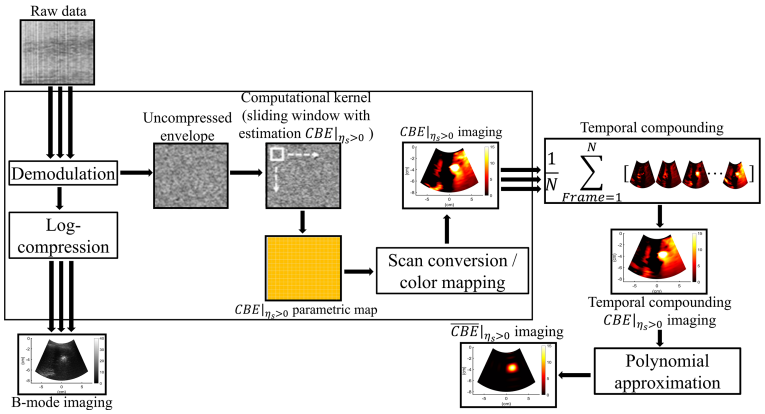

FIGURE 3
The algorithmic scheme for ultrasound single-phase CBE imaging. The uncompressed envelope signals were processed by the sliding window technique to obtain $CBE|_{\eta_s}>0$ images at different time points, which were further combined by temporal compounding. Polynomial approximation of the temporal compounding $CBE|_{\eta_s}>0$ image (denoted by $\overline{CBE}|_{\eta_s>0}$) was subsequently applied to visualize temperature distributions and heat conduction behaviors.

zone sizes using Spearman correlation coefficients r_s (significant differences were identified at $p < 0.05$). Furthermore, data of $S_{\overline{CBE}|_{\eta_s>0}}$, the tumor sizes, and the ablation zone sizes were compared by using paired sample t test, and the Bland-Altman plot was used to compare measurements $S_{\overline{CBE}|_{\eta_s>0}}$ with tumor size and ablation zone size, respectively, in order to evaluate the applicability of ultrasound single-phase CBE imaging in monitoring RFA. Statistical analyses were conducted using SigmaPlot 14.0 (Systat Software, Inc., CA, USA) and MedCalc software (MedCalc Software Ltd, Ostend, Belgium).

Results

Figures 4A, B depict the B-mode and $CBE|_{\eta_s}>0$ images obtained during RFA of the liver tumor at different time points. Due to the generation of gas bubbles associated with the ablation zone, hyperechoic areas were observed in the B-mode image. Although there was no significant change in the image brightness of the ablation zone over time, the spatial distribution of speckle patterns in hyperechoic areas seemed to have increased, presumably due to heat conduction in the liver tumor reflected in increased gas bubble levels. This phenomenon can be revealed in each $CBE|_{\eta_s}>0$ image, which were further combined as the temporal compounding $CBE|_{\eta_s}>0$ and $\overline{CBE}|_{\eta_s>0}$ images, as shown in Figures 4C, D, respectively. Compared with B-scan, $\overline{CBE}|_{\eta_s>0}$ imaging largely suppressed information related to nonablated tissues, and artifacts were also not found to enable estimations of the ablation zone.

Figure 5 shows the tumor size, ablation zone size, and $S_{\overline{CBE}|_{\eta_s>0}}$ for each subject estimated according to various contour criteria. By adjusting the criteria from −1 to −6 dB contours, $S_{\overline{CBE}|_{\eta_s>0}}$ increased accordingly and approximated the size of the tumor. However, both tumor sizes and $S_{\overline{CBE}|_{\eta_s>0}}$ were smaller than the ablation zone sizes, suggesting that the liver tumors were completely covered by the ablation zones; $S_{\overline{CBE}|_{\eta_s>0}}$ was less dependent on the size of the ablation zone. Figures 6, 7 illustrate the dependence of $S_{\overline{CBE}|_{\eta_s>0}}$, respectively, on the size of the ablation zone and the size of the tumor. The values of $S_{\overline{CBE}|_{\eta_s>0}}$ using various contour criteria correlated with the size of the liver tumor ($p < 0.05$; r_s = 0.81 to 0.86 corresponding to −1 to −6 dB contours). No significant differences between $S_{\overline{CBE}|_{\eta_s>0}}$ (−4 to −6 dB contours) and the tumor size were found, as shown in Table 2. Comparatively, r_s between $S_{\overline{CBE}|_{\eta_s>0}}$ and the ablation zone size were approximately 0.3 for each contour criterion, which indicates that $S_{\overline{CBE}|_{\eta_s>0}}$ is not able to characterize the ablation zone. Figure 8 shows the Bland-Altman plots of the differences between the tumor sizes and $S_{\overline{CBE}|_{\eta_s>0}}$ values against the averages of the two sets of measurements. The red lines represent the 95% confidence interval (CI) of the mean difference. The black lines mean the limits of agreement, which are defined as the mean difference plus and minus 1.96 times the standard deviation of the differences. About 95% of the data points fell within the limits of agreement, indicating good agreement between real tumor size and the value estimated by ultrasound single-phase CBE imaging. In particular, 58% of the data fell within the 95% CI when the contour criteria of −6 dB was used. In contrast, less than 30% of the data fitted into the 95% CI when Bland-Altman plots were used to compare the ablation zone size and $S_{\overline{CBE}|_{\eta_s>0}}$, as shown in Figure 9. According to the correlation analysis and Bland-Altman plots, the contour criteria of −6 dB was suggested for using single-phase CBE imaging to measure tumor size.

10.3389/fonc.2022.894246

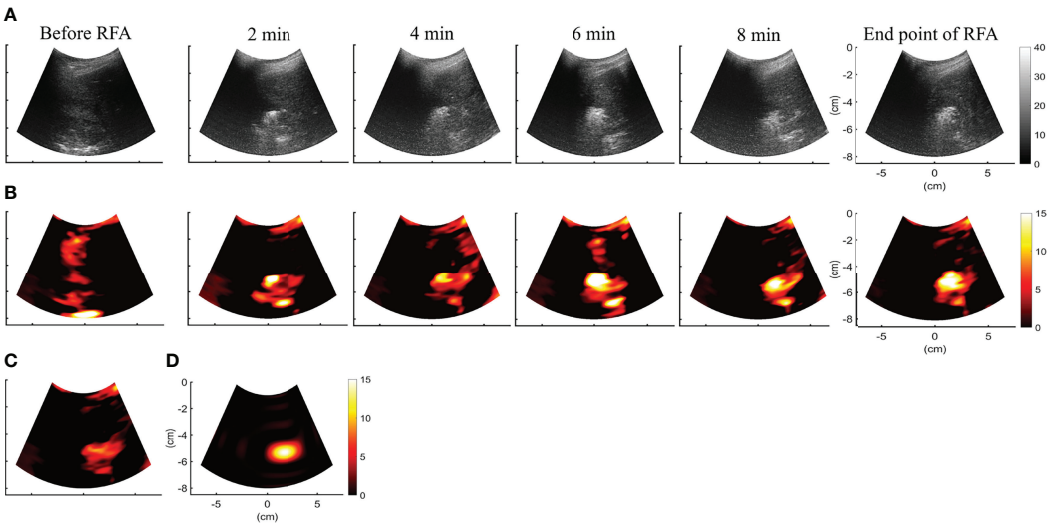

FIGURE 4
(A, B) depict the B-mode and $CBE|_{\eta_s}>0$ images obtained during RFA of the liver tumor at different time points. $CBE|_{\eta_s}>0$ images were further temporally combined as **(C)** $CBE|_{\eta_s}>0$ and **(D)** $\overline{CBE}|_{\eta_s>0}$ images, respectively. Compared with B-scan, $\overline{CBE}|_{\eta_s>0}$ imaging largely suppressed information related to nonablated tissues, and artifacts were also not found to enable estimations of the ablation zone.

Discussion

A successful RFA relies on the application of a thermal dose sufficient to cause coagulation necrosis of the liver tumor (26). Local tumor progression rates may be reduced by generating an adequate ablation zone surrounding the target tumor (27). Therefore, intraoperative monitoring of RFA and estimating the size of the ablation zone and the range of the target tumor should be considered as pointers that clinicians can use to make more precise evaluations of RFA effectiveness. In light of the advances made in CBE imaging, it is now possible to monitor RFA by ultrasound in a clinical setting. During this study, we validated the use of ultrasound single-phase CBE imaging for monitoring RFA of liver tumors. It has been demonstrated that ultrasound single-phase CBE imaging offers better visualization of gas bubbles generated during RFA than conventional B-scan. Further, the assessment of the spatial distribution of gas bubbles according to single-phase ultrasound CBE imaging directly correlated with tumor size; less dependence was seen on the ablation zone. This is the first study that reports *in vivo* CBE-based imaging for the clinical assessment of hepatic tumors. The following sections will discuss physical interpretations, possible underlying mechanisms, implications, applications, and limitations.

According to two kinds of existing theories, the physical meanings of ultrasound single-phase CBE imaging in the RFA procedure are involved in a number of effects. Straube and Arthur (18) proposed their first theory whereby the behavior of CBE is determined by the properties of scatterers (i.e., the thermal effects on the backscatter coefficient). When the temperature increases, the backscattering energies measured from lipid-based scatterers linearly increase, and those returned from aqueous-based scatterers linearly decrease (18–20). Besides temperature, CBE sensitivity is also affected by ultrasound frequency (28), which is an important factor affecting ultrasound backscattering strength (29). CBE is partially explained by the second theory (30), where local changes in speckle patterns are caused by thermal effects to further alter the sound speed and the waveform features of the backscattered ultrasound signal. However, we should note that the above interpretation models are only applicable for temperatures between 30°C and 50°C. Currently, there is no appropriate model to explain the behavior of CBE imaging at high temperatures; however, the previous study suggested that stiffness increases, tissue necrosis, and gas bubble formation might be dominant reasons for CBE under high-temperature RFA (23).

Studies have indicated that the spatial distribution of gas bubbles caused by RFA correlates with the size of the ablation zone (13–16). An *in vitro* study using porcine muscle samples has shown that the range of gas bubbles corresponds to the ablation zone (31). Validation *in vitro* using the porcine liver model also demonstrated that the area of gas bubble distribution observed on ultrasound single-phase CBE imaging was correlated with the size of the ablation zone (23). However, clinical validation in this study indicated that ultrasound single-phase CBE imaging reflected tumor size rather than ablation zone size. Discrepancy between this

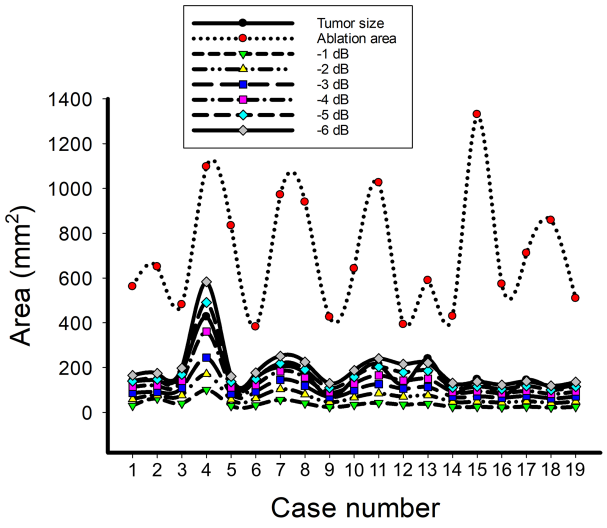

FIGURE 5
The data of the tumor size, ablation zone size, and $S_{\overline{CBE}|_{\eta_s>0}}$ for each subject estimated according to various contour criteria. By adjusting the criteria from −1 to −6 dB contours, $S_{\overline{CBE}|_{\eta_s>0}}$ increased accordingly and approximated the size of the tumor; nevertheless, the ablation zone size was smaller and less dependent on the ablation zone size.

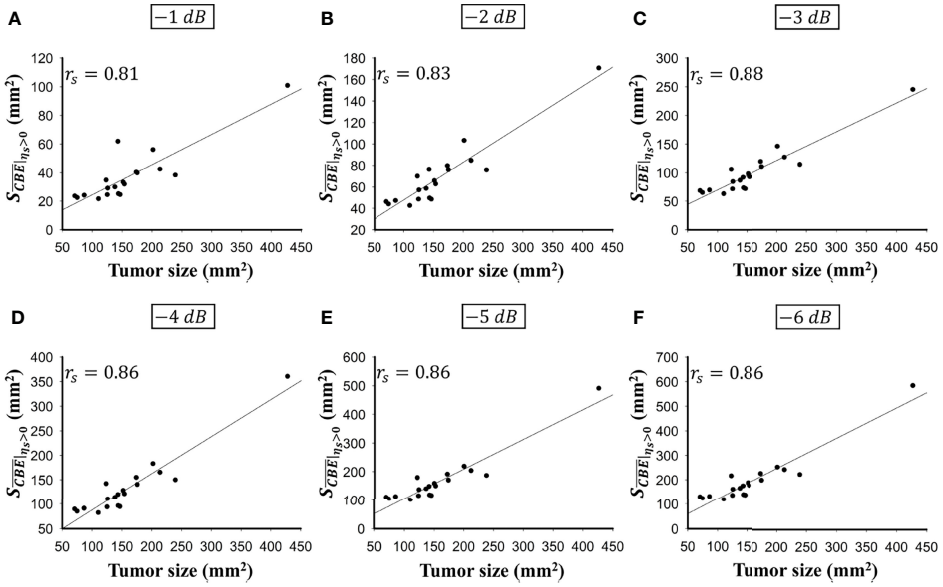

FIGURE 6
The relationship between the tumor size and $S_{\overline{CBE}|_{\eta_s>0}}$ obtained according to various contour criteria. **(A)** −1 dB; **(B)** −2 dB; **(C)** −3 dB; **(D)** −4 dB; **(E)** −5 dB; **(F)** −6 dB. The values of $S_{\overline{CBE}|_{\eta_s>0}}$ using various contour criteria correlated with the size of the liver tumor ($p < 0.05$; r_s = 0.81 to 0.86 corresponding to −1 to −6 dB contours).

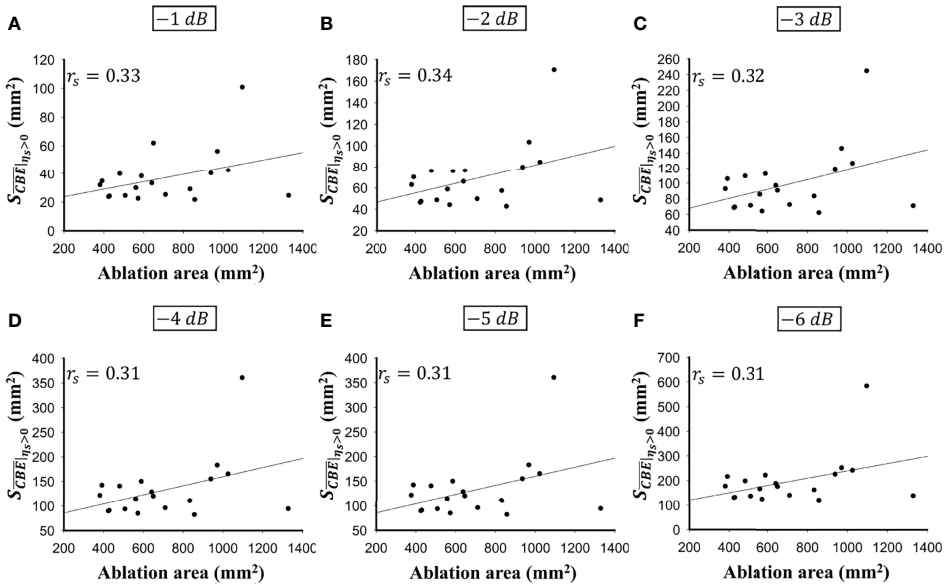

FIGURE 7
The relationship between the ablation zone size and $S_{\overline{CBE}|_{\eta_s>0}}$ obtained according to various contour criteria. **(A)** −1 dB; **(B)** −2 dB; **(C)** −3 dB; **(D)** −4 dB; **(E)** −5 dB; **(F)** −6 dB. The correlation r_s between $S_{\overline{CBE}|_{\eta_s>0}}$ and the ablation zone size were approximately 0.3 for each contour criterion, which indicates that $S_{\overline{CBE}|_{\eta_s>0}}$ is not able to characterize the ablation zone.

finding and previous reports should be discussed for clarification of considerations regarding the proposed method in clinical applications. For the liver, when the tissue temperature rises above 60°C and remains for a few seconds, irreversible damage may occur due to coagulation necrosis (32). A temperature of 60°C was also a critical temperature for generating gas bubbles (31). Therefore, gas bubbles may be considered as a sign of coagulation necrosis.

Note that water content is related to the efficiency of gas bubble formation to some extent, since gas bubbles are a direct result of water vaporization under high-temperature ablation. As previously noted, liver cancer growth requires the formation of new blood vessels (angiogenesis) (33) and HCC is a typically hyper-vascular tumor that exhibits abundant and tortuous vessels (34). Consequently, liver tumors have a relatively high water content, which facilitates significant gas bubble formation when the temperature reaches the threshold level. In practice, a complete ablation zone includes the target tumor that is heated, as well as an adequate margin that is free of tumor tissue for the successful completion of RFA (35). In comparison with the liver tumor, the density of the vascular structures in non-tumor tissues may be relatively low, resulting in less concentration of gas bubbles during RFA, which cannot contribute significant backscattered signals for CBE imaging. Single-phase CBE is unable to describe the ablation zone accurately, however, its ability to depict the tumor size may be considered as a new strategy to evaluate RFA. As the tumor size estimated by ultrasound single-phase CBE imaging corresponds to CT examinations prior to RFA, it indicates that the thermal dose distributed within the target tumor is sufficient to generate gas bubbles, which represent tissue necrosis and fulfill the minimum RFA efficacy requirement.

TABLE 2 Comparisons of data between $S_{\overline{CBE}|_{\eta_s>0}}$ (−1 to −6 dB contours), the tumor sizes, and the ablation zone sizes by using paired sample *t* test.

	Contour of $S_{\overline{CBE}|_{\eta_s>0}}$					
	-1 dB	**-2 dB**	**-3 dB**	**-4 dB**	**-5 dB**	**-6 dB**
Tumor size	9×10^{-7}*	4×10^{-5}*	3×10^{-3}*	0.12	0.41	0.12
Ablation area	1×10^{-9}*	2×10^{-9}*	5×10^{-9}*	9×10^{-9}*	1×10^{-8}*	4×10^{-8}*

*No significant differences between $S_{\overline{CBE}|_{\eta_s>0}}$ (−4 to −6 dB contours) and the tumor size were found, representing that ultrasound single-phase CBE imaging reliably measured tumor size. $p < 0.05$ significant difference.

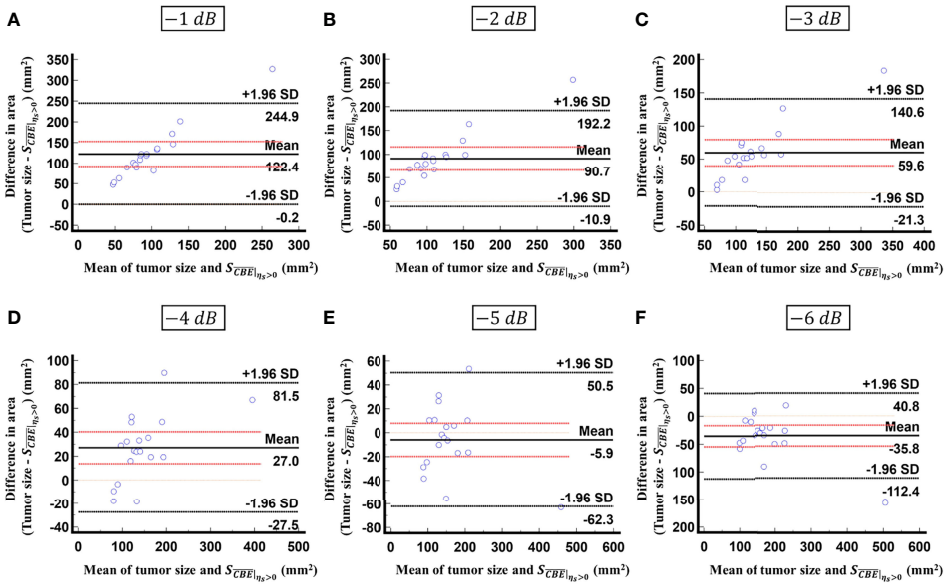

FIGURE 8
Bland-Altman plots of the differences between the tumor sizes and $S_{\overline{CBE}|_{\eta_s>0}}$ values against the averages of the two sets of measurements obtained according to various contour criteria. **(A)** −1 dB; **(B)** −2 dB; **(C)** −3 dB; **(D)** −4 dB; **(E)** −5 dB; **(F)** −6 dB. The red lines represent the 95% CI of the mean difference. The black lines mean the limits of agreement. About 95% of the data points fell within the limits of agreement; in particular, 58% of the data fell within the 95% CI when the contour criteria of −6 dB was used.

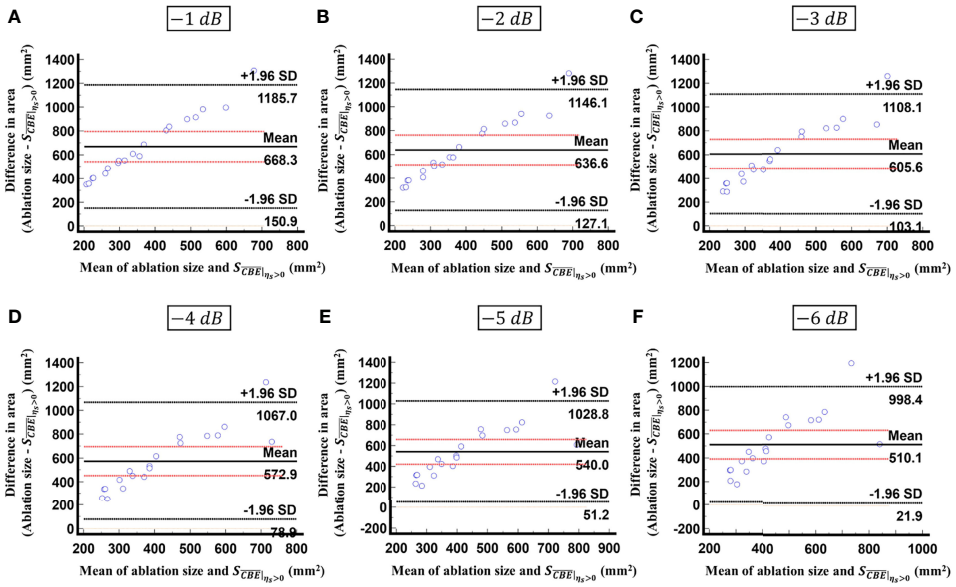

FIGURE 9
Bland-Altman plots of the differences between the ablation zone sizes and $S_{\overline{CBE}|_{\eta_s>0}}$ values against the averages of the two sets of measurements obtained according to various contour criteria. **(A)** −1 dB; **(B)** −2 dB; **(C)** −3 dB; **(D)** −4 dB; **(E)** −5 dB; **(F)** −6 dB. The red lines represent the 95% CI of the mean difference. The black lines mean the limits of agreement. In comparison with the results in **Figure 8**, less than 30% of the data fitted into the 95% CI, indicating that $S_{\overline{CBE}|_{\eta_s>0}}$ is inappropriate for estimating the ablation zone size.

The study has some limitations. The first issue is that the number of patients is not sufficient. There is a need to conduct large-scale clinical trials to more precisely calibrate the correlation between tumor sizes obtained from ultrasound single-phase CBE imaging and CT scans. Additionally, the proposed CBE technique is based on the analysis of ultrasound backscattered echoes returned from gas bubbles, which are however not available in residual tumors due to insufficient thermal dose or unsuccessful ablation. Under this circumstance, CBE is unable to detect residual tumors. Also, CBE-based imaging may not be suitable for monitoring RFA of lower water-content tissues that do not generate gas bubbles easily. Third, freehand handling of the transducer may result in measurement error. Further development of a probe fixer or RF needle guide attached to the ultrasound transducer is needed to improve measurement accuracy by increasing needle visibility and stability. In addition, the monitoring of RFA using single-phase CBE requires an ultrasound imaging system capable of accessing raw image data. The majority of clinical systems are unable to output raw data, so further development of algorithms for ultrasound CBE imaging using B-scan data may be needed to facilitate clinical applications.

In conclusion, the single-phase CBE method is able to detect gas bubbles, which serve as natural contrast agents during RFA to enhance ultrasound backscattering, enabling the use of ultrasound imaging to estimate the tumor size and establish whether the minimum level of RFA efficiency has been achieved.

Data availability statement

The original contributions presented in the study are included in the article/supplementary material, Further inquiries can be directed to the corresponding authors.

Ethics statement

The studies involving human participants were reviewed and approved by the Institute Review Board (IRB) of National Taiwan University Hospital (NTUH) approved this study (IRB number: 201804053RINC). The patients/participants provided their written informed consent to participate in this study.

Author contributions

C-YW and ZZ are equally contributed. C-HW and P-HT contributed to this paper with conception and design. C-YW collected the data and performed ultrasound scan. Y-HC and M-CH performed CT scan and provided interpretation. C-YW, ZZ, and C-ML performed image and statistical analysis. C-YW, ZZ, and P-HT drafted the manuscript. C-HW contributed revision. All authors contributed to the article and approved the submitted version.

Funding

This work was supported by the Ministry of Science and Technology in Taiwan (Grant No. MOST 109-2223-E-182-001-MY3), Chang Gung Memorial Hospital at Linkou in Taiwan (Grant Nos. CMRPD1L0251 and CMRPD1L0081) and National Taiwan University Hospital (Grant No. 108-M4430 and 109-M4557).

Conflict of interest

The authors declare that the research was conducted in the absence of any commercial or financial relationships that could be construed as a potential conflict of interest.

Publisher's note

All claims expressed in this article are solely those of the authors and do not necessarily represent those of their affiliated organizations, or those of the publisher, the editors and the reviewers. Any product that may be evaluated in this article, or claim that may be made by its manufacturer, is not guaranteed or endorsed by the publisher.

References

1. Yang JD, Hainaut P, Gores GJ, Amadou A, Plymoth A, Roberts LR. A global view of hepatocellular carcinoma: trends, risk, prevention and management. *Nat Rev Gastro Hepatol* (2019) 16:589–604. doi: 10.1038/s41575-019-0186-y

2. Lurje I, Czigany Z, Bednarsch J, Roderburg C, Isfort P, Neumann UP, et al. Treatment strategies for hepatocellular carcinoma–a multidisciplinary approach. *Int J Mol Sci* (2019) 20:1465. doi: 10.3390/ijms20061465

3. Daher S, Massarwa M, Benson AA, Khoury T. Current and future treatment of hepatocellular carcinoma: an updated comprehensive review. *J Clin Trans Hepatol* (2018) 6:69–78. doi: 10.14218/JCTH.2017.00031

4. Shibata T, Iimuro Y, Yamamoto Y, Maetani Y, Ametani F, Itoh K, et al. Small hepatocellular carcinoma: comparison of radio-frequency ablation and percutaneous microwave coagulation therapy. *Radiology* (2002) 223:331–7. doi: 10.1148/radiol.2232010775

5. Mukund A, Vats P, Jindal A, Patidar Y, Sarin SK. Early hepatocellular carcinoma treated by radiofrequency ablation-mid- and long-term outcomes. *J Clin Exp Hepatol* (2020) 10:563–73. doi: 10.1016/j.jceh.2020.04.016

6. Yun BY, Lee HW, Min IK, Kim SU, Park JY, Kim DY, et al. Prognosis of early-stage hepatocellular carcinoma: comparison between trans-arterial chemoembolization and radiofrequency ablation. *Cancers* (2020) 12:2527. doi: 10.3390/cancers12092527

7. Lee DH, Lee JM, Lee JY, Kim SH, Yoon JH, Kim YJ, et al. Radiofrequency ablation of hepatocellular carcinoma as first-line treatment: long-term results and prognostic factors in 162 patients with cirrhosis. *Radiology* (2014) 270:900–9. doi: 10.1148/radiol.13130940

8. Zhang Z, Shao G, Zheng J, Wen S, Zeng H, Hao W, et al. Electromagnetic navigation to assist with computed tomography-guided thermal ablation of liver tumors. *Mini Inva Ther Alli Tech* (2020) 29:1–8. doi: 10.1080/13645706.2019.1649699

9. Ziemlewicz TJ, Wells SA, Lubner MG, Brace CL, Lee FT, Hinshaw JL. Hepatic tumor ablation. *Sur Clin North Am* (2016) 96:315–39. doi: 10.1016/j.suc.2015.12.006

10. Yuan C, Yuan Z, Cui X, Gao W, Zhao P, He N, et al. Efficacy of ultrasound-, computed tomography-, and magnetic resonance imaging-guided radiofrequency ablation for hepatocellular carcinoma. *J Cancer Res Ther* (2019) 15:784–92. doi: 10.4103/jcrt.JCRT_836_18

11. Park BK, Kim CK, Choi HY, Lee HM, Jeon SS, Seo SI, et al. Limitation for performing ultrasound-guided radiofrequency ablation of small renal masses. *Eur J Radiol* (2010) 75:248–52. doi: 10.1016/j.ejrad.2009.03.050

12. Lee DH, Lee JM. Recent advances in the image-guided tumor ablation of liver malignancies: radiofrequency ablation with multiple electrodes, real-time multimodality fusion imaging, and new energy sources. *Korean J Radiol* (2018) 19:545–59. doi: 10.3348/kjr.2018.19.4.545

13. Winkler I, Adam D. Monitoring radio-frequency thermal ablation with ultrasound by low frequency acoustic emissions-*in vitro* and *in vivo* study. *Ultrasound Med Biol* (2011) 37:755–67. doi: 10.1016/j.ultrasmedbio.2010.11.008

14. Wang CY, Geng X, Yeh TS, Liu HL, Tsui PH. Monitoring radiofrequency ablation with ultrasound nakagami imaging. *Med Phys* (2013) 40:072901. doi: 10.1118/1.4808115

15. Zhou Z, Wang Y, Song S, Wu W, Wu S, Tsui PH. Monitoring microwave ablation using ultrasound echo decorrelation imaging: an ex vivo study. *Sensors* (2019) 19:977. doi: 10.3390/s19040977

16. Nouso K, Shiraga K, Uematsu S, Okamoto R, Harada R, Takayama S, et al. Prediction of the ablated area by the spread of microbubbles during radiofrequency ablation of hepatocellular carcinoma. *Liver Int* (2005) 25:967–72. doi: 10.1111/j.1478-3231.2005.01145.x

17. Amiri H, Makkiabadi B. A review of ultrasound thermometry techniques. *Front Biol Tech* (2020) 7:82–91. doi: 10.18502/fbt.v7i2.3852

18. Straube WL, Arthur RM. Theoretical estimation of the temperature dependence of backscattered ultrasonic power for noninvasive thermometry. *Ultrasound Med Biol* (1994) 20:915–22. doi: 10.1016/0301-5629(94)90051-5

19. Arthur RM, Straube WL, Trobaugh JW, Moros EG. Non-invasive estimation of hyperthermia temperatures with ultrasound. *Int J Hyperth* (2005) 21:589–600. doi: 10.1080/02656730500159103

20. Trobaugh JW, Arthur RM, Straube WL, Moros EG. A simulation model for ultrasonic temperature imaging using change in backscattered energy. *Ultrasound Med Biol* (2008) 34:289–98. doi: 10.1016/j.ultrasmedbio.2007.07.015

21. Tsui PH, Chien YT, Liu HL, Shu YC, Chen WS. Using ultrasound CBE imaging without echo shift compensation for temperature estimation[1]. *Ultrasound* (2012) 52:925–35. doi: 10.1016/j.ultras.2012.03.001

22. Xia J, Li Q, Liu HL, Chen WS, Tsui PH. An approach for the visualization of temperature distribution in tissues according to changes in ultrasonic backscattered energy. *Comput Math Methods Med* (2013) 2013:1–10. doi: 10.1155/2013/682827

23. Zhang L, Li Q, Wang CY, Tsui PH. Ultrasound single-phase CBE imaging for monitoring radiofrequency ablation. *Int J Hyperth* (2018) 25:548–58. doi: 10.1080/02656736.2018.1512160

24. Wu CH, Liang PC, Su TH, Lin MC, Chang UH, Shih TTF. Iodized oil computed tomography versus ultrasound-guided radiofrequency ablation for early hepatocellular carcinoma. *Hepatol Int* (2021) 15:1247–57. doi: 10.1007/s12072-021-10236-0

25. Zhou Z, Wu S, Wang CY, Ma HY, Lin CC, Tsui PH. Monitoring radiofrequency ablation using real-time ultrasound nakagami imaging combined with frequency and temporal compounding techniques. *PloS One* (2015) 10:118030. doi: 10.1371/journal.pone.0118030

26. Izzo F, Granata V, Grassi R, Fusco R, Palaia R, Delrio P, et al. Radiofrequency ablation and microwave ablation in liver tumors: an update. *Oncologist* (2019) 24:990–1005. doi: 10.1634/theoncologist.2018-0337

27. Kim JH, Kim PN, Won HJ, Shin YM. Percutaneous radiofrequency ablation using internally cooled wet electrodes for the treatment of hepatocellular carcinoma. *Am J Roentgenol* (2012) 198:471–6. doi: 10.2214/AJR.11.6583

28. Tsui PH, Chien YT. Effect of frequency on the change in backscattered ultrasound energy as a function of temperature. *Jpn J Appl Phys* (2012) 51:57001. doi: 10.1143/JJAP.51.057001

29. Shung KK. Diagnostic ultrasound: Imaging and blood flow measurements. *Boca Raton* (2005) 2:28. doi: 10.1201/b18323

30. Li X, Ghoshal G, Lavarello RJ, Oelze ML. Exploring potential mechanisms responsible for observed changes of ultrasonic backscattered energy with temperature variations. *Med Phys* (2014) 41:052901. doi: 10.1118/1.4870964

31. Huang W, Lu J, Tang R, Wu Z, Wang Q, Ding X, et al. Phase contrast imaging based microbubble monitoring of radiofrequency ablation: an ex vivo study. *Front Oncol* (2020) 10:1709. doi: 10.3389/fonc.2020.01709

32. Kim Y, Rhim H, Lim HK, Choi D, Lee MW, Park MJ. Coagulation necrosis induced by radiofrequency ablation in the liver: histopathologic and radiologic review of usual to extremely rare changes. *Radiographics* (2011) 31:377–90. doi: 10.1148/rg.312105056

33. Seo HR. Roles of tumor microenvironment in hepatocelluar carcinoma. *Curr Cancer Ther Rev* (2015) 11:82–93. doi: 10.2174/1573394711666151022203313

34. Zhu XD, Tang ZY, Sun HC. Targeting angiogenesis for liver cancer: past, present, and future. *Genes Dis* (2020) 7:328–35. doi: 10.1016/j.gendis.2020.03.010

35. McDermott S, Gervais D. Radiofrequency ablation of liver tumors. *Semin Int Radiol* (2013) 30:49–55. doi: 10.1055/s-0033-1333653

frontiers | Frontiers in Oncology

TYPE Original Research
PUBLISHED 09 November 2022
DOI 10.3389/fonc.2022.818953

OPEN ACCESS

EDITED BY
Giuseppe Esposito,
MedStar Georgetown University Hospital, United States

REVIEWED BY
Eiichiro Nagata,
Tokai University Isehara Hospital, Japan
Ek Tsoon Tan,
Hospital for Special Surgery, United States

*CORRESPONDENCE
Dian Wang
dian_wang@rush.edu
Xian-Shu Gao
doctorgaoxs@126.com

SPECIALTY SECTION
This article was submitted to Cancer Imaging and Image-directed Interventions, a section of the journal Frontiers in Oncology

RECEIVED 20 November 2021
ACCEPTED 11 October 2022
PUBLISHED 09 November 2022

CITATION
Cao X, Gao X-S, Li W, Liu P, Qin S-B, Dou Y-B, Li H-Z, Shang S, Gu X-B, Ma M-W, Qi X, Xie M and Wang D (2022) Contouring lumbosacral plexus nerves with MR neurography and MR/CT deformable registration technique. *Front. Oncol.* 12:818953. doi: 10.3389/fonc.2022.818953

Contouring lumbosacral plexus nerves with MR neurography and MR/CT deformable registration technique

Xi Cao[1], Xian-Shu Gao[1]*, Wei Li[2], Peilin Liu[1], Shang-Bin Qin[1], Yan-Bin Dou[1], Hong-Zhen Li[1], Shiyu Shang[3], Xiao-Bin Gu[4], Ming-Wei Ma[1], Xin Qi[1], Mu Xie[1] and Dian Wang[5]*

[1]Department of Radiation Oncology, Peking University First Hospital, Beijing, China, [2]Department of Radiology, Peking University First Hospital, Beijing, China, [3]Department of Oncology, Hebei North University, Zhangjiakou, Hebei, China, [4]Department of Radiation Oncology, First Affiliated Hospital of Zhengzhou University, Zhengzhou, Henan, China, [5]Department of Radiation Oncology, Rush University Medical Center, Chicago, IL, United States

Purpose: It is difficult to contour nerve structures with the naked eye due to poor differentiation between the nerve structures with other soft tissues on CT images. Magnetic resonance neurography (MRN) has the advantage in nerve visualization. The purpose of this study is to identify one MRN sequence to better assist the delineation of the lumbosacral plexus (LSP) nerves to assess the radiation dose to the LSP using the magnetic resonance (MR)/CT deformable coregistration technique.

Methods: A total of 18 cases of patients with prostate cancer and one volunteer with radiation-induced lumbosacral plexopathy (RILSP) were enrolled. The data of simulation CT images and original treatment plans were collected. Two MRN sequences (Lr_NerveVIEW sequence and Cs_NerveVIEW sequence) were optimized from a published MRN sequence (3D NerveVIEW sequence). The nerve visualization ability of the Lr_NerveVIEW sequence and the Cs_NerveVIEW sequence was evaluated *via* a four-point nerve visualization score (NVS) scale in the first 10 patients enrolled to determine the better MRN sequence for assisting nerve contouring. Deformable registration was applied to the selected MRN sequence and simulation CT images to get fused MR/CT images, on which the LSP was delineated. The contouring of the LSP did not alter treatment planning. The dosimetric data of the LSP nerve were collected from the dose–volume histogram in the original treatment plans. The data of the maximal dose (D_{max}) and the location of the maximal radiation point received by the LSP structures were collected.

Results: The Cs_NerveVIEW sequence gained lower NVS scores than the Lr_NerveVIEW sequence (Z=-2.887, p=0.004). The LSP structures were successfully created in 18 patients and one volunteer with MRN (Lr_NerveVIEW)/CT deformable registration techniques, and the LSP structures conformed with the anatomic distribution. In the patient cohort, the percentage of the LSP receiving doses exceeding 50, 55, and 60 Gy was

10.3389/fonc.2022.818953

68% (12/18), 33% (6/18), and 17% (3/18), respectively. For the volunteer with RILSP, the maximum irradiation dose to his LSP nerves was 69 Gy.

Conclusion: The Lr_NerveVIEW MRN sequence performed better than the Cs_NerveVIEW sequence in nerve visualization. The dose in the LSP needs to be measured to understand the potential impact on treatment-induced neuropathy.

KEYWORDS

lumbosacral plexus, contouring, radiation-induced plexopathy, MR neurography, multi-modality registration

Introduction

The use of stereotactic body radiation therapy (SBRT) has been increasing for the treatment of abdominal and pelvic malignancies, including prostate cancer and its abdominal/pelvic lymphatic drainage sites (1–4). Although SBRT showed comparable outcomes and toxicities with intensity-modulated radiation therapy in general, there are reports that some patients treated with SBRT developed neurological symptoms, which has prompted us to better delineate the lumbosacral plexus (LSP) for accurate dosimetry analysis during the high-dose irradiation of pelvic tumors (5).

Radiation-induced lumbosacral plexopathy (RILSP) is rare but can cause severe signs and symptoms following pelvic radiation, which often manifests as lower leg pain, numbness, weakness, and paralysis in extreme cases (6). It has been assumed that the pathogenesis of RILSP is related to the fibrosis of the neurovascular bundle following radiation therapy (RT) (7). Limiting the dose to the LSP is therefore considered to reduce the incidence of RILSP, which requires an accurate delineation of the LSP for dosimetric analysis during the high-dose irradiation of pelvic tumors.

The challenge of LSP contouring lies in the poor differentiation between nerves and other soft tissues with similar Hounsfield unit (HU) values (e.g., vessels and muscles) on simulation CT (8). There are generally two methods to contour the LSP at present. The first method is to contour a range of LSPs using anatomical reference points on CT (7). The second method is to contour single or multiple nerves under the guidance of MR *via* image fusion techniques. The former method requires the knowledge of gross/imaging anatomy, which is often not precise, whereas in the latter method, finding the nerve structures on traditional MRI sequences (without the specialized nerve visualization method) is also not easy.

MR neurography (MRN) is a specialized MR technique that visualizes the peripheral nerves *via* suppressing the signals of the fat and blood flow, with the advantage of a high contrast of nerve signals relative to other soft tissues, enabling physicians to identify and track nerve travel more easily on MR (9–11). Furthermore, considering the fact of the change in the spinal curvature between CT and MR examinations, rigid registration may not achieve satisfying results. Deformable registration can match organs with position or shape variations due to body position changes and has been widely applied during clinical RT practice (12–14). The combination of the two novel techniques may be able to address the challenges of LSP nerve contouring. The purpose of this study is to identify one special MR neuroimaging sequence to better delineate the LSP to assess the radiation dose to the LSP using an MR/CT deformable coregistration technique.

Materials and methods

Participants

This prospective study was approved by the Institutional Review Board of the Peking University First Hospital (No. 2021-313). The study design is shown in Figure 1.

Any adult patients with prostate cancer who were required to receive radiation treatment to the pelvis and gave consent to MRN examination were eligible for this study. The inclusion criteria included simulation CT and MRN images ranging from minimally T12 vertebrae to the femoral neck and treatment plan with dose constraints to the conventional pelvic organ at risk (OAR) only (not including dose constraints to LSP nerves). Additional exclusion criteria were general contraindications to MR imaging (e.g., claustrophobia and metal implants) and an interval between MR and CT scanning of more than 2 weeks.

Abbreviations: D_{max}, maximal dose; DVH, dose–volume histogram; EQD2, the equivalent dose in 2 Gy per fraction; FN, L2–L4 nerve roots plus femoral nerve; LSP, lumbosacral plexus; MRN, magnetic resonance neurography; NVS, nerve visualization score; OAR, organ at risk; RILSP, radiation-induced lumbosacral plexopathy; SBRT, stereotactic body radiation therapy; SN, L5-S3 nerve roots plus sciatic nerve.

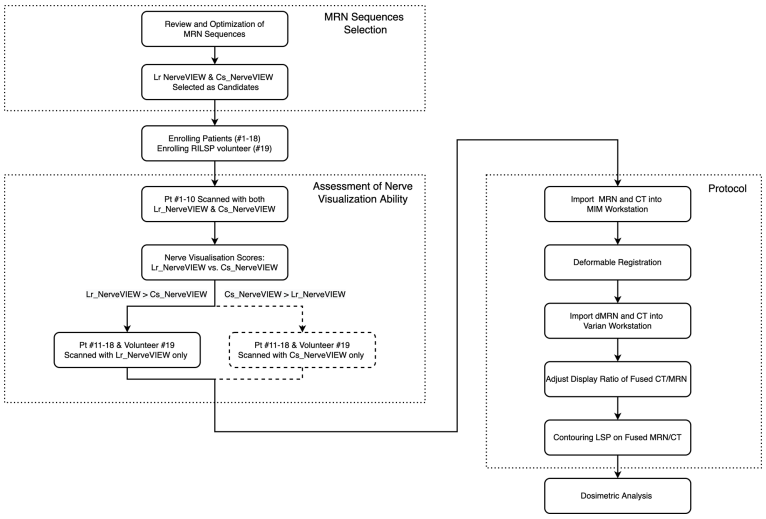

FIGURE 1
Study design flowchart. The flowchart boxes represented by dashed lines refer to the case when cs_NerveVIEW performed better than Lr_NerveVIEW in the assessment of nerve visualization ability, which did not occur in this study. Pt #., patient number; dMR, deformed MR.

In addition to the patient cohort, one volunteer with RILSP also participated in this study. This volunteer was diagnosed with prostate cancer with bone metastases to the right sacrum and the left iliac bone and treated with RT to both the primary site and the metastatic lesions. One month after the completion of RT, the patient developed mild persistent motor weakness in both lower extremities, which is considered as RILSP.

The MRN sequence was applied to 18 patients (patient #1 to #18) as well as the volunteer (#19) with RILSP. To determine the better MRN sequence for this study, the first 10 patients enrolled (#1 to #10) underwent MRN examinations with two different MRN sequences (Lr_NerveVIEW sequence and Cs_NerveVIEW sequence). After determining the sequence that was performing better in the nerve visualization ability, the remaining eight patients (#11 to #18) and the volunteer (#19) underwent this one particular sequence only. Tumor, imaging, and treatment details for all 19 participants are summarized in Table 1.

Imaging technique and magnetic resonance neurography sequences

All MRN images were obtained from a Philips Ingenia 3.0 T (Philips Healthcare, Amsterdam, Netherlands) using a dStream Torso phased array coil. The patients were scanned in the supine position on a plane table with arms crossed on the chest, ranging from the T12 vertebrae to the superior border of the femoral neck. The plane table was used to mitigate the spinal curvature change between CT simulation and MRN examinations.

Two MRN sequences (Lr_NerveVIEW sequence and Cs_NerveVIEW sequence) were established from the optimization of the parameters of an existing MRN sequence, the 3D NerveVIEW sequence (9). The Lr_NerveVIEW sequence is a heavy T2-weighted fast spin-echo MRN sequence with a small voxel of 1.22 mm × 1.25 mm × 2.00 mm. The short tau inversion recovery technique was used as a fat suppression method, and the motion-sensitized driven-equilibrium technique was used to suppress the signals of blood flow to further enhance the contrast of nerve signals to the background. Compared with the 3D NerveVIEW sequence, the field of view of Lr_NerveVIEW was extended to cover from the T12 vertebral body superiorly, the superior margin of the femoral neck inferiorly, the anterior superior iliac spine anteriorly, and the entire lumbosacral foramens posteriorly. The voxel of the Cs_NerveVIEW sequence was further narrowed to 1.2 mm isotropically on the base of the Lr_NerveVIEW sequence to investigate whether a smaller voxel could result in better nerve visualization. To compensate for the weakening of the signal intensity and the prolonged scanning time due to voxel reduction (15, 16), the spectral attenuated in-version recovery technique and the compressed sensing technique were applied to improve the signal-to-noise ratio and reduce the scanning time, respectively.

Evaluation of nerve visualization ability

The MRN images of patients #1 to #10 were reviewed on a PACS system (Philips Healthcare, Netherlands) by a radiation oncologist with over 10 years working experience (XBQ) and a resident (XC). The ability of nerve visualization was evaluated using a four-point grading scale [nerve visualization score

TABLE 1 Participants, tumor, imaging, and treatment.

No.	MRN NerveVIEW	TNM Stage	Purpose	GTV	Dose	Interval
1	Lr and Cs	cT4N0M0	Radical	Prostate and seminal sac	70Gy/25f; 2.8 Gy/f	3d
2	Lr and Cs	cT2N0M0	Radical	Prostate and seminal sac[∫]	70Gy/25f; 2.8 Gy/f	0d
3	Lr and Cs	cT2NxM0	Radical	Prostate and seminal sac	70Gy/25f; 2.8 Gy/f	1d
4	Lr and Cs	cT2cN0M0	Radical	Prostate and seminal sac[∫]	70Gy/25f; 2.8 Gy/f	1d
5	Lr and Cs	pT3bN0M0	Adjuvant	Tumor bed and seminal sac	62.75Gy/25f; 2.5 Gy/f	1d
6	Lr and Cs	cT3bN0M0	Radical	Prostate and seminal sac	70Gy/25f; 2.8 Gy/f	10d
7	Lr and Cs	pT2cN0M0	Adjuvant	Tumor bed and seminal sac	62.75Gy/25f; 2.5 Gy/f	14d
8	Lr and Cs	cT3bN0M0	Radical	Prostate and seminal sac	70Gy/25f; 2.8 Gy/f	1d
9	Lr and Cs	cT2cN0M0	Radical	Prostate and seminal sac	70Gy/25f; 2.8 Gy/f	2d
10	Lr and Cs	cT2aN0M0	Radical	Prostate and seminal sac[∫]	70Gy/25f; 2.8 Gy/f	11d
11	Lr	pT2cN0M0	Adjuvant	Tumor bed and seminal sac	62.75Gy/25f; 2.5 Gy/f	1d
12	Lr	cT2aN0M0	Radical	Prostate[∫]	67.5Gy/25f; 2.7 Gy/f	2d
13	Lr	cT1bN0M0	Radical	Prostate and seminal sac	67.5/25f; 2.7 Gy/f	0d
14	Lr	cT4N1M0	Radical	Prostate, seminal sac and iliac mLNs	70Gy/25f; 2.8 Gy/f	1d
15	Lr	cT2cN0M0	Radical	Prostate and seminal sac[∫]	70Gy/25f; 2.8 Gy/f	5d
16	Lr	cT4N1M0	Radical	Prostate, seminal sac and pelvic mLNs	70Gy/25f; 2.8 Gy/f	2d
17	Lr	cT4N1M0	Radical	Prostate, seminal sac and pelvic mLNs	70Gy/25f; 2.8 Gy/f	0d
18	Lr	cT3bN1M1	Radical	Prostate, seminal sac and pelvic mLNs Left iliac bone metastasis	70Gy/25f; 2.8 Gy/f 50Gy/10f; 5 Gy/f	4d
19	Lr	cT2cN0M1	Radical	Prostate and seminal sec Bone metastases	70Gy/25f; 2.8 Gy/f 65Gy/25f; 2.6 Gy/f	/

No., patient number; GTV, gross tumor volume; CTV, clinical target volume; mLNs, metastatic lymph nodes; Interval, the time interval between the date of simulation CT and MRN. A total of 15 patients in this cohort received radical RT, and 3 patients received adjuvant RT after prostatectomy. The median time interval of CT and MR scanning was 1.5 days.
[∫] No prophylactic whole-pelvic radiation. Otherwise, treated with whole-pelvic radiation (47.5Gy/15f) simultaneously.

(NVS)]: 4, excellent (the entire LSP structure is clearly visualized and is of excellent signal intensity); 3, good (the entire LSP structure is visualized and is of good signal intensity); 2, moderate (a part of the LSP structure is visualized and is of moderate signal intensity); and 1, poor (the LSP structure is not visualized and is of poor signal intensity) (17).

Delineation of lumbosacral plexus with magnetic resonance/CT deformable registration

The MRN sequences with better performance in terms of nerve visualization and simulation CT were imported into the software package MIM (V6.9.4, MIM Software Inc., Cleveland, OH, USA). The workflow "MR to CT—Deformable Registration (Multi-modality method)" was used to achieve the deformable registration of two sets of images. The aligned secondary image (deformed MR), as well as the original simulation CT, was sent to Eclipse v13.5 (Varian Medical Systems, CA, USA).

Deformed MR and simulation CT were automatically registered in Eclipse because they shared the same DICOM frame of reference. The windows and the display ratio of the two images were adjusted to a state in which the nerves "light up" on the CT images (Figure 2). The nerves were contoured by the following steps. First, contour the L2–L4 nerve roots on the axial view and track down (move the plane downward) to contour the femoral nerve as far as possible (the structure contoured in this step was named as "FN"). Second, contour the L5 to S3 roots and track down to contour the sciatic nerve to the superior border of the femoral neck (the structure contoured in this step was named as "SN"). Sometimes, the coronal view may be used to determine the confluence points of the nerve roots and trace these nerves' travel if unclear on the axial view. Finally, move the plane to the top and contour the L1 and T12 roots.

Dosimetric data from dose–volume histogram

All dosimetric analyses were done retrospectively without influencing the original treatment dose planning. The prescription isodoses of the original treatment plan were transferred from Eclipse v13.5. The volumes of the LSP, FN,

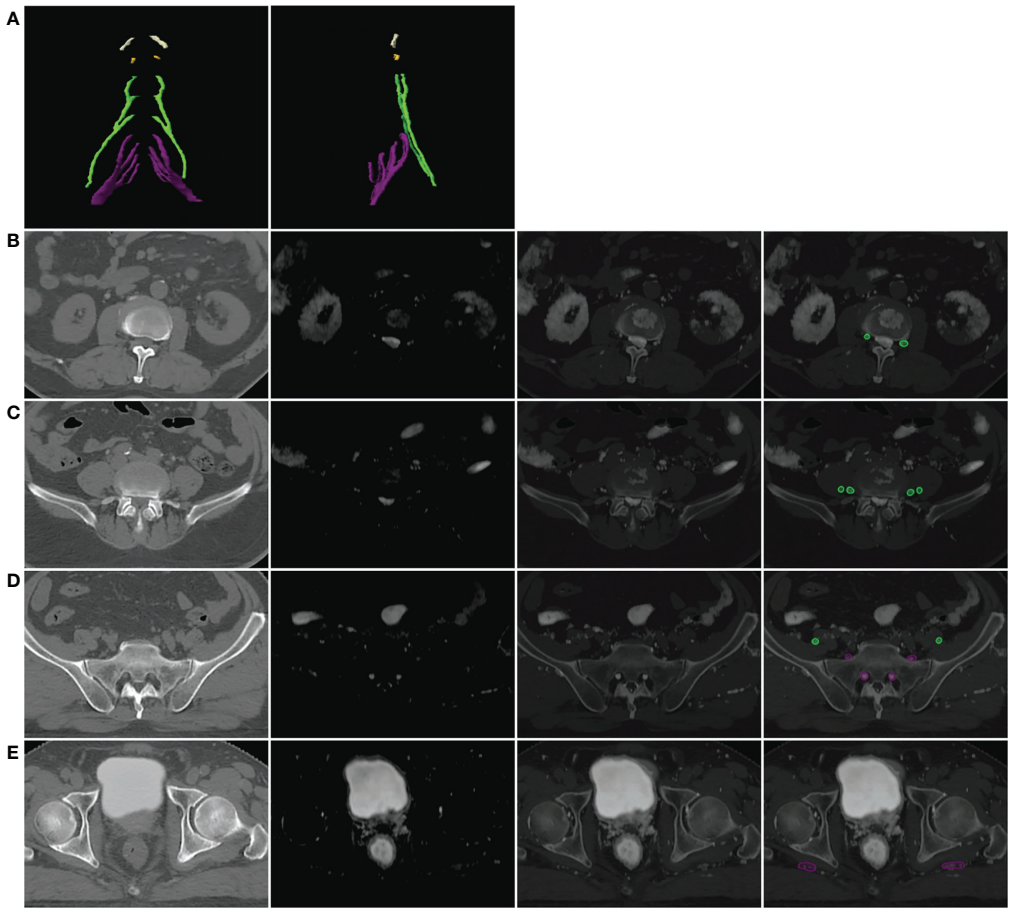

FIGURE 2
Example of the lumbosacral plexus (LSP) in three-dimensional (3D) and axial views. **(A)** LSP in the 3D view: white, T12 nerve root; yellow, L1 nerve root; green, L2–L4 nerve roots and femoral nerve; purple, L5–S3 nerve roots and sciatic nerve. **(B–E)** Axial view of the LSP on the level of L2 intervertebral foramina **(B)**, L4 intervertebral foramina **(C)**, sacrum **(D)**, and the femoral head **(E)**. The first column presented the original simulation CT images. The second column presented deformed MR in the axial view. The third column presented the automatically registered CT and deformed MR images on Eclipse with the display ratio adjusted to a state in which the nerves "light up" on the fusion images. The last column presented the contours of nerves on fusion images.

and SN were calculated. The maximum dose, the mean dose of the LSP, and the percentage of the volume receiving dose ≥50, ≥55, and ≥60 Gy were calculated and recorded. The equivalent dose in 2 Gy per fraction (EQD2) was calculated using a linear quadratic model with $\alpha/\beta_{\text{peripheral nerve}} = 2$ (18).

Statistical analysis

All analyses were done using SPSS v24.0 (IBM, Armonk, NY, USA). A nonparametric test for two related samples (Wilcoxon signed mean rank test) was performed with the NVS during the comparison of the nerve visualization ability, with $p < 0.05$ considered statistically significant. Descriptive statistics were performed with the LSP volume and DVH parameters for patients #1–18 and the volunteer #19.

Results

The whole LSP structures were successfully created in 18 patients and one volunteer utilizing the method described above. An example of this OAR structure in the axial view and the three-dimensional (3D) view is shown from patient #1 in Figure 2.

Nerve visualization

Of the 20 MRN images of patients #1–10, 19 were scored as "4" or "3" by two observers, which means that 95% (19/20) of the MRN images showed clear LSP nerve structures with an excellent or good intensity of signals. There was no statistical difference in the NVS between the two observers ($Z = -1.633$, $p >$

0.05). However, Lr_NerveVIEW gained a higher score than cs_NerveVIEW (median: 4, average: 3.65 *vs*. median: 3, average: 3.15, Z = -2.887, p = 0.004), which indicated that the Lr_NerveVIEW sequence performed better in this study. An example of MRN and traditional MR sequences is shown from patient #7 in Figure 3.

Dose–volume histogram parameters

In the patient cohort (#1–18), the mean LSP volume, the mean FN volume, and the mean SN volume were 52.6 ± 6.5 cm^3 (range, 41.4–68.2 cm^3), 17.5 ± 3.2 cm^3 (range, 13.2–23.5 cm^3), and 33.4 ± 3.7 cm^3 (range, 27.0–42.0 cm^3), respectively. The median maximal dose to the LSP was 53.0 Gy (range: 5.1–74.3 Gy). The percentage of patients whose LSP nerves received a dose over 50, 55, and 60 Gy was 68% (12/18), 33% (6/18), and 17% (3/18), respectively. After excluding the five patients who did not receive prophylactic whole-pelvic radiotherapy (WPRT), the percentage of patients receiving doses exceeding 50, 55, and 60 Gy to the LSP nerves was 92% (12/13), 46% (6/13), and 23% (3/13), respectively (Figure 4). For the volunteer (#19), the maximum doses occurred at the right (69 Gy in actual dose, EQD2 79.4 Gy) and left (62 Gy in actual dose, EQD2 71.3 Gy) sacral nerve roots, respectively (Figure 5).

Discussion

It has been long recognized that high-dose radiation therapy can cause neurotoxicity (19). To avoid delivering unexpected high-dose radiation to the LSP nerves, accurate contouring is the first and foremost condition. In this study, we identified the Lr_NerveVIEW sequence as a suitable MRN sequence for LSP nerve contouring and successfully contoured the LSP nerve structures in 19 participants based on the MRN/CT deformation registration technique. Further dosimetric analysis showed that a considerable proportion of patients (3/13) who underwent regular pelvic radiation had unexpected high-dose radiation to their LSP nerves, which could have been avoided if the LSP nerves were contoured and protected during treatment planning. This is also the case for the patient with RILSP.

In 2012, Sun K. Yi et al. first proposed an empirical method for contouring the LSP based on anatomy and imaging atlas (20). Anatomic structures such as the great vessels and muscles were used as reference points to define the range of LSPs. Although it is a pioneering proposal, there are still several problems associated with complex pelvic anatomy such as a steep learning curve and poor contouring consistency in certain areas (21). Our protocol integrates the advantage of the intuitive nerve visualization of MRN into simulation CT directly, which lowers the requirement for the knowledge of the complex anatomy. It is also not necessary to contour the whole LSP in a case when the tumor is only close to a certain nerve root or nerve. Our protocol enables physicians to personalize the contouring of the LSP as indicated.

Studies concerning radiation-induced plexopathy have been mainly focused on the brachial plexus (BP) in recent years. While contouring guidelines and dose constraints for BP have been well developed (22–24), there are few studies focused on the LSP. Due to the lack of a widely acknowledged method for LSP nerve contouring in the past, the relationship between the dose to LSP nerves and the development of LSP nerve injury was poorly understood. The incidence of RILSP is approximately 1.3%–6.7% (25, 26), but this rate might be underestimated due to the lack of routine screening (6). Most RILSP cases occur when D_{max} exceeds 60 Gy (6, 27), but nerve injury can also occur at a maximum dose at as low as 37 Gy (28). Taking the tolerance

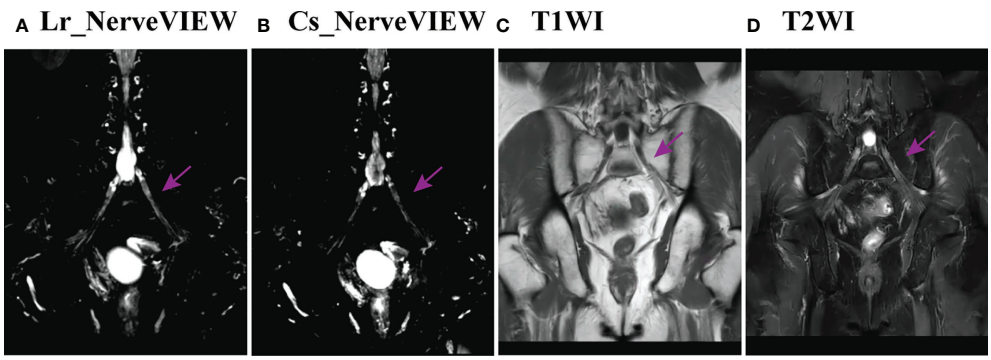

FIGURE 3
Example of the LSP structure in Lr_NerveVIEW **(A)**, cs_NerveVIEW **(B)**, T1-weighted **(C)** sequences, and T2-weighted fat-suppressing sequence **(D)** in the coronal view from patient #7. The purple arrow indicated the left S1 nerve root. The S1 nerve root was clearly seen on Lr_NerveVIEW and Cs_NerveVIEW sequences but appeared slightly "brighter" on the Lr_NerveVIEW sequence. Meanwhile, the same nerve root on T1WI and T2WI sequences appeared vaguer and had worse differentiation with surrounding tissues.

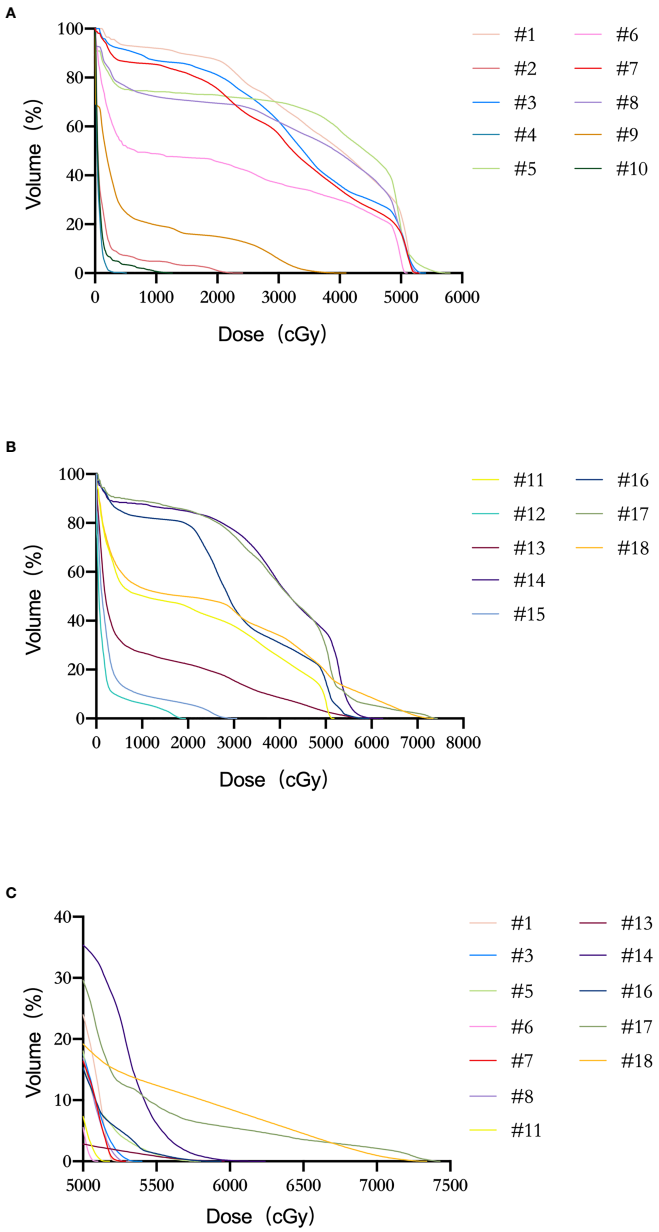

FIGURE 4
Dose–volume histogram (DVH) of LSP nerves for patients #1–18. **(A)** Patients #1–10. **(B)** Patients #11–18. **(C)** Patient with the dose delivered to LSP ≥ 50 Gy.

dose for BP, 66 Gy in conventionally fractionated RT, as a reference (22, 23), it may be reasonable to constrain the LSP dose to 60–66 Gy.

To the best of our knowledge, this is the first study that used MRN to aid the contouring of LSP nerves. Traditional MRI sequences were mainly used in previous studies about MRI-assisted nerve contouring (29–32). A 3D MRN sequence such as Lr_NerveVIEW with superior nerve-to-background contrast could provide improved assistance in LSP nerve contouring. Furthermore, the scanning time of the Lr_NerveVIEW sequence was 7 min and 40 s, which is more clinically acceptable compared with the sequences of research purpose with even smaller voxels but longer scanning time (33). Another originality of this study lies in the deformable registration technique to achieve the precise fusion of images (Supplement Table 2). The use of deformable registration addresses the limitation of rigid registration in real clinical scenarios; that is, the patient is rarely in the same position during two examinations because

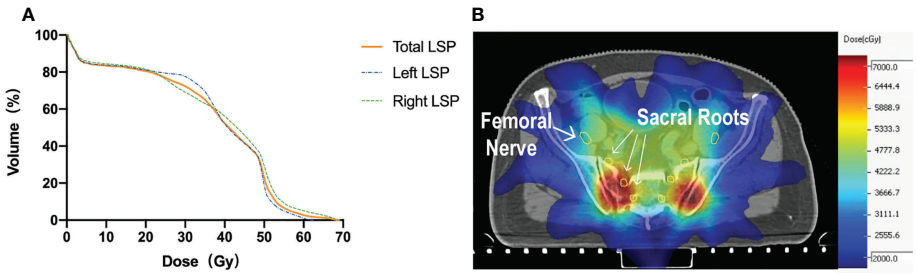

FIGURE 5
(A) DVH of the volunteer (#19) with radiation-induced nerve injury after radiation. **(B)** Isodose level lines and contours of the nerves on simulation CT. Yellow circle: the femoral nerves and sacral nerve roots.

thermoplastic masks are not used during MR scanning. Compared with rigid registration, deformable registration can provide a better localization of LSP nerves.

One limitation of our study is the lack of direct comparison of MRN and traditional MRI sequences. Although not supported by data, MRN does outperform traditional MRI sequences in nerve visualization based on clinical experience and a direct impression of MR images. Additionally, although MRN sequences are available in routine clinical protocols, they are not as widely used as traditional MR sequences. There is also a concern about the economic burden of this additional examination. Both factors limit the wide application of this MRN-based protocol to the daily clinical routine. However, for those who prioritize the protection of LSP nerves (e.g., patients with long life expectancy or patients with strong desire for nerve function preservation), they should be fully informed of this option to perform an MRN as an aiding method to contour LSP nerves for protection.

It is also unclear whether a large dose of radiation delivered to these smaller nerve branches can cause severe neurologic symptoms or not. Even with the Lr_NerveVIEW sequence, we are still unable to assess smaller nerve branches due to the inadequate spatial resolution and suppression of slow-flowing vessels. To address this challenge, more advanced imaging techniques, such as the use of gadolinium-based contrast agents to improve small nerve conspicuity, could be implemented (34).

The small number of patients enrolled is also one of the limitations. Moreover, the cases enrolled all received moderately hypofractionated radiation therapy, although the contouring of the LSP may be more meaningful in the setting of SBRT because SBRT provides an even higher biological equivalent dose. However, considering that this study focused only on the contouring, whether patients received MHRT or SBRT did not affect the conclusion. As for treatment planning, we are now working on collecting more SBRT cases and hope that this method still shows its superiority in correlation with clinical outcomes.

Conclusions

This study identified the Lr_NerveVIEW sequence as a suitable MRN sequence to aid the contouring of LSP nerves. Contouring LSP nerves *via* the MRN/CT deformable registration technique is practical and operable.

Data availability statement

The raw data supporting the conclusions of this article will be made available by the authors, without undue reservation.

Ethics statement

The studies involving human participants were reviewed and approved by Peking University First Hospital. The patients/participants provided their written informed consent to participate in this study.

Author contributions

Study conception and design: X-SG, DW, and XC. Data acquisition: WL, S-BQ, Y-BD, H-ZL, SS, M-WM, XQ, and MX. Data and statistical analysis: XC and PL. Drafting of the manuscript: XC and S-BQ. Critical editorial and writing contributions: X-SG, DW, and XC. All authors contributed to the article and approved the submitted version.

Funding

We are grateful to the funding provided by China International Medical Foundation (grant number: 2019-N-11-08).

Acknowledgments

The authors greatly thank the Department of Radiology, Peking University First Hospital, for teaching MRN interpretation and reserving MR time slots for patients participating in this study.

Conflict of interest

The authors declare that the research was conducted in the absence of any commercial or financial relationships that could be construed as a potential conflict of interest.

Publisher's note

All claims expressed in this article are solely those of the authors and do not necessarily represent those of their affiliated organizations, or those of the publisher, the editors and the reviewers. Any product that may be evaluated in this article, or claim that may be made by its manufacturer, is not guaranteed or endorsed by the publisher.

Supplementary material

The Supplementary Material for this article can be found online at: https://www.frontiersin.org/articles/10.3389/fonc.2022.818953/full#supplementary-material

References

1. Reshko LB, Richardson MK, Spencer K, Kersh CR. Stereotactic body radiation therapy (SBRT) in pelvic lymph node oligometastases. *Cancer Invest* (2020) 38:599–607. doi: 10.1080/07357907.2020.1801713

2. Jackson WC, Silva J, Hartman HE, Dess RT, Kishan AU, Beeler WH, et al. Stereotactic body radiation therapy for localized prostate cancer: A systematic review and meta-analysis of over 6,000 patients treated on prospective studies. *Int J Radiat Oncol Biol Phys* (2019) 104:778–89. doi: 10.1016/j.ijrobp.2019.03.051

3. Yoon SM, Luterstein E, Chu F-I, Cao M, Lamb J, Agazaryan N, et al. Clinical outcomes of stereotactic magnetic resonance image-guided adaptive radiotherapy for primary and metastatic tumors in the abdomen and pelvis. *Cancer Med* (2021) 10:5897-5906. doi: 10.1002/cam4.4139

4. Ito M, Kodaira T, Koide Y, Okuda T, Mizumatsu S, Oshima Y, et al. Role of high-dose salvage radiotherapy for oligometastases of the localised abdominal/pelvic lymph nodes: A retrospective study. *BMC Cancer* (2020) 20:540. doi: 10.1186/s12885-020-07033-7

5. Dagoglu N, Mahadevan A, Nedea E, Poylin V, Nagle D. Stereotactic body radiotherapy (SBRT) reirradiation for pelvic recurrence from colorectal cancer. *J Surg Oncol* (2015) 111:478–82. doi: 10.1002/jso.23858

6. Georgiou A, Grigsby PW, Perez CA. Radiation induced lumbosacral plexopathy in gynecologic tumors: clinical findings and dosimetric analysis. *Int J Radiat Oncol Biol Phys* (1993) 26:479–82. doi: 10.1016/0360-3016(93)90966-y

7. Shimazaki H, Nakano I. [Radiation myelopathy and plexopathy]. *Brain Nerve Shinkei Kenkyu No Shinpo* (2008) 60:115–21.

8. Gebarski KS, Gebarski SS, Glazer GM, Samuels BI, Francis IR. The lumbosacral plexus: Anatomic-radiologic-pathologic correlation using CT. *Radiogr Rev Publ Radiol Soc N Am Inc* (1986) 6:401–25. doi: 10.1148/radiographics.6.3.2825251

9. De Paepe KN, Higgins DM, Ball I, Morgan VA, Barton DP, deSouza NM. Visualizing the autonomic and somatic innervation of the female pelvis with 3D MR neurography: a feasibility study. *Acta Radiol Stockh Swed* (2020) 1987:61. doi: 10.1177/0284185120909337

10. Grasso D, Borreggine C, Melchionda D, Bristogiannis C, Stoppino LP, Macarini L. Role of 3D MRI with proset technique in the evaluation of lumbar radiculopathy. *J Biol Regul Homeost Agents* (2013) 27:817–25.

11. Bergamino C, Hoey SE, de Swarte M, Skelly C. Improved visualization of the lumbar spine nerve roots in dogs using water excitation (ProSet) as opposed to short tau inversion recovery: A retrospective study of two fat suppression MRI sequences. *Vet Radiol Ultrasound Off J Am Coll Vet Radiol Int Vet Radiol Assoc* (2019) 60:323–9. doi: 10.1111/vru.12714

12. Taylor A, Sen M, Prestwich RJD. Assessment of the impact of deformable registration of diagnostic MRI to planning CT on GTV delineation for radiotherapy for oropharyngeal carcinoma in routine clinical practice. *Healthc Basel Switz* (2018) 6:135. doi: 10.3390/healthcare6040135

13. Hamdan I, Bert J, Rest CCL, Tasu JP, Boussion N, Valeri A, et al. Fully automatic deformable registration of pretreatment MRI/CT for image-guided prostate radiotherapy planning. *Med Phys* (2017) 44:6447–55. doi: 10.1002/mp.12629

14. Dyer BA, Yuan Z, Qiu J, Shi L, Wright C, Benedict SH, et al. Clinical feasibility of MR-assisted CT-based cervical brachytherapy using MR-to-CT deformable image registration. *Brachytherapy* (2020) 19:447–56. doi: 10.1016/j.brachy.2020.03.001

15. Chhabra A, Lee PP, Bizzell C, Soldatos T. 3 Tesla MR neurography–technique, interpretation, and pitfalls. *Skeletal Radiol* (2011) 40:1249–60. doi: 10.1007/s00256-011-1183-6

16. Brandão S, Nogueira L, Matos E, Nunes RG, Ferreira HA, Loureiro J, et al. Fat suppression techniques (STIR vs. SPAIR) on diffusion-weighted imaging of breast lesions at 3.0 T: preliminary experience. *Radiol Med (Torino)* (2015) 120:705–13. doi: 10.1007/s11547-015-0508-2

17. Bao H, Wang S, Wang G, Yang L, Hasan M-U, Yao B, et al. Diffusion-weighted MR neurography of median and ulnar nerves in the wrist and palm. *Eur Radiol* (2017) 27:2359–66. doi: 10.1007/s00330-016-4591-0

18. Gillette EL, Mahler PA, Powers BE, Gillette SM, Vujaskovic Z. Late radiation injury to muscle and peripheral nerves. *Int J Radiat Oncol* (1995) 31:1309–18. doi: 10.1016/0360-3016(94)00422-H

19. Chen AM, Hall WH, Li J, Beckett L, Farwell DG, Lau DH, et al. Brachial plexus-associated neuropathy after high-dose radiation therapy for head-and-neck cancer. *Int J Radiat Oncol Biol Phys* (2012) 84:165–9. doi: 10.1016/j.ijrobp.2011.11.019

20. Yi SK, Mak W, Yang CC, Liu T, Cui J, Chen AM, et al. Development of a standardized method for contouring the lumbosacral plexus: A preliminary dosimetric analysis of this organ at risk among 15 patients treated with intensity-modulated radiotherapy for lower gastrointestinal cancers and the incidence of radiation-induced lumbosacral plexopathy. *Int J Radiat Oncol* (2012) 84:376–82. doi: 10.1016/j.ijrobp.2011.11.074

21. Min M, Roos D, Keating E, Kerr L, Mukherjee R, Potter A, et al. External validation of the lumbosacral plexus-contouring protocol developed by yi et al. (IJROBP 2012; 84: 376-82) for pelvic malignancies: Lumbosacral plexus-contouring protocol. *J Med Imaging Radiat Oncol* (2014) 58:117–24. doi: 10.1111/1754-9485.12106

22. Hall WH, Guiou M, Lee NY, Dublin A, Narayan S, Vijayakumar S, et al. Development and validation of a standardized method for contouring the brachial plexus: Preliminary dosimetric analysis among patients treated with IMRT for head-and-neck cancer. *Int J Radiat Oncol Biol Phys* (2008) 72:1362–7. doi: 10.1016/j.ijrobp.2008.03.004

23. Kong F-MS, Ritter T, Quint DJ, Senan S, Gaspar LE, Komaki RU, et al. Consideration of dose limits for organs at risk of thoracic radiotherapy: Atlas for lung, proximal bronchial tree, esophagus, spinal cord, ribs, and brachial plexus. *Int J Radiat Oncol Biol Phys* (2011) 81:1442–57. doi: 10.1016/j.ijrobp.2010.07.1977

24. Yi SK, Hall WH, Mathai M, Dublin AB, Gupta V, Purdy JA, et al. Validating the RTOG-endorsed brachial plexus contouring atlas: An evaluation of reproducibility among patients treated by intensity-modulated radiotherapy for head-and-neck cancer. *Int J Radiat Oncol Biol Phys* (2012) 82:1060–4. doi: 10.1016/j.ijrobp.2010.10.035

25. Dahele M, Davey P, Reingold S, Shun Wong C. Radiation-induced lumbosacral plexopathy (RILSP): An important enigma. *Clin Oncol* (2006) 18:427–8. doi: 10.1016/j.clon.2006.03.004

26. Saphner T, Gallion HH, Van Nagell JR, Kryscio R, Patchell RA. Neurologic complications of cervical cancer. *A Rev 2261 cases. Cancer* (1989) 64:1147–51. doi: 10.1002/1097-0142(19890901)64:5<1147::aid-cncr2820640530>3.0.co;2-1

27. Tunio M, Al Asiri M, Bayoumi Y, Abdullah O Balbaid A, AlHameed M, Gabriela SL, et al. Lumbosacral plexus delineation, dose distribution, and its correlation with radiation-induced lumbosacral plexopathy in cervical cancer patients. *OncoTargets Ther* (2015) 8:21–7. doi: 10.2147/OTT.S71086

28. Coulombe G, Thiessen B, Balkwill S, Aquino-Parsons C. Polyradiculopathy post-concomitant chemoradiation for carcinoma of the uterine cervix treated with pelvic and para-aortic fields. *Gynecol Oncol* (2005) 99:774–7. doi: 10.1016/j.ygyno.2005.08.005

29. Truong MT, Nadgir RN, Hirsch AE, Subramaniam RM, Wang JW, Wu R, et al. Brachial plexus contouring with CT and MR imaging in radiation therapy planning for head and neck cancer. *Radiogr Rev Publ Radiol Soc N Am Inc* (2010) 30:1095–103. doi: 10.1148/rg.304095105

30. Biau J, Dunet V, Lapeyre M, Simon C, Ozsahin M, Grégoire V, et al. Practical clinical guidelines for contouring the trigeminal nerve (V) and its branches in head and neck cancers. *Radiother Oncol J Eur Soc Ther Radiol Oncol* (2019) 131:192–201. doi: 10.1016/j.radonc.2018.08.020

31. Li C-H, Wu VW, Chiu G. A dosimetric evaluation on applying RTOG-based and CT/MRI-based delineation methods to brachial plexus in radiotherapy of nasopharyngeal carcinoma treated with helical tomotherapy. *Br J Radiol* (2019) 92:20170881. doi: 10.1259/bjr.20170881

32. Hwang ME, Mayeda M, Shaish H, Elliston CD, Spina CS, Wenske S, et al. Dosimetric feasibility of neurovascular bundle-sparing stereotactic body radiotherapy with periprostatic hydrogel spacer for localized prostate cancer to preserve erectile function. *Br J Radiol* (2021) 94:20200433. doi: 10.1259/bjr.20200433

33. Van de Velde J, Audenaert E, Speleers B, Vercauteren T, Mulliez T, Vandemaele P, et al. An anatomically validated brachial plexus contouring method for intensity modulated radiation therapy planning. *Int J Radiat Oncol Biol Phys* (2013) 87:802–8. doi: 10.1016/j.ijrobp.2013.08.004

34. Sneag DB, Daniels SP, Geannette C, Queler SC, Lin BQ, de Silva C, et al. Post-contrast 3D inversion recovery magnetic resonance neurography for evaluation of branch nerves of the brachial plexus. *Eur J Radiol* (2020) 132:109304. doi: 10.1016/j.ejrad.2020.109304

Frontiers in Oncology

Advances knowledge of carcinogenesis and tumor progression for better treatment and management

The third most-cited oncology journal, which highlights research in carcinogenesis and tumor progression, bridging the gap between basic research and applications to imrpove diagnosis, therapeutics and management strategies.

Discover the latest Research Topics

See more →

Frontiers

Avenue du Tribunal-Fédéral 34
1005 Lausanne, Switzerland
frontiersin.org

Contact us

+41 (0)21 510 17 00
frontiersin.org/about/contact